ISBN 978-82-326-2492-8 (printed version)
ISBN 978-82-326-2493-5 (electronic version)
ISSN 1503-8181

Doctoral theses at NTNU, 2017:210

Mohammad Amin

# Small-signal Stability Characterization of Interaction Phenomena between HVDC System and Wind Farms

**NTNU**
Norwegian University of Science and Technology
Faculty of Information Technology and Electrical Engineering
Department of Engineering Cybernetics

NTNU
Norwegian University of Science and Technology

Doctoral Thesis
Mohammad Amin
Doctoral theses at NTNU, 2017:210
NTNU

Mohammad Amin

# Small-signal Stability Characterization of Interaction Phenomena between HVDC System and Wind Farms

Thesis for the degree of Philosophiae Doctor

Trondheim, June 2017

Norwegian University of Science and Technology
Faculty of Information Technology and Electrical Engineering
Department of Engineering Cybernetics

NTNU

Innovation and Creativity

**NTNU**

Norwegian University of Science and Technology

Thesis for the degree of Philosophiae Doctor

Faculty of Information Technology and Electrical Engineering
Department of Engineering Cybernetics



ISBN 978-82-326-2492-8 (printed version)
ISBN 978-82-326-2493-5 (electronic version)
ISSN 1503-8181

ITK-report: 2017-13-W

Doctoral theses at NTNU, 2017:210

Printed by Skipnes Kommunikasjon AS

# Abstract

The main objectives of this research work are to determine the underlying mechanisms leading to instability in a system with dominant presence of tightly regulated power electronics components and to identify the causal relationship between power electronics component control algorithm and the grid stability with the purpose of establishing design guidelines that can guarantee the system stability. The research focuses on the analytical investigation of the small-signal stability and interactions between components of an offshore DC grid and verification of such investigation by benchmarking with numerical simulations and laboratory tests. The simulations are employed to assess the influence of active and passive parameter uncertainties while the experiments verify their impact. The research results identify the critical configurations leading to unexpected interactions based on the theoretical analysis and the simulation results, and specify general guidelines for avoiding failures and restoring stability. Small-signal stability analysis in the frequency domain based on the state-space modeling and eigenvalue analysis, and the impedance-based analysis are carried out for the VSC-based HVDC transmission system and wind farms integration through the HVDC system. In this scenario, the stability properties of converter controllers widely used today have been identified and compared using the equivalent impedance analysis. Through this analysis, a controller that emulates the synchronous machine (The synchronverter) was found to exhibit an R-L (resistive-inductive) circuit nature on its equivalent impedance, which conferred this controller a better ability in keeping stability compared to PLL based dq-domain control in point of stability and control in integrating offshore wind farm through an HVDC system. A Grey-Box method for extracting critical controllers bandwidth, when limited information is available about the system, has been developed based on the impedance measurements. This method has proven to be effective in identifying critical parameters and in re-shaping the impedance to restore the stability.

رَبِّ ارْحَمْهُمَا كَمَا رَبَّيَانِىْ صَغِيْرًا

"And look after them with kindness and love, and say:
"O Lord, have mercy on them as they nourished me
when I was small."
(Al-Quraan S.17, V.24)

# To My Parents

# Preface

This Thesis is submitted to the Norwegian University of Science and Technology (NTNU) for partial fulfilment of the requirements for the degree of philosophie doctor. This research work has been conducted at the Department of Engineering Cybernetics, NTNU, Trondheim, with Professor Marta Molinas as main supervisor, co-supervisor Professor Elisabetta Tedeschi and Mentor Dr. Jon Are Suul. Besides the research project, the PhD work also included compulsory course studies corresponding to one semester of full-time studies, and one year of faculty duties. This work has been performed in the period from August 2013 to June 2017. In 2015, The author has been a visiting scholar at Wind Power Research Center, Shanghai Jiao Tong University, China.

This work is partly funded by the project Protection and Fault Handling in Offshore HVDC Grids (ProOfGrids), managed by SINTEF Energy Research and financed by the Norwegian Research Council together with industry partners; EDF, NVE, National Grid, Siemens, Statkraft, Statnett and Statoil. The experiments have been carried out at the Wind Power Research Center, Shanghai Jiao Tong University, China.

# Acknowledgement

First and foremost, I would like to express my deep gratitude to my main supervisor Professor Marta Molinas, for her supervision, continuous support, encouragement and guidance throughout this research work. As a PhD student, I have been so fortunate to have a supervisor with such an enthusiasm and dedication. It has been an honor to have worked with her in these years, and this work could not have formed without her help. Many thanks go to my co-supervisor Professor Elisabetta Tedeschi. I am also grateful to Jon Are Suul for his consistent support, suggestions and guidance in the beginning of my PhD. I greatly acknowledge the support from Salvatore D'Arco, Atle Rygg and Jing Lyu.

Thanks to all the professors of the Department of Engineering Cybernetics and the Department of Electric Power Engineering at NTNU. I appreciate their contributions of time and intriguing ideas to make my study experience productive and stimulating. I humbly thank my fellow PhD candidates at both departments for the nice and friendly working environment I have had during this period.

I would like to thank my friends for their support and help.

I never find words to express my most profound gratitude to my family. I am so grateful to my parents and sisters (Kusum, Shamim and Ayesha) for their help and support which I will never forget in my life. Last, but certainly not least, heartfelt thanks go to my wife, Sakiba, for her love, encouragement and understanding.

June 2017, Trondheim **Mohammad Amin**

# Contents

# List of Tables

# List of Figures

# List of Abbreviations

**ACC** AC Collection

**AC** Alternating Current

**ALSS** Analytical Linearized State-space

**CCSC** Circulating Current Suppression Controller

**CPL** Constant Power Load

**DC** Direct Current

**DSP** Digital Signal Processor

**EMF** Back Electromotive Force

**FFT** Fast Fourier Transform

**FPGA** Field Programmable Gate Array

**GINC** Generalized Inverse Nyquist Criterion

**GNC** Generalized Nyquist Stability Criterion

**GTO** Gate Turn-off Thyristor

**HVDC** High Voltage Direct Current

**IGBT** Insulated-Gate Bipolar Transistor

**LCC** Line Commutated Converter

**MIMO** Multi-input Multi-output

**MMC** Modular Multi-level Converter

**MT-HVDC** Multi-terminal HVDC

**OHL** Overhead Lines

**PCC** Point of Common Coupling

**PF** Power Factory

**PI** Proportional and Integral

**PLL** Phase Locked Loop

**PR** Proportional and Resonance

**pu** Per Unit

**PWM** Pulse Width Modulation

**RHP** Right Half-Plane

**SCR** Short Circuit Ratio

**SG** Synchronous Generator

**SM** Sub-modules

**SRF** Synchronous Reference Frame

**SSO** Sub-synchronous Oscillation

**VSC** Voltage Source Converter

**VSM** Virtual Synchronous Machine

**WECS** Wind Energy Conversion System

**WF** Wind Farm

**WTG** Wind Turbine Generator

# Chapter 1

# Introduction

*The purpose of this introductory chapter is to provide a short overview of the thesis and present the motivation, scope, and contributions.*

## 1.1 Context and Motivation

### 1.1.1 HVDC System Overview

The high voltage direct current (HVDC) transmission system is an efficient, flexible method and economically sound to transmit a large amount of power over a long distance by overhead lines or underground/submarine cables compared to alternating current (AC) transmission system. It is also used to interconnect separate power systems with different power frequencies where the traditional AC transmission system cannot be used. With the development of power electronics, the HVDC transmission is becoming more and more attractive resulting in a steady increase in the application all around the world [1]–[11].

The semiconductor switches used in HVDC converters are thyristor, Gate turn-off thyristor (GTO) or Insulated Gate Bipolar Transistors (IGBT). The HVDC system based on the thyristors is called traditional HVDC or classic HVDC. It also refers to line commutated converter HVDC (LCC-HVDC). Fig. 1.1 shows a configuration of a six pulse LLC converter. The LCC-HVDC has been widely used for five decades. The LCC-HVDC converter produces harmonic on the AC side and these must be prevented from injecting into the AC networks. This converter consumes reactive power in all operating modes. This reactive power is supplied by the reactive power compensation devices e.g. capacitor banks and partly by the AC filters. The classic HVDC system has many advantages over conventional AC transmission [12]. This system has no limits in transmitted distance. It is valid for both overhead lines and cables. It can carry more power for given size of conductors. The control is very fast and accurate. The magnitude and direction of the power flow can be changed very quickly. One disadvantage of this technology is that the commutation for an inverter must be provided by the AC system and cannot provide black start capability.

The HVDC system based on the Voltage source converters (VSCs) is called HVDC light or HVDC plus. It also refers to VSC-based HVDC (VSC-HVDC) system [1], [13]. Fig. 1.2 shows the configuration of two-level and three-level VSC. The semiconductor used in this technology

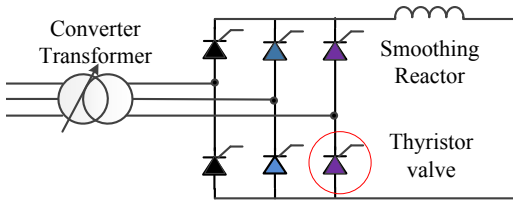


**Figure 1.1:** Configuration of a six pulse LCC converter

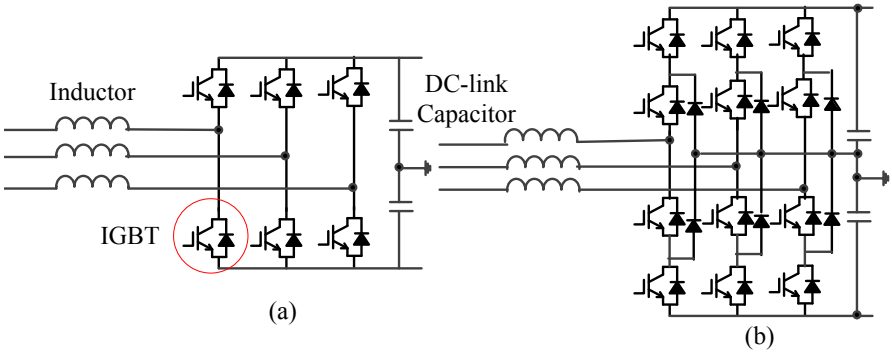


**Figure 1.2:** VSC converter (a) two level and (b) three level

is GTO or IGBT and they operate with high switching frequency typically 1-2 kHz utilizing Pulse Width Modulation (PWM). It can create any waveform of voltage up to a certain limit (phase angle and magnitude of the fundamental component) with the PWM pattern. Therefore, the VSC is considered as a controllable voltage source. It can control both active and reactive power flow in any direction. The high controllability of the VSC allows for wide range of applications. A VSC-HVDC system consists of VSCs, AC filters, transformers, phase reactors, DC capacitors and DC lines or cables. The converter used in actual transmission application is composed a number of elementary converters, that is, of three phase, two level, six-pulse bridges or three-level, 12-pulse bridges. The two-level bridge is the most simple circuit configuration, has been widely used in the various application in wide range of power levels. The two-level bridges consist of six valves and each valve consists of IGBTs or GTOs with an anti-parallel diode.

In the VSC-HVDC system, the converters are connected to the AC networks through a transformer. The transformer is mainly utilized to transform the voltage of the AC system to a level suitable for the converter. High-pass AC filters are installed to prevent the harmonic entering into the AC network. The phase reactors are used to regulate the power flow by regulating the current through them. It does not need to compensate any reactive power consumed by the converter itself. The current harmonic on the AC side is directly related to the PWM frequency and low order harmonic in the current is very small that dramatically reduce the amount of filters compared to the LCC-HVDC system. The design of the capacitor is very important in designing the two-level VSC-HVDC system. It must be considered for both transient and steady state

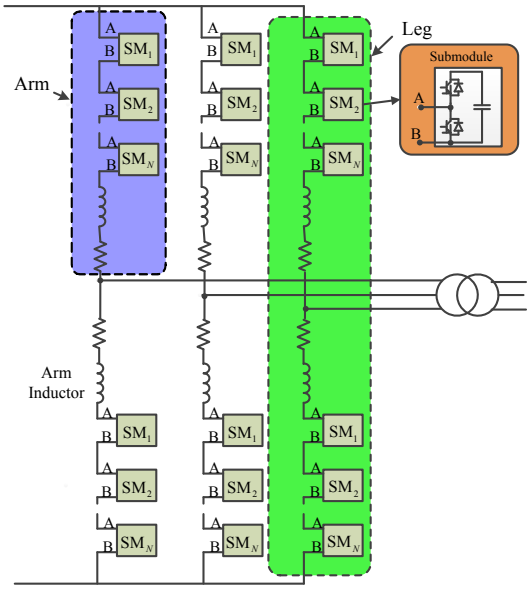


**Figure 1.3:** Basic structure of MMC topology for MMC-HVDC system.

operation. There are two capacitor stacks of the same size are used in the two-level and three-level VSC. The size of the capacitor depends on the required DC voltage level and the amount of power transfer. The main objective of this capacitors is to provide a low inductive path for the turned-off the current and an energy storage to be able to control the power flow and also to reduce the voltage ripple on the DC side.

Recently modular multilevel converter (MMC) has become the most attractive converter topology for the VSC-HVDC systems. Fig. 1.3 shows a configuration of MMC. The MMC has several attractive features compared to the two/three level VSC such as a modular structure, easy scalability in terms of voltage and current, less/no filtering requirement, low expense for redundancy and fault tolerant operation, utilization of standard components, and excellent quality of the output wave forms [14]–[22]. However, MMC has more complex internal dynamics such as required circulating current suppression controller and sub-module (SM) capacitor voltage balancing algorithm, it requires much care in designing and implementing the control system. A basic structure of three-phase MMC topology consists of one upper and one lower arm in each phase leg connected in series with DC terminal. Each arm has a number of identical half-bridge or full-bridge SM and series connected arm inductor and also its equivalent resistor. The arm inductors suppress the high-frequency components from the arm currents. The SMs provide two different voltage level at its terminal depending on the stage of the complementary switches.

Due to having superior advantages of the VSCs which include two-level, three-level and MMC compared to the LCC, in this thesis, the VSC-based HVDC technology is a clear focus.

### 1.1.2 Existing and Proposed VSC-based HVDC Projects

With the expected developments of large-scale offshore wind farms at long distances from the shore, the VSC-HVDC transmission is emerging as the preferred solution for interconnection with the existing onshore power systems [1], [23]. In the long term, it is also expected that the HVDC transmission systems for wind farms are going to be interconnected with the VSC-based point-to-point HVDC interconnections between existing AC grids and gradually form multi-terminal meshed HVDC (MT-HVDC) grids. Such plans have especially been considered relevant in the North Sea region, due to the significant plans for offshore activities in renewable and oil exploration requiring infrastructure for electric power transmission, as well as the possible benefits of more interconnections between the countries surrounding the North Sea [23], [24]. Similar plans for offshore MT-HVDC grids are also considered in the Mediterranean region and for the east coast of the US. Meshed VSC-based HVDC grids have further been envisioned as a large-scale overlay grid for avoiding power system limitations and congestions in mainland Europe [23]. Although there are still significant challenges with the implementation of protection systems and interruption of fault currents in the HVDC grids, construction and operation of large-scale MT-HVDC systems are considered technically feasible with available cables and VSC technology.

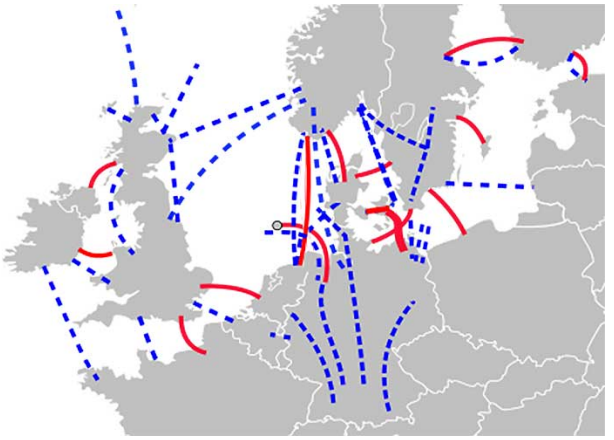

**Figure 1.4:** "Existing (red) and Planned (blue) HVDC links in Europe (courtesy of Dr D van Hertem, KU Leuven, adapted from Messerly, Wikimedia Commons)" [25]

Many VSC-based HVDC projects have been put into operation recently. The first commercial application of HVDC transmission between the Swedish mainland and the island of Gotland used mercury-arc valves in 1954. Nanhui Wind Farm Grid Integration is the first VSC-based project commissioned in Asia in 2011. The MMC structure is used in this project which has a capacity of 18 MW, $\pm 30$ kV DC with a transmission length of approximately 8 km [26]. Zhoushan five-terminal HVDC Project is the World's first MT-HVDC system officially put into operation in 2014 [27]. Some other HVDC transmission systems have been commissioned in Europe. Fig. 1.4 shows the existing and planned HVDC links in Europe [25]. BorWin1 is one of the most remote offshore wind farm clusters in the world connected to the German grid by a 400 MW $\pm 150$ kV HVDC Light transmission system [28]. Several other wind farms integration projects like BorWin2, HelWin1, HelWin2, DolWin1 are adding power to the German

grid through the VSC-based HVDC system [5]. The Skagerrak 4 is another VSC-based HVDC system connected between hydroelectric power based Norwegian grid and thermal power based Danish grid with a capacity of 700 MW [29]. Several HVDC projects such as the Plains & Eastern Clean Line HVDC Project, the Western Spirit Clean Line HVDC project, the Southern Cross HVDC project, the TransWest Express Transmission HVDC Project, have been envisioned to interconnect different states in the USA to supply reliable electric power [30]. More than 200 HVDC projects have been planned or put into operation around the world from which around 35 projects are based on the VSC HVDC system [5]. All the recent HVDC projects are based on VSCs which indicates that the VSC-HVDC is the most popular choice for the power system planner because of having many advantages such as avoidance of commutation failures due to disturbances in the AC network, independent control of the reactive and active power, possibility to connect to a weak AC network, black start capability, faster dynamic response, needed less filtering, even no filtering for MMC-HVDC, no need of transformers to assist the commutation process [1]. The existing AC power systems are therefore combined with the HVDC system to have reliable power supply capability. Initially, the two AC systems will be connected a point-to-point HVDC system which will gradually be expanded to MT-HVDC system.

### 1.1.3 Stability of VSC-HVDC Systems

Despite of its many advantages, VSC-based HVDC transmission systems can experience unexpected instability and interaction phenomena that can lead to failure if proper care has not been taken in designing the system [31], [32]. Therefore, before installing the HVDC system and expanding to MT-HVDC system, there is a significant need for studying such a hybrid AC-DC system that guarantees the reliable and stable operation and prevent the unexpected failure.

There are not yet any practical installations or established test systems available for large-scale MT-HVDC grids to study. Previous studies have been based on simulations of various system configurations and parameters depending on the main issue under investigation. The B4 working groups of CIGRE has proposed a DC grid test system intended as a common reference allowing for easier comparison of results from various types of investigations [33]. This test system can be used to study in a different perspective, for example, to study the large- and small-signal stability analysis, design the protection system, etc. It is also important to understand which interaction or instability phenomena can arise during the stepwise expansion from two-terminal HVDC system to MT-HVDC system. The study of the basic point-to-point configurations needs to be followed by the analysis of a three/four-terminal sub-system, before proceeding to the analysis of the very large MT-HVDC system. Based on the results from a common reference MT-HVDC system, it can be shown the particular instability and interaction that can occur when multiple HVDC converters are connected into a meshed MT-HVDC grid similar to what is expected in the long term for the offshore HVDC grid development.

In classical power systems, the definition of the power system stability is well established. Power system stability is defined in [34], as:

*"The ability of an electric power system, for a given initial operating condition, to regain a state of operating equilibrium after being subjected to a physical disturbance, with most system variables bounded so that practically the entire system remains intact".*

Power systems may undergo various forms of instabilities. The classification of power system instability proposed in [35] is based on

(i) the physical nature of the instability phenomena such as voltage instability, frequency instability, rotor angle instabilities,

(ii) the size of the disturbance considered such as small-signal and large-signal stability and

(iii) the time span that is short-term and the long-term disturbances.

*"Large-signal voltage stability refers to the system's ability to maintain steady voltages following large disturbances such as system faults, loss of generations, or circuit contingencies".* and

*"Small-signal stability is the ability of the power system to maintain synchronism under small disturbances* [35].

Small disturbances occur continually in these systems due to the continuous variation of the loads and generations. In power systems dominated by power electronics, the converters enable the integration of non-conventional power sources to the grid (e.g. wind farms via HVDC system). Due to the complexity of the power electronics converter, different instability and interaction phenomena have been observed in these systems. In the case of wind farms and HVDC systems, small-signal disturbances are expected to occur continually. This thesis limits its focus on this type of instability phenomena and applies small-signal stability analysis to scenarios of wind farm integration via HVDC system.

## 1.2 Problem Statement and Research Questions

### 1.2.1 State-of-the-art in Small-signal Stability and Interaction Analysis of the VSC-based HVDC System

Due to the complexity of the VSC based interconnections and a high number of components with nonlinear nature, different instability and interaction phenomena have been observed in offshore wind farms and installations that comprise a high number of power electronics components. An example is the case of the BorWin1 HVDC transmission system in Germany that remained shut-down for about a year reportedly facing several technical faults which resulted with unplanned shutdowns of the network connection. It did not become clear whether the cause of this lay on the HVDC substation or in the wind farm [31]. The Nanao wind farm HVDC project in China is another example of unexpected phenomena. This wind farm was experiencing sub-synchronous oscillations in the initial phase, which later were found to be caused by particular controllers configurations. The root causes of the oscillation phenomena observed in the cases of BorWin1 and Nanao wind farms are yet poorly understood and rigorous explanation of the origins of these oscillations are not yet reported. Therefore, there is a significant need for developing new methods and tools for assessing the stability of these systems. These methods and tools should enable pre-assessing the impact of these subsystems on the main AC grids or their stability as stand-alone systems. Continuous efforts have been made to investigate the stability and interaction analysis of such systems by different approaches in the time domain and the frequency domain, and some of them are shown in Fig. 1.5. Instability and interaction phenomena such as the interaction of the converters controllers and the grid have

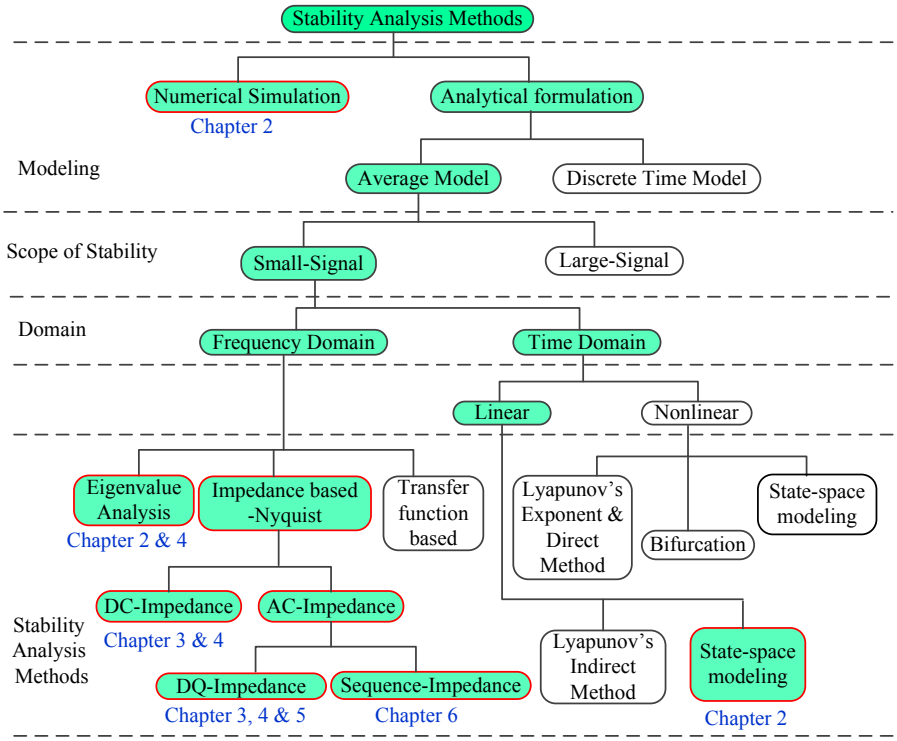


**Figure 1.5:** State-of-the-art in stability analysis methods for power systems dominated by power electronics. Green color indicates the methods treated in this thesis.

not been studied in detailed [23], [33], [36]–[39]. Generalized methods to minimize the control interaction between converters systems and the AC grid, and to design the control of converters that guarantees stable operation, remain open research questions.

One of the well-established methods for stability and interaction analysis for VSC-HVDC systems is based on the state-space modeling and the eigenvalue analysis [36], [37], [40]–[43]. This method can be used to study the large-scale MT-HVDC system. In order to use this method, the system needs to be represented by a small-signal state-space form analytically. Deriving the state-space model analytically for a large system requires much derivation and computational effort and is not an easy task. Transmission System Operators (TSOs) and network developers usually use traditional tools like PSS/E or DigSilent Power Factory for large-scale stability studies. These tools contain separate modules for linearized system eigenvalue analysis. DigSilent Power Factory, as an example of a commercial power system simulation tool, can be used for identifying the critical eigenvalues of the interconnected AC and DC power systems and on revealing how these modes are related to the grid configuration and the various parts of the HVDC converter controllers. The electrical systems are represented by algebraic equations in the phasor-domain in DigSilent Power Factory when calculating the properties of the linearized system model where the dynamics of the AC networks are neglected. The VSC-based HVDC

schemes have time responses that are faster and can exhibit dynamic interactions at higher frequencies than the traditional LCL-oscillations studied in large-scale power systems. Therefore, an important research question is what simplifications are reasonable when studying the stability of the VSC-based HVDC systems.

The state-space modeling and eigenvalue-based approach is a global stability analysis method and this approach determines the stability of the system, regardless of the location of the source of the instability. Two main drawbacks noticed when analyzing the stability and interaction phenomena in VSC-based HVDC systems. The first drawback is that it requires detailed modeling of the VSC system. Secondly, the VSC systems are modeled based on the average modeling of the converters which neglects the pulse width modulation (PWM) and digital signal processing (DSP) delays resulting in that it cannot identify sustained harmonic oscillation in the VSC-based HVDC system [44]. Therefore, an alternate approach is needed to overcome these drawbacks when studying the VSC-based HVDC system.

Another small-signal stability and interaction analysis method is the impedance based analysis. Recently the impedance-based method has been widely used to determine the stability of power electronics based power systems. This method initially used for DC-DC converters [45] and is widely used now in AC-DC converters. The impedance-based method is used on the AC side at interfacing point connecting to the main AC grid either in the sequence-domain [46]–[49] or the dq-domain [50]–[55]. A relation between the modified sequence-domain impedance and the dq-domain impedance for VSCs has been developed [56] and the impact of the off-diagonal term on the stability has been discussed [57]. The impact of the current control-loop bandwidth and the PLL-loop bandwidth of the VSC, converter $LC$ filter has been investigated in the AC side using the impedance-based method [49], [50]. In those cases, it is assumed that the DC-link voltage is stable and decoupled by the DC-link capacitance; thus the DC-link capacitance and other dynamics are neglected and have been replaced by a DC source. The resonance caused by the DC-link capacitance in a VSC-HVDC system has been investigated by the impedance method at the DC side interfacing point [58]. Moreover, Xu *et. al.* in [58] reported that the instability resulting from the grid strength cannot be determined by the impedance-based method applied in the DC interfacing point. Moreover, the instability caused by an imperfect tuning of the outer-loop power-controller cannot be determined by the DC impedance-based method [59]; however, the impedance-based method used at the AC interfacing point can accurately determine the stability. The impedance-based stability analysis method provides a good way to assess the stability and interaction phenomena of VSC-based HVDC transmission systems. The impedance-based method can be used to tune the individual converters of the VSC-HVDC system that guarantees the system stability and minimize the interaction phenomena.

Researchers have so far focused on determining the stability of the power electronics-based power system either by the eigenvalue-based method [36], [37], [40]–[43] or the impedance-based method [45]–[48], [50]–[52]. A weakness of the impedance method is the limited observability of certain states given its dependence on the definition of local source-load subsystems which makes it necessary to investigate the stability at different subsystems interfaces. A comparison and relation between these two methods have not yet been established. What is the relation between these two methods and what are the advantages and disadvantages when these two methods are used to assess the stability of the HVDC system needs to be better understood.

### 1.2.2 Impact of Power Flow Direction on the Stability- Control Challenges

A common practice when designing the control of an HVDC is that the DC voltage controlled-converter operates as an inverter and the power controlled-converter operates as a rectifier [58], [60]. Thus, the active power flows in one direction from the power control to the DC voltage controlled-converter. If it is necessary to change the power flow direction, the control mode between the converters needs to be changed. However, the HVDC systems are appearing more and more and it is becoming a requirement that the VSCs operate both as an inverter and a rectifier without changing the controls to provide the flexibility of having power flows both directions, as an AC transmission system in which two AC networks support each other. It has been observed that the HVDC system operates stably when the power flow direction is from the power controlled-converter to the DC voltage controlled-converter and it becomes unstable when the power flow direction has been altered. Existing impedance-based stability methods cannot determine the stability when the power flow direction has been altered. Moreover, in the literature most researchers have so far focused on the AC impedance modeling either in the positive-negative sequence [48], [49] or in the dq-frame [51], [61], and considered to have an ideal voltage source or a current source on the DC side in which the DC lines/cables impedance are neglected. However, in a VSC-based HVDC system, the DC side network dynamics have a significant impact on the system stability. Therefore, the impact of the DC line impedance must be considered in the stability analysis. A DC impedance-based resonance analysis for the VSC-HVDC system is investigated for different value of the DC link capacitance in [58]; however, it doesn't include the detailed stability analysis. Another DC impedance-based stability method has been presented in [62]; however, these papers have not discussed the impact of the power flow direction on the stability.

In order to apply the impedance-based stability method, it is necessary to determine the source and the load impedances. A method for determining the current source and the voltage source for the DC system has been presented in [63] in which the subsystem connected in series with an inductor is assumed to be the current source while the subsystem connected in parallel with a capacitor is assumed to be the voltage source. Moreover, in the literature the subsystem which regulates the voltage is assumed to be the voltage source and other converter is assumed to be the current source regardless of the direction of the current (power flow). Hence, the system can be represented by an equivalent small-signal impedance model consisting of both the voltage source and the current source, and the stability can be determined from the minor loop gain which is the ratio of the voltage source to the current source impedance [46]. However, the stability of a system consisting of a current source and a voltage source system cannot be determined for both directions of the active power flow. A method based on the Generalized Inverse Nyquist Criteria (GINC) has been presented in [64] which could be useful to analyze such instability problem but it does not give any indication when to use the Generalized Nyquist Criteria (GNC) or GINC for a case when the power flow direction has been altered.

It is, therefore, important to design the control system which makes the system operate stably in both directions of power flows. In order to design the appropriate control, the instability problem needs to be defined analytically. In an attempt to do that, an impedance based method is proposed and the HVDC converter stations are represented by its Norton equivalent current source with parallel connected impedance, and the source and the load impedance are determined based on the power flow direction. The identification of the source and the load impedance


**Figure 1.6:** Experimental setup of VSC- and MMC-HVDC system.

is based on the power flow direction which is a new method presented in this work. The stability analysis has been performed for two different directions of power flow where the method can determine the stability for both directions of power flow and the theoretical analysis has been verified by time domain simulation and by experiments. Fig. 1.6 shows the setup used for the experimental validation of the theoretical analysis.

### 1.2.3 Interaction Phenomena between Offshore Grid and Wind Farms

The stability of the offshore wind power network connected through HVDC transmission line is a critical problem since the offshore AC collection (ACC) bus is not connected to a strong AC grid. Moreover, no rotating machine is connected directly to the AC collection bus since the wind turbine generators are connected to the AC collection point through AC-DC-AC converters due to their variable speed operation. Field experience has shown that sub-synchronous oscillation (SSO) and harmonic resonance can occur between the wind farms and HVDC systems [32], [49], [65]. The oscillations can appear in the presence of background harmonics from the controller interaction of the wind energy conversion system (WECS) inverter controller and HVDC rectifier controller [49], [55]. These SSO and harmonic resonance phenomena are reported by many researchers [66]–[71] but the mechanism at the source of it, it is yet poorly understood. Therefore, pre-assessing the stability of the offshore wind farms connected via HVDC systems is mandatory before connecting to an existing grid. Existing approaches for the stability analysis are based on the small-signal stability analysis such as modeling the interconnected system in state-space form and finding the eigenvalues [36], [41], [43] and the impedance-based analysis [49], [65].

The eigenvalue-based analysis has broadly been used to determine the stability of wind turbine system [72], two-terminal and multi-terminal VSC- and MMC-based HVDC transmission system [41], [42], [73], and harmonic stability assessment [74]. The state-space modeling and eigenvalue-based approach is a global stability analysis method that determines the stability of the system regardless of the location of the source of the instability. For state-space modeling, detailed information of the system is required. However, in the case of an interconnected system of wind farms and HVDC, the detailed modeling of the wind turbine generator might not be available due to industry secrecy and confidentiality and the interconnected system can

not be modeled in a state-space form due to the lack of detailed information about the model. On the other hand, the impedance-based stability criterion does not require the detailed internal modeling of the interconnected system to assess the stability.

The impedance-based analysis has been proven to be a useful method to assess the stability of the interconnected system of wind farms and HVDC transmission system [49], [55], [65]. The impedance measurement is the basis of the impedance-based approach for the Nyquist criterion to estimate the stability [46]. In order to apply this approach, deriving the analytical impedance model of inverters is the prerequisite [47]–[50], [53], [58]–[62], [75]. The analytical impedance model is a continuous transfer function and the Nyquist criterion is checked on the transfer function of the source-load impedance ratio. To derive the analytical model of the impedance, a detailed modeling of the power electronics converters is required. However, the detailed modeling of the WECS is generally not available due to industry secrecy and confidentiality. The WECS is then assumed as a 'black/grey- box' system since no information about the internal control dynamics is available from the vendors. Due to this lack of availability, an analytical impedance model for the WECS can not be obtained with good accuracy. One can argue that it would be enough to measure the impedance of the inverter and then apply the Generalized Nyquist criterion on the measured source-load impedance and this can be true for a grid-tied inverter; however, in the case of offshore wind farms application, the system has multiple wind power inverters which are powered by the HVDC system rather than a strong AC grid and the aggregated impedance frequency responses of the wind farms can only be obtained from measurement if the interconnected system of wind farms and HVDC operates stably. In real world application, there is no guarantee that the system will operate stably unless adequate stability measures have been taken before installation.

Therefore, to ensure stable operation, it is necessary to assess the stability of the interconnected system analytically before connecting to the AC grid. In order to evaluate the stability analytically before connecting to the main AC grid, it is necessary to have a continuous transfer function for the analytical formulation of the impedance model from the black-box approach of the WECS. Moreover, it is necessary to extract the controller dynamics of the inverters to identify participation contribution in the observed oscillation and avoid the interaction phenomenon between the controllers of the HVDC rectifier and wind power inverters by reshaping the impedance. To the author knowledge, extraction of the controllers' dynamics of an inverter from a non-parametric impedance model has not been reported, when information on the controller parameters is not available. A technique for finding an aggregated non-parametric continuous impedance model based on the measurement to extract the internal controllers' dynamics of the wind power inverter from available information is needed for the wind industry when the WECS is assumed to be a black/grey- box. Since the transfer function of the WECS impedance cannot be derived analytically due to lack of detailed modeling information, this work proposes a method to obtain the aggregated non-parametric impedance transfer function from the measured impedance data of a single WECS by using system identification [76], [77] and the measurement data is used to extract the internal control dynamics of the WECS inverter when the WECS is assumed to be a 'black/grey- box'. These internal dynamics are used to explain interaction phenomena.

The eigenvalue analysis with the aid of the participation factor analysis has been so far the method used to identify which parts of the systems are having a major impact on the oscillat-

ory behaviour and interaction phenomena. Until now, there has been no method suggested to extract information related to internal dynamics from the impedance measurement. This work developed such method based on the non-parametric impedance measurements to enable identification of which parts of the controllers are participating in observed oscillatory behaviour and interaction phenomena.

The understanding of the oscillatory phenomena at its source remain of crucial importance since they not only decrease the power quality and cause a poor system performance but can greatly impact the stability of the overall interconnected system. Even if the active damping scheme proposed in [49], [55] has been effective in suppressing the oscillatory phenomena, the various configurations and controllers in real life systems are not always known in the details due to confidentiality and industry secrecy. Therefore, research efforts are needed to better understand the implications of the different components and controllers in the manifestation of these oscillatory phenomena. It is often argued in the literature that controller interactions are the likely sources of these oscillations, but rigorous proofs of this claim and practical solutions that are feasible have not yet been reported. A very likely cause for this might simply be the lack of well-established tools for analyzing and proving interactions in multi-converter multi-controller power electronics systems. Among the tools available today and widely used in power systems research to analyze the interactions between components and controllers of the system, the participation factor and sensitivity analysis tool is a good candidate. However, this tool will require a very detailed knowledge of every single parameter of the system under investigation. This Thesis is focusing on this gap by providing new answers and explanations for these interaction phenomena and a practical tool to assess the stability of these systems, based on measurements.

## 1.3 Scope of the Thesis

The thesis focuses on the analytical investigation of the small-signal stability and interaction phenomena between components of an offshore DC grid and verification of such investigation by benchmarking with numerical simulations and laboratory tests. The simulations are employed to assess the influence of active and passive parameter uncertainties. The research results identify the critical configurations leading to unexpected interactions based on the theoretical analysis and the simulation results and specify general guidelines for avoiding failures. The main objectives of the work are motivated by the following research gaps.

- Determining the underlying mechanisms leading to instability in a system with dominant presence of tightly regulated power electronics components;
- Identifying the causal relationship between power electronics component control algorithm and the grid stability with the purpose of establishing design guidelines that can guarantee the system stability.

In an attempt to partially answer these research questions, small-signal stability analyses are carried out for the VSC-based HVDC transmission system and wind farms integration through HVDC system based on the state-space modeling and eigenvalue analysis, and the impedance-based stability analysis. The stability properties of converter controllers widely used today have been identified and compared using the equivalent impedance analysis and the eigenvalue

analysis. From these, new explanations to interaction phenomena within these systems and new guidelines for controllers design, that can guarantee and restore the small-signal stability, were established.

## 1.4 Main Contribution of the Thesis

This work has contributed in the area of frequency domain small-signal stability and interaction analysis of the VSC- and MMC-based HVDC transmission system in wind farm integration. The stability and interaction analysis has been performed based on the two methods i.e., (i) the state-space modeling and the eigenvalue analysis, and (ii) the impedance-based analysis. The contributions of the Thesis comprise the following:

- In chapter 2, this work presents the impact of the simplifications implied by the RMS/phasor modeling approach on the small-signal stability properties of a VSC-based HVDC system to shed some light on the effects of commonly used simplifications for large-scale power system studies [78].

- In chapter 3 and 4, the impedance-based stability and interaction analysis of the VSC-based HVDC system are investigated. The impedance models for the HVDC VSCs and MMC with different control objectives such as the current control, power control, DC voltage control, the AC voltage control, and synchronverter-based control are analytically derived. Once the source and load impedances are identified, the impedance-based stability analysis is applied to determine the stability of the VSC-HVDC system and the impedance is reshaped by re-tuning the controllers of VSCs to guarantee the system operates stably. The system will remain stable as long as the minor-loop gain of negative feedback control system, that is the impedance ratio of the source (grid) - HVDC VSCs (load) subsystem, satisfies the Nyquist stability criterion. Moreover, the critical locations in the systems where the application of the impedance-based method can reveal the impact of passive components and the controller gains of the VSC-based HVDC system on the stability have been identified [79]. The impact of power flow direction on the stability of the VSC-HVDC system has been presented and a new method based on the impedance Nyquist plot is proposed to investigate the instability problem caused by a change of power flow direction [59].

- In chapter 5, the potential causes of electrical oscillations observed between the wind farms and the HVDC system are identified by investigating the impact of the controllers and the components in the wind farm (WF) inverter and in the VSC-HVDC transmission system. A discussion of the role of the ratio between the bandwidths of the controllers of the interconnected areas is introduced, and their essential role as the root cause of the instability is proposed and taken into account in re-shaping the impedances to maintain the stability [55].

- In chapter 5, a novel technique is presented to reveal and extract the internal control dynamics (critical controllers bandwidth) of the WECS inverter when the WECS system is assumed to be a 'grey box'. A non-parametric impedance model is developed with this aim, using a system identification technique and based on impedance measurements [80]. The method has potential immediate applicability in the wind industry based on

the simplicity it offers to black/grey-box types of systems to guarantee the stability of the interconnection.

- In chapter 6, a WECS inverter controller that emulates a synchronous machine, based on the synchronverter concept, is characterized by its equivalent impedance. The impedance model of the synchronverter has been derived to understand the stability properties of the synchronverter control scheme. The results revealed a R-L (resistive-inductive) nature of the equivalent impedance of this converter control scheme, which explains the ability of this controller in keeping better performance compared to PLL based dq-domain control. The synchronverter control exhibits better stability properties compared to PLL based dq-domain control in point of stability and control in integrating offshore wind farm through MMC-based HVDC system, due to its simple R-L (resistive-inductive) characteristic [81].

## 1.5 List of Publication

The publication results of this projects are:

### Journal Papers


[$J1$] **M. Amin**, M. Molinas, J. Lyu and X. Cai, "Impact of Power Flow Direction on the Stability of VSC-HVDC Seen from the Impedances Nyquist Plot," *IEEE Transactions on Power Electronics*, vol. 32, no. 10, pp. 8204-8217, Oct. 2017. DOI: 10.1109/TPEL.2016.2608278

[$J2$] **M. Amin** and M. Molinas, "Understanding the Origin of Oscillatory Phenomena Observed Between Wind Farms and HVdc Systems," *IEEE Journal of Emerging and Selected Topics in Power Electronics*, vol. 5, no. 1, pp. 378-392, March 2017. DOI: 10.1109/JESTPE.2016.2620378

[$J3$] **M. Amin**, A. Rygg and M. Molinas, "Self-synchronisation of wind farm in MMC-based HVDC system: Stability Investigation," *IEEE Transaction on Energy Conversion*, vol. 32, no. 2, pp. 458-470, June 2017. DOI: 10.1109/TEC.2017.2661540

[$J4$] **M. Amin** and M. Molinas, Small-Signal Stability Assessment of Power Electronics based Power Systems: A Discussion of Impedance- and Eigenvalue-based Methods, *IEEE Transaction on Industry Application*, To be published. Published online: 06 June 2017. DOI: 10.1109/TIA.2017.2712692

[$J5$] **M. Amin** and M. Molinas, "A Grey-box Method for Controller Parameter Estimation in HVDC-connected Wind Farms based on Non-parametric Impedance", *IEEE Transaction on Industrial Electronics*, 2017 (In Review)

[$J6$] J. Lyu, X. Cai, **M. Amin** and M. Molinas,"Instability Mechanism Analysis of Wind Farm Integration via an MMC-HVDC Transmission System" *IET Generation, Transmission and Distribution*, (In Review) 2017

### Conference papers

[$C1$] **M. Amin**, M. Zadeh, J. A. Suul, E. Tedeschi, M. Molinas and O. B. Fosso, "Stability analysis of interconnected AC power systems with multi-terminal DC grids based on the Cigre DC grid test system," *3rd Renewable Power Generation Conference (IET RPG 2014)*, Naples, 2014, pp. 1-6.

[$C2$] M. K. Zadeh, **M. Amin**, J. A. Suul, M. Molinas and O. B. Fosso, "Small-signal stability study of the Cigre DC grid test system with analysis of participation factors and parameter sensitivity of oscillatory modes," *2014 Power Systems Computation Conference (PSCC 2014)*, Wroclaw, 2014, pp. 1-8.

[$C3$] **M. Amin**, J. A. Suul, S. D'Arco, E. Tedeschi and M. Molinas, "Impact of state-space modelling fidelity on the small-signal dynamics of VSC-HVDC systems," *11th IET International Conference on AC and DC Power Transmission (IET ACDC 2015)*, Birmingham, 2015, pp. 1-11.

[$C4$] **M. Amin** and M. Molinas, "Impedance based stability analysis of VSC-based HVDC system," *2015 IEEE Eindhoven PowerTech*, Eindhoven, 2015, pp. 1-6.

[$C5$] **M. Amin**, A. Rygg and M. Molinas, "Impedance-based and eigenvalue based stability assessment compared in VSC-HVDC system," *2016 IEEE Energy Conversion Congress and Exposition (IEEE ECCE 2016)*, Milwaukee, WI, USA, 2016, pp. 1-8.

[$C6$] **M. Amin**, M. Molinas and J. Lyu, "Oscillatory phenomena between wind farms and HVDC systems: The impact of control," *2015 IEEE 16th Workshop on Control and Modeling for Power Electronics (IEEE COMPEL 2015)*, Vancouver, BC, 2015, pp. 1-8.

[$C7$] **M. Amin** and M. Molinas, "Self-synchronisation of wind farm in MMC-based HVDC system," in *2016 IEEE Electrical Power and Energy Conference (IEEE EPEC 2016)*, Ottawa, Canada, 2016

[$C8$] **M. Amin**, A. Rygg and M. Molinas, "Active power flow direction effect on stability in multi-terminal VSC-HVDC transmission system in integrating wind farm," *2016 IEEE 17th Workshop on Control and Modeling for Power Electronics (IEEE COMPEL 2016)*, Trondheim, 2016, pp. 1-8.

[$C9$] A. K. Broen, **M. Amin**, E. Skjong and M. Molinas, "Instantaneous frequency tracking of harmonic distortions for grid impedance identification based on Kalman filtering," *2016 IEEE 17th Workshop on Control and Modeling for Power Electronics (IEEE COMPEL 2016)*, Trondheim, 2016, pp. 1-7.

[$C10$] A. Rygg, **M. Amin**, M. Molinas and B. Gustavsen, "Apparent impedance analysis: A new method for power system stability analysis," *2016 IEEE 17th Workshop on Control and Modeling for Power Electronics (IEEE COMPEL 2016)*, Trondheim, 2016, pp. 1-7.

## 1.6 Outline of the Thesis

The rest of the thesis is organized in the following.

Chapter 2 presents the state-space small-signal modeling of the VSC- and MMC-HVDC system. The eigenvalue-based small-signal stability and interaction analysis have been carried out for a tow terminal VSC-based HVDC system which followed for MT-HVDC systems. Critical modes of the system under worst case operating conditions are investigated by participation factor

analysis to show the influence of different states and identify the physical effects associated with the various eigenvalues. The same test-case is investigated by using DigSilent Power Factory (PF), as an example of a commercial power system simulation tool, to assess small-signal stability and dynamic behaviour of the system. Thus, the effects of commonly used simplifications for large-scale power system studies on the stability assessment of a VSC-based HVDC transmission scheme are identified, and their influence on the location of critical poles in the system is analyzed. Moreover, this chapter illustrates the particular challenges that can occur during a step-wise construction of a large-scale MT-HVDC transmission system.

Chapter 3 presents the impedance based stability analysis of VSC-HVDC systems. Analytical impedance models for the VSC-HVDC converters have been derived for different control modes and the impedance frequency response is verified by the perturbation method. Once the source and load impedance are identified, an impedance based stability method is adopted in order to determine the stability of the VSC-based HVDC system. The system stability can be predicted from characteristics loci of minor-loop gain and the phase margin shows the strength of the system. Moreover, this chapter discusses the impact of the power flow direction on the stability of VSC-based HVDC system. In order to analyze such instability problem and to design the local control, a new impedance-based method is proposed.

Chapter 4 presents the comparison between the impedance-based and the eigenvalue-based stability analysis methods for power electronics-based power systems more specifically for HVDC system. A relation between the characteristics equation of the eigenvalues, and poles and zeros of the minor-loop gain from the impedance-based analysis has been derived. Moreover, the advantages and the disadvantages of these two small-signal stability methods have been described.

Chapter 5 explores the possible causes of these oscillations by investigating the impact of controllers and components in the wind farm and in the VSC-based HVDC transmission system. The role of the ratio between the bandwidths of the interconnected areas, as having an essential role in the root cause of the instability is discussed. Moreover, this chapter presents a simple method that enables to identify the specific part of the equivalent impedance (e.g. controller's bandwidth) that has a major impact on the stability of the system.

Chapter 6 presents a controller for WECS inverter based on the synchronverter concept. The design of the synchronverter is embedded in the VSC to mimic the way synchronous generator synchronize. The detailed analysis and the results presented show the benefits of this controller and its potential for stability. The results highlight the synchronverter's ability in keeping better performance in point of stability and control in integrating offshore wind farm through MMC-based HVDC system.

Chapter 7 presents the concluding remarks of the thesis and discusses some recommendations for the future investigation.

# Part I

# Small-Signal Stability of the HVDC System

# Chapter 2

# State-space Modeling and Eigenvalue-based Stability Analysis

*This Chapter presents the state-space small-signal modeling of the VSC- and MMC-base HVDC system. The eigenvalue-based small-signal stability and interaction analysis have been carried out for a two terminal VSC-based HVDC system analytically which followed for large-scale MT-HVDC systems numerically to highlight the challenges that an analytical approach poses on large-scale multi vendor systems. Critical modes of the system under worst case operating conditions are investigated by participation factor analysis to show the influence of different states and identify the physical effects associated with the various eigenvalues. Moreover, this chapter illustrates the particular challenges that can occur during a step-wise construction of a large-scale MT-HVDC transmission system.*

This chapter is based on the following articles.

[1] **M. Amin**, J. A. Suul, S. D'Arco, E. Tedeschi and M. Molinas, "Impact of state-space modelling fidelity on the small-signal dynamics of VSC-HVDC systems," *11th IET International Conference on AC and DC Power Transmission (IET ACDC 2015)*, Birmingham, 2015, pp. 1-11.

[2] **M. Amin**, M. Zadeh, J. A. Suul, E. Tedeschi, M. Molinas and O. B. Fosso, "Stability analysis of interconnected AC power systems with multi-terminal DC grids based on the Cigre DC grid test system," *3rd Renewable Power Generation Conference (IET RPG 2014)*, Naples, 2014, pp. 1-6.

[3] M. K. Zadeh, **M. Amin**, J. A. Suul, M. Molinas and O. B. Fosso, "Small-signal stability study of the Cigre DC grid test system with analysis of participation factors and parameter sensitivity of oscillatory modes," *2014 Power Systems Computation Conference (PSCC 2014)*, Wroclaw, 2014, pp. 1-8.

## 2.1 Introduction

This chapter investigates the effect of state-space modeling fidelity on the small-signal stability characteristics of HVDC systems based on VSCs. For this purpose, a small-signal state-space model of VSC and MMC HVDC system, including the dynamics of the AC networks and the converter control loops is developed analytically and verified by comparison to time responses of a detailed model including the nonlinear effects. The small-signal state-space model has been developed for a VSC-HVDC system. Critical modes of the system under worst-case operating conditions are investigated by participation factor analysis to show the influence of different states and identify the physical effects associated with the various eigenvalues. The same test-case is investigated by using DigSilent Power Factory (PF), as an example of a commercial power system simulation tool, to assess the small-signal stability and dynamic behaviour of the system. Thus, the effects of commonly used simplifications for large-scale power system studies on the stability assessment of a VSC-based HVDC transmission scheme are identified, and their influence on the location of critical poles in the system is analyzed. The results are used as a basis towards general guidelines on how to assess the results from traditional power system stability studies of networks containing VSC-HVDC transmission schemes and to shed light on the impact of the simplifications on the stability estimate. This approach will aim at revealing if any poles of importance to the stability properties of the system will be ignored by the phasor domain modeling and the effect of the simplified modeling of the electrical systems on the location of the critical poles. This study contributes to a better understanding of which simplifications are justifiable for large scale power system studies and how these simplifications are influencing the stability properties of the linearized system models.

In order to identify interaction phenomena and critical modes that can occur with different typical system configurations, the analysis is presented in several steps. Firstly, a case with point-to-point HVDC connection is analyzed, followed by the analysis of a four-terminal DC system, before the stability of the large-scale MT-HVDC system is studied. The presented results illustrate particular challenges that can occur during a step-wise construction of a large-scale MT-HVDC transmission system. This chapter also presents the parameter sensitivities of critical modes and it's most likely sources in power systems containing large-scale MT-HVDC transmission schemes.

## 2.2 State-space Modeling of VSC

This section presents a small-signal state-space modeling of the VSC system analytically.

### 2.2.1 Mathematical Modeling of VSC

The electrical circuit of an inverter for analytical modeling is shown in Fig. 2.1 where $L_c$ and $R_c$ are the total series inductance and resistance between the inverter and point of common coupling (PCC); $C_{dc}$ is the DC link capacitor; $C_f$ is the filter capacitance connected at PCC and $R_g$ and $L_g$ are the grid resistance and inductance including the series resistance and inductance of the transformer. The modeling, analysis and control of the system will be presented in a synchronous reference frame (SRF). The transformation of the three phase quantity from the stationary reference frame to SRF is based on the amplitude-invariant Park transformation, with the d-axis aligned with the voltage vector $v_0$ and q-axis leading the d-axis by $90^0$. The dynamic

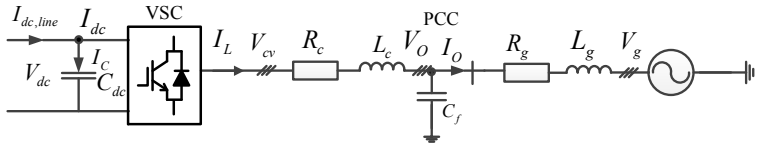


**Figure 2.1:** Overview of a VSC HVDC inverter station

equations of the inverter system in per unit (pu) can be given by

$$\frac{di_{Ld}}{dt} = \frac{\omega_b}{L_c} v_{cvd} - \frac{\omega_b}{L_c} v_{od} - \frac{\omega_b R_c}{L_c} i_{Ld} + \omega_b \omega_g i_{Lq} \tag{2.1a}$$

$$\frac{di_{Lq}}{dt} = \frac{\omega_b}{L_c} v_{cvq} - \frac{\omega_b}{L_c} v_{oq} - \omega_b \omega_g i_{Ld} - \frac{\omega_b R_c}{L_c} i_{Lq} \tag{2.1b}$$

$$\frac{d\,v_{dc}}{dt} = \frac{\omega_b}{C_{dc}} i_{dc,line} - \frac{\omega_b}{C_{dc}} i_{dc} \tag{2.1c}$$

where $\omega_b$ is base angular grid frequency; $\omega_g$ is grid frequency in pu; voltages and currents of these equations are indicated in Fig. 2.1 [82], [83]. An ideal lossless average model is assumed for the converter. Therefore power balance constraint between DC and AC side can be given by

$$i_{dc} v_{dc} = i_{Ld} v_{cvd} + i_{Lq} v_{cvq}. \tag{2.2}$$

### 2.2.2 Current Controller

The inner loop current controller is assumed to be a widely used SRF proportional and integral (PI) controller of the VSC with decoupling term and is shown in Fig. 2.2. The output voltage reference obtained from the current controllers, including the feed-forward terms can be given by

$$v_{cvd,ref} = k_{pc}(i_{d,ref} - i_{Ld}) + k_{ic}\gamma_{Ld} + v_{od} - \omega_{pll} L_c i_{Lq} - v_{od,AD} \tag{2.3a}$$

$$v_{cvq,ref} = k_{pc}(i_{q,ref} - i_{Lq}) + k_{ic}\gamma_{Lq} + v_{oq} + \omega_{pll} L_c i_{Ld} - v_{oq,AD} \tag{2.3b}$$

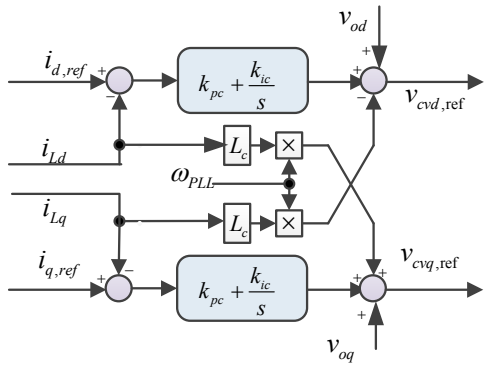


**Figure 2.2:** Current Controller in SRF

where $i_{d,ref}$ and $i_{q,ref}$ are the reference active and reactive current components obtained from the outer loop controller; $k_{pc}$ and $k_{ic}$ are the proportional and integral gain of the current controller; $\gamma_{Ld}$ and $\gamma_{Lq}$ are auxiliary variable introduced to represent the integral part of the current controller and can be written by (2.4) in state-space form; $v_{od,AD}$ and $v_{oq,AD}$ are output voltage references from the AC active damping and $\omega_{pll}$ is the frequency of the PLL in pu.

$$\frac{d\gamma_{Ld}}{dt} = i_{d,ref} - i_{Ld} \tag{2.4a}$$

$$\frac{d\gamma_{Lq}}{dt} = i_{q,ref} - i_{Lq} \tag{2.4b}$$

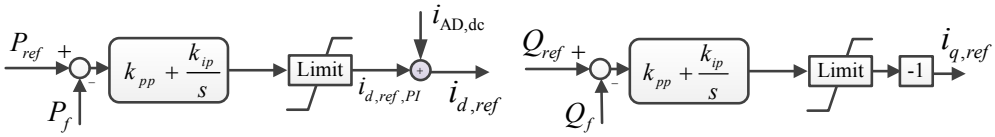


**Figure 2.3:** Outer-loop active and reactive power controller

### 2.2.3 Active and Reactive Power Controller

The active and reactive power at PCC that will be controlled, is calculated by (2.5). A low-pass filter is introduced to eliminate measurement noise. The measurement filter (MF) in state-space form is represented by (2.6) where $P_f$ and $Q_f$ are the filtered active and reactive power and $\omega_{PQ}$ is the cut-off frequency of the MF.

$$P_{meas} = v_{od}i_{od} + v_{oq}i_{oq} \tag{2.5a}$$

$$Q_{meas} = v_{oq}i_{od} - v_{od}i_{oq} \tag{2.5b}$$

$$\frac{dP_f}{dt} = -\omega_{PQ}P_f + \omega_{PQ}P_{meas} \tag{2.6a}$$

$$\frac{dQ_f}{dt} = -\omega_{PQ}Q_f + \omega_{PQ}Q_{meas} \tag{2.6b}$$

Outer loop PI controller is used to obtain the d-axis and q-axis current references. The reference current $i_{d,ref,PI}$ and $i_{q,ref}$ can be defined by

$$i_{d,ref,PI} = k_{pp}(P_{ref} - P_f) + k_{ip}\gamma_P \tag{2.7a}$$

$$i_{q,ref} = [k_{pp}(Q_{ref} - Q_f) + k_{ip}\gamma_Q](-1) \tag{2.7b}$$

where, $P_{ref}$ and $Q_{ref}$ are the reference active and reactive power to the controller; $k_{pp}$ and $k_{ip}$ are the proportional and integral gain of the controller; $\gamma_P$ and $\gamma_Q$ are auxiliary variable introduced to represent the integral part of the controller and can be written by (2.8) in state-space form.

$$\frac{d\gamma_P}{dt} = P_{ref} - P_f \tag{2.8a}$$

$$\frac{d\gamma_Q}{dt} = Q_{ref} - Q_f \tag{2.8b}$$

The controllers implemented in nonlinear model are shown in Fig. 2.3 where an active DC damping term, $i_{AD,dc}$ is introduced to suppress the DC link voltage oscillation [84].

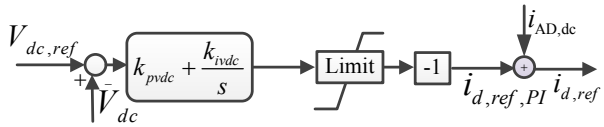


**Figure 2.4:** Outer-loop PI DC voltage controller

### 2.2.4 DC voltage controller

An outer-loop PI controller is assumed to regulate the DC-link voltage of the HVDC system. Fig. 2.4 depicts the DC voltage controller. The reference current, $i_{dc,ref,PI}$ obtained from the DC voltage controller can be given by

$$i_{d,ref,PI} = [k_{pvdc}(v_{dc,ref} - v_{dc}) + k_{ivdc}\gamma_{dc}]\ (-1) \tag{2.9}$$

where, $v_{dc,ref}$ is the reference DC voltage to the controller; $k_{pvdc}$ and $k_{ivdc}$ are the proportional and integral gains of the controller; $\gamma_{dc}$ is a variable introduced to represent the integral part of the controller and can be written in state-space form by

$$\frac{d\gamma_{dc}}{dt} = (v_{dc,ref} - v_{dc}). \tag{2.10}$$

### 2.2.5 Active AC Damping

The active AC damping is designed to suppress the $LC$ oscillations in the filter [85]. There are several concepts developed for damping such oscillations; in this case, the active damping is based on injecting a voltage component of counter-phase with detected oscillation in order to produce a cancellation effect. The oscillation is first isolated by high pass filtering and is then multiplied by a gain $k_{AD}$. The high pass filter function is implemented by subtracting measure voltage signals from a low pass filtered version of the same voltages. The implemented active damping scheme is depicted in Fig. 2.5 (a). The damping voltage reference is given by

$$v_{o,dq,AD} = k_{AD}(-\varphi_{dq} + v_{o,dq}) \tag{2.11}$$

where $\varphi_{dq}$ is the low pass filtered voltage signal of measure voltages signal. The corresponding internal states $\varphi_d$ and $\varphi_q$ of low pass filter can be given by (2.12), where $\omega_{AD}$ is the cut-off frequency of the applied low-pass filter.

$$\frac{d\varphi_d}{dt} = -\omega_{AD}\varphi_d + \omega_{AD}v_{od} \tag{2.12a}$$

$$\frac{d\varphi_q}{dt} = -\omega_{AD}\varphi_q + \omega_{AD}v_{oq} \tag{2.12b}$$

### 2.2.6 Active DC Damping

The active DC damping proposed in [84] is assumed for attenuating the oscillation in the DC side of the converter. Fig. 2.5 (b) depicts the implemented active DC damping which is identical from a functional point of view to the active AC damping that was described in the previous

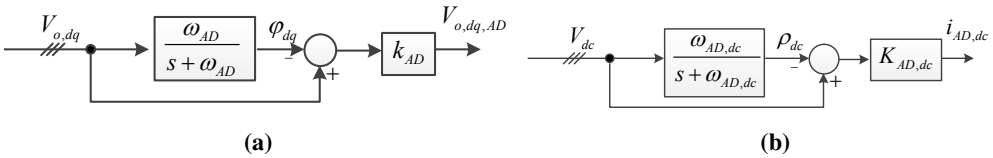


**Figure 2.5:** Active damping: (a) active AC damping (b) active DC damping.

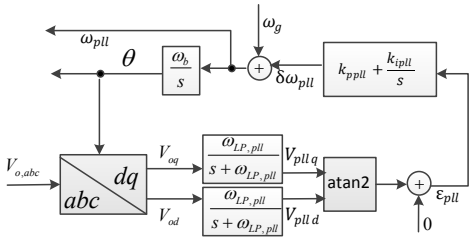


**Figure 2.6:** Phase Locked Loop

subsection. The same approach of isolating the oscillating component of the voltage is applied by high-pass filtering function. Then, the detected oscillatory component is multiplied by a gain to produce a current reference. The current reference resulting from the active DC damping, $i_{AD,dc}$ is added to the d-axis current reference for the AC side current controllers as given by

$$i_{d,ref} = i_{d,ref,PI} + i_{AD,dc} = i_{d,ref,PI} + k_{AD,dc}(-\rho_{dc} + v_{dc}) \tag{2.13}$$

where, $k_{AD,dc}$ is the active DC damping gain and $\rho_{dc}$ is the state of the low pass filter used for implementing the active damping, as defined by (2.14).

$$\frac{d\rho_{dc}}{dt} = -\omega_{AD,dc}\rho_{dc} + \omega_{AD,dc}v_{dc} \tag{2.14}$$

### 2.2.7 Phase Locked Loop

The phase locked loop (PLL) is used to track the actual grid frequency [86]. An inverse tangent function is used on first order low-pass filtered output of q- and d-axis voltage to estimate the actual phase angle error as shown in Fig. 2.6. This phase angle error is the input to the PI controller for tracking the frequency of the measured voltage. The states of the low-pass filter of the PLL are given by (2.15) where $\omega_{LP,PLL}$ is the cut-off frequency of the low-pass filter.

$$\frac{dv_{plld}}{dt} = -\omega_{LP,pll}v_{plld} + \omega_{LP,pll}v_{od} \tag{2.15a}$$

$$\frac{dv_{pllq}}{dt} = -\omega_{LP,pll}v_{pllq} + \omega_{LP,pll}v_{oq} \tag{2.15b}$$

The frequency deviation, $\delta\omega_{pll}$ of the PLL with respect to the grid frequency can be defined by (2.16) where $k_{ppll}$ and $k_{ipll}$ are the proportional and integral gain of the PI controller; $\varepsilon_{pll}$ is the variable introduced to represent the integrator state and can be defined by (2.17).

$$\delta\omega_{pll} = k_{ppll}\arctan\left(\frac{v_{pllq}}{v_{plld}}\right) + k_{ipll}\varepsilon_{pll} \tag{2.16}$$

$$\frac{d\,\varepsilon_{pll}}{dt} = \arctan\left(\frac{v_{pllq}}{v_{plld}}\right) \tag{2.17}$$

The corresponding phase angle difference, $\delta\theta_{pll}$ between the grid voltage and orientation of the PLL is represented by (2.18) and the grid voltage represented by its amplitude $\hat{v_g}$ can be transformed into PLL reference frame as given by (2.19). Frequency of the PLL can be given by (2.20).

$$\frac{d\delta\theta_{pll}}{dt} = \delta\omega_{pll}\omega_b = \omega_b k_{ppll} \arctan\left(\frac{v_{pllq}}{v_{plld}}\right) + \omega_b k_{ipll}\varepsilon_{pll} \tag{2.18}$$

$$v_g = \hat{v}_g e^{-j\delta\theta_{pll}} \tag{2.19}$$

$$\omega_{pll} = \delta\omega_{pll} + \omega_g \tag{2.20}$$

### 2.2.8 State-space Matrix Realization

After manipulation of the equations (2.1) and changes of variable, the final nonlinear differential equations of VSC for P-Q control mode can be given by

$$\begin{aligned}\frac{di_{Ld}}{dt} =& -\frac{\omega_b}{L_c}k_{AD}v_{od} - \frac{\omega_b}{L_c}(k_{pc}+R_c)i_{Ld} - \omega_b(k_{ppll}\arctan\left(\frac{v_{pllq}}{v_{plld}}\right) + k_{ipll}\varepsilon_{pll})i_{Lq} + \frac{\omega_b}{L_c}k_{ic}\gamma_{Ld} \\ &+ \frac{\omega_b}{L_c}k_{AD}\varphi_d - \frac{\omega_b}{L_c}k_{pc}k_{pp}P_f + \frac{\omega_b}{L_c}k_{pc}k_{AD,dc}(v_{dc}-\rho_{dc}) + \frac{\omega_b}{L_c}k_{pc}k_{ip}\gamma_P + \frac{\omega_b}{L_c}k_{pc}k_{pp}P_{ref}\end{aligned} \tag{2.21a}$$

$$\begin{aligned}\frac{di_{Lq}}{dt} =& -\frac{\omega_b}{L_c}k_{AD}v_{oq} + \omega_b(k_{ppll}\arctan\left(\frac{v_{pllq}}{v_{plld}}\right) + k_{ipll}\varepsilon_{pll})i_{Ld} - \frac{\omega_b}{L_c}(k_{pc}+R_c)i_{Lq} + \frac{\omega_b}{L_c}k_{ic}\gamma_{Lq} \\ &+ \frac{\omega_b}{L_c}k_{AD}\varphi_q + \frac{\omega_b}{L_c}k_{pc}k_{pp}Q_f + \frac{\omega_b}{L_c}k_{pc}k_{ip}\gamma_Q - \frac{\omega_b}{L_c}k_{pc}k_{pp}Q_{ref}\end{aligned} \tag{2.21b}$$

$$\begin{aligned}\frac{dv_{dc,j}}{dt} =& \frac{\omega_b}{C_{dc}}i_{dc,line} - \frac{\omega_b(1-k_{AD})}{C_{dc}v_{dc}}(i_{Ld}v_{od} + i_{Lq}v_{oq}) + \frac{\omega_b k_{pc}}{C_{dc}v_{dc}}(i_{Ld}^2 + i_{Lq}^2) - \frac{\omega_b k_{pc}k_{AD,dc}}{C_{dc}}i_{Ld} \\ &- \frac{\omega_b k_{ic}}{C_{dc}v_{dc}}(i_{Ld}\gamma_{Ld} + i_{Lq}\gamma_{Lq}) - \frac{\omega_b k_{AD}}{C_{dc}v_{dc}}(i_{Ld}\varphi_d + i_{Lq}\varphi_q) + \frac{\omega_b k_{pc}k_{pp}}{C_{dc}v_{dc}}(i_{Ld}P_f - i_{Lq}Q_f) \\ &+ \frac{\omega_b k_{pc}k_{AD,dc}}{C_{dc}v_{dc}}i_{Ld}\rho_{dc} - \frac{\omega_b k_{pc}k_{ip}}{C_{dc}v_{dc}}(i_{Ld}\gamma_P + i_{Lq}\gamma_Q) - \frac{\omega_b k_{pc}k_{pp}}{C_{dc}v_{dc}}(i_{Ld}P_{ref} - i_{Lq}Q_{ref})\end{aligned} \tag{2.22}$$

The states of the integrator of the current-controller are represented by

$$\frac{d\gamma_{Ld}}{dt} = k_{pp}P_{ref} - k_{pp}P_f + k_{ip}\gamma_P - k_{AD,dc}\rho_{dc} + k_{AD,dc}v_{dc} - i_{Ld} \tag{2.23a}$$

$$\frac{d\gamma_{Lq}}{dt} = -k_{pp}Q_{ref} + k_{pp}Q_f + k_{ip}\gamma_Q - i_{Lq}. \tag{2.23b}$$

The filter capacitor voltage and grid inductor current in state-space form can be presented in

SRF by

$$\frac{dv_{od}}{dt} = \frac{\omega_b}{C_f} i_{Ld} - \frac{\omega_b}{C_f} i_{od} + \omega_b \omega_g v_{oq} \tag{2.24a}$$

$$\frac{dv_{oq}}{dt} = \frac{\omega_b}{C_f} i_{Lq} - \frac{\omega_b}{C_f} i_{oq} - \omega_b \omega_g v_{od} \tag{2.24b}$$

$$\frac{di_{od}}{dt} = \frac{\omega_b}{L_g} v_{od} - \frac{\omega_b}{L_g} \hat{v}_g \cos(\delta\theta_{pll}) - \frac{\omega_b R_g}{L_g} i_{od} + \omega_b \omega_g i_{oq} \tag{2.25a}$$

$$\frac{di_{oq}}{dt} = \frac{\omega_b}{L_g} v_{oq} + \frac{\omega_b}{L_g} \hat{v}_g sin(\delta\theta_{pll}) - \omega_b \omega_g i_{od} - \frac{\omega_b R_g}{L_g} i_{oq}. \tag{2.25b}$$

The system is presented in state-space form by (2.26) through a nonlinear model, where x(t) is the state vector and u(t) is the input vector.

$$\frac{dx(t)}{dt} = f(x(t), u(t)) \tag{2.26a}$$

$$y(t) = g(x(t), u(t)) \tag{2.26b}$$

The non-linearity of the model prevents direct application of classical linear analysis techniques. Therefore, a small-signal representation is derived for a steady-state operating point as given by

$$\frac{d\Delta x}{dt} \simeq A.\Delta x + B.\Delta u \tag{2.27a}$$

$$\Delta y \simeq C.\Delta x + D.\Delta u \tag{2.27b}$$

where,

$$A = \Delta_x f, \quad B = \Delta_u f, \quad C = \Delta_x g, \quad D = \Delta_u g \tag{2.28}$$

where, for example, $\Delta_x f$ denotes the Jacobian matrix of $f$ with respect to $x$.

The states and input vectors, for example, of P-Q control converter including one states for DC-line inductor are given by (2.29). The A- and B- matrices of the resulting linearized state-space small-signal model are given in Appendix A.

$$x = [v_{od}\ v_{oq}\ i_{Ld}\ i_{Lq}\ \gamma_{Ld}\ \gamma_{Lq}\ i_{od}\ i_{oq}\ \varphi_d\ \varphi_q\ \varphi_P\ \varphi_Q\ v_{plld}\ v_{pllq}\ \varepsilon_{pll}\ \delta\theta_{pll}\ v_{dcj}\ i_{dc,line}\ \rho_{dc}\ \gamma_P\ \gamma_Q]^T \tag{2.29a}$$

$$u = [P_{\text{ref}}\ \ Q_{\text{ref}}\ \ v_{\text{dc,i}}\ \hat{v}_g\ \ \omega_g]^T \tag{2.29b}$$

The analytical state-space small-signal model has been validated by simulation with a detailed model of the VSC system. The results from simulations with the nonlinear simulation model are therefore compared with results obtained from the linearized state-space small-signal model. Fig. 2.7 (a) shows d- and q-axis voltages at PCC and Fig. 2.7 (b) shows the d- and q-axis currents of the converter for a step change of power reference. As can be seen, both the nonlinear and the state-space small-signal model capture the dynamics of the converter which validates the correctness of the derived model.

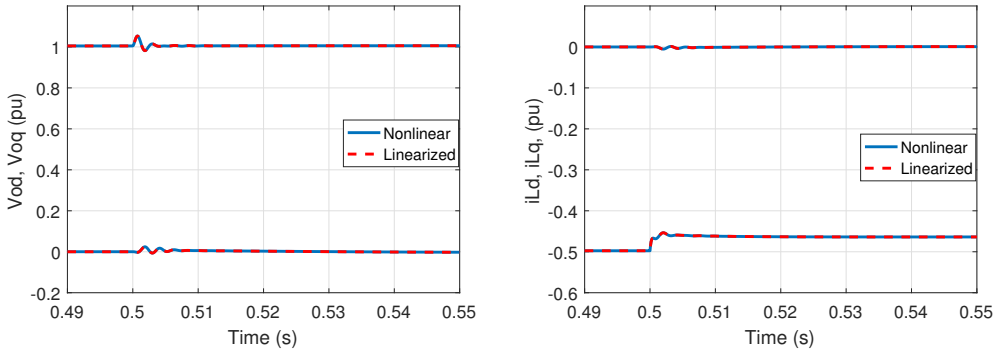


**(a)** **(b)**

**Figure 2.7:** Time domain responses comparison between the state-spcae linearized model and the nonlinear model: (a) voltages at PCC and (b) VSC currents.

Similarly, an analytical state-space model has been developed for the DC voltage control VSC. The states and the input vector for the DC voltage control converter can be given by

$$x = [v_{od}\ v_{oq}\ i_{Ld}\ i_{Lq}\ \gamma_{Ld}\ \gamma_{Lq}\ i_{od}\ i_{oq}\ \varphi_d\ \varphi_q\ \varphi_{dc}\ \varphi_Q\ v_{plld}\ v_{pllq}\ \varepsilon_{pll}\ \delta\theta_{pll}\ v_{dc}\ \rho_{dc}\ \gamma_{dc}\ \gamma_Q]^T \quad (2.30a)$$

$$u = [V_{\text{dc,ref}}\ \ Q_{\text{ref}}\ \ i_{\text{dc,i}}\ \ \hat{v}_g\ \ \omega_g]^T. \quad (2.30b)$$

The validated small-signal model is then used to further analyze the characteristics of the investigated system.

## 2.3 State-space Modeling of MMC

A basic structure of MMC topology for MMC-based HVDC system is depicted in Fig. 2.8. Each phase leg of MMC consists of one upper and one lower arm i.e., an upper arm represented by subscript $u$ and a lower arm represented by $l$, connected in series with DC-terminal. Each arm has $N$ number of identical sub-modules (SMs) and series connected arm inductor $L_a$ and also its equivalent resistor $R_a$ to represent the losses within the arm. The arm inductors suppress the high-frequency components from the arm currents, $i_u^k$ and $i_l^k$ where $k$ stands for three phase system and $k \in abc$. The SMs provide two different voltage level at its terminal depending on the stage of the complementary switches.

The circulating currents which flow through the upper and lower arms can be described by

$$i_c^k = \frac{i_u^k + i_l^k}{2} \quad (2.31)$$

and the AC phase current can be expressed as

$$i_s^k = i_u^k - i_l^k. \quad (2.32)$$

The single phase equivalent circuit of the MMC including a transformer/filter impedance is depicted in Fig. 2.9. From the single phase equivalent circuit, by applying Kirchhoff's voltage

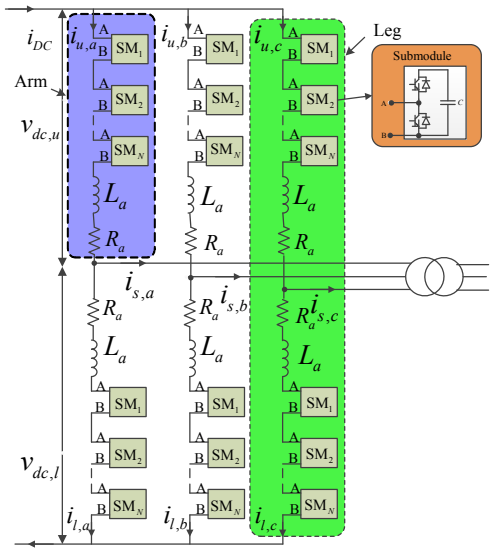


**Figure 2.8:** Basic structure of MMC topology for MMC-HVDC system.

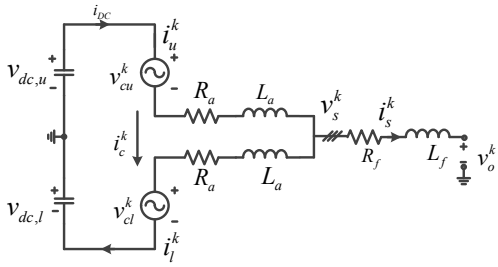


**Figure 2.9:** Single-phase equivalent circuit of MMC.

law it can be obtained

$$v_o^k + L_a \frac{di_u^k}{dt} + R_a i_u^k + v_{cu}^k + L_f \frac{di_s^k}{dt} + R_f i_s^k = \frac{v_{dc}}{2} \tag{2.33a}$$

$$v_o^k - L_a \frac{di_l^k}{dt} - R_a i_l^k - v_{cl}^k + L_f \frac{di_s^k}{dt} + R_f i_s^k = -\frac{v_{dc}}{2}. \tag{2.33b}$$

From continuous model of the MMC, the sum capacitor voltage in an arm can be defined by

$$v_{cu}^k = N n_u^k v_{cu}^k = n_u^k v_{cu}^{\sum k} \tag{2.34a}$$

$$v_{cl}^k = N n_l^k v_{cl}^k = n_l^k v_{cl}^{\sum k} \tag{2.34b}$$

where $n_u^k$ and $n_l^k$ are insertion indexes of the upper and lower arm, respectively and $v_{cl}^{\sum}$ and $v_{cu}^{\sum}$ are the sum of the SM capacitor voltages of the upper and lower arms, respectively. The

dynamics of the sum capacitive voltage can be expressed as

$$\frac{dv_{cu}^{\sum k}}{dt} = \frac{N}{C_{sm}} n_u^k i_u^k = \frac{1}{C_{eq}} n_u^k \left( i_c^k + \frac{i_s^k}{2} \right) \tag{2.35a}$$

$$\frac{dv_{cl}^{\sum k}}{dt} = \frac{N}{C_{sm}} n_l^k i_l^k = \frac{1}{C_{eq}} n_l^k \left( i_c^k - \frac{i_s^k}{2} \right) \tag{2.35b}$$

where $C_{eq} = C_{sm}/N$.

It is assumed that direct modulation is used. Hence, the insertion indexes can be given by

$$n_u = \frac{\frac{V_{dc}}{2} - v_s^{ref} - v_c^{ref}}{V_{dc}} \tag{2.36a}$$

$$n_l = \frac{\frac{V_{dc}}{2} + v_s^{ref} - v_c^{ref}}{V_{dc}} \tag{2.36b}$$

where $v_s^{ref}$ is the reference voltage generated by the inner-loop current-controller and $v_c^{ref}$ is reference voltage generated by circulating current suppression controller (CCSC).

After manipulation of (2.33), the circulation currents can be represented as

$$\frac{di_c^k}{dt} = -\frac{R_a}{L_a} i_c^k + \frac{1}{L_a}\frac{v_{dc}}{2} - \frac{1}{L_a}\left( \frac{n_u^k v_{cu}^{\sum k} + n_l^k v_{cl}^{\sum k}}{2} \right). \tag{2.37}$$

The state-space model of the MMC states can be expressed as

$$\frac{d}{dt}\begin{pmatrix} i_c^k \\ v_{cu}^{\sum k} \\ v_{cl}^{\sum k} \end{pmatrix} = \begin{pmatrix} -\frac{R_a}{L_a} & -\frac{n_u^k}{2L_a} & -\frac{n_l^k}{2L_a} \\ \frac{n_u^k}{C_{eq}} & 0 & 0 \\ \frac{n_l^k}{C_{eq}} & 0 & 0 \end{pmatrix} \begin{pmatrix} i_c^k \\ v_{cu}^{\sum k} \\ v_{cl}^{\sum k} \end{pmatrix} + \begin{pmatrix} \frac{1}{2L_a} & 0 \\ 0 & \frac{n_u^k}{2C_{eq}} \\ 0 & -\frac{n_l^k}{2C_{eq}} \end{pmatrix} \begin{pmatrix} v_{dc} \\ i_s \end{pmatrix} \tag{2.38}$$

After manipulation of (2.33), the phase currents can be represented in state-space form as

$$\frac{di_s^k}{dt} = -\frac{R'}{L'} i_s^k + \frac{1}{L'} v_s^k - \frac{1}{L'} v_o^k \tag{2.39}$$

where

$$L' = \frac{L_a}{2} + L_f$$

$$R' = \frac{R_a}{2} + R_f$$

$$v_s^k = \frac{-n_u^k v_{cu}^{\sum k} + n_l^k v_{cl}^{\sum k}}{2}.$$

The $v_s^k$ is the modulation voltage reference, that drives the phase current of the MMC. It can be given directly for the case of open-loop control or it can be obtained from the current-controller and can be expressed as

$$v_s^k = v_s^{k,ref}. \tag{2.40}$$

It is assumed that the MMC has internal current-controller and the CCSC in rotating dq-frame. Therefore, the state-space model is derived in dq-frame. The states, variables and input signals in (2.38) are in sequence domain, they can be converted in dq-domain as in the following.

$$n_u^k = \left(\frac{1}{2}\right)_o - \frac{n_d}{2} - \frac{n_q}{2} - \frac{n_{2d}}{2} - \frac{n_{2q}}{2} \tag{2.41a}$$

$$n_l^k = \left(\frac{1}{2}\right)_o + \frac{n_d}{2} + \frac{n_q}{2} - \frac{n_{2d}}{2} - \frac{n_{2q}}{2} \tag{2.41b}$$

$$i_c^k = i_{c0} + i_{c2d} + i_{c2q} \tag{2.41c}$$

$$i_s^k = i_{sd} + i_{sq} \tag{2.41d}$$

$$v_{cu}^{\sum k} = v_{cu0}^{\sum} + v_{cud}^{\sum} + v_{cuq}^{\sum} + v_{cud2}^{\sum} + v_{cuq2}^{\sum} \tag{2.41e}$$

$$v_{cl}^{\sum k} = v_{cl0}^{\sum} + v_{cld}^{\sum} + v_{clq}^{\sum} + v_{cld2}^{\sum} + v_{clq2}^{\sum} \tag{2.41f}$$

where the assumptions are

- The insertion indexes have the inputs at fundamental frequency from the current-controller and at twice the fundamental from the CCSC.
- The circulating current is a DC component plus the second harmonic component.
- The phase currents have only fundamental components.
- The sum capacitor voltages consist of DC components, fundamental and second harmonic components.

Inserting (2.41), the nonlinear equations of sum capacitor voltage can be expressed as

$$\frac{dv_{cu0}^{\sum}}{dt} = \frac{1}{8c_{eq}}\left((4i_{c0} - 2n_{2d}i_{c2d} - 2n_{2q}i_{c2q}) - (n_d i_{cvd} + n_q i_{cvq})\right) \tag{2.42a}$$

$$\frac{dv_{cud}^{\sum}}{dt} = \omega_1 v_{cuq} - \frac{1}{8c_{eq}}\left((4n_d i_{c0} + 2n_d i_{c2d} + 2n_q i_{c2q}) - (2i_{cvd} - n_{2d}i_{cvd} - n_{2q}i_{cvq})\right) \tag{2.42b}$$

$$\frac{dv_{cuq}^{\sum}}{dt} = -\omega_1 v_{cud} - \frac{1}{8c_{eq}}\left((4n_q i_{c0} - 2n_q i_{c2d} + 2n_d i_{c2q}) - (2i_{cvq} + n_{2d}i_{cvq} - n_{2q}i_{cvd})\right) \tag{2.42c}$$

$$\frac{dv_{cud2}^{\sum}}{dt} = 2\omega_1 v_{cuq2} + \frac{1}{8c_{eq}}\left((-4n_{2d}i_{c0} + 4i_{c2d}) - (n_d i_{cvd} - n_q i_{cvq})\right) \tag{2.42d}$$

$$\frac{dv_{cuq2}^{\sum}}{dt} = -2\omega_1 v_{cud2} + \frac{1}{8c_{eq}}\left((-4n_{2q}i_{c0} + 4i_{c2q}) - (n_q i_{cvd} + n_d i_{cvq})\right) \tag{2.42e}$$

$$\frac{dv_{cl0}^{\sum}}{dt} = \frac{1}{8c_{eq}}\left((4i_{c0} - 2n_{2d}i_{c2d} - 2n_{2q}i_{c2q}) - (n_d i_{cvd} + n_q i_{cvq})\right) \tag{2.43a}$$

$$\frac{dv_{cld}^{\sum}}{dt} = \omega_1 v_{clq} + \frac{1}{8c_{eq}}\left((4n_d i_{c0} + 2n_d i_{c2d} + 2n_q i_{c2q}) - (2i_{cvd} - n_{2d}i_{cvd} - n_{2q}i_{cvq})\right) \tag{2.43b}$$

$$\frac{dv_{clq}^{\sum}}{dt} = -\omega_1 v_{cld} + \frac{1}{8c_{eq}}\left((4n_q i_{c0} - 2n_q i_{c2d} + 2n_d i_{c2q}) - (2i_{cvq} + n_{2d}i_{cvq} - n_{2q}i_{cvd})\right) \tag{2.43c}$$

$$\frac{dv_{cld2}^{\sum}}{dt} = 2\omega_1 v_{clq2} + \frac{1}{8c_{eq}}\left((-4n_{2d}i_{c0} + 4i_{c2d}) - (n_d i_{cvd} - n_q i_{cvq})\right) \tag{2.43d}$$

$$\frac{dv_{clq2}^{\sum}}{dt} = -2\omega_1 v_{cld2} + \frac{1}{8c_{eq}}\left((-4n_{2q}i_{c0} + 4i_{c2q}) - (n_q i_{cvd} + n_d i_{cvq})\right). \tag{2.43e}$$

From (2.42) and (2.43), it is concluded that

$$v_{cu0}^{\sum} = v_{cl0}^{\sum}, v_{cud}^{\sum} = -v_{cld}^{\sum}, v_{cuq}^{\sum} = -v_{clq}^{\sum}, v_{cud2}^{\sum} = v_{cld2}^{\sum}, v_{cuq2}^{\sum} = v_{clq2}^{\sum}.$$

Hence inserting (2.41), the nonlinear equation of the circulating current can be expressed as

$$\frac{di_{c0}}{dt} = -\frac{R_a}{L_a}i_{c0} + \frac{1}{L_a}\frac{v_{dc}}{2} - \frac{1}{4L_o}\left(2v_{cu0}^{\sum} - n_d v_{cud}^{\sum} - n_q v_{cuq}^{\sum} - n_{2d}v_{cud2}^{\sum} - n_{2q}v_{cuq2}^{\sum}\right) \tag{2.44a}$$

$$\frac{di_{cd2}}{dt} = -\frac{R_a}{L_a}i_{cd2} + 2\omega_1 i_{cq2} - \frac{1}{4L_o}\left(-n_d v_{cud}^{\sum} + n_q v_{cuq}^{\sum} - 2n_{2d}v_{cu0}^{\sum} + 2v_{cud2}^{\sum}\right) \tag{2.44b}$$

$$\frac{di_{cq2}}{dt} = -\frac{R_a}{L_a}i_{cq2} - 2\omega_1 i_{cd2} - \frac{1}{4L_o}\left(-n_q v_{cud}^{\sum} - n_d v_{cuq}^{\sum} - 2n_{2q}v_{cu0}^{\sum} + 2v_{cuq2}^{\sum}\right). \tag{2.44c}$$

The MMC can be modelled in state-space form through a 8th order nonlinear equations where sum capacitor voltage has five states and circulating current has three states and can be given by

$$\frac{dX_{mmc}}{dt} = f(X(t)_{mmc}, U(t)) \tag{2.45a}$$

$$Y = g(X(t)_{mmc}, U(t)) \tag{2.45b}$$

where

$$X_{mmc} = \left(v_{cu0}^{\sum} \quad v_{cud}^{\sum} \quad v_{cuq}^{\sum} \quad v_{cud2}^{\sum} \quad v_{cuq2}^{\sum} \quad i_{c0} \quad i_{cd2} \quad i_{cq2}\right)^T. \tag{2.46}$$

The MMC used in the HVDC transmission system is assumed to have a close-loop current-controller similar to the one discuss for the two-level VSC discuss in the previous section as shown in Fig. 2.2. In active power control mode, the d-axis current reference can be obtained from the outer-loop PI controller or can be calculated directly from the voltage power relationship. In the case of the DC voltage control mode, the d-axis current reference can be obtained from the outer-loop DC voltage controller. The state-space model developed here is assumed to have only a current-controller which can be extended for other control mode application by

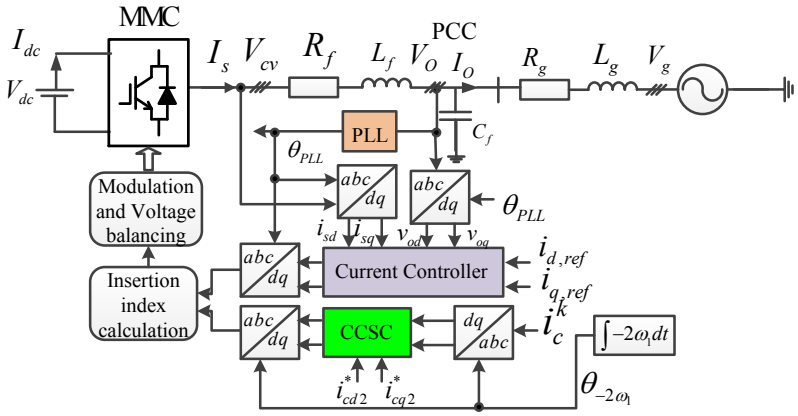


**Figure 2.10:** MMC system including the control block diagram.

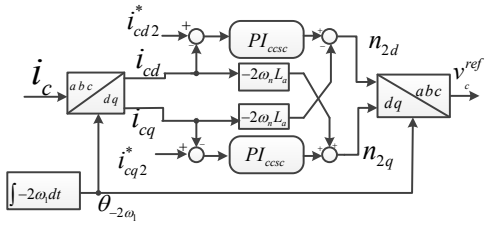


**Figure 2.11:** Circulating current suppression controller of MMC.

extending with an outer-loop controller. Fig. 2.10 shows the MMC HVDC system including the current-controllers, CCSC and the PLL. The The d-axis and q-axis insertion indexes at fundamental frequency are obtained from the current controller as

$$n_d = v_{sd,ref} = k_{pc}(i_{d,ref} - i_{sd}) + k_{ic}\gamma_{Ld} + v_{od} - \omega_{pll}L'i_{Lq} - v_{od,AD} \tag{2.47a}$$

$$n_q = v_{sq,ref} = k_{pc}(i_{q,ref} - i_{sq}) + k_{ic}\gamma_{Lq} + v_{oq} + \omega_{pll}L'i_{Ld} - v_{oq,AD}. \tag{2.47b}$$

The CCSC is implemented to limit the second harmonic circulating current through switch and is shown in Fig. 2.11. The d-axis and q-axis insertion indexes at twice the fundamental frequency obtained from the CCSC can be expressed as

$$n_{d2} = k_{pcc}\left(i^*_{cd2} - i_{cd2}\right) + k_{icc}\gamma_{d2} - 2\omega_1 l_a i_{cq2} \tag{2.48a}$$

$$n_{q2} = k_{pcc}\left(i^*_{cq2} - i_{cq2}\right) + k_{icc}\gamma_{q2} + 2\omega_1 l_a i_{cd2} \tag{2.48b}$$

where $i^*_{cd2}$ and $i^*_{cq2}$ are the d- and q-axis circulating current reference which are set to zero; $k_{p,ccsc}$ and $k_{i,ccsc}$ are the proportional and integral gain of the CCSC, respectively and the $\gamma_{d2}$ and $\gamma_{q2}$ are the auxiliary variables introduced to represent the integral term of the CCSC and can be defined as

$$\frac{d\gamma_{d2}}{dt} = i^*_{cd2} - i_{cd2} \tag{2.49a}$$

$$\frac{d\gamma_{q2}}{dt} = i^*_{cq2} - i_{cq2}. \tag{2.49b}$$

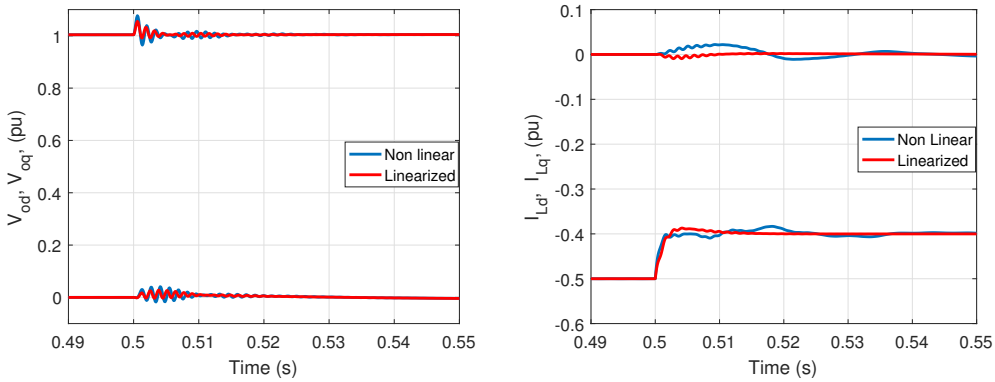


**(a)** **(b)**

**Figure 2.12:** Time domain responses comparison between the state-spcae linearized model and the nonlinear model: (a) voltages at PCC and (b) MMC phase currents.

Hence the MMC model including the states of the current controller, PLL, CCSC and AC dynamics can be presented in state-space form by a 24th order nonlinear equation as

$$\frac{dx_{mmc,HVDC}}{dt} = f(x(t)_{mmc,HVDC}, u(t)) \tag{2.50a}$$

$$y = g(x(t)_{mmc,HVDC}, u(t)) \tag{2.50b}$$

where

$$\begin{aligned} x_{mmc,HVDC}(t) =& [v_{od}\ v_{oq}\ i_{sd}\ i_{sq}\ \gamma_d\ \gamma_q\ i_{od}\ i_{oq}\ \varphi_d\ \varphi_q\ v_{plld}\ v_{pllq}\ \varepsilon\ \delta\theta \\ & v_{cu0}^{\sum}\ v_{cud}^{\sum}\ v_{cuq}^{\sum}\ v_{cud2}^{\sum}\ v_{cuq2}^{\sum}\ i_{c0}\ i_{cd2}\ i_{cq2}\ \gamma_{d2}\ \gamma_{q2}]^T \end{aligned} \tag{2.51a}$$

$$u(t) = [i_{d,ref}\ i_{q,ref}\ v_{dc}\ i_{cd2}^*\ i_{cq2}^*\ v_g\ \omega_g]^T. \tag{2.51b}$$

The nonlinear model of the MMC HVDC system has been linearized around an operating point and linearized A, B, C and D matrices are obtained. The MMC HVDC system has also been implemented in MATLAB/Simulink with the association of Simpower System. The results obtained from the linearized model are then compared with the results from the simulation model. Fig. 2.12 (a) shows the d- and q-axis voltages at PCC and Fig. 2.12 (b) shows d- and q-axis phase currents of the MMC both from the nonlinear model and small-signal state-space linearized model. A step 0.1 pu current is applied at 0.5 s. As can be seen both nonlinear and the linearized model have similar behaviour in response to the step change of current which validates the effectiveness of the derived model.

## 2.4 Impact of the State-space Small-signal Modeling Fidelity

The state-space model relies on the development of supporting equations and modeling assumption and can be studied by using general simulation system or power system specific software. In this study, an analytical linearized small-signal state-space (ALSS) model developed for VSC in the previous section has been expanded for a point-to-point VSC-HVDC transmission system. The configuration of the investigated point-to-point HVDC system is shown in Fig. 2.13.

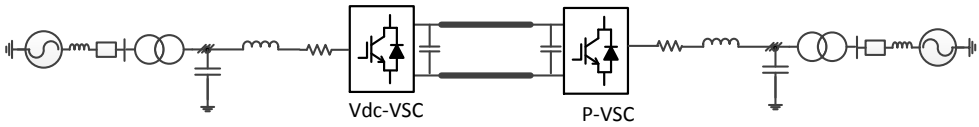


**Figure 2.13:** Schematic of investigated point-to-point VSC HVDC system

**Table 2.1:** Data used for the point-to-point HVDC system

| Parameter | Value | Parameter | Value |
|---|---|---|---|
| Rated Power, $S_b$ | 1200 MVA | $V_{dc}$ | 400 kV |
| Rated AC voltage | 204 kV | $L_c$ | 0.10 pu |
| Rated frequecy | 50 Hz | $R_c$ | 0.0015 pu |
| Trans. inductance | 0.15 pu | $C_f$ | 0.074 pu |
| Trans. resistance | 0.005 pu | $L_{dc}$ | 0.2042 pu |
| Grid inductance | 0.0027 pu | $R_{dc}$ | 0.0029 pu |
| Grid resistance | 0.27E-7 pu | $C_{dc}$ | 4.2224 pu |

The time domain responses obtained from ALSS model are therefore compared with a nonlinear model. After validation of the ALSS model with the nonlinear model, the small-signal stability analysis has been carried out using the ALSS model for further investigation of the HVDC system.

The system is also investigated by using the PF simulation tool developed by DIgSILENT GmbH [87] as an example of a commercial power system simulation tool to have a comparison of small-signal stability assessment between ALSS model and PF model. PF is a software package for analysis of transmission, distribution and industrial electrical power systems (Version 15.0.2 is used in this study) [87]. PF has two simulation options; one is based on the detailed Electromagnetic Transient mode (EMT) and the other is based on the simplified electrical transient mode (RMS). In EMT simulation, voltages and currents are represented by their instantaneous values where the dynamic behavior of the network components is included. Electromagnetic dynamics of electrical networks are neglected in RMS simulation and the voltages and currents are represented by magnitude and phase angle. In the network, they are found as algebraic equations rather than differential equations. In PF, the small-signal stability analysis can be investigated only in RMS mode. Since this mode is neglecting the dynamics of electrical network components, it is necessary to understand the effect of this simplification on the system stability.

### 2.4.1 Comparison of Time Domain Simulation Results

The parameters listed in Table 2.1 are used for analysis of the system performance. The control objectives implemented in the investigated system are the DC voltage and reactive power control on Vdc-VSC, the active and the reactive power control on P-VSC. The transformers are represented by an equivalent series impedance. The initial condition of the power reference is set to 0.9 pu and the voltage reference is 1.0 pu and reactive power reference for both converters is set to 0 pu. For this control strategy and settings, the system is investigated to validate

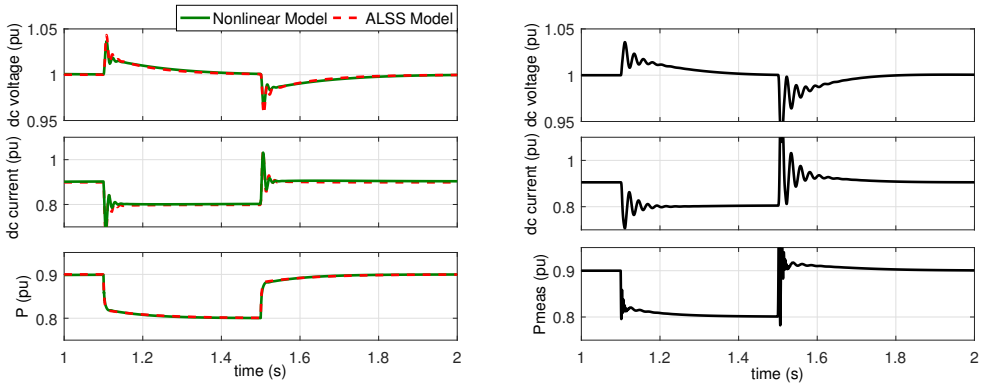


**Figure 2.14:** DC voltage, DC line current and active power: (a) ALSS model and (b) RMS model.

the performance in time domain response. After reaching to steady state, two transient events are applied to observe the dynamic behavior and stability of the system. At 1.1 s the power reference steps down to 0.8 pu and after reaching steady state, second event is introduced by stepping up the power reference to 0.9 pu at 1.5 s. The result from the time domain simulation is depicted in Fig. 2.14 (a) for both ALSS model and nonlinear model. The DC-link voltage, DC-line current and measured active power at PCC as shown in Fig. 2.14 (a), have quite similar behavior with same transient oscillation frequency and damping both for the ALSS model and nonlinear model. The time domain simulation result confirms the satisfactory operation of these models.
The performance of the active power and the DC voltage controller is confirmed by time domain analysis and is found to be satisfactory for both ALSS model and the nonlinear model. The DC voltage and current have a transient oscillation with a frequency of 68.6 Hz, which is found to be damped well in steady state operation. The oscillation frequency is the same for the ALSS model and the nonlinear model.

The system with the same parameters and control is investigated in PF environment. In PF model the converters are connected to the grid through a transformer of 380/204 kV, 50 Hz with the same rating as the converter whereas in averaged model they are represented by an equivalent inductance and resistance. The $\pi$-model DC cable is used for DC transmission line instead of representing them by equivalent impedance. Same transient events are applied as discussed for the ALSS model and the nonlinear model. The DC voltage at voltage control terminal, power at PCC and DC line current from time domain simulation from the PF model are shown Fig. 2.14 (b). The DC voltage and current have an oscillation with a frequency of 42.4 Hz in the transient period and they damped well in the steady state. The current controller, DC voltage controller and power controller work properly at the same tuning applied in the ALSS model and the nonlinear model. The measured active power has an oscillation frequency of 293 Hz with a high damping when a transient step of the power is applied; however, in the ALSS model, no such oscillation is noticed. The overall system performance is found to be satisfactory for the ALSS model, nonlinear model and RMS model in PF for the same parameters and references when the same tuning criteria are applied for the inner-loop current-

controller and the outer-loop power or DC voltage controller.

### 2.4.2 Comparison of Eigenvalue-based Stability Analysis Obtained by Analytically and Numerical Simulation

The small-signal stability analysis is investigated for the point-to-point HVDC system and the resulting eigenvalues calculated analytically are depicted in Fig. 2.15. The ALSS model has 40 modes, among which 11 pairs are complex conjugate. Most of the complex conjugate poles are located twice in the same position, since all the controls and passive components for both VSCs are the same except the outer-loop controller in the d-axis. Further, the poles are analyzed by participation factor analysis. They are identified to a group based on the maximum participation contribution of individual states, marked them with different colors. Four pairs of complex conjugate poles with the highest complex frequency of oscillation and shorter damping time constant are related to states of the grid inductance and filter capacitance. Next four pair complex conjugate poles with a quite high damping and relatively low corresponding oscillation frequency are related to the states of the converter series inductance and AC active damping. Other three pairs of complex conjugate poles are located close to the imaginary axis and have more impact on the system stability. The pole located $-98.9 \pm j431$ corresponding frequency of oscillation 68.6 Hz is identified as responsible for the oscillation of the DC-link voltage and current. The state of the DC-line current and the states of the DC-link capacitance has the highest contribution to this mode. A pair of complex conjugate poles with low damping and frequency is related to the state of the PLL. All other modes are real negative modes. There are four poles located at $-4.71 \pm j0$ corresponding to the integrator of the current controller. Three real poles located around $-8 \pm j0$ are corresponding to the integrator of the outer loop power controller and the pole corresponding to the integrator of the DC voltage controller is located at $-10.8 \pm j0$.

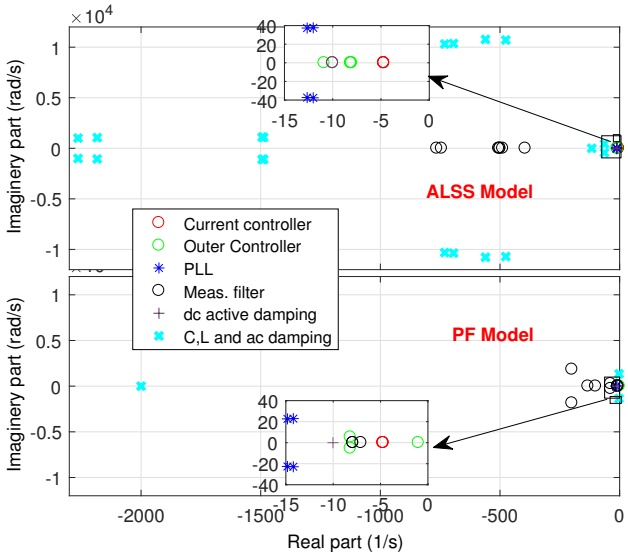


**Figure 2.15:** Eigenvalue plot for ALSS and P.F. model

**Table 2.2:** Eigenvalues of associated states based-on maximum participation factor

| Associated states | ALSS Model, $\lambda$=$\sigma$±j$\omega$ | P.F. Model, $\lambda$=$\sigma$±j$\omega$ |
|---|---|---|
| $\gamma_{Ld}$,$\gamma_{Lq}$ | -4.71±j0, -4.71±j0 | -4.71±j0.02, -4.76±j0 |
| $\gamma_{Vdc}$ | -10.89+j0 | -8.18±j5.30 |
| $\gamma_P$,$\gamma_Q$ | -8.03+j0, -8.15+j0, -8.11+j0 | -7.06+j0, -7.91±j0.04 |
| $\varepsilon_{pll}$, $\delta\theta_{pll}$ | -12.02±j37.62, -12.65±j37.34 | -14.83±j22.63, -14.21±j22.89 |
| $\rho_{dc}$ | -10+j0, -10+j0, | -10.02+j0, -10.02+j0 |
| $v_{dc}$, $i_{dc,line}$ | -116.47+j0.00, -63.63 ±j441.3 | Non-existent |
| $i_{od}$, $i_{oq}$, $v_{od}$, $v_{oq}$ | -475.79±j10708.38, -560.77±j10772.17<br>-694.37±j10360.51, -730.93±j10314.40 | Non-existent |
| $i_{Ld}$, $i_{Lq}$ | -1494.07±j1099.87, -1487.75±j 1091.04 | Non-existent |
| Unidentified | Non-existent | -2.25±j1355.7, -2000+j0,<br>-37.39±j266.45 |

The eigenvalues resulting from the numerical simulation by PF are depicted in Fig. 2.15. These modes are calculated in PF by selective modal analysis using the Arnoldi/Lanczos method. They are also further analyzed by participation factor analysis. Eight pairs of complex conjugate poles are identified by PF tool. The participation factor for some poles cannot be identified in PF, they are denoted as unidentified poles as shown in Table 2.2. For example, the participation contribution of states for a pair of complex pole located $-2.25 \pm j1355.70$ cannot be identified. This pole has very low damping and high oscillation frequency with dominant impact on the system stability. The exact participation contribution of the states for the pole located at $-37.39 \pm j266.45$ also cannot be identified; however, it shows that states of low-pass measurement filter, DC voltage controller, active DC damping and PLL have a small participation contribution (<0.1% for each states) on that mode. MF has high participation contribution; therefore, it is shown in the group of MF pole. Moreover, this pole is identified for the oscillation of the DC voltage and current in the transient period with a damping oscillation frequency of 42.4 Hz. Other complex conjugate poles are located much closer to the center point $(0, j0)$ and can lead the system to instability in the case of improper tuning and modeling. Complex conjugate pole pairs located at $-8.18 \pm j5.30$ and $-4.71 \pm j0.01$ are corresponding to the states of the outer loop PI controller and inner loop current controller, respectively. The poles related to the states of the integrator of the PLL are located at $-14.0 \pm j22.0$.

The investigated VSC HVDC system has two converters with same control loop and parameters except for the difference in outer loop d-axis control. Therefore, most of the complex conjugates poles are located twice in the same position in the ALSS model; however, there are not twice in the case of PF (RMS) model except for the pole corresponding to the integrator states of the PLL. To show the difference more clearly, the eigenvalues calculated analytically from the ALSS model and identified from PF model are presented in Table 2.2. The damping of the pole corresponding to the integrator of inner-loop current-control is equal for both PF model and ALSS model; however, the oscillation frequency is zero for the ALSS model, but it is not zero for the PF model. The poles related to the outer loop control are real poles for the ALSS model and they are oscillatory with low frequency for the PF model. The damping of the pole related to the DC voltage oscillation is quite low for the PF model. Some of the main observations are

as follows-

- It is observed that not all the eigenvalues can be identified from the PF which is given in Table 2.2. There is a pole with very low damping and high oscillation frequency that appears in the PF model, but no such a pole appeared in the analytical model.
- The modeling in RMS works fine as long as the poles related to the network dynamics do not have a significant impact on the system stability due to the proper design of the $LC$ components.
- The P.F. model requires less computation time compared to the nonlinear model developed in MATLAB/Simulink association with SimPower system. To study the large system P.F. model is more suitable due to less computation time in the PF if it is ensured that the system will not be influenced by the $LC$ components.

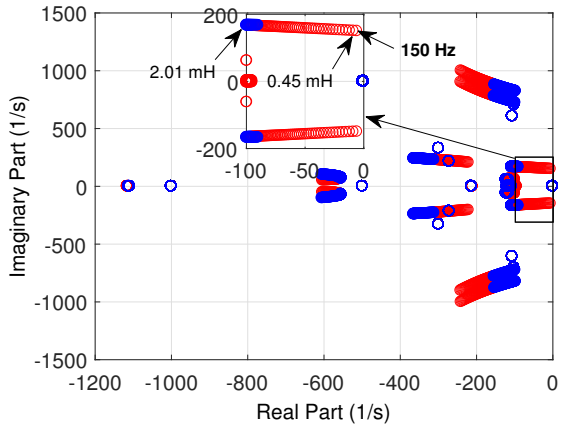


**Figure 2.16:** Trajectory of eigenvalues for a change of series inductor of DC voltage-controlled VSC

## 2.5 Impact of the $LC$ Component on the Stability

In order to study the impact of the $LC$ parameter on the stability, the converter series inductor of the DC voltage control VSC has been varied. The parameters used in the simulation are given in Table A.1 in Appendix A where the parameters have been chosen for the low voltage and low power level so that the theoretical analysis can be verified by experiments. The series inductor of the Vdc-VSC has been varied from 2.01mH to 0.45mH and the VSC has been designed for a power level with a short circuit ratio of 5. Fig. 2.16 shows the eigenvalue trajectory for a change of VSC's series inductor when the converter current controller has been re-tuned for each inductor value. As can be seen, for lower value of the series inductor, a complex conjugate eigenvalue around 150 Hz is moving toward the unstable region and is more prone to make the system unstable. Time domain simulations have been carried out for these two inductor values of 2.01 mH and 0.45 mH and the resulting time domain responses are shown in Figures 2.17. As can be seen, the system operates stably for higher value of the inductor and however, the system has a harmonic oscillation around 150 Hz for lower value of the inductor.

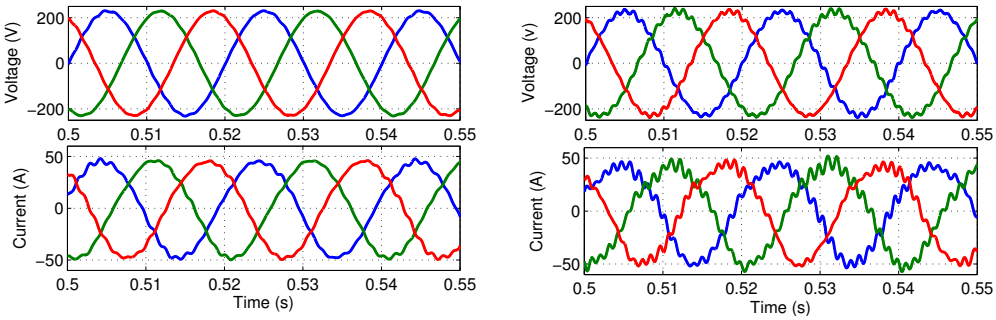


**Figure 2.17:** Simulation result: Three phase AC voltages and currents for DC voltage-controlled converter series inductance of (a) 2.01 mH and (b) 0.45 mH.

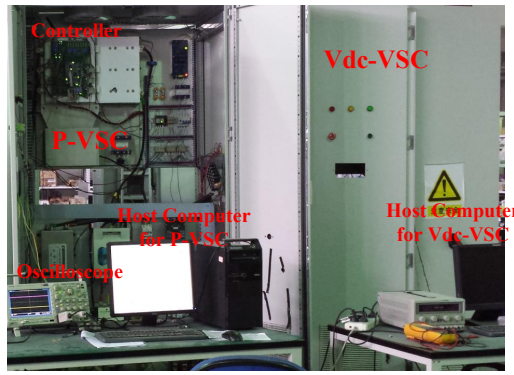


**Figure 2.18:** Experimental setup of VSC-HVDC system.

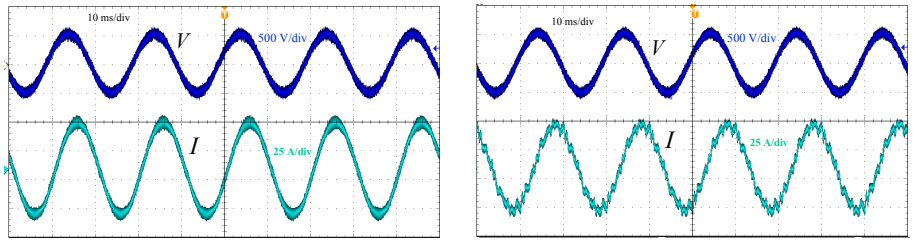


**Figure 2.19:** Experimental result: Phase-A AC voltage and current for the DC voltage-controlled converter series inductance of (a) 2.01 mH and (b) 0.45 mH

To further verify the theoretical analysis and the time domain simulations, an experimental setup has been built in the laboratory with two level VSCs. The controls have been implemented in the digital signal processor (DSP) and the PWM signal implemented in the field programmable gate array (FPGA) board. The experiments have been carried out for these two inductor values

of 2.01 mH and 0.45 mH and the resulting time domain responses are shown in Fig. 2.19, respectively. As can be seen, both the simulation and experiment prove the existences 150 Hz harmonic oscillation in the system for lower value of the inductor as predicted by the analytical small-signal stability analysis. This harmonic instability is caused by the $LC$ parameters of the Vdc-VSC and it can not be predicted in the RMS model since the impact of the $LC$ components on the stability is neglected in the RMS modeling.

## 2.6 Eigenvalue-based Stability and Interaction Analysis of Large-scale MT-HVDC Systems

This stability and interaction analysis is based on the CIGRE DC-grid test system [33], which is designed to resemble a generalized future configuration of MT-HVDC systems. Fig. 2.20 shows the CIGRE DC grid test system. The small-signal stability of the system is investigated to identify critical modes related to different parts of the interconnected AC and DC power systems. Firstly, a case with point-to-point HVDC connection is analyzed (Case 1 in Fig. 2.20), followed by the analysis of a four-terminal DC system (Case 2 in Fig. 2.20), before the stability of the entire CIGRE DC grid configuration is studied. Since the CIGRE DC grid system is a large power system including many VSCs, it is not feasible modeling the system analytically in a state-space form. Therefore, the systems have been modeled and simulated in the DIgSILENT Power Factory environment. As discussed in the previous section that the LC parts can have a significant impact on the system stability. Hence it is assumed that the LC parts of the system have designed carefully so that they do not have an impact on the system stability. Hence, the

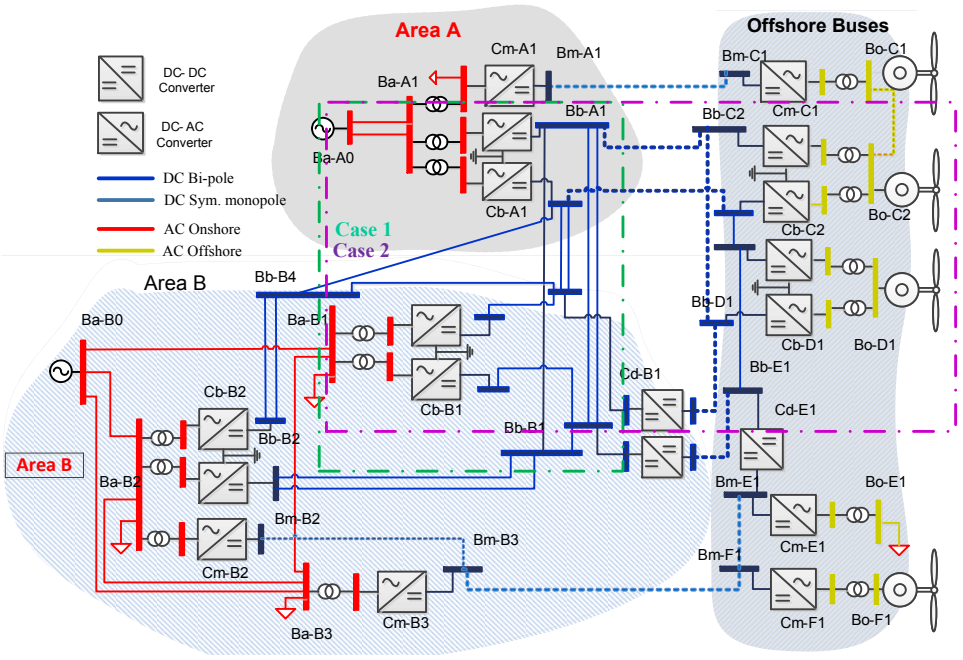


**Figure 2.20:** CIGRE DC Grid test system.

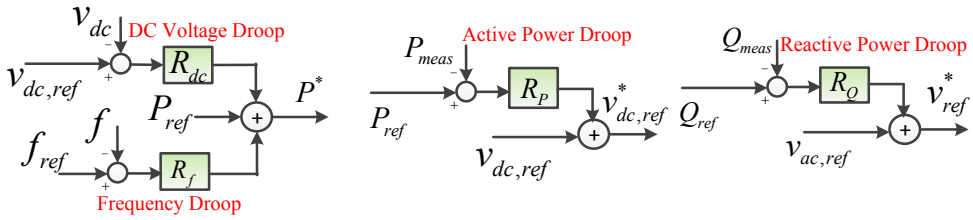


**Figure 2.21:** Droop Control Implementation.

focus of this study will be the controller interaction analysis.

The VSCs are utilized to control different parameters based on the control objectives. The converters control two quantities: one in the real d-axis and the other in the imaginary q-axis. In real d-axis, the converter can be used to regulate the real power or the DC voltage. When a VSC regulates the DC link voltage, the d-axis current is obtained from an outer-loop PI controller; in the case of power control mode, the d-axis reference current is obtained from (2.52a). Similarly, the same controls follow for the reactive power or AC voltage control. The input reference current to the inner-loop current controller can be given by (2.52b).

$$i_{d,ref} = \begin{cases} \frac{P^* v_d + Q^* v_q}{v_d^2 + v_q^2}; & P \ \ Control \\ \left(k_{pvdc} + \frac{k_{ivdc}}{s}\right)(v_{dc} - v_{dc,ref}); & V_{dc} \ \ Control \end{cases} \tag{2.52a}$$

$$i_{q,ref} = \begin{cases} \frac{P^* v_q - Q^* v_d}{v_d^2 + v_q^2}; & Q \ \ Control \\ \left(k_{pvac} + \frac{k_{ivac}}{s}\right)(v_{ac} - v_{ac,ref};) & V_{ac} \ \ Control \end{cases} \tag{2.52b}$$

The control modes used to control the converter are in the following: (i) DC and AC voltage (Vdc-Vac) control, (ii) active and reactive power (P-Q) control, (iii) P-Vac control, Vdc-Q control and (iv) AC slack. In the case of AC slack, the converter behaves as a voltage source at the AC terminal and functions as an AC grid for the offshore wind farms and the load.

In MT-HVDC systems, the active power controller includes a DC voltage droop to contribute to the voltage control of the DC grid. In the distributed control approach [38], for an MT-HVDC system, one converter has the main responsibility for DC voltage control and others have the power control with a droop functions in their outer loop. If the DC voltage controlled-converter is lost, the DC voltage is regulated by this droop function so that the MT-HVDC can keep in operation. In addition to the DC voltage droop in power control VSCs, they have frequency droop to contribute in regulating AC system frequency. The DC voltage droop and frequency droop for power controlled VSCs are illustrated in Fig. 2.21. Similarly, an active power droop on a DC voltage and a reactive power droop on the AC voltage have been modeled as depicted in Fig. 2.21 [39] to contribute in the DC and AC voltage regulation, respectfully.

### 2.6.1 Analysis of Point-to-point Bi-pole HVDC System (Case 1)

The point-to-point bi-pole connection between busses Ba-A1 and Ba-B1 will be investigated, as indicated with a green dashed-dotted line in the middle of Fig. 2.20. Since AC system area-A has active power surplus, the bi-pole HVDC link is used to export the power to the AC system area-B. Converter station Cb-A1 acts as rectifier while regulates the HVDC link DC voltage and

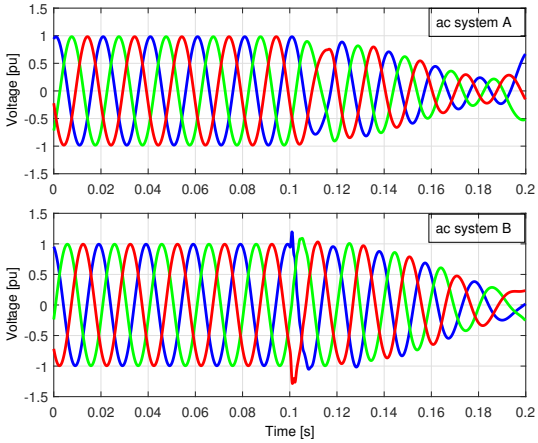


**Figure 2.22:** The AC voltages of the bipole point-to-point HVDC system with weak grid of SCR 2 for stepping power from 0.75 pu to 0.85 pu at 0.1 s.

AC voltage magnitude, while converter station Cb-B1 acts as an inverter controlling the active and reactive power flow. Since this is a bi-pole connection, each converter station consists of two VSCs connected in series on the DC side, with the mid-point grounded. Thus, this link can also be operated as an asymmetric monopole, allowing for transferring 50% of rated power even if one converter is out of operation. Each converter unit is rated 1200 MVA, has $75\mu F$ DC link capacitance and is connected to the AC grids through a 380/204 kV two winding transformer with the same MVA rating as the converter. The converter stations are connected through $\pm 400$ kV DC overhead lines (OHL), thus the total DC link voltage rating of one bi-pole converter station is $800$ kV with a total power rating of 2400 MVA.

Considering the electrical parameters in [33], and properly tuned parameters for the controllers in the system, the investigated subsystem operates stably. However, the system can easily become unstable if AC transmission line impedance has not been considered in the control tuning. In order show the impact of the AC transmission line, the system is therefore first studied without AC transmission lines and operates properly for current controller proportional gain of 0.5 and integrator time constant of 0.01 s. The proportional gain of the DC-link voltage controller is 2 and the integrator time constant is 0.1 s. The small-signal stability has been carried out for this tuning and setting and the eigenvalues are calculated by numerical simulation in Power Factory. Including the two AC transmission lines in the system (Case 1 in Fig. 2.20), two pairs of unstable complex conjugate eigenvalues at $17.005 \pm j86.755$ and $1.684 \pm j21.472$ are found for full loading. These modes are mainly influenced by the frequency and voltage angle of the AC system, the PLLs and the integrator of the DC voltage controller. The small-signal stability analysis has been verified in the time domain simulation. The resulting AC voltage of the converters with this tuning for a step from 0.75 pu to 0.85 pu power reference is presented in Fig. 2.22. This figure clearly shows how the voltage becomes unstable and quickly collapses at the rectifier terminal, bringing the entire system into instability. It should also be noticed that the analysis confirms how the system can become unstable due to the tuning of the PI controller

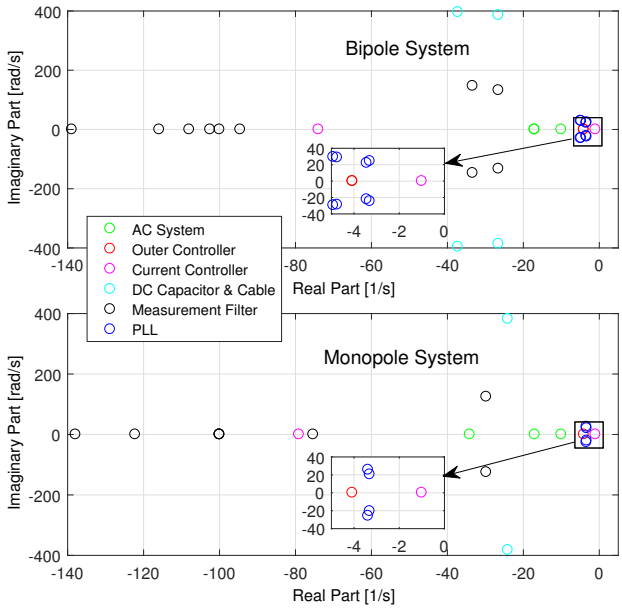


**Figure 2.23:** Eigenvalue plot of (a) point-to-point bi-pole VSC HVDC system and (b) monopole equivalent to the investigated bi-pole point-to-point HVDC system.

[88].

In order to improve the system stability, the grid impedance needs to include in the design of the control-loop bandwidth. Therefore, further investigations have been carried by increasing the current control-loop bandwidth by increasing the proportional gain to 4 and the corresponding system eigenvalues found from the small-signal analysis are shown in Fig. 2.23. They are sorted manually according to their dominant participation factors and plotted with different colors and markers to identify the various types of poles. As the system has satisfactory performance and there are no unstable modes, but there are eight pairs of oscillating modes that can be noticed in Fig. 2.23. The most oscillatory of these pole pairs are located at $-37.226 \pm j397.812$ and $-26.558 \pm j387.017$, corresponding to a damped oscillation frequency of 63.04 and 61.45 Hz, and are found to be mainly associated with the DC link dynamics. There is also four pole pair with relatively slow damping at $-4.918 \pm j29.413$, $-4.744 \pm j28.751$, $-3.301 \pm j24.457$ and $-3.440 \pm j22.127$ associated with the integrator of the PLL. The last two pair of complex conjugate poles is located at $-26.548 \pm j132.55$ and $-4.918 \pm j29.413$, and has a relatively fast response related to the use of measurement filters in the converter control.

Having more bi-pole HVDC converter in the simulation model increases the computational complexity and requires more time in the simulation. Therefore, a symmetrical monopole point-to-point VSC HVDC system with the same rating and control condition as the studied bi-pole configuration has also been investigated for a comparison and later the bi-pole converter stations can be replaced by monopole converter stations in the full CIGRE DC grid system for

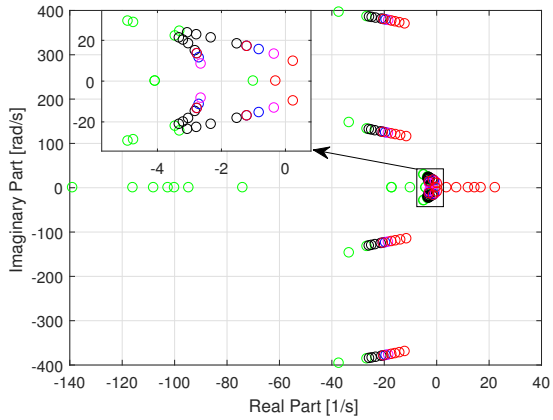


**Figure 2.24:** Eigenvalue trajectory for the biople point-to-point HVDC system with SCR of 1-4 of the AC grid.

simplification of the modeling. In the equivalent monopole HVDC system, the rating of the transformers is increased to 2400 MVA and the converter side voltage is 408 kV. To be equivalent to the bi-pole converter station, the DC voltage of the symmetric monopole converter is 800 kV and the DC link capacitance is 37.5 $\mu$F. The resulting eigenvalues of this system under the same operating conditions as the bi-pole connection are shown in Fig. 2.23. Comparing the eigenvalues for the bi-pole and the monopole configurations it is clearly seen that the bi-pole has twice the number of poles and that the most noticeable poles are doubled poles in similar locations as the corresponding eigenvalues for the monopole system. It is especially noticeable how the most oscillatory poles have higher oscillation frequency, but also a more negative real part for the bi-pole configuration than the equivalent monopole configuration. From a general comparison of the bi-pole configuration and the equivalent monopole configuration, it is also noticed that some of the real poles have quite different locations. However, these are all fast poles with no critical influence on the operation of the system. The poles close to 0 are all the same for both systems, except that the bi-pole configuration has double sets of poles located very close to each other.

The small-signal stability has been carried out to investigate the impact of the short circuit ratio (SCR) on the stability. The trajectory of eigenvalues for different SCR with 0.625 pu power reference is shown in Fig. 2.24, where the SCR is reduced from 4 to 1. A pair of complex conjugate poles corresponding to the PLL of converter Cb-A1 shown in Fig. 2.24 is responsible for the instability and is moving towards unstable region if SCR is smaller than 1.75. Another complex conjugate poles with relatively slow response, associated with the PLL of converter Cb-B1 is also moving towards the real axis. Moreover, some other poles are found to be influenced, for example two complex conjugates poles related to the DC voltage measurement filter of converter Cb-A1 are moving towards the imaginary axis, but they have less impact of the system dynamics. This investigation confirms how the system becomes unstable if the grid becomes weak [88], [89]. The system becomes unstable if SCR is smaller 2 and the power transfer is high (> 0.5 pu) and in the case of SCR reduced to 1, the system can only transfer about 50 % of rated power, without provoking a voltage collapse.

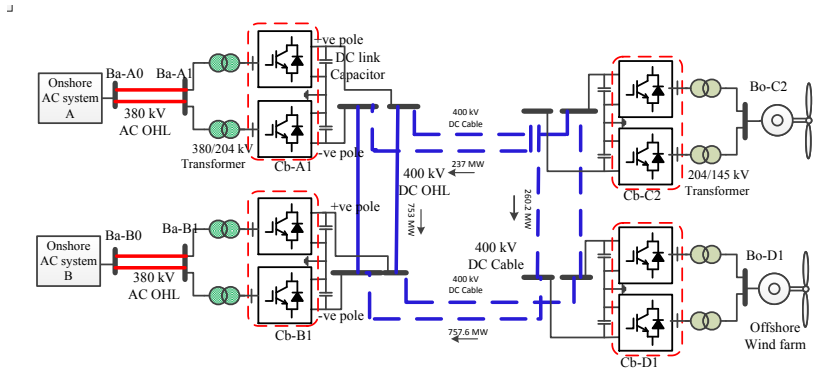


**Figure 2.25:** Four terminal bi-pole VSC-HVDC system.

### 2.6.2 Analysis of Four-Terminal HVDC System (Case 2)

In this case, two more converter stations named Cb-C2 and Cb-D1 are added to the subsystems studied in case 1. These four bi-pole AC-DC converter stations are then forming a ring configuration as indicated with purple dashed-dotted lines in Fig. 2.20. The stations Cb-C2 and Cb-D1 behave as a voltage source at the AC terminal and are used to integrate offshore wind farms. The controls of the Converter station Cb-A1 and Cb-B1 remain the same as discussed for the point-to-point system. In addition, an active power droop on the DC voltage and reactive power droop on the AC voltages have been assumed for the converter stations Cb-A1 to contribute in the AC and DC voltage regulation for a change of active power and AC voltage, respective. Moreover, the control system of converter station Cb-B1 has introduced the DC voltage droop and frequency droop in the power control. As a starting point, this case will be studied without any DC-DC converter, but the influence of including the DC-DC converter for controlling the power flow in the DC grid will also be investigated. The power rating of converter Cb-C2 is 2x400 MVA and converter Cb-D1 is rated for 2x800 MVA. The AC voltage is 145 kV, and the transformers are 204/145 kV with the same ratings as the corresponding converters. Each of the wind farms is producing 500 MW. The resulting power flow solution for the system is indicated in Fig. 2.25. The power produced by the wind farms is exported to the onshore system B through the DC grid, together with some additional power injected from the onshore AC system area-A.

The small-signal stability analysis has been carried out for the system and the resulting eigenvalue plot is shown in Fig. 2.26 (a). An unstable mode $8.086 \pm j338.214$ with a complex frequency of oscillation of 53.8 Hz is noticed. The DC link dynamics has highest participation contribution to this mode; however, the current controller has also a significant influence on this unstable mode. The voltage measurement filter and the PLLs are also associated to this mode. Since this mode is sensitive to the DC link capacitance, this value is increased to $312\mu F$, ensuring that the system has sufficient stability margin with full loading. The resulting eigenvalues of the stable four-terminal HVDC system are plotted in Fig. 2.26 (b). As can be seen, the system has always double sets of complex conjugate poles, since the converters are the bi-pole configuration, and that most of these poles are located in similar positions as for the point-to-point connection. Since the added converters are operated as AC slack busses without

much dynamics of the control, there are not significant new poles added in the system. There is an additional set of double pole pairs associated with the measurement filters of the converters. There are also additional sets of complex poles close to the real axis, whereof one of them have relatively poor damping.

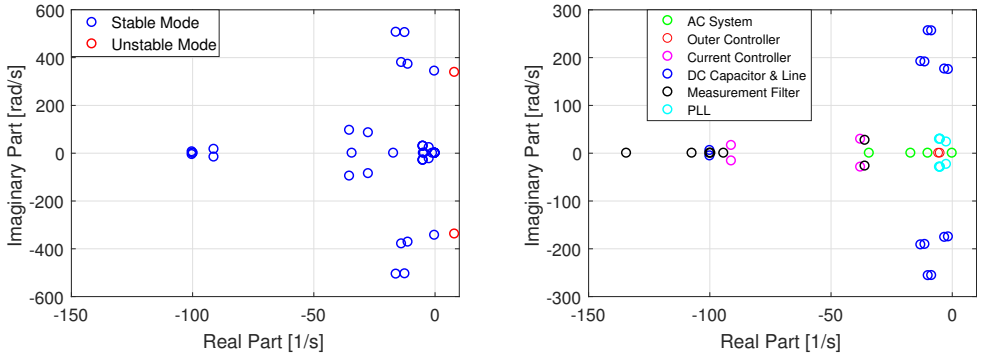


**(a)** **(b)**

**Figure 2.26:** Four Terminal HVDC System: (a) Eigenvalue plot of four terminal HVDC system with $75\mu F$ DC link capacitance and (b) Eigenvalue plot of four terminal HVDC system (Stable case).

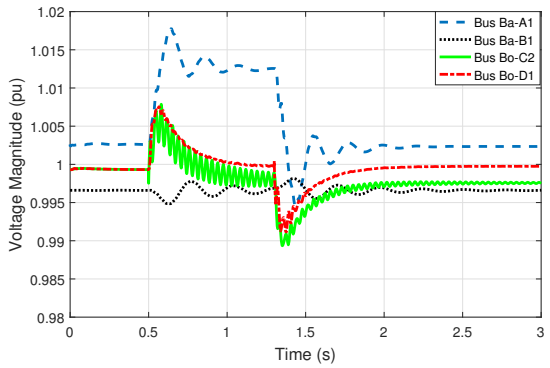


**Figure 2.27:** Four Terminal HVDC System: RMS value of the AC bus voltages of four terminal HVDC system.

Time domain simulations have also been carried out to further investigate how the poles of the system influence the dynamic response of some of the main variables. One example of such simulations is shown in Fig. 2.27, showing the dynamic response of the AC voltages at selected busses in the system when there is a change in wind power injection into the DC grid. Starting from a steady-state, the output power of the wind farm connected to bus Bo-C2 is increased by 20% at 0.5 s of simulation time, and at 1.3 s the output power of the wind farm connected to bus Bo-D1 is decreased by 20%. Further studying the results in Fig. 2.26 and Fig. 2.27 it can be found that the oscillation mode at $-37.60 \pm j28.41$ is corresponding with the voltage oscillation of bus Ba-A1. This oscillation model is associated with measurement filter of the

DC voltage, the PI controller of the PLL and the DC voltage controller. Similarly, voltage oscillation at bus Ba-B1 is coinciding with the oscillation mode given by the complex pole at $-2.37 \pm j23.385$. The real part of this eigenvalue is small, and it takes a relatively long time to damp the oscillation. The state of the PLL for the converter Cb-b1 has a high participation contribution in this mode. The voltage oscillations at busses Bo-C2 and Bo-D1 are mainly corresponding to the eigenvalues at $-1.41 \pm j174.75$ and $-12.91 \pm j191.77$, respectively. It is noticeable from Fig. 2.26 that in the 4T-HVDC system, the most oscillatory poles associated with DC link dynamics are now closer to the imaginary axis.

**Table 2.3:** Overview of Converters and Control Objectives

| AC-DC Converter | Control Objective and set-point | |
|---|---|---|
| Cm-A1 | VDC,ref = 1pu | Qref = 0 |
| Cm-C1 | AC Slack | |
| Cm-B2 | VDCref = 0.99pu | Qref = 0 |
| Cm-B3 | Pref = 0.75 pu Droop on VDC and fAC | VAC,ref = 1pu Droop on Q |
| Cm-E1 | AC Slack | |
| Cm-F1 | AC Slack | |
| Cb-A1 | VDC,ref = 1.01pu | VAC,ref = 1pu Droop on Q |
| Cb-B1 | P ref= 0.625 pu Droop on VDC and fAC | Qref = 0 |
| Cb-B2 | Pref = 0.71 pu Droop on VDC and fAC | Qref=0 |
| Cb-C2 | Pref = - 0.75 pu Droop on VDC and fAC | VAC,ref = 1pu Droop on Q |
| Cb-D1 | AC Slack | |

### 2.6.3 Analysis of the CIGRE DC Grid Test System

To study the dynamics of a more complex system of MT-HVDC, the full CIGRE DC grid test system is investigated. An overview of all the AC-DC converters and their control modes and reference set-points are given in Table 2.3. The current controller proportional gain is in the range 2-0.4 depending on the parameters and rating of the converter and the integrator time constant is kept 0.01 s. The DC and AC voltage controller proportional gain and integral time constant are 2, 0.1 s and 6, 0.25 s, respectively. Time domain simulations have been carried out for the tuning and setting and the resulting time domain responses are shown in Fig. 2.28. As can be seen, the system is unstable. The onshore AC system B voltages have an oscillation frequency around 4.9 Hz which is propagating to the rest of the system. The onshore AC system A and all the offshore AC system exhibit the same frequency of the oscillation as the onshore AC system B. In addition, the voltage magnitude of the offshore AC system C is higher than the nominal value as shown in Fig. 2.28 (b).

The small-signal stability analysis has been carried out to find the source of this instability. Two unstable eigenvalues of $1.974 \pm j31.199$ and $33.728 \pm j0$ are identified which provokes the instability. Participation factor analysis has been carried out to identify the participation contribution of the states in the unstable eigenvalues. The PLL of converter CB-B1 has high participation contribution in the unstable eigenvalue of $1.974 \pm j31.199$. Moreover, the PLL of converter Cb-B2, the integrator of the DC voltage controller of converter Cb-A1, the frequency of the AC system A and the measurement filters are also associated with this eigenvalue which indicates that it is an interaction mode. This unstable eigenvalue is resulting from the interaction

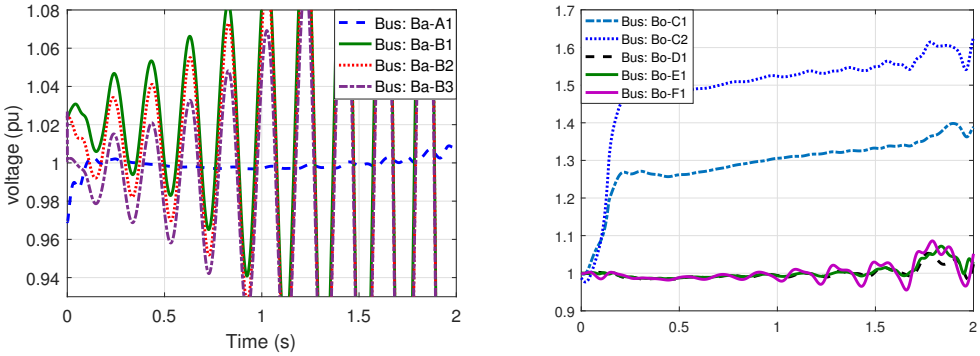


**Figure 2.28:** Unstable System: (a) Onshore and (b) offshore AC system voltages (RMS) of CIGRE DC Grid Test system.

of the controller of the different HVDC converters and the AC system, therefore this oscillation is making consequently the whole system unstable. Since the most dominant state of PLL of CB-B1 in the unstable mode, $1.974 \pm j31.199$, therefore the system can be made stable by redesigning the system controller of the corresponding converter. The voltage becomes unstable, therefore an AC voltage droop has been implemented in the converter stations Cb-B1 and Cb-B2 to contribute AC voltage regulation.

The participation factor analysis has been carried out for the unstable eigenvalue of $33.728 \pm j0$. The states of the AC voltage controller of converter Cb-C2 has a maximum contribution on the unstable eigenvalue. In addition, PLL and AC voltage measurement filter of the corresponding converter have small participation contribution on this mode. Since there is no contribution from states of the other converters controller, it is a local unstable mode and is not an interaction mode. The AC voltage becomes higher than the nominal value due to the overflow of the reactive power produced by AC cable connected between converters CB-C2 and Cm-C1. The system can be made stable by redesigning the controls of the converter CB-C2. A reactive power droop has been implemented as discuss before in converter station Cb-C2. Moreover, the frequency droop and the DC voltage droop are included in the control systems of the converters controlling active power.

After redesigning the controls, the small-signal stability analysis has been carried out and a selected plot of the most important eigenvalues is shown in Fig. 2.29. Now there is no unstable eigenvalues and the system is expected to operate stably. It is observed that the most oscillatory poles that occur when expanding the system appear to be related to the DC-link dynamics of the transmission line and the converters. The poles associated with the current controller show the similar behavior as four-terminal HVDC system when it expands point-to-point to MT-HVDC system. There are also a significant set of complex conjugate poles with low oscillation frequencies related to the PLLs and the outer-loop controllers of the converters, and some additional oscillatory poles with more negative real values associated with the measurement filters of the control systems. However, the grouping of the poles is not changing significantly by expanding the system, as long as individual converters are kept in stable operation. Although further,

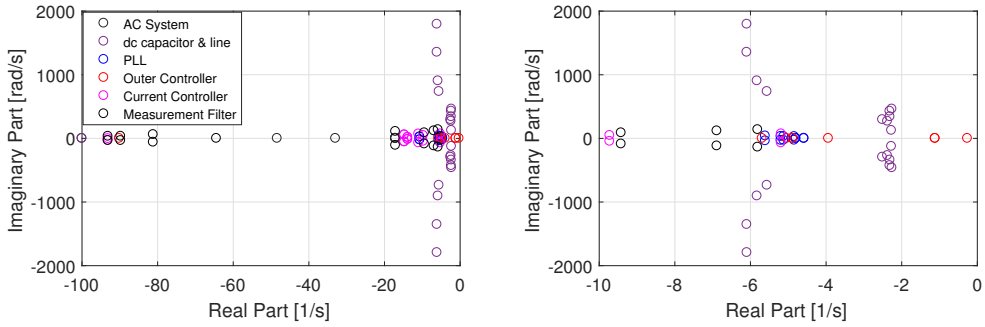


**Figure 2.29:** Eigenvalue plot of Cigre DC Grid Test system for stable operation (a) Full view (b) Critical pole.

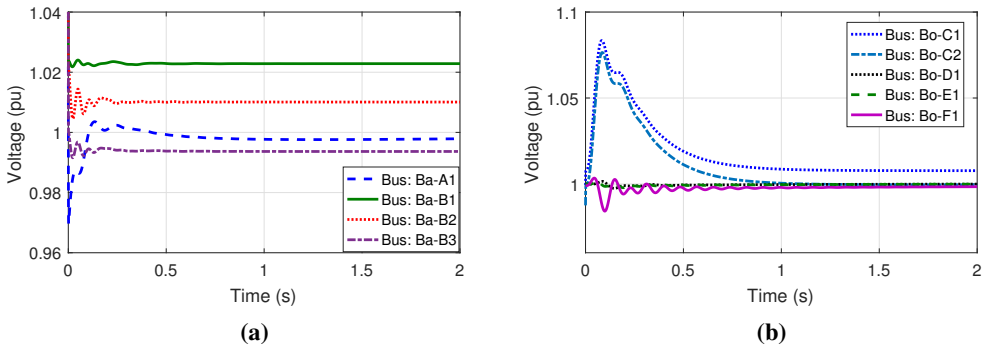


**Figure 2.30:** Stable System: (a) Onshore and (b) offshore AC system voltages (RMS) of CIGRE DC Grid Test system.

and more systematic, analysis is required, this indicates that such MT-HVDC system can easily be expanded step by step, as long as sufficient care is taken on the design and tuning of the individual converter controllers.

The voltages of the onshore and offshore systems from time domain simulation are shown in Fig. 2.30. The system operates stably as predicted by the small-signal stability analysis. The AC system voltage at bus Ba-A1 is close to 1 pu since the converter connected to that bus is controlling the AC voltage. The voltage at bus Ba-B1 is however higher because the converter at that bus is injecting real power to the AC system while controlling 0 reactive power. The AC system voltages of all the onshore busses are also within their operating ranges from 0.95 pu to 1.05 pu. In the offshore wind farm systems C, the voltages are slightly above the nominal values since the AC cables are producing reactive power. Converter Cb-C2 is exporting power to the DC system and producing reactive power. Proper AC voltage control is obtained by implementing a reactive power droop at that converter. The resulting voltage has a slightly oscillatory response during transient events but the system is stable and steady state operation is satisfactory.

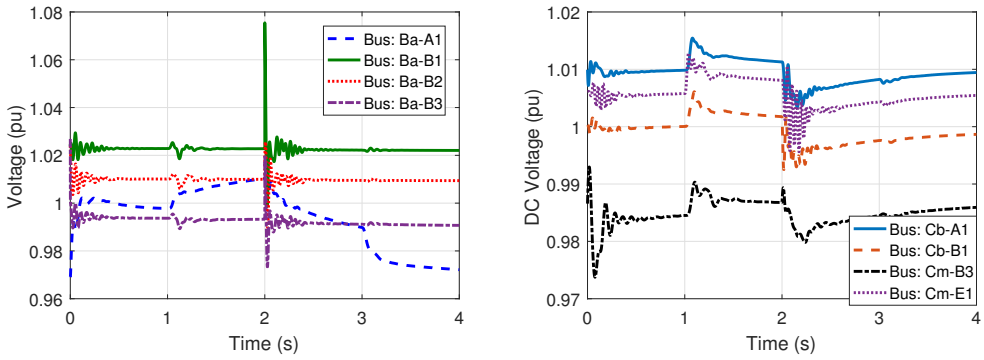


**Figure 2.31:** Transient Stability: (a) Onshore AC system voltages and (b) HVDC link DC bus voltage of CIGRE DC Grid Test system.

#### 2.6.3.1 Transient Stability

In this section, the transient event is introduced to observe the stability of the test system in time-domain RMS simulations. The generated power of wind farm connected at bus Bo-D1 is increased by 20 % at 1 s of simulation time and at 2 s the reference power of converter Cb-B1 is set to 0.8 pu whereas the initial power setting is 0.625 p.u. At 3 s, the generated power by the wind farm connected to bus Bo-C2 is reduced by 20 %. The onshore AC voltages for the transients are presented in Fig. 2.31 (a). The complex frequency of voltage oscillation of the area B is $-10.736 \pm j108.17$. Based on the participation analysis for this mode, the voltage controller of Cb-B2 and Cb-B1, the PLL and the frequency of AC system B have the highest contributions to this mode.

The DC system voltage is presented in Fig. 2.31 (b). The oscillating mode of the voltage of converter Cb-A1 is $-4.082 \pm j132.745$. The DC link capacitor has a significant influence on this oscillation, and the state variable of DC voltage controller is associated with this mode. The complex oscillating mode of DC voltage on converter Cb-B1 is $-86.102 \pm j35.641$. From the participation factor analysis, it is identified that measurement filters on the system A, PLL, and voltage controller have high participation of contribution to this oscillating mode.

#### 2.6.3.2 Sensitivity Analysis

For the sensitivity analysis, the trajectory of the eigenvalues has been analyzed for a variation of the system parameters and the controller coefficient. First, the capacitors of the DC link between onshore Area A and offshore Areas are varied. The pole placement of the system is indicated in Fig. 2.32 (a). When the capacitances are increased, the modes are moving towards the real axis in the complex plane, but some of the poles are also moving towards the right.

The droop gain for DC voltage droop control of converter Cb-B1 is varied to investigate its impact on the stability and the trajectory of the eigenvalues is shown in Fig. 2.32 (b). When the droop gain $R_{Vdc}$ is increased, one specific mode is moving toward the imaginary axis. However, the other modes of the system are only slightly changed, indicating that the contribution of the

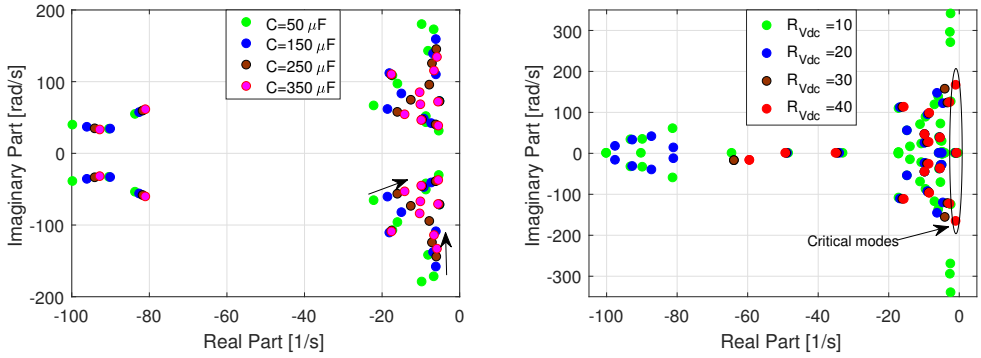


**Figure 2.32:** Sensitivity Analysis: (a) Trajectory of eigenvalue sensitive to DC link capacitance and (b) Trajectory of eigenvalue sensitive to DC voltage droop coefficient.

DC droop on the other modes is negligible. The Fig. 2.32 (b) shows that the droop gain $R_{vdc} = 40$ is the border of stability, and after that, the system will be in the risk of instability. This kind of analysis should be done when a new converter is added to an existing multi-converter system. This analysis enables to develop a large MT-HVDC system by step by step control design for each converter.

## 2.7 Conclusion

This chapter presents the impact of the state-space modeling fidelity on the small-signal stability assessments of VSC-based HVDC systems. A detailed analytical state-space small-signal model is developed for VSCs and MMC for different control objectives. The effectiveness of the models is ensured by comparing the result obtained from a detailed analytical model with the nonlinear model. For general observation and to understand the impact of modeling fidelity, a point-to-point connected VSC-based HVDC system has been studied. Time domain responses, as well as the small-signal analysis, are performed to investigate the stability of the system. This result is also compared with a model implemented in PF environment, a widely used power system analysing tool. The following points need to be considered as a basis towards general guidelines on assessing the results obtained from the traditional power system stability studies containing VSC-based transmission scheme.-

- The results obtained from RMS model ignored states corresponding to all the inductor currents and capacitor voltages. This simplification is justifiable in limited cases when these poles do not have significant impact on the system stability.
- The RMS model do not present the exact participation contribution of states on each mode, because some of the modes related to the inductor current and capacitor voltage are already ignored.
- The result obtained from RMS model do not reflect the actual system stability. Underestimation or overestimation of the system stability is observed from small-signal stability

analysis in RMS model. To estimate the actual system stability, all the states need to be considered in system modeling when the small-signal stability analysis is carried out for power electronics based power system.

Moreover. This chapter illustrates the particular challenges that can occur during a step-wise construction of a large-scale MT-HVDC transmission system. In order to show the challenges, firstly, a case with a point-to-point HVDC connection is analyzed, followed by the analysis of a four-terminal DC system, before the stability of the large-scale MT-HVDC system is studied. During step-wise expansion, the critical poles move towards the imaginary axis which provokes the system to lose stability. Moreover, the negative real poles in a point-to-point connection become oscillatory in MT-HVDC systems which indicates that adding more converters, the system becomes more prone to voltage instability. The stability has been improved by tuning the controller properly and by ensuring the optimized value of the DC-link capacitor for MT-HVDC systems.

# Chapter 3

# Impedance based Stability Analysis of VSC-HVDC System

*This chapter presents the impedance based stability analysis of VSC-HVDC systems as an alternative measurement-based approach to limit the high dependence on detail information of components in large-scale systems. Analytical impedance models for the VSC-HVDC converters have been derived for different control modes and the impedance frequency response is verified by the perturbation method via measurements. Once the source and load impedance are identified, an impedance based stability method is adopted in order to determine the stability of the VSC-based HVDC system. The system stability can be predicted from characteristics loci of minor-loop gain and the phase margin shows the stability strength of the system.*

This chapter is based on the following articles.

[1] **M. Amin** and M. Molinas, "Impedance based stability analysis of VSC-based HVDC system," *2015 IEEE Eindhoven PowerTech*, Eindhoven, 2015, pp. 1-6.

[2] **M. Amin**, A. Rygg and M. Molinas, "Active power flow direction effect on stability in multi-terminal VSC-HVDC transmission system in integrating wind farm," *2016 IEEE 17th Workshop on Control and Modeling for Power Electronics (IEEE COMPEL 2016)*, Trondheim, 2016, pp. 1-8.

[3] **M. Amin**, M. Molinas, J. Lyu and X. Cai, "Impact of Power Flow Direction on the Stability of VSC-HVDC Seen from the Impedances Nyquist Plot," *IEEE Transactions on Power Electronics*, vol. 32, no. 10, pp. 8204-8217, Oct. 2017.

## 3.1 Introduction

With increasing activities in the development of VSC-based HVDC transmission system, it is necessary to pre-asses their impact on the system stability before connecting to the main AC grid. Existing approaches to study such instability are mainly based on the state-space small-signal modeling of the VSC-HVDC system and analyzing the eigenvalue of the system. It requires the detailed analytical modeling information to derive the state-space small-signal model

for studying the stability of the HVDC system. Recently the impedance-based small-signal stability analysis method is broadly used to determine the stability of the power electronics based power system which does not require the detailed modeling of the system [46]. This chapter presents the impedance-based small-signal stability analysis of the VSC-based HVDC system. An impedance model for the VSC of the HVDC transmission system is analytically derived and the derived model is validated by comparing the frequency response of the analytical impedance model and the impedance measured at the AC terminal from a detailed model of VSC-based HVDC transmission system in MATLAB/Simulink. Once the source and the load impedance are identified, the impedance-based stability analysis is adopted in order to determine the stability of the VSC-based HVDC system. The system remains stable as long as the minor loop gain of the negative feedback control system, that is the source-load impedance ratio of the HVDC system, satisfies the Generalized Nyquist Criterion (GNC). The system stability can be well predicted from the Nyquist plot of the impedance ratio and the phase margin shows the stability strength of the system.

In order adopt the impedance based stability analysis of the VSC-HVDC system, deriving the analytical impedance model is the prerequisite. The impedance-based analysis can be adopted on the AC side of the VSC either in sequence domain [48], [49] or $dq$-domain [50], [53] and the DC side based on the DC impedance [58], [59], [75]. The impedance-based method predicts the stability of the system accurately and the frequency of the oscillation is predicted from the cross section point of the unit circle in the Nyquist plot [48]–[50], [53], [65]. In this work, both the DC and AC impedance model of the VSC are derived. Since the controllers of the HVDC VSCs are implemented in $dq$-domain, therefore the AC impedance model is derived in $dq$-domain.

The rest of the chapter is organized as follows. Section 3.2 shows the analytical AC impedance modeling of the VSC in dq-frame and the section 3.3 verifies the analytical model in the numerical simulation. Section 3.4 presents the analytical DC impedance modeling of the VSC. Impedance-based frequency domain stability analysis is presented in section 3.5. Section 3.6 discusses the impact of the control-loop bandwidth on the impedance frequency responses. Section 3.7 explains the control design for the HVDC system that allow the power flows both direction in the system. Finally, the chapter is concluded in section 3.8.

## 3.2 AC Impedance Modeling of the VSC in $dq$-frame

This section presents the impedance model derivation of the VSCs for different control objectives such as current control, active power control and the DC voltage control.

### 3.2.1 Analytical Modeling of VSC-HVDC

The electrical circuit of a VSC-HVDC converter for analytical modeling, including the controller block diagram is shown in Fig. 3.1. The modeling, analysis and the control of the system will be presented in a synchronous reference frame (SRF). The transformation of the three phase quantity from the stationary reference frame to the SRF is based on the amplitude-invariant Park transformation, with the d-axis aligned with the voltage vector $v_o$ and q-axis leading the d-axis

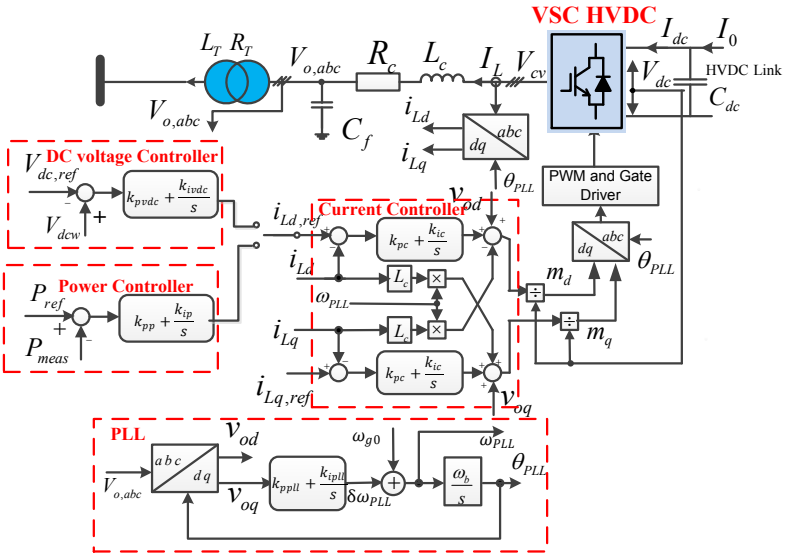


**Figure 3.1:** The VSC-HVDC Converter system including control block diagram.

by $90^0$. The dynamic equations of the converter in pu can be given by [82], [83]

$$\begin{bmatrix} v_{od}^s \\ v_{oq}^s \end{bmatrix} = \begin{bmatrix} m_d^s & 0 \\ m_q^s & 0 \end{bmatrix} \begin{bmatrix} v_{dc} \\ 0 \end{bmatrix} - \overbrace{\begin{bmatrix} R_c + \frac{sL_c}{\omega_b} & -\omega_1 L_c \\ \omega_1 L_c & R_c + \frac{sL_c}{\omega_b} \end{bmatrix}}^{\mathbf{Z_0}(s)} \begin{bmatrix} i_{Ld}^s \\ i_{Lq}^s \end{bmatrix} \tag{3.1}$$

where $m_d$ and $m_q$ are the $d$- and $q$-axis modulation index, respectively; the variable, $s$ is used as the differential operator, s=d/dt, the superscript 's' stands for converting the $dq$-rotating frame at system fundamental frequency and the voltages and the currents are indicated in Fig. 3.1. Throughout the thesis, the **Bold Font** in the equation is used to represent in a matrix form, and Tilde,˜is used to represent the variables in small-signal form.

### 3.2.2 Current Controller of the VSC

The current-controller as shown in Fig. 3.1 is assumed to be the widely used SRF PI controller of the VSC with decoupling term. The modulation index references obtained from the current controllers can be given by

$$\begin{bmatrix} m_{d,ref}^c \\ m_{q,ref}^c \end{bmatrix} = \mathbf{G_{PWM}}(s)\mathbf{G_{cc}}(s) \begin{bmatrix} i_{Ld,ref} \\ i_{Lq,ref} \end{bmatrix} - \mathbf{G_{PWM}}(s) \left(\mathbf{G_{cc}}(s) + \mathbf{Z_{del}}\right) \begin{bmatrix} i_{Ld}^c \\ i_{Lq}^c \end{bmatrix} + \mathbf{G_{PWM}}(s) \begin{bmatrix} v_{od}^c \\ v_{oq}^c \end{bmatrix} \tag{3.2}$$

where

$$\mathbf{G_{cc}}(s) = \begin{bmatrix} H_{cc}(s) & 0 \\ 0 & H_{cc}(s) \end{bmatrix};$$
$$\mathbf{Z_{del}} = \begin{bmatrix} 0 & \omega_{PLL}L_c \\ -\omega_{PLL}L_c & 0 \end{bmatrix};$$
$$\mathbf{G_{PWM}(s)} = \begin{bmatrix} H_{PWM}(s) & 0 \\ 0 & H_{PWM}(s) \end{bmatrix};$$
$$H_{PWM}(s) = e^{-sT_s}\frac{1-e^{-sT_s}}{sT_s};$$

and $H_{PWM}(s)$ models the PWM delays; $i_{Ld,ref}$ and $i_{Lq,ref}$ are the d- and q-axis current references, respectively; the current compensator transfer function is $H_{cc}(s) = k_{pc} + k_{ic}/s$ where $k_{pc}$ and $k_{ic}$ are the proportional and integral (PI) gain of the current controller, respectively; $\omega_{PLL}$ is the frequency of the PLL in pu and $T_s$ represents the sampling delay. The superscript 'c' represents variables in $dq$-frame at PLL frequency.

### 3.2.3 Transformation Variables from PLL Reference to System Reference

The modulation index references in (3.2) are in PLL reference. It is necessary to convert them into system reference. The following subsection describes how the variables are transformed from the PLL reference to the system reference.

The PLL is used to track the frequency [86] which acts as a closed control loop. A second order PLL is assumed as shown in Fig. 3.1, the instantaneous frequency deviation, $\delta\omega_{PLL}$ can be given by

$$\frac{d\delta\theta_{PLL}}{dt} = \delta\omega_{PLL} = H_{PLL}(s)v^c_{oq} \tag{3.3}$$

and the angle difference,

$$\delta\theta_{PLL} = \theta_{PLL} - \theta_1 \tag{3.4}$$

where PI controller transfer function, $H_{PLL}(s) = k_{ppll} + k_{ipll}/s$, where $k_{ppll}$ and $k_{ipll}$ are the PI gain of the PLL compensator, $\theta_{PLL}$ is the transformation angle of the PLL and $\theta_1$ is the transformation angle at the system fundamental frequency. The frequency of the PLL, $\omega_{PLL}$ can be found by adding the nominal frequency, $\omega_1$ with frequency deviation and is given by

$$\omega_{PLL} = \delta\omega_{PLL} + \omega_1 \tag{3.5}$$

and the transformation angle can be found by

$$\frac{d\theta_{PLL}}{dt} = H_{PLL}(s)v^c_{oq} + \omega_1. \tag{3.6}$$

The transformation from the stationary reference to the $dq$-frame can be described as $v^s_{o,\alpha\beta} = e^{j\theta_1}v^s_{o,dq}$ at grid frequency and $v^s_{o,\alpha\beta} = e^{j\theta_{PLL}}v^c_{o,dq}$ at VSC's PLL frequency. The relation between grid and converter $dq$-frame can be written by

$$\begin{aligned} v^c_{o,dq} &= e^{-j\delta\theta_{PLL}}v^s_{o,dq} \\ &= (cos(\delta\theta_{PLL}) - jsin(\delta\theta_{PLL}))\left(v^s_{od} + jv^s_{oq}\right) \end{aligned} \tag{3.7}$$

and $\delta\theta_{PLL}$ is assumed to be very small which gives

$$v_{od}^{c} + jv_{oq}^{c} = (v_{od}^{s} + v_{oq}^{s}\delta\theta_{PLL}) + j(v_{oq}^{s} - v_{od}^{s}\delta\theta_{PLL}). \tag{3.8}$$

Inserting this relation and applying Laplace transformation on (3.3), the PLL transfer function can be written by

$$\delta\theta_{PLL} = \overbrace{\frac{H_{PLL}(s)}{s + V_{od0}H_{PLL}(s)}}^{G_{PLL}(s)} \Delta v_{oq}^{s}. \tag{3.9}$$

The integral part of $H_{PLL}(s)$ is used to remove the quasi-steady-state phase error and it appears when the synchronous frequency deviates from its nominal value. In steady-state, $\tilde{v}_{oq}$ is zero, $H_{PLL} = k_{ppll}$ is sufficient to keep $\delta\theta_{PLL}$ to zero. $G_{PLL}(s)$ is assumed to be a first-order low pass filter. The bandwidth of the PLL-loop must be sufficiently small to reject the harmonic resonance [90]. By a rule, it should be 10 times less than the inner current control loop bandwidth, $\alpha_{cc}$=$k_{pc}/L_c$ [91].

The voltage, current and the modulation index in the system reference can be converted using the transfer function of the PLL derived in (3.9) and can be written as [51]

$$\begin{bmatrix}\tilde{i}_{Ld}^{c}\\ \tilde{i}_{Lq}^{c}\end{bmatrix} = \begin{bmatrix}\tilde{i}_{Ld}^{s}\\ \tilde{i}_{Lq}^{s}\end{bmatrix} + \overbrace{\begin{bmatrix}0 & G_{PLL}(s)I_{Lq}^{s}\\ 0 & -G_{PLL}(s)I_{Ld}^{s}\end{bmatrix}}^{\mathbf{G_{PLL}^{i}}(s)} \begin{bmatrix}\tilde{v}_{od}^{s}\\ \tilde{v}_{oq}^{s}\end{bmatrix} \tag{3.10a}$$

$$\begin{bmatrix}\tilde{v}_{od}^{c}\\ \tilde{v}_{oq}^{c}\end{bmatrix} = \overbrace{\begin{bmatrix}1 & G_{PLL}(s)V_{oq}^{s}\\ 0 & 1 - G_{PLL}(s)V_{od}^{s}\end{bmatrix}}^{\mathbf{G_{PLL}^{v}}(s)} \begin{bmatrix}\tilde{v}_{od}^{s}\\ \tilde{v}_{oq}^{s}\end{bmatrix} \tag{3.10b}$$

$$\begin{bmatrix}\tilde{m}_{d}^{c}\\ \tilde{m}_{q}^{c}\end{bmatrix} = \begin{bmatrix}\tilde{m}_{d}^{s}\\ \tilde{m}_{q}^{s}\end{bmatrix} - \overbrace{\begin{bmatrix}0 & -G_{PLL}(s)D_{q}^{s}\\ 0 & G_{PLL}(s)D_{d}^{s}\end{bmatrix}}^{\mathbf{G_{PLL}^{d}}(s)} \begin{bmatrix}\tilde{v}_{od}^{s}\\ \tilde{v}_{oq}^{s}\end{bmatrix}. \tag{3.10c}$$

### 3.2.4 DQ-Impedance Model of Current-Controlled VSC

In order to solve (3.1) for the impedance in frequency domain, the modulating signal, $\mathbf{m_{dq}}$ needs to be found as a functions of $\mathbf{i_{L,dq}}$ and $\mathbf{v_{o,dq}}$ in frequency domain. Now assume that the VSC has only inner-loop current control. Taking the PLL into accounts, the modulation signal, (3.2) from the current controller can be expressed in small-signal form as

$$\begin{aligned}\begin{bmatrix}\tilde{m}_{d}^{s}\\ \tilde{m}_{q}^{s}\end{bmatrix} = &\left(-\mathbf{G_{PWM}}(s)\left(\mathbf{G_{cc}}(s) + \mathbf{Z_{del}}\right)\mathbf{G_{PLL}^{i}}(s) + \mathbf{G_{PWM}}(s)\mathbf{G_{PLL}^{v}}(s) + \mathbf{G_{PLL}^{d}}(s)\right)\begin{bmatrix}\tilde{v}_{od}^{s}\\ \tilde{v}_{oq}^{s}\end{bmatrix}\\ &- \mathbf{G_{PWM}}(s)\left(\mathbf{G_{cc}}(s) + \mathbf{Z_{del}}\right)\begin{bmatrix}\tilde{i}_{Ld}^{s}\\ \tilde{i}_{Lq}^{s}\end{bmatrix}\end{aligned} \tag{3.11}$$

Since the current control VSC regulates the AC current, the input DC voltage is assumed to be a constant and Eqn. (3.1) can be rewritten for the constant DC voltage in small-signal form as

$$\begin{bmatrix}\tilde{v}_{od}^{s}\\ \tilde{v}_{oq}^{s}\end{bmatrix} = \begin{bmatrix}\tilde{m}_{d}^{s}\\ \tilde{m}_{q}^{s}\end{bmatrix} V_{dc} - \mathbf{Z_0}(s)\begin{bmatrix}\tilde{i}_{Ld}^{s}\\ \tilde{i}_{Lq}^{s}\end{bmatrix}. \tag{3.12}$$

The impedance model of the current-control VSC can be obtained by inserting (3.11) into (3.12) and can be given by

$$\mathbf{Z^i_{dq}}(s) = \left(\mathbf{I} - \mathbf{G^i_C}(s)V_{dc}\right)^{-1}\left(\mathbf{Z_0}(s) + \mathbf{G_{PWM}}(s)\left(\mathbf{G_{cc}}(s) + \mathbf{Z_{del}}\right)V_{dc}\right) \tag{3.13}$$

where

$$\mathbf{G^i_C(s)} = -\mathbf{G_{PWM}(s)}\left(\mathbf{G_{cc}(s)} + \mathbf{Z_{del}}\right)\mathbf{G^i_{PLL}(s)} + \mathbf{G_{PWM}(s)G^v_{PLL}(s)} + \mathbf{G^d_{PLL}(s)}.$$

### 3.2.5 DQ-Impedance Model of the Power-Controlled VSC

In the case of power-controlled VSC, an outer-loop PI controller is assumed to obtain the d-axis current reference and the q-axis current reference is simply set to zero. The impedance modeling of the power-controlled VSC including the outer-loop is presented in the following subsection.

The current reference to the current-controller can be defined by

$$\begin{bmatrix} i^c_{Ld,ref} \\ i^c_{Lq,ref} \end{bmatrix} = \begin{bmatrix} H_P(s)\left(P_{ref} - P_{meas}\right) \\ 0 \end{bmatrix} \tag{3.14}$$

where the measured power is

$$P_{meas} = v^c_{od}i^c_{Ld} + v^c_{oq}i^c_{Lq}. \tag{3.15}$$

and the power controller compensator transfer function $H_p(s) = k_{pp} + k_{ip}/s$. The reference current, $\tilde{\mathbf{i}}^{\mathbf{c}}_{\mathbf{Ldq,ref}}$ in small-signal form can be obtained in terms of $\tilde{\mathbf{i}}^{\mathbf{c}}_{\mathbf{Ldq}}$ by linearizing (3.14) and (3.15) as

$$\begin{bmatrix} \tilde{i}^c_{Ld,ref} \\ \tilde{i}^c_{Lq,ref} \end{bmatrix} = -H_P(s)\overbrace{\begin{bmatrix} V_{od} & V_{oq} \\ 0 & 0 \end{bmatrix}}^{\mathbf{G_{vp}}}\begin{bmatrix} \tilde{i}^c_d \\ \tilde{i}^c_q \end{bmatrix} - H_P(s)\overbrace{\begin{bmatrix} I_{Ld} & I_{Lq} \\ 0 & 0 \end{bmatrix}}^{\mathbf{G_{ip}}}\begin{bmatrix} \tilde{v}^c_{od} \\ \tilde{v}^c_{oq} \end{bmatrix} \tag{3.16}$$

Now inserting (3.16), linearizing (3.2) and taking the PLL into account, the modulation signal can be written in small-signal form as

$$\begin{bmatrix} \tilde{m}^s_d \\ \tilde{m}^s_q \end{bmatrix} = \mathbf{G_{PWM}}(s)\left(-\mathbf{G_{cc}}(s)H_P(s)\mathbf{G_{vp}} - \left(\mathbf{G_{cc}}(s) + \mathbf{Z_{del}}\right)\right)\begin{bmatrix} \tilde{i}^s_{Ld} \\ \tilde{i}^s_{Lq} \end{bmatrix} + \mathbf{G^P_C}(s)\begin{bmatrix} \tilde{v}^s_{od} \\ \tilde{v}^s_{oq} \end{bmatrix} \tag{3.17}$$

where

$$\begin{aligned}\mathbf{G^P_C(s)} =& \mathbf{G_{PWM}}(s)\left(-\mathbf{G_{cc}}(s)H_P(s)\mathbf{G_{vp}} - \left(\mathbf{G_{cc}}(s) + \mathbf{Z_{del}}\right)\right)\mathbf{G^i_{PLL}}(s) \\ &+ \mathbf{G_{PWM}}(s)\left(\mathbf{I} - \mathbf{G_{cc}}(s)H_P(s)\mathbf{G_{ip}}\right)\mathbf{G^v_{PLL}}(s) + \mathbf{G^d_{PLL}}(s).\end{aligned}$$

The impedance model of the power control VSC can be derived by inserting (3.17) into (3.12) and can be written by

$$\mathbf{Z^P_{dq}}(s) = \left(\mathbf{I} - V_{dc}\mathbf{G^P_C}(s)\right)^{-1}\left(-\mathbf{Z_0}(s) + V_{dc}\mathbf{G_{PWM}}(s)\left(-H_P(s)\mathbf{G_{cc}}(s)\mathbf{G_{vp}} - \mathbf{G_{cc}}(s) - \mathbf{Z_{del}}\right)\right) \tag{3.18}$$

### 3.2.6 DQ-Impedance Model of the DC Voltage-controlled VSC

This subsection describes the impedance model derivation of the DC voltage-controlled VSC. In order to solve (3.1) for impedance in frequency domain, the modulating signal, $\mathbf{m_{dq}}$ needs to be found as functions of $\mathbf{i_{L,dq}}$ and $\mathbf{v_{o,dq}}$ in frequency domain and also it is necessary to find the relation between AC and DC side variables. An ideal lossless model of the VSC is assumed for simplification of modeling. Therefore power balance constraint between DC and AC side can be given by

$$P = i_{dc}v_{dc} = (i^s_{Ld}m^s_d + i^s_{Lq}m^s_q)v_{dc}. \tag{3.19}$$

$$i_{dc} = (i^s_{Ld}m^s_d + i^s_{Lq}m^s_q). \tag{3.20}$$

The dynamic equation of the DC-link voltage in pu can be written by

$$\frac{sC_{dc}}{\omega_b}v_{dc} = I_0 - i_{dc}. \tag{3.21}$$

Assuming that the output power of the VSC is constant and the VSC behaves as a constant power source/load. Therefore, the input DC current to the VSC can be written as

$$I_o = \frac{P}{v_{dc}}. \tag{3.22}$$

Inserting (3.22) and after linearization, (3.21) can be be written in small-signal form as

$$\tilde{i}_{dc} = -\overbrace{\left(\frac{sC_{dc}}{\omega_b} + \frac{P}{V^2_{dc}}\right)}^{Y_{dc}(s)}\tilde{v}_{dc}. \tag{3.23}$$

Now inserting (3.23), eqn. (3.20) can be expressed in small-signal form as

$$\begin{bmatrix}\tilde{v}_{dc}\\ 0\end{bmatrix} = -\overbrace{\begin{bmatrix}\frac{M_d}{Y_{dc}(s)} & \frac{M_q}{Y_{dc}(s)}\\ 0 & 0\end{bmatrix}}^{\mathbf{G_{vi}}}\begin{bmatrix}\tilde{i}^s_{Ld}\\ \tilde{i}^s_{Lq}\end{bmatrix} - \overbrace{\begin{bmatrix}\frac{I_{Ld}}{Y_{dc}(s)} & \frac{I_{Lq}}{Y_{dc}(s)}\\ 0 & 0\end{bmatrix}}^{\mathbf{G_{vd}}}\begin{bmatrix}\tilde{m}^s_d\\ \tilde{m}^s_q\end{bmatrix}. \tag{3.24}$$

The d-axis current reference is obtained from the outer-loop PI controller and the q-axis current reference is set to zero. The current reference can be given by

$$\begin{bmatrix}i^c_{Ld,ref}\\ i^c_{Lq,ref}\end{bmatrix} = \begin{bmatrix}H_{vdc}(s)\,(-v_{dcref} + v_{dc})\\ 0\end{bmatrix} \tag{3.25}$$

where $H_{vdc}(s) = k_{pvdc} + k_{ivdc}/s$ is the DC voltage controller compensator transfer function and in small-signal it can be written as

$$\begin{bmatrix}\tilde{i}^c_{Ld,ref}\\ \tilde{i}^c_{Lq,ref}\end{bmatrix} = \overbrace{\begin{bmatrix}H_{vdc}(s) & 0\\ 0 & 0\end{bmatrix}}^{\mathbf{G_{Vdc}(s)}}\begin{bmatrix}\tilde{v}_{dc}\\ 0\end{bmatrix}. \tag{3.26}$$

Inserting (3.26) and (3.24), and solving for modulation index, (3.2) can be written in small-signal form as

$$\begin{bmatrix}\tilde{m}_d\\ \tilde{m}_q\end{bmatrix} = \mathbf{G_A^{-1}}(s)\left(\mathbf{G_B}(s)\begin{bmatrix}\tilde{i}_{Ld}\\ \tilde{i}_{Lq}\end{bmatrix} + \mathbf{G_C^{Vdc}}(s)\begin{bmatrix}\tilde{v}_{od}\\ \tilde{v}_{oq}\end{bmatrix}\right) \tag{3.27}$$

where

$$\begin{aligned}
\mathbf{G_C^{Vdc}}(s) &= \mathbf{G_{PWM}}(s)\left(\left(\mathbf{G_{cc}}(s)+\mathbf{Z_{del}}\right)\mathbf{G_{PLL}^{i}}(s)+\mathbf{G_{PLL}^{v}}(s)-\mathbf{G_{cc}}(s)\mathbf{G_{Vdc}}(s)\mathbf{G_{vq}}\right)\\
\mathbf{G_B}(s) &= \mathbf{G_{PWM}}(s)\left(-\mathbf{G_{cc}}(s)-\mathbf{Z_{del}}-\mathbf{G_{cc}}(s)\mathbf{G_{Vdc}}(s)\mathbf{G_{vi}}\right)\\
\mathbf{G_A}(s) &= \left(\mathbf{I}+\mathbf{G_{PWM}}(s)\mathbf{G_{cc}}(s)\mathbf{G_{Vdc}}(s)\mathbf{G_{vd}}\right)
\end{aligned}$$

and defined the modulation index at operating point,

$$\mathbf{G_D} = \begin{bmatrix}M_d & 0\\ M_q & 0\end{bmatrix}.$$

The impedance model of the DC voltage-controlled VSC can be derived in frequency domain by inserting (3.24) and (3.27) into (3.1) and can be written by

$$\begin{aligned}
\mathbf{Z_{dq}^{Vdc}}(s) =& \left(\mathbf{I}-V_{dc}\mathbf{G_A^{-1}}(s)\mathbf{G_C^{Vdc}}(s)+\mathbf{G_D}\mathbf{G_{vd}}\mathbf{G_A^{-1}}(s)\mathbf{G_C^{vdc}}(s)\right)^{-1}\\
&\left(-\mathbf{Z_0}(s)+V_{dc}\mathbf{G_A^{-1}}(s)\mathbf{G_B}(s)-\mathbf{G_D}\mathbf{G_{vi}}-\mathbf{G_D}\mathbf{G_{vd}}\mathbf{G_A^{-1}}(s)\mathbf{G_B}(s)\right).
\end{aligned} \tag{3.28}$$

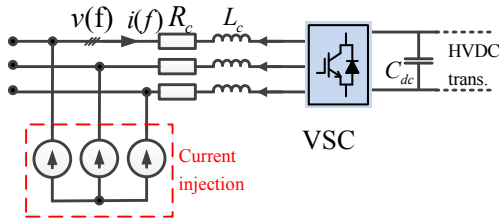


**Figure 3.2:** The VSC's impedance verification setup based on shunt current injection.

## 3.3 DQ-frame Impedance Model Verification

The effectiveness of the impedance based stability analysis result depends on the correctness of the analytical impedance model; therefore the analytical impedance model derivation is considered to be the most important part in the impedance based stability analysis. The correctness of the impedance model derivation can be verified by comparing the impedance frequency responses obtained either by numerical simulation or experiment. In this case, the correctness of the impedance model is verified by comparing the frequency responses obtained from the numerical simulation. Fig. 3.2 shows the setup used to obtain the impedance frequency responses from the simulation. A shunt perturbation current (<5% of rated steady-state current) at different frequencies is applied as shown in Fig. 3.2 and the voltage is measured. Fast Fourier Transformation (FFT) tool is used to analyze the different harmonic voltages and currents. The impedance is calculated by dividing the voltage by current at each frequency. The impedance

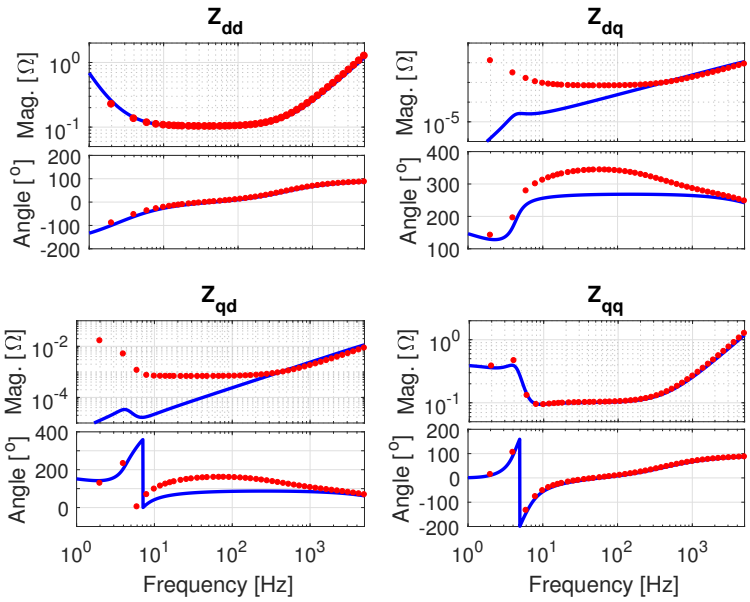


**Figure 3.3:** The impedance frequency responses of the current-controlled VSC (Solid line is the analytical model and points are from numerical simulation).

models are derived in $dq$-domain which is a 2x2 matrix. The frequencies are referred to the $dq$-frame, therefore the perturbation is transformed back to the phase domain in order to be compatible with the injection structure as shown in Fig. 3.2 [92], [93].

Fig. 3.3 shows the impedance frequency responses of the current-controlled VSC. The solid line is representing the impedance frequency responses from the analytical model and the circles show the results obtained from the numerical simulation. Both analytical and simulation impedance magnitude and phase are in good agreement which validates the correctness of the impedance model derivation. In the analytical model, the delay caused by the anti-aliasing filter is neglected which cause a little deviation in simulation in the off-diagonal elements.

Fig. 3.4 shows the impedance frequency responses of the DC voltage-controlled VSC. As like as the current-controlled VSC, both analytical and simulation impedance frequency responses are in good agreement which validates the correctness of the impedance model derivation.

## 3.4 DC Impedance modeling of the VSC

In this section, the DC impedance models will be derived for a switching model of the VSCs including the PWM delay and the PLL dynamics. The details impedance model derivation is described below.

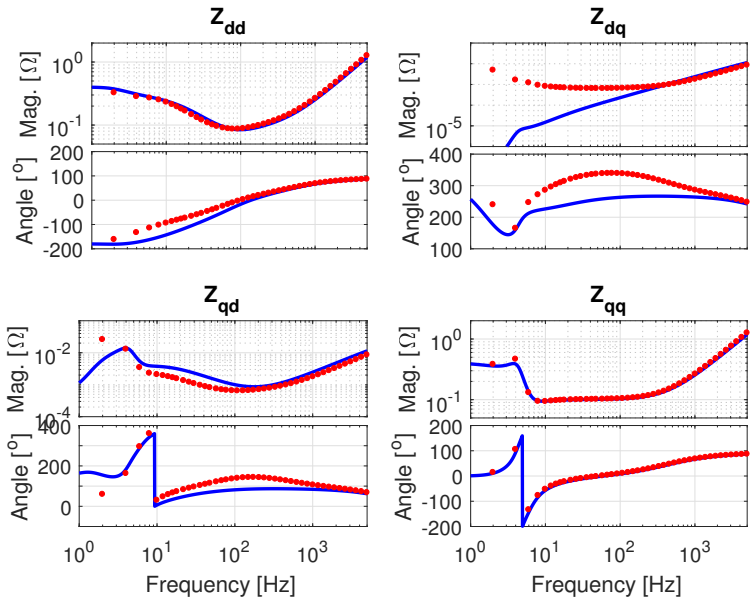


**Figure 3.4:** The impedance frequency responses of the DC voltage-controlled VSC (Solid line is the analytical model and points are from numerical simulation).

### 3.4.1 Small-signal Analytical Modeling of the VSCs

The impedance model will be derived based on the analytical model of the VSC-HVDC system described in Chapter 2. Applying Laplace transformation, the dynamic equations of the converter, capacitive filter and grid inductor, in small-signal form can be written in pu as

$$\begin{bmatrix} M_d \\ M_q \end{bmatrix} \tilde{v}_{dc} + V_{dc} \begin{bmatrix} \tilde{m}_d^s \\ \tilde{m}_q^s \end{bmatrix} - \mathbf{Z_0}(\mathbf{s}) \begin{bmatrix} \tilde{i}_{Ld}^s \\ \tilde{i}_{Lq}^s \end{bmatrix} = \begin{bmatrix} \tilde{v}_{od}^s \\ \tilde{v}_{oq}^s \end{bmatrix} \tag{3.29}$$

$$\begin{bmatrix} \tilde{i}_{od}^s \\ \tilde{i}_{oq}^s \end{bmatrix} = \begin{bmatrix} \tilde{i}_{Ld}^s \\ \tilde{i}_{Lq}^s \end{bmatrix} - \mathbf{Y_{Cf}}(s) \begin{bmatrix} \tilde{v}_{od}^s \\ \tilde{v}_{oq}^s \end{bmatrix} \tag{3.30}$$

$$\begin{bmatrix} \tilde{v}_{od}^s \\ \tilde{v}_{oq}^s \end{bmatrix} = \begin{bmatrix} \tilde{v}_{gd}^s \\ \tilde{v}_{gq}^s \end{bmatrix} + \mathbf{Z_g}(s) \begin{bmatrix} \tilde{i}_{od}^s \\ \tilde{i}_{oq}^s \end{bmatrix} \tag{3.31}$$

where

$$\mathbf{Z_g}(s) = \begin{bmatrix} R_g + sL_g/\omega_b & -\omega_1 L_g \\ \omega_1 L_g & R_g + sL_g/\omega_b \end{bmatrix}$$

$$\mathbf{Y_{cf}}(s) = \begin{bmatrix} sC_f/\omega_b & -\omega_1 C_f \\ \omega_1 C & sC_f/\omega_b \end{bmatrix}.$$

Assuming that the grid voltage $v_g$ is stable and $\begin{bmatrix} \tilde{v}_{gd}^s & \tilde{v}_{gq}^s \end{bmatrix}^T = 0$, Eqn. (3.31) gives the relation

between $\tilde{\mathbf{i}}_{\mathbf{o,dq}}$ and $\tilde{\mathbf{v}}_{\mathbf{o,dq}}$ and can be given by

$$\begin{bmatrix} \tilde{i}^s_{od} \\ \tilde{i}^s_{oq} \end{bmatrix} = \mathbf{Y_g}(s) \begin{bmatrix} \tilde{v}^s_{od} \\ \tilde{v}^s_{oq} \end{bmatrix} \tag{3.32}$$

where

$$\mathbf{Y_g}(s) = \mathbf{Z_g^{-1}}(s).$$

The relation between the PCC voltage, $\mathbf{v_{o,dq}}$ and converter current, $\mathbf{i_{L,dq}}$ can be found by inserting (3.32) into (3.30) and can be written by

$$\begin{bmatrix} \tilde{v}^s_{od} \\ \tilde{v}^s_{oq} \end{bmatrix} = \overbrace{\left(\mathbf{Y_{Cf}}(s) + \mathbf{Y_g}(s)\right)^{-1}}^{\mathbf{Z_s}(s)} \begin{bmatrix} \tilde{i}^s_{Ld} \\ \tilde{i}^s_{Lq} \end{bmatrix}. \tag{3.33}$$

### 3.4.2 Current Controller in System Reference

The modulation voltage references obtained from the current controllers in $dq$-frame at PLL reference is given in (3.2). Taking PLL into accounts, the modulation signal from the current controller can be expressed in small-signal form as

$$\begin{bmatrix} m^s_d \\ m^s_q \end{bmatrix} = \mathbf{G_{PWM}}(s)\mathbf{G_{cc}}(s) \begin{bmatrix} i_{Ld,ref} \\ i_{Lq,ref} \end{bmatrix} - \mathbf{G_{PWM}}(s)\left(\mathbf{G_{cc}}(s) + \mathbf{Z_{del}}\right) \begin{bmatrix} i^s_{Ld} \\ i^s_{Lq} \end{bmatrix} + \mathbf{G^i_C}(s) \begin{bmatrix} v^s_{od} \\ v^s_{oq} \end{bmatrix}. \tag{3.34}$$

### 3.4.3 Power Balance Constraint between AC and DC side

By neglecting the losses due to switching, the power balance constraint between the AC and the DC side can be given by (3.35) and linearized equation of (3.36) is given by (3.37).

$$v_{dc} i_{dc} = i^s_{Ld} v^s_{cvd} + i^s_{Lq} v^s_{cvq} \tag{3.35}$$

$$i_{dc} = i^s_{Ld} m^s_d + i^s_{Lq} m^s_q \tag{3.36}$$

$$\tilde{i}_{dc} = \begin{bmatrix} M_d & M_q \end{bmatrix} \begin{bmatrix} \tilde{i}^s_{Ld} \\ \tilde{i}^s_{Lq} \end{bmatrix} + \begin{bmatrix} I_{Ld} & I_{Lq} \end{bmatrix} \begin{bmatrix} \tilde{m}^s_d \\ \tilde{m}^s_q \end{bmatrix}. \tag{3.37}$$

### 3.4.4 DC Impedance Model of the Power-Controlled VSC

As shown in Fig. 3.1, the current reference to the current controller can be written by

$$\begin{bmatrix} i^c_{Ldref} \\ i^c_{Lqref} \end{bmatrix} = \begin{bmatrix} H_P(s)P_{ref} - H_P(s)\overbrace{\left(v^c_{od} i^c_{Ld} + v^c_{oq} i^c_{Lq}\right)}^{P_{meas}} \\ 0 \end{bmatrix}. \tag{3.38}$$

In small-signal form including the PLL dynamics, the current references can be given by

$$\begin{bmatrix} \tilde{i}_{Ldref} \\ \tilde{i}_{Lqref} \end{bmatrix} = -H_P(s)\mathbf{G_{vp}} \begin{bmatrix} \tilde{i}^s_{Ld} \\ \tilde{i}^s_{Lq} \end{bmatrix} - \left(H_P(s)\mathbf{G_{vp}}\mathbf{G^i_{PLL}}(s) + H_P(s)\mathbf{G_{ip}}\mathbf{G^v_{PLL}}(s)\right) \begin{bmatrix} \tilde{v}^s_{od} \\ \tilde{v}^s_{oq} \end{bmatrix} \tag{3.39}$$

where

$$\mathbf{G_{vp}} = \begin{bmatrix} V_{od} & V_{oq} \\ 0 & 0 \end{bmatrix}$$
$$\mathbf{G_{ip}} = \begin{bmatrix} I_{Ld} & I_{Lq} \\ 0 & 0 \end{bmatrix}.$$

Now inserting (3.39) and (3.33) into (3.34), the modulation index can be written by

$$\begin{bmatrix} \tilde{m}_d^s \\ \tilde{m}_q^s \end{bmatrix} = \mathbf{G_Z^P}(s) \begin{bmatrix} \tilde{i}_{Ld}^s \\ \tilde{i}_{Lq}^s \end{bmatrix} \tag{3.40}$$

where

$$\begin{aligned}\mathbf{G_Z^P}(s) = &(-\mathbf{G_{PWM}}(s)\mathbf{G_{cc}}(s)H_P(s)\mathbf{G_{vp}} - \mathbf{G_{PWM}}(s)\left(\mathbf{G_{cc}}(s) + \mathbf{Z_{del}}\right)) \\ &+ \mathbf{Z_s}(s)\left(-\mathbf{G_{PWM}}(s)\mathbf{G_{cc}}(s)\left(H_P(s)\mathbf{G_{vp}}\mathbf{G_{PLL}^i}(s) + H_P(s)\mathbf{G_{vp}}\mathbf{G_{PLL}^v}(s)\right) + \mathbf{G_c^i}(s)\right)\end{aligned}$$

The DC impedance of the converters can be calculated as $\tilde{v}_{dc}/\tilde{i}_{dc}$. Eqn. (3.29) indicates that the derivation should involve both AC and DC side, therefore the AC side quantities have to be expressed in terms of the DC side quantities in order to get an expression of the dc impedance, $Z_{dc} = \tilde{v}_{dc}/\tilde{i}_{dc}$. Hence, the relation between the DC voltage and AC currents can be obtained from (3.29) by inserting (3.33) and (3.40) as

$$\overbrace{\left(\mathbf{Z_s}(s) + \mathbf{Z_0}(s) - V_{dc}\mathbf{G_Z^P}(s)\right)^{-1}\begin{bmatrix} M_d \\ M_q \end{bmatrix}}^{\mathbf{Y_{AC}^P}(s)} \tilde{v}_{dc} = \begin{bmatrix} \tilde{i}_{Ld}^s \\ \tilde{i}_{Lq}^s \end{bmatrix}. \tag{3.41}$$

The DC impedance of the converters can be calculated by inserting (3.41) into (3.37) and can be expressed as

$$Z_{dc}^p(s) = \frac{\tilde{v}_{dc}}{\tilde{i}_{dc}} = \frac{Z_{dc,base}}{\left(\begin{bmatrix} M_d & M_q \end{bmatrix} + \begin{bmatrix} I_{Ld} & I_{Lq} \end{bmatrix}\mathbf{G_Z^P}(s)\right)\mathbf{Y_{AC}^P}(s)} \tag{3.42}$$

where $Z_{dc,base}$ is the DC base impedance.

### 3.4.5 DC Impedance Model of the DC Voltage-Controlled VSC

As shown in Fig. 3.1, the current reference to the current controller can be written by

$$\begin{bmatrix} i_{Ldref}^c \\ i_{Lqref}^c \end{bmatrix} = \begin{bmatrix} -H_{vdc}(s)v_{dc,ref} + H_{vdc}(s)v_{dc} \\ 0 \end{bmatrix}. \tag{3.43}$$

In small-signal form, the current references can be given by

$$\begin{bmatrix} \tilde{i}_{Ldref} \\ \tilde{i}_{Lqref} \end{bmatrix} = \begin{bmatrix} H_{vdc} \\ 0 \end{bmatrix} \tilde{v}_{dc} \tag{3.44}$$

Now inserting (3.44) and (3.33) into (3.34), the modulation index can be written by

$$\begin{bmatrix}\tilde{m}_d^s\\ \tilde{m}_q^s\end{bmatrix} = \mathbf{G_{PWM}}(s)\mathbf{G_{cc}}(s)\begin{bmatrix}H_{vdc}(s)\\ 0\end{bmatrix}\tilde{v}_{dc} + \mathbf{G_Z^{Vdc}}(s)\begin{bmatrix}\tilde{i}_{Ld}^s\\ \tilde{i}_{Lq}^s\end{bmatrix} \tag{3.45}$$

where

$$\mathbf{G_Z^{Vdc}}(s) = \left(-\mathbf{G_{PWM}}(s)\left(\mathbf{G_{cc}}(s) + \mathbf{Z_{del}}\right) + \mathbf{Z_s}(s)\mathbf{G_c^i}(s)\right)$$

The relation between the DC voltage and AC currents can be obtained from (3.29) by inserting (3.33) and (3.45) as

$$\overbrace{\left(\mathbf{Z_0}(s) + \mathbf{Z_s}(s) - V_{dc}\mathbf{G_Z^{Vdc}}(s)\right)^{-1}\left(V_{dc}\mathbf{G_{PWM}}(s)\mathbf{G_{cc}}(s)\begin{bmatrix}H_{vdc}(s)\\ 0\end{bmatrix} + \begin{bmatrix}M_d\\ M_q\end{bmatrix}\right)}^{\mathbf{Y_{AC}^{Vdc}}(s)}\tilde{v}_{dc} = \begin{bmatrix}\tilde{i}_{Ld}^s\\ \tilde{i}_{Lq}^s\end{bmatrix}. \tag{3.46}$$

The modulation index can be expressed in terms of DC voltage from (3.29) inserting (3.46) and (3.33) as

$$\begin{bmatrix}\tilde{m}_d^s\\ \tilde{m}_q^s\end{bmatrix} = \frac{1}{V_{dc}}\left(\left(\mathbf{Z_0}(s) + \mathbf{Z_s}(s)\right)\mathbf{Y_{AC}^{Vdc}}(s) - \begin{bmatrix}M_d\\ M_q\end{bmatrix}\right)\tilde{v}_{dc} \tag{3.47}$$

The DC impedance of the converters can be calculated by solving (3.37), (3.46) and (3.47) and can be expressed as

$$\mathbf{Z_{dc}^v}(s) = \frac{\tilde{v}_{dc}}{\tilde{i}_{dc}} = \frac{Z_{dc,base}}{\begin{bmatrix}M_d & M_q\end{bmatrix}\mathbf{Y_{AC}^{Vdc}}(s) + \frac{1}{V_{dc}}\begin{bmatrix}I_{Ld} & I_{Lq}\end{bmatrix}\left(\left(\mathbf{Z_0}(s) + \mathbf{Z_s}(s)\right)\mathbf{Y_{AC}^{Vdc}}(s) - \begin{bmatrix}M_d\\ M_q\end{bmatrix}\right)}. \tag{3.48}$$

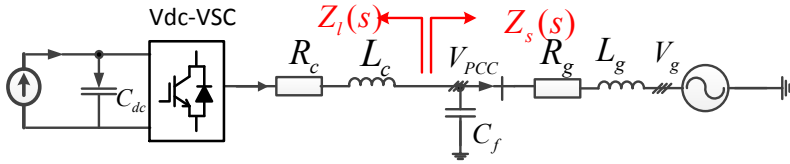


**Figure 3.5:** The DC voltage control terminal of the VSC-HVDC system.

## 3.5 Frequency Domain Stability Analysis based on the DQ-Impedance model

Impedance based stability analysis has been carried out for the point-to-point connection VSC-based HVDC system discussed in the previous chapter, section 2.4. Stability analysis needs to be carried out for each VSC station at the point of common coupling to the grid. This section

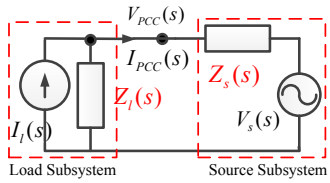


**Figure 3.6:** Equivalent small-signal impedance model.

will present the stability analysis for the DC voltage controlled VSC as an example of the impedance-based stability analysis.

Fig 3.5 depicts the DC voltage control terminal of the point-to-point connection VSC-based HVDC system. The equivalent small-signal impedance model of the DC voltage-controlled VSC station is depicted in Fig. 3.6 where the source subsystem is modeled by its Thevenin equivalent circuit consisting of an ideal voltage source $\mathbf{V_s}(s)$ in series with an equivalent impedance $\mathbf{Z_s}(s)$, while the DC voltage-controlled VSC subsystem is modeled by its Norton equivalent circuit with an ideal current source in parallel with an admittance $\mathbf{Y_l}(s) = 1/\mathbf{Z_l}(s)$ of the VSC. Since the impedance models are derived in $dq$-frame, all the variables in Fig. 3.6 are in $dq$-domain. The subscript for the $dq$ has been dropped in the equivalent circuit.

In $abc$-frame the inductance and the resistance can be written by

$$\mathbf{Z_{RL,abc}}(s) = \begin{bmatrix} R+sL & 0 & 0 \\ 0 & R+sL & 0 \\ 0 & 0 & R+sL \end{bmatrix} \tag{3.49}$$

and the capacitor impedance is

$$\mathbf{Z_{C,abc}}(s) = \begin{bmatrix} sC & 0 & 0 \\ 0 & sC & 0 \\ 0 & 0 & sC \end{bmatrix}^{-1}. \tag{3.50}$$

The impedance model of the converter is derived in $dq$-domain, therefore it is necessary to convert the $abc$-frame impedance into $dq$-frame impedance which can be given by

$$\mathbf{Z_{RL,dq}}(s) = \begin{bmatrix} R+sL & -\omega_1 L \\ \omega_1 L & R+sL \end{bmatrix} \tag{3.51}$$

$$\mathbf{Z_{C,dq}} = \begin{bmatrix} sC & -\omega_1 C \\ \omega_1 C & sC \end{bmatrix}^{-1}. \tag{3.52}$$

Hence, the source equivalent impedance in $dq$-frame can be give by

$$\mathbf{Z_{s,dq}}(s) = \left[ \begin{bmatrix} R_g + sL_g & -\omega_1 L_g \\ \omega_1 L_g & R_g + sL_g \end{bmatrix}^{-1} + \begin{bmatrix} sC_f & -\omega_1 C_f \\ \omega_1 C_f & sC_f \end{bmatrix} \right]^{-1} \tag{3.53}$$

and the load impedance for the DC voltage controlled converter is obtained from (3.28) and can be given by

$$\mathbf{Z}_{\mathbf{l,dq}}(s) = \mathbf{Z}^{\mathbf{dq}}_{\mathbf{Vdc}}(s). \tag{3.54}$$

Based on this representation in Fig. 3.6, the response of the PCC bus voltage can be written as

$$\mathbf{V}_{\mathbf{PCC,dq}}(s) = \left(\mathbf{V}_{\mathbf{s,dq}}(s) + \mathbf{Z}_{\mathbf{s,dq}}(s)\mathbf{I}_{\mathbf{s,dq}}(s)\right)\left(\mathbf{I} + \left(\mathbf{Z}_{\mathbf{s,dq}}(s)\right)\left(\mathbf{Z}_{\mathbf{l,dq}}(s)\right)^{-1}\right)^{-1}. \tag{3.55}$$

For system stability studies, it is assumed that

1. The AC voltage of the grid is always stable when unloaded; and
2. The DC voltage-controlled VSC is stable when it is connected to a stable source.

Therefore, the stability of the interconnected system depends on the second term of right-hand side of (3.55) and the PCC bus voltage will be stable if and only if the impedance ratio, $\left(\mathbf{Z}_{\mathbf{s,dq}}(s)\right)\left(\mathbf{Z}_{\mathbf{l,dq}}(s)\right)^{-1}$ which can be defined as the minor loop gain of a feedback control system as

$$\mathbf{G}(s)\mathbf{H}(s) = \left(\mathbf{Z}_{\mathbf{s,dq}}(s)\right)\left(\mathbf{Z}_{\mathbf{l,dq}}(s)\right)^{-1} \tag{3.56}$$

meets the Generalized Nyquist Stability Criterion (GNC) [45], [46]. The stability of the system depends on the multi-input multi-output (MIMO) Nyquist variables and it is necessary to include all the elements of the matrix **G**(s)**H**(s) as described in [52]. Fig. 3.7 (a) shows the characteristics loci (eigenvalues, $\lambda_1$ and $\lambda_2$) of the minor-loop gain with full power loading with the SCR of 5. The inner-loop current controller is tuned with $90^o$ phase margin at 400 Hz crossover frequency and the outer-loop DC voltage controller is tuned with $80^o$ phase margin at 25 Hz crossover frequency. As can be seen, the characteristics loci of the minor gain do not encircle the point (-1,j0), therefore the system is predicted to be stable.

To further validate the frequency domain analysis, a detailed time domain simulation model of the HVDC system as depicted in Fig. 3.5 has been implemented in the Matlab/Simulink environment associated with the SimPower System Blockset. Fig. 3.7 (b) shows the three-phase voltages and currents at PCC of the VSC. As predicted in the small-signal impedance-based analysis, the HVDC system operates stably in the time domain simulation. At 0.3 s a step change of 0.025 pu DC voltage reference is applied to observe the performance of the system. Since the characteristics loci is stable with sufficient phase margin, the system operates stably.

Now the grid strength has been reduced purposely to show an interaction example between the grid and the HVDC system. The SCR is reduced to 2 when the VSC is operating with full power loading. Fig. 3.8 (a) shows the characteristics loci of the minor-loop gain. As can be seen, the phase margin of $\lambda_2$ becomes low ($11.5^o$) at frequency 4 Hz. Since the phase margin is very low, it can provoke the instability even with a small disturbance. To validate the theoretical analysis, a time domain simulation has been carried out, the resulting time domain responses are shown in Fig. 3.8 (b). The system operates stably in the initial simulation. At 0.3 s a step change of o.025 pu DC voltage reference is applied. Even the disturbance is very small, the system becomes unstable with a frequency around 4 Hz as predicted by the frequency domain analysis.

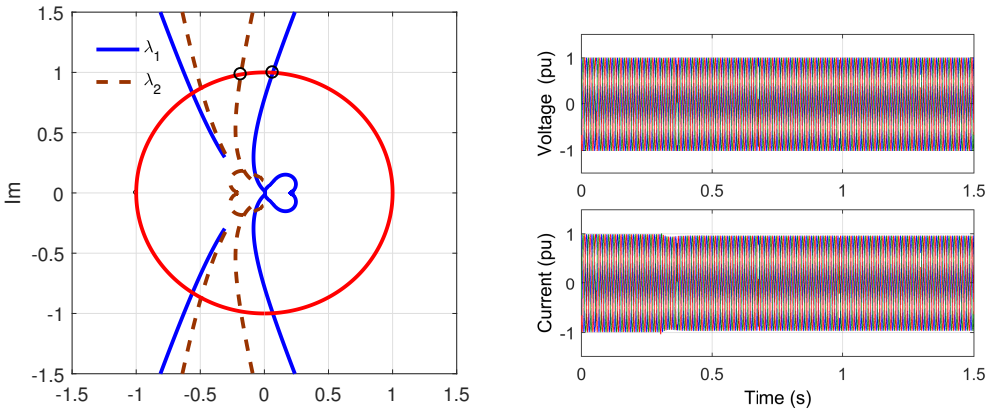


(a) (b)

**Figure 3.7:** (a) Characteristics loci of the minor-loop gain with full loading and SCR 5, and (b) Three phase voltages and currents at PCC of the VSC for SCR 5.

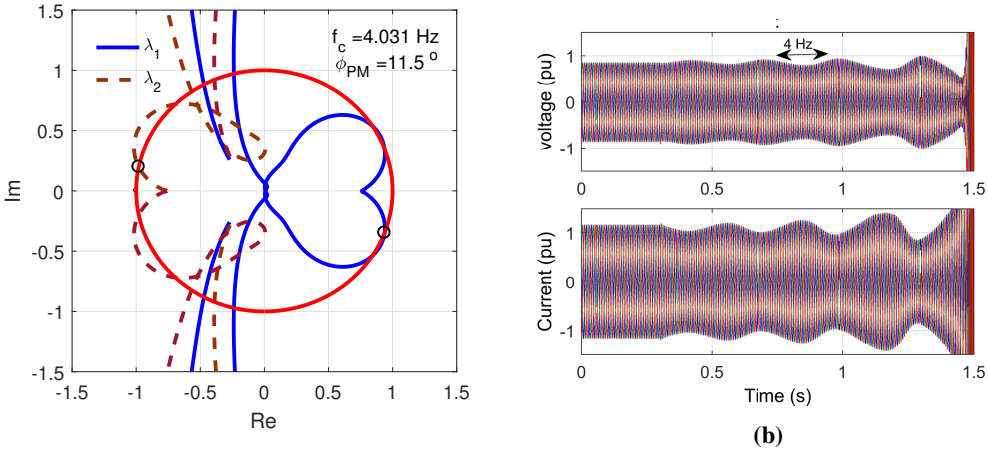


(a) (b)

**Figure 3.8:** (a) Characteristics loci of the minor-loop gain with full loading and SCR 2, and (b) Three phase voltages and currents at PCC of the VSC for SCR 2.

## 3.6 Impact of the Control-loop Bandwidth on the Impedance Frequency Responses

The analytical impedance models of (3.13), (3.18) and (3.28) indicate that the impedance frequency responses of the HVDC VSC depend on the converter series inductance, control-loop bandwidth, and the steady-state operating point. This section presents two examples of the impedance reshaping by re-tuning control-loop gain and how it affects the stability of the VSC-

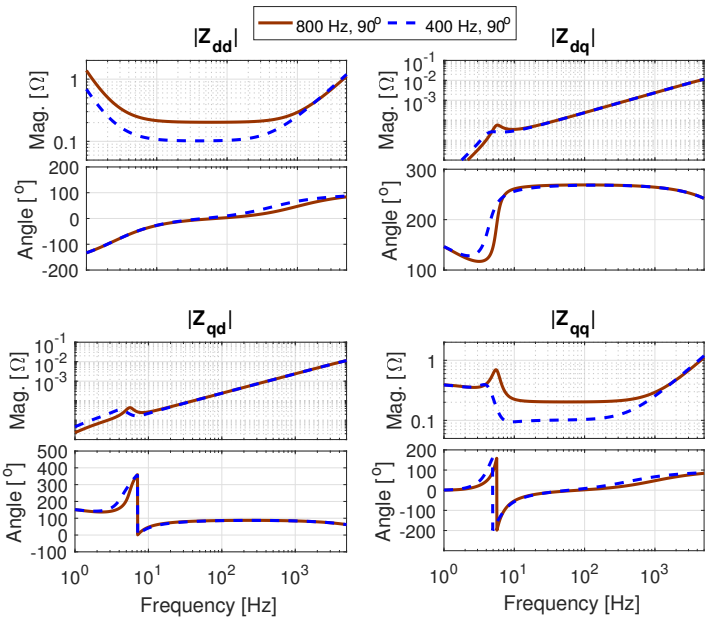


**Figure 3.9:** The impedance frequency responses of the current-controlled for the current control-loop bandwidth of 800 Hz and 400 Hz with $90^o$ phase margin.

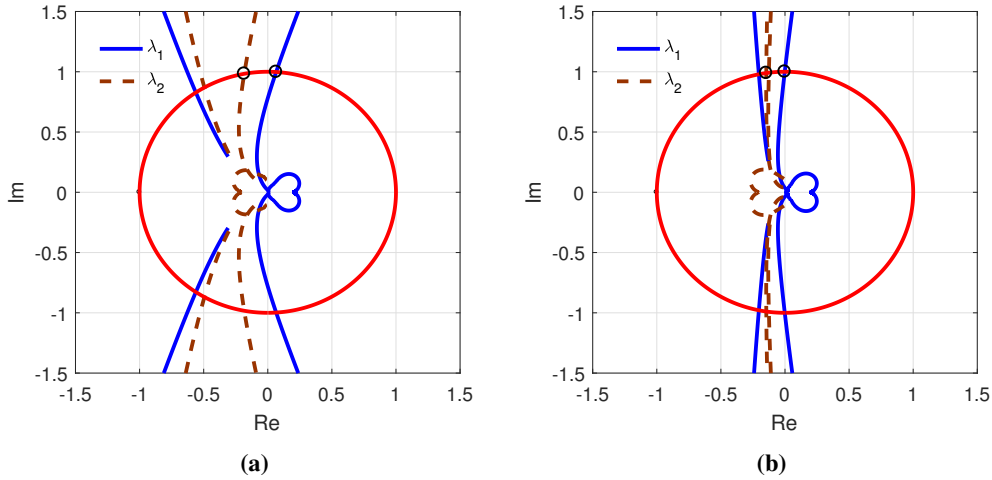


**Figure 3.10:** Characteristics loci of the minor-loop gain with full loading: (a) the current control-loop bandwidth of 400 Hz and (b) the current control-loop bandwidth of 800.

based HVDC system.

Fig. 3.9 shows the impedance frequency responses of the current-controlled VSC for two design

of the current control-loop. Initially, the current control-loop is designed with a phase margin of $90^o$ at 400 Hz crossover frequency. The impedance frequency response is shown in fig. 3.9 with dash line. The proportional gain is increased to two times the original gain to have the control-loop gain at twice the initial bandwidth while the phase margin remains the same. The impedance frequency response is shown Fig. 3.9 with solid line. As can be seen, with a higher control bandwidth, both the magnitudes of the diagonal elements of the impedance become larger which indicates that system stability increases with the increase of the current-loop bandwidth. Fig. 3.10 shows the characteristics loci of the minor-loop gain of the DC voltage-controlled VSC for 800 Hz bandwidth of the current control-loop. By comparing between Fig. 3.10 (a) and (b), it can be concluded that higher control bandwidth of the current control-loop increases the stability margin of the system by increasing the phase margin in the characteristics loci of the minor-loop gain.

Fig. 3.11 shows the impedance frequency responses of the DC voltage-controlled VSC for two design example of the DC voltage control-loop bandwidth. Initially, the DC voltage control-loop is designed with a phase margin of $80^o$ at 25 Hz crossover frequency. The impedance frequency response is shown in fig. 3.11 with dash line. The proportional gain is increased to two times the original gain to have the control-loop gain at twice the initial bandwidth while the phase margin remains the same. The impedance frequency response is shown Fig. 3.11 with solid line. As can be seen, the DC voltage control-loop does not have any impact on the qq-axis impedance since the DC voltage controller has been implemented on the d-axis. The d-axis impedance has an impact on a change of the DC voltage control-loop bandwidth. The

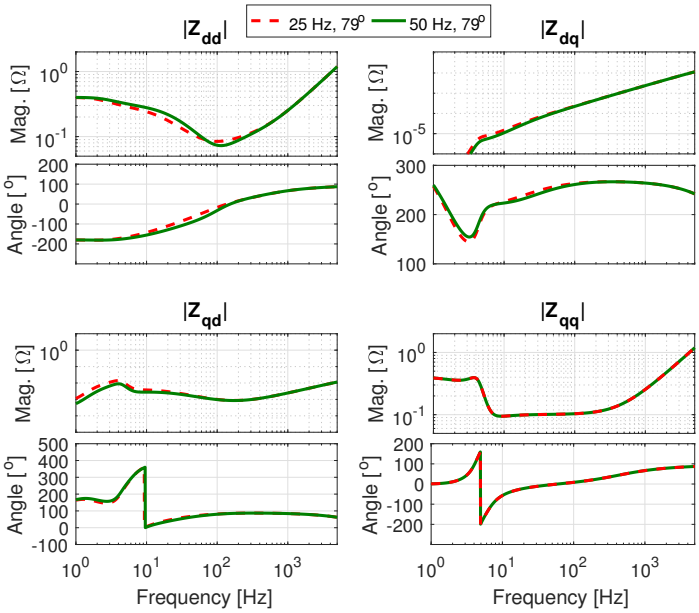


**Figure 3.11:** The impedance frequency responses of the DC voltage-controlled VSC for the control-loop bandwidth of 50 Hz and 25 Hz with $80^o$ phase margin.

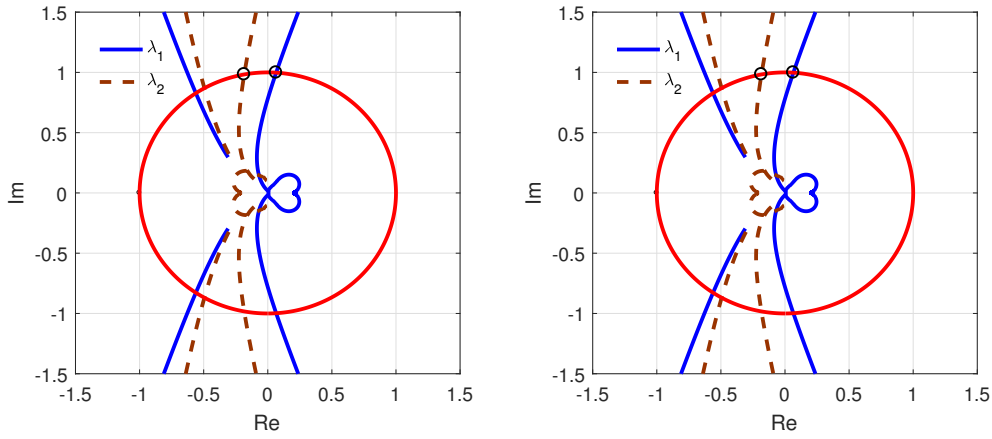


**Figure 3.12:** Characteristics loci of the minor-loop gain with full loading: (a) the DC voltage control-loop bandwidth of 25 Hz and (b) the DC voltage control-loop bandwidth of 50 Hz.

impact on the impedance is not much since the AC side impedance does not much related to the DC side dynamics. Fig. 3.12 shows the characteristics loci of the minor-loop gain of the DC voltage-controlled VSC for 50 Hz bandwidth of the DC voltage control-loop. By comparing between Fig. 3.12 (a) and (b), it can be concluded that the control bandwidth of the DC voltage control-loop does not have a significant impact on the stability margin at the AC interfacing point of the VSC system.

## 3.7 Control Design of VSC-HVDC for both Direction of Power Flow

This section presents the impact of the power flow direction on the stability for a VSC-HVDC system. Existing methods of determining the source and the load impedances cannot predict the stability when the power flow direction has been altered; therefore a method based on the power flow direction has been presented to determine the source and the load impedance [59]. The control has been redesigned based on the proposed method such that the power flows both directions without changing the control between the converters.

### 3.7.1 Problem Identification

The point-to-point VSC-based HVDC system under this study is depicted in Fig. 2.13 in Chapter 2. The VSC-HVDC system is implemented in MATLAB/Simulink with detailed switching model of the VSCs. In addition, the simulation results are also compared with the set-up of a two-terminal system built in the laboratory as discussed in the chapter 2. The theoretical analysis and simulations have been performed to a low voltage level in order to compare with the same voltage and system parameters in the experiments. The electrical circuit parameters of the system are given in Table A.1 in Appendix. The inner-loop current controller of the P-VSC is tuned at $H_{cc}(s) = 4 + 800/s$ and the close-loop control bandwidth is 160 Hz with 150-degree phase margin. The active power compensator transfer function is

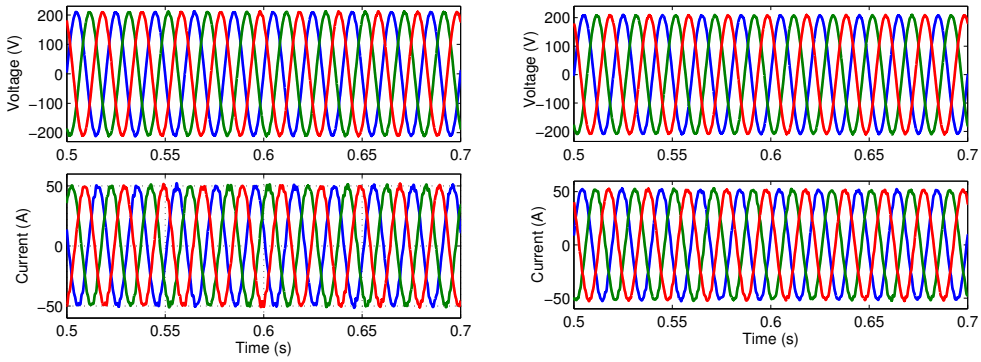


**Figure 3.13:** Simulation results for -10 kW power reference to the P-VSC (Stable case): (a) Three-phase AC voltages and currents at PCC of P-VSC and (b) Three-phase AC voltages and currents at PCC of Vdc-VSC of the HVDC system.

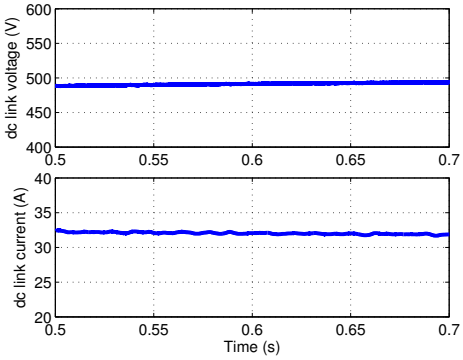


**Figure 3.14:** The DC link voltage and current of VSC HVDC system.

$H_P(s) = 0.005 + 1/s$, and the close-loop control bandwidth is 27 Hz. The current compensator of Vdc-VSC is $H_{cc}(s) = 5 + 1000/s$ and the close-loop control bandwidth is 157 Hz with 150-degree phase margin, and the DC voltage compensator transfer function is $H_{vdc}(s) = 4.5 + 3/s$ and the control bandwidth 8 Hz. The control tunings satisfy the standard bandwidth requirements and the system is expected to operate stably.

The DC voltage reference to Vdc-VSC is set to 500 V. The active power reference to P-VSC is set -10 kW. The negative power reference to P-VSC means that P-VSC is exporting active power to the DC system and is operating as a rectifier. Thus, Vdc-VSC is extracting power from the DC system and operates as an inverter. A time domain simulation has been carried out for these tuning and setting, and the resulting time domain responses are shown in Fig. 3.13 and Fig. 3.14 which show that the system operates stably. Fig. 3.15 shows the experimental results. The system operates stably in both the time domain simulation and the experiment.

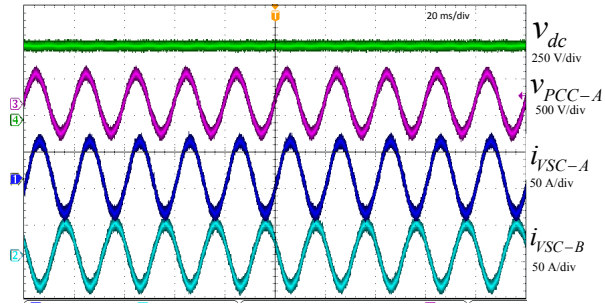


**Figure 3.15:** Experimental results for -10 kW power reference to the P-VSC (Stable case): (i) the DC link voltage, (ii) voltage at PCC of VSC (phase-A), (iii) current of P-VSC (phase-A) and (iv) current of Vdc-VSC (phase-A).

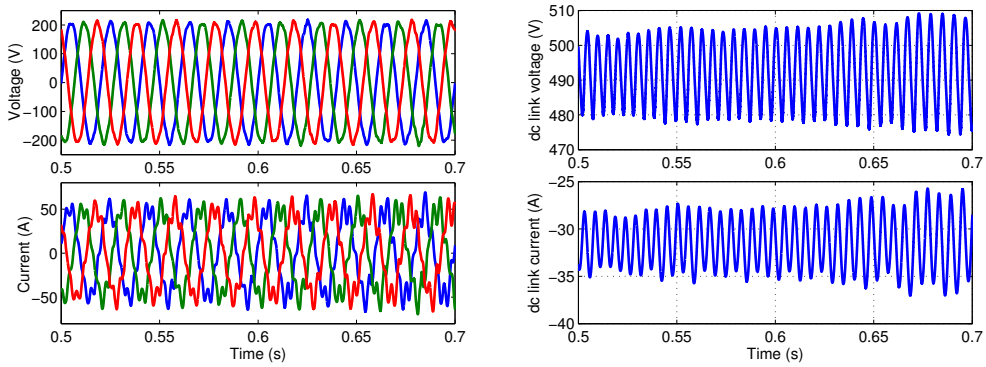


**Figure 3.16:** Simulation results for +10 kW power reference to the P-VSC (Unstable case): (a) Three-phase AC voltages and currents at PCC of Vdc-VSC and (b) the DC link voltage and current of VSC HVDC system.

The HVDC system is expected to operate stably for both directions of the power flow. Therefore, the opposite direction of the power flow is tested for the same control tuning. The active power reference is now set to +10 kW which is opposite to the previous direction. For this power reference, P-VSC is extracting the power from the DC system and operates as an inverter and Vdc-VSC is exporting power to the DC system. The power reference has been altered from the negative reference to the positive while the controls of the VSCs remain the same. A time domain simulation has been carried out and the resulting time domain responses are shown in Fig. 3.16. As can be seen in Fig. 3.16, the system has become unstable and the PCC voltages and currents have different harmonic components. The DC-link voltage and current have also the different frequency of oscillation. An experiment has been carried out for the same setup and power reference. Fig. 3.17 shows the results from the experiment. The experimental result has confirmed that the system is unstable and has polluted by the different harmonic. Moreover, it cannot be continued the operation in the experiment since protection system has been tripped.

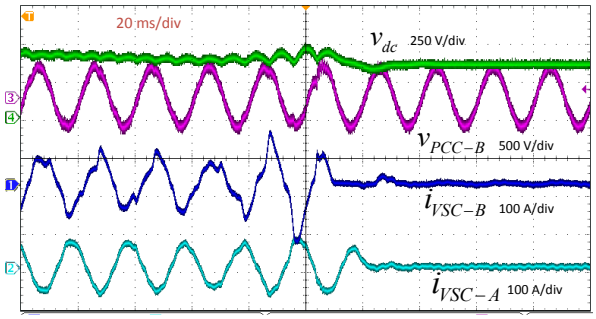


**Figure 3.17:** Experimental results for +10 kW power reference to the P-VSC (Unstable case): (i) the DC link voltage, (ii) voltage at PCC of VSC (phase-A), (iii) current of P-VSC (phase-A) and (iv) current of Vdc-VSC (phase-A).

The system operates stably when the power flow direction is from the power controlled-converter to the DC voltage controlled-converter and becomes unstable when the power flow direction has been altered. To analyze the stability and find the causes of this instability, an impedance based-stability method is adopted. The next two Sections have presented the stability analysis of the system and the possible solution to overcome this instability.

### 3.7.2 Impedance-based Stability Analysis based on the Literature

The investigated two-terminal VSC-HVDC system including the shunt current injection structure for the impedance model verification is depicted in Fig. 3.18. For stability analysis, the equivalent small-signal impedance model of the VSC-HVDC system is shown in Fig. 3.19. The power controlled-converter subsystem including the DC-line impedance is modeled by its Norton equivalent circuit consisting of an ideal current source, $I_P$ in parallel with an equivalent impedance, $Z_P(s)$ while the DC voltage controlled-converter subsystem is modeled by its Thevenin equivalent consisting of a voltage source with a series equivalent impedance, $Z_{Vdc}(s)$ [63].

The current source impedance can be given by

$$Z_P(s) = \frac{Z^p_{dc}(s)}{1 + sC_{dc}Z^p_{dc}(s)} + Z_{dc,cable}(s) \tag{3.57}$$

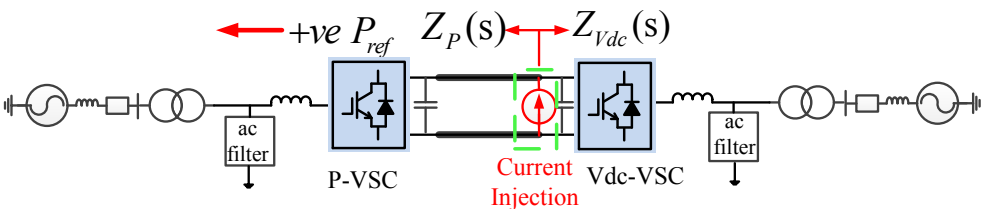


**Figure 3.18:** Investigated point-to-point VSC-based HVDC system including current injection structure for impedance model verification

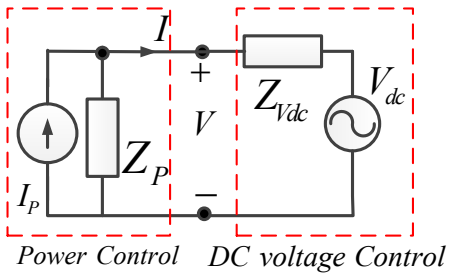


**Figure 3.19:** Equivalent small-signal impedance model of VSC-HVDC system consisting of both the voltage source and the current source.

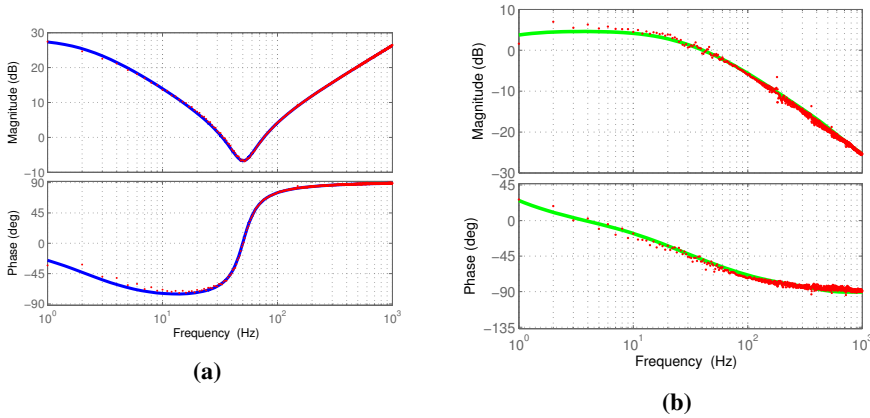


**Figure 3.20:** Frequency response of the impedance: (a) the impedance of the current source subsystem and (b) the impedance of the voltage source subsystem (solid-line is from model prediction and the red-points are from detailed simulation).

where $Z_{dc,cable}$ is the impedance of the HVDC-link cable and the voltage source impedance is

$$Z_{V\,dc}(s) = \frac{Z^v_{dc}(s)}{1 + sC_{dcB}Z^v_{dc}(s)}. \tag{3.58}$$

The analytical impedance model developed for the VSCs in (3.57) and (3.58) are validated by simulation with detailed switching model of the VSCs. A perturbation current (1% of rated dc steady-state current) at different frequencies from 1 Hz to 1 kHz is injected as shown in Fig. 3.18 and the voltage is measured. The FFT tool from the SimPower System is used to analyze the different frequency voltages and currents, and the impedance is calculated by dividing the voltage by current at each frequency. The analytical and simulation impedance frequency reponses are shown in Fig. 3.20 and the electrical circuit parameters of this system are given in Table A.1 in Appendix A. The solid-line is the analytical impedance and the red-points show the results from detailed simulation. Both the analytical and the simulation impedance

magnitude and phase have a good agreement which validates the correctness of the impedance model derivation.

The equivalent small-signal impedance model of the VSC-HVDC shown in Fig. 3.19 is a hybrid system consisting of both a voltage source and a current source. Therefore, the DC voltage at the interconnection of Fig. 3.19 can be given by

$$v(s) = (v_{dc}(s) + i_P(s)Z_{vdc}(s)) \left( \frac{1}{1 + \frac{Z_{Vdc}(s)}{Z_P(s)}} \right) \tag{3.59}$$

where the second part of the equation resembles a closed-loop transfer function and the stability of the system can be determined by checking the Nyquist plot of the voltage source to the current source impedance ratio regardless of the current source behaves as a source or a sink. Moreover, this criterion indicates that a point-to-point connection VSC-HVDC system should be designed to have high output impedance as possible in the current source subsystem and low input impedance in the voltage source subsystem in order to operate stable under a wide range of frequencies.

Fig. 3.21 (a) shows the impedance frequency response of the voltage source and the current source subsystem for the negative power reference of the power controlled-converter. As can be seen, the impedance of the current source subsystem, ($Z_P(s)$) is higher than the impedance of the voltage source subsystem, ($Z_{Vdc}(s)$) at all frequencies which is desirable to have the stable system. Fig. 3.21 (b) shows the Nyquist plot of the impedance ratio. Since the magnitude of the $Z_P(s)$ is higher than the magnitude of the $Z_{Vdc}(s)$ at all frequencies, the Nyquist plot stays inside the unit circle and it never encircles the point (-1, j0). Moreover, there is no pole in the right half-plane (RHP), therefore, the system is stable for the negative power reference. The system is found to be stable in time domain simulation and in the experiment.

Since the impedance also depends on the steady-state operating point, the impedance is calculated for the +10 kW power reference to P-VSC (which is the new operating point). Fig. 3.22 (a) shows the impedance frequency response for the positive (+10 kW) power reference. As

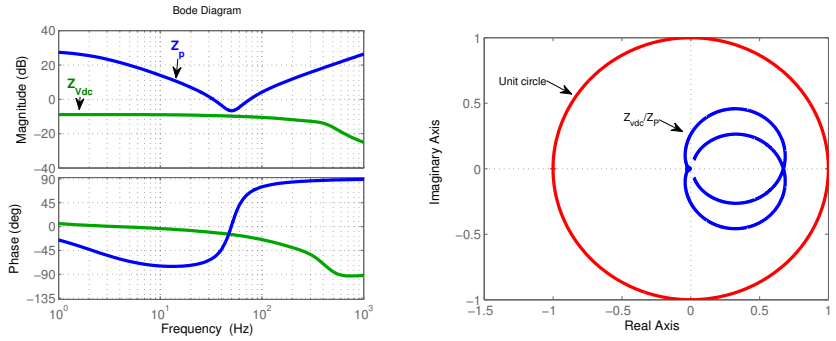


**(a)** **(b)**

**Figure 3.21:** Negative power reference: (a) Impedance frequency response of the voltage source and current source subsystem and (b) the Nyquist plot of the impedance ratio ($Z_{Vdc}(s)/Z_P(s)$).

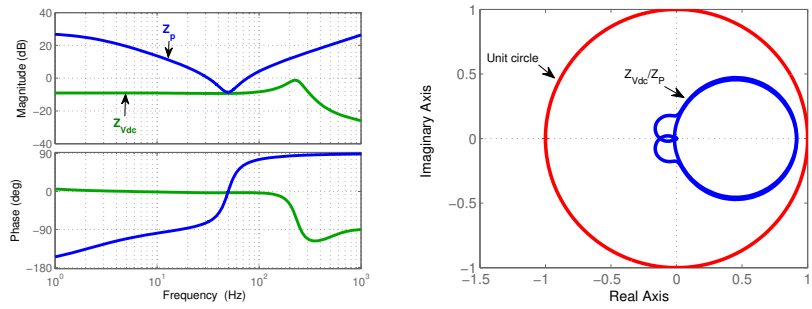


(a) (b)

**Figure 3.22:** Positive power reference: (a) Impedance frequency response of the voltage source and current source subsystem and (b) the Nyquist plot of the impedance ratio ($Z_{Vdc}(s)/Z_P(s)$).

can be seen in Fig. 3.22 (a), the impedance of the current source subsystem, ($Z_P(s)$) is higher than the impedance of the voltage source subsystem, ($Z_{Vdc}(s)$) at all frequencies, therefore, the Nyquist plot of the impedance ratio stays inside the unit circle and it never encircles the point (-1, j0) as shown in Fig. 3.22 (b). and There is no pole in the right half-plane (RHP) for the open-loop gain, therefore, the system is predicted to be stable from frequency domain analysis by the existing impedance based stability method; however, the system is found to be unstable in the time domain simulation and the experiments. Therefore, existing method can not determine the stability of the system when the power flow direction has been altered.

### 3.7.3 Stability Analysis and Control Design that Enables both Direction of Power Flow

In the previous section it has been observed that the existing impedance-based method cannot determine the stability of the system when the power flow direction has been altered. Therefore, to overcome this limitation in this work an impedance-based stability method is proposed where the subsystems are represented by only a Norton equivalent current source instead of representing them by a hybrid system consisting of both a voltage source and a current source. This assumption is valid, since the voltage controlled-subsystem can be represented by its Norton equivalent current-source with parallel connected impedance [46]. The modified equivalent small-signal impedance-model of the two-terminal HVDC system is shown in Fig. 3.23.

Now assume that the power reference of the power controlled-converter, P-VSC is negative, this means that P-VSC injects power into the DC system and works as a current source and the DC voltage controlled-converter, Vdc-VSC operates as an inverter and extracts active power from the DC system. Therefore, P-VSC operates as a current source while the Vdc-VSC is a current sink or load. For this condition, the current, $I(s)$ at interconnection in Fig. 3.23 can be given by

$$I(s) = \left( I_P(s) - I_V(s) \frac{Z_{Vdc}(s)}{Z_P(s)} \right) \frac{1}{1 + \frac{Z_{Vdc}(s)}{Z_P(s)}}. \tag{3.60}$$

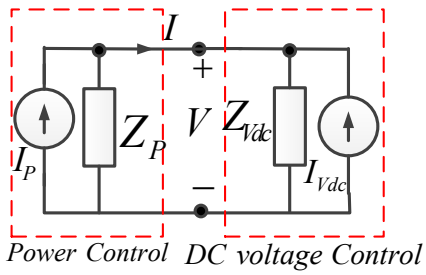


**Figure 3.23:** Equivalent small-signal impedance model of VSC-HVDC system: current source equivalent model.

Note that the second part of (3.60) resembles the close-loop transfer function of a negative feedback control system with a forward gain of unity and the feedback gain is $Z_{Vdc}(s)/Z_P(s)$. Hence based on (3.60), the HVDC system will operate stably if the ratio of the DC voltage controlled-converter impedance to the power controlled-converter impedance, $Z_{Vdc}(s)/Z_P(s)$ satisfies the Nyquist Stability Criterion. Fig. 3.21 shows the impedance frequency response and the Nyquist plot of the impedance ratio for the negative power reference and the system is predicted to be stable. The system operates stably in the time domain simulation and the experiments as shown in Fig. 3.13 and 3.15, respectively.

Now the reference power of P-VSC is set to +10 kW, this means that the P-VSC is extracting power from the DC system and working as a current sink or load, while the Vdc-VSC is working as a current source. In that case, the current $I(s)$ at interconnection can be given by

$$I(s) = \left( I_V(s) - I_P(s) \frac{Z_P(s)}{Z_{Vdc}(s)} \right) \frac{1}{1 + \frac{Z_P(s)}{Z_{Vdc}(s)}}. \tag{3.61}$$

Therefore, based on (3.61) the stability of the HVDC system depends on the impedance ratio

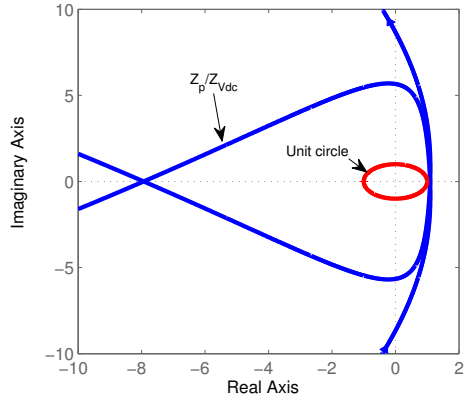


**Figure 3.24:** Nyquist plot of impedance ratio, $Z_P(s)/Z_{Vdc}(s)$.

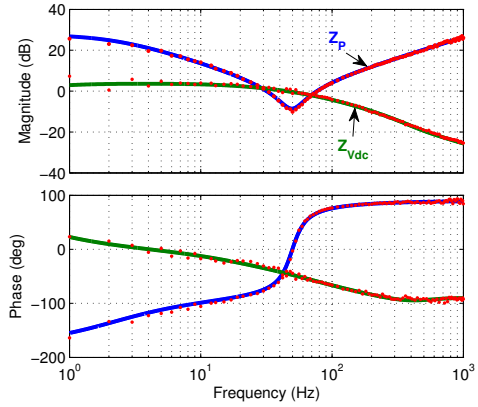


**Figure 3.25:** Frequency response of the impedance model at interfacing point for modified control tuning (the solid-line is from model prediction and the red-points are from detailed simulation).

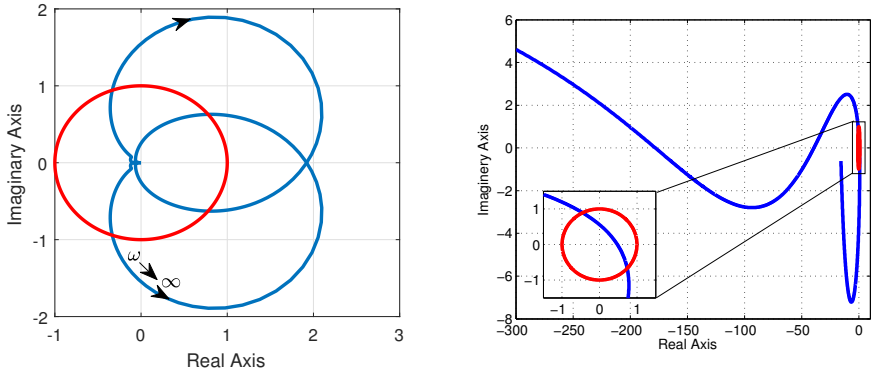


**(a)** **(b)**

**Figure 3.26:** Nyquist plot of impedance ratio for modified control tuning: (a) Negative power reference: $Z_{Vdc}(s)/Z_P(s)$ and (b) Positive power reference: $Z_P(s)/Z_{Vdc}(s)$.

of the input impedance of the power controlled-subsystem to the output impedance of the DC voltage controlled-subsystem, $Z_P(s)/Z_{Vdc}(s)$ which is the inverse of the previous assumption of (3.60). The system operates stably if $Z_P(s)/Z_{Vdc}(s)$ satisfies the Nyquist Stability Criterion.

Fig. 3.24 shows the Nyquist plot of the impedance ratio, $Z_P(s)/Z_{Vdc}(s)$ for the positive power reference of P-VSC. As can be seen in Fig. 3.22 (a), the magnitude of the $Z_P(s)$ is higher than the magnitude of the $Z_{Vdc}(s)$ and the Nyquist plot of $Z_P(s)/Z_{Vdc}(s)$ (Fig. 3.24) does not cross the unit circle; however it encircles the point (-1, j0) and there is a pole in the right half-plane (RHP) of the open-loop system, hence the system is predicted to be unstable. Therefore, the system has become unstable in the simulation and experiments as shown in Fig. 3.16 and Fig. 3.17, respectively.

Eqn. (3.61) indicates that the system stability can be improved by increasing the magnitude of

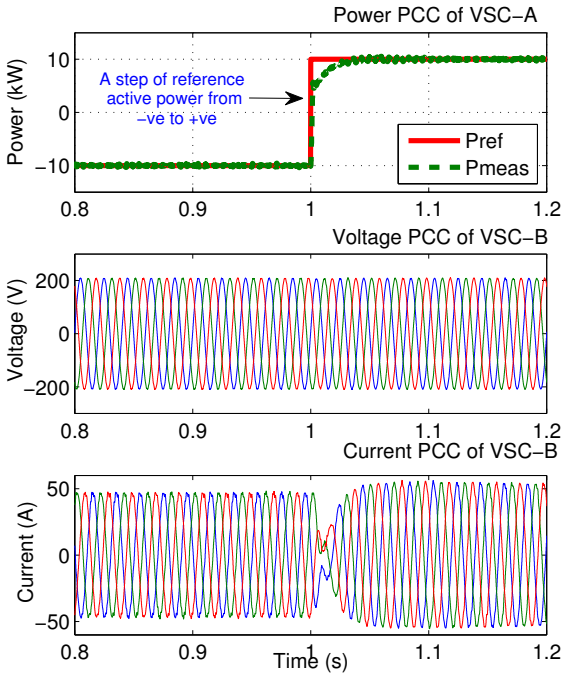


**Figure 3.27:** Simulation results for a step change of power reference from negative to positive 10 kW.

$Z_{Vdc}(s)$ which can be done by modifying the converter passive components and the controller bandwidth. It is not a good choice to modify the passive components instead it is better to reshape the impedance by re-tuning the controller gain.

Hence, the voltage controller gain is re-tuned at $H_{Vdc}(s) = 1+3/s$ and the close-loop crossover frequency is 7.2 Hz. Fig. 3.25 shows the impedance frequency response of the subsystems for the negative power reference. The impedance magnitude crosses each other at frequencies of 30.6 Hz and 65.8 Hz with a phase margin of $160^0$ and $66.5^0$, respectively. Fig. 3.26 depicts the Nyquist plot of impedance ratio, $Z_{Vdc}(s)/Z_P(s)$. As can be seen in Fig. 3.26 (a), the Nyquist plot does not encircle the point (-1, j0). Therefore, it has been predicted that the system operates stably for the negative power reference. Now stability analysis is performed for the positive power reference, and the resulting Nyquist plot of the impedance ratio, $Z_P(s)/Z_{Vdc}(s)$ is shown in Fig. 3.26 (b) and the Nyquist plot predicts that the system will operate stably. The system is predicted to be stable for both directions of the power flow.

A time domain simulation has been carried out for a step change of active power reference from -10 kW to +10 kW and the resulting time domain simulation is shown in Fig. 3.27. The system operates stably for both directions of power flow which is further confirmed in the experiments. Both the simulation and the experiments have validated the theoretical analysis.

## 3.8 Conclusion

This chapter presents the impedance based stability analysis of a VSC-HVDC system as an alternative measurement-based approach to limit the high dependence on detail information of components in large-scale systems. Analytical impedance models for the VSC-HVDC converters have been derived for different control modes and the impedance frequency response is verified by the perturbation method via measurements. Once the source and load impedance are identified, an impedance based stability method is adopted in order to determine the stability of the VSC-based HVDC system. Moreover, this chapter presents the impact of the power flow direction on the stability for VSC-HVDC systems. Existing methods of determining the source and the load impedances cannot predict the stability when the power flow direction has been altered; therefore a method based on the power flow direction has been presented to determine the source and the load impedance. The control has been redesigned based on the proposed method such that the power flows both directions without changing the control between the converters.

The system stability can be predicted from characteristics loci of minor-loop gain and the phase margin shows the stability strength of the system. The system is found to be stable as long as the impedance ratio satisfies the Nyquist stability criterion. The frequency domain stability analysis based on impedance ratio is further validated by time domain response for the VSC-based HVDC transmission system. From the observation, it can be concluded that the impedance based method could be a good tool for modeling, control and the stability assessments of VSC-based HVDC transmission systems.

# Chapter 4

# Impedance-based and Eigenvalue-based Stability Assessment Comparison

*This chapter presents a comparison between the impedance-based and the eigenvalue-based stability analysis methods for power electronics-based power systems more specifically for an HVDC system. Advantages and disadvantages of these two methods have been discussed when assessing the stability of power electronics based power system.*

This chapter is based on the following articles.

[1] **M. Amin**, A. Rygg and M. Molinas, "Impedance-based and eigenvalue based stability assessment compared in VSC-HVDC system," *2016 IEEE Energy Conversion Congress and Exposition (ECCE)*, Milwaukee, WI, USA, 2016, pp. 1-8.

[2] **M. Amin** and M. Molinas, Small-Signal Stability Assessment of Power Electronics based Power Systems: A Discussion of Impedance- and Eigenvalue-based Methods, *IEEE Transaction on Industry Application*, To be published. Online available: 06 June 2017. DOI: 10.1109/TIA.2017.2712692

## 4.1 Introduction

As shown in Fig. 1.5, existing approaches for the small-signal stability study of power electronics-based power system are based on the transfer function [94], state-space modeling and eigenvalues analysis [36], [40]–[43], nonlinear methods [95]–[98], and the impedance-based method [45], [46], [49], [50], [59], [64], [65]. The transfer function based stability analysis does not include the impact of the grid impedance and it is mainly adopted to tune the control-loop of the converters. The nonlinear methods have computational complexity and are difficult to study for large-scale power electronics based power systems. On the other hand, the impedance-based and the eigenvalue based analysis need less computation and include the impact of controller dynamics and the grid impedance; therefore, these two methods are more suitable for the stability analysis of power electronics-based power systems.

The state-space modeling and the eigenvalue-based approach is a global stability analysis method that determines the stability of the system regardless of the location of the source of the instabil-

ity. The eigenvalue-based analysis has broadly been used to determine the stability of a wind turbine system [72], harmonic stability assessment [74], the stability of two-terminal and multi-terminal VSC- and MMC-based HVDC transmission systems [40], [41], [73].

Impedance-based small-signal stability analysis has broadly been used to determine the stability of power electronics based power systems. Impedance-based analysis has been investigated for a grid-tied inverter at interfacing point connecting to the grid, either in the AC side by the sequence domain impedance by checking the Nyquist stability criterion on the positive and the negative sequence impedance ratio [46]–[49] and the dq-domain impedance based on the generalized Nyquist stability criterion [50], [53] or in the DC side [44], [58], [59], [79]. When the analysis is carried out in the AC impedance-based method, it is assumed that the DC-link voltage is stable and decoupled by the DC-link capacitance [49], [65], and the DC-link capacitance and other dynamics are neglected. Hence, the instability caused by the DC-link dynamics has been overlooked in the AC impedance-based approach. Resonance caused by the DC-link capacitance has been investigated by the DC impedance-based approach [58]. According to the literature, some instability phenomena in power systems with AC-DC power electronics converters cannot be identified from the DC impedance based approach [58], [59] while the instability caused by the DC-link dynamics has been overlooked in the AC impedance-based approach since the DC-link dynamics are decoupled by the DC-link capacitance [49], and the DC-link dynamics are neglected in the AC impedance model of AC-DC converters. In addition, there is no clear idea about the critical locations where the application of the impedance-based method can reveal the impact of a passive component or a controller gain of the grid-tied power converters on the stability.

Researchers have so far focused on determining the stability of the power electronics-based power system either by the eigenvalue-based method or the impedance-based method. As far as the author knows, a comparison and the relation between these two methods have not yet been established. This chapter aims at filling this gap. This chapter presents the comparison between the impedance-based and the eigenvalue-based stability analysis methods for power electronics-based power systems more specifically for an HVDC system. A relation between the characteristics equation of the eigenvalues, and poles and zeros of the minor-loop gain from the impedance-based analysis has been derived. In the case of the impedance-based method, a low phase-margin in the Nyquist plot of the minor-loop gain indicates that the system can exhibit harmonic oscillations. A weakness of the impedance method is the limited observability of certain states given its dependence on the definition of the local source-load subsystems which makes it necessary to investigate the stability at different subsystems. To address this limitation, this work discusses the critical locations where the application of the method can reveal the impact of a passive component or a controller gain on the stability. On the other hand, the eigenvalue-based method, being global, can determine the stability of the entire system, however it cannot unambiguously predict sustained harmonic oscillations caused by an AC-DC power converter. To generalize the observations, the two methods have been applied to a DC-DC converter and the results of their assessment are compared. To illustrate the difference and the relation between the two-methods, the two stability analysis methods are then applied to a two-terminal VSC-based HVDC system as an example of power electronics based power systems and the theoretical analysis has been further validated by simulation and experiments.

The rest of the chapter is organized as follows. Section 4.2 shows the equivalence between the

state-space model and the impedance-based model analytically. The characteristics equation of the eigenvalues for DC-DC converters has been analytically derived and a relation between the eigenvalues, and the poles and zeros of the minor-loop gain from the impedance-based analysis has been shown analytically. Section 4.3 presents the stability assessment comparison for a VSC-based HVDC system. Time domain simulation and experimental results are also presented in Section 4.3. Finally, the chapter is concluded in section 4.4.

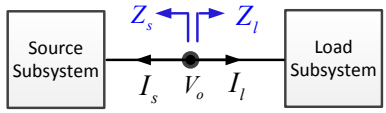


**Figure 4.1:** Source-load system.

## 4.2 Equivalence Between the State-space Model and the Impedance-based Model

Consider the power electronics system shown in Fig. 4.1 which splits between a source and load subsystems. The source subsystem can be represented in small-signal state-space form by

$$\Delta \dot{X}_s = A_s \Delta X_s + B_s \Delta U_s \tag{4.1a}$$

$$\Delta Y_s = C_s \Delta X_s \tag{4.1b}$$

where $A_s$ is a $n$x$n$ matrix for the source subsystem and $n$ is the number of state variable; matrix $B_s$ has a dimension of $n$x1; $C_s$ has a dimension of 1x$n$; $\Delta U_s$ is the single input as $\Delta U_s = \Delta I_s$ and $\Delta Y_s$ is the single output as $\Delta Y_s = \Delta V_o$. The source impedance can be calculated from the input-output relation of (4.1) as

$$Z_s(s) = \frac{\tilde{v}_o(s)}{\tilde{i}_s(s)} = C_s(sI - A_s)^{-1}B_s \tag{4.2}$$

where $s$ is the Laplace operator and $I$ is an identity matrix. Note that it has been assumed that the output, $Y_s$ of (4.1) is a state variable. if it is not a state variable, the D matrix must be included in (4.1) to find the impedance of the subsystem [99].

Similarly, assume that the load subsystem has $m$-number of state with a single input, $\Delta U_l = \Delta V_o$ and single output, $\Delta Y_l = \Delta I_l$ and matrix $B_l$ has a dimension of $m$x1, $C_l$ has a dimension of 1x$m$. The load admittance can be calculated from the input-output relation of state-space model as

$$Z_l^{-1}(s) = \frac{\tilde{i}_l(s)}{\tilde{v}_o(s)} = C_l(sI - A_l)^{-1}B_l. \tag{4.3}$$

The close-loop feedback gain of the system is [100]

$$T(s) = \frac{G(s)}{1 + G(s)H(s)} \tag{4.4}$$

where the minor-loop gain

$$G(s)H(s) = Z_s(s)Z_l^{-1}(s) \tag{4.5}$$

and the stability of the system can be found by checking the Nyquist criterion on (4.5).

For the eigenvalue-based stability, the full-system (FS) of Fig. 4.1 is presented in state-space form as

$$\Delta\dot{X}_{FS} = A_{FS}\Delta X_{FS} + B_{FS}\Delta U_{FS}. \tag{4.6}$$

By combining the state-space model of the source-load subsystem, the $A_{FS}$ matrix can be found as

$$A_{FS} = \begin{array}{c} \begin{matrix} C_1 & \ldots\ldots & C_n & C_{n+1} & & C_{n+m} \end{matrix} \\ \begin{bmatrix} \ddots & \vdots & \vdots & 0 & \cdots & 0 \\ \vdots & A_s & \cdots & \vdots & \ddots & \vdots \\ -B_l^T & \cdots & \cdots & 0 & \cdots & 0 \\ 0 & \cdots & 0 & B_s & \cdots & \cdots \\ \vdots & \ddots & \vdots & \vdots & A_l & \cdots \\ 0 & \cdots & 0 & \vdots & \cdots & \ddots \end{bmatrix} \end{array} \tag{4.7}$$

which has a dimension of $(m+n)$x$(m+n)$. $C_{i=1,2,..n+1,..n+m}$ represents the column of matrix $A_{FS}$ and row follows the column. The stability of the system can be checked from the eigenvalue of the system as

$$|sI - A_{FS}| = 0 \tag{4.8}$$

which gives the close-loop poles of (4.4).

**Example 1**

To illustrate the difference and the relation between the two-methods, and to generalize the observations, the two methods have been applied to a DC-DC converter depicted in Fig. 4.2. The converter can be represented in state-space form by (4.9) where $L$ and $R$ are the source inductance and resistance; $C$ is the filter capacitance; $P_o$ is the power of the constant power load (CPL); $V_o$ is the linearized voltage at operating point; D is the duty ratio of the switch; and $d_1$ is its complement, $d_1 = 1 - D$, and voltages and currents are shown in the circuit of Fig. 4.2.

$$\frac{d}{dt}\begin{bmatrix} i_L \\ v_o \end{bmatrix} = \begin{bmatrix} -\frac{R}{L} & -\frac{d_1}{L} \\ \frac{d_1}{C} & \frac{P_o}{CV_o^2} \end{bmatrix} x + \begin{bmatrix} \frac{1}{L} \\ 0 \end{bmatrix} u_s \tag{4.9}$$

The small-signal stability of the system can be assessed by the impedance-based approach through the frequency domain Nyquist criterion. For this approach, the system model is split between the impedance of the source and the load. The $LC$ filter is assumed to be the part of the source impedance; hence the source impedance transfer function can be found as

$$Z_s(s) = -\frac{v_o(s)}{i_o(s)} = \frac{\frac{1}{C}\left(s + \frac{R}{L}\right)}{\left(s^2 + s\frac{R}{L} + \frac{d_1^2}{LC}\right)} \tag{4.10}$$

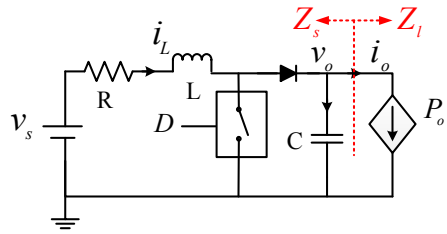


**Figure 4.2:** Converter 1: DC-DC step-up converter with constant power load.

**Table 4.1:** Parameters of the DC-DC converters

| Parameter | Value | Parameter | Value |
|---|---|---|---|
| $V_s$ | 12 V | $L$=$L_1$=$L_2$ | 150 $\mu$H |
| $V_o$ | 24 V | $R = R_1 = R_2$ | 0.015 $\Omega$ |
| $P_o$ | 12 W | $C$=$C_1$=$C_2$ | 470 $\mu$F |
| D | 0.5 | $f_{sw}$ | 20 kHz |

**Table 4.2:** Eigenvalues and the close-loop Poles of the DC-DC converter system.

| | Eigenvalues | Close-loop Poles |
|---|---|---|
| Converter 1 (Fig. 4.2) | $-27.8 \pm j1881$ | $-27.8 \pm j1881$ |
| Converter 2 (Fig. 4.4) | $-40.3 \pm j5500$ | $-40.3 \pm j5500$ |
| | $-37.5 \pm j1287$ | $-37.5 \pm j1287$ |

and the linearized gain of the CPL is

$$Z_l(s) = -\frac{P_o}{V_o^2}. \tag{4.11}$$

The minor-loop gain can now be expressed as,

$$G(s)H(s) = Z_s(s)Z_l^{-1}(s) = -\frac{P_o}{CV_o^2}\overbrace{(s+\frac{R}{L})}^{Z_{GH}(s)}/\underbrace{\left(s^2 + s\frac{R}{L} + \frac{d_1^2}{LC}\right)}_{P_{GH}(s)} \tag{4.12}$$

and the stability of the system can be found by checking the Nyquist criterion on (4.12).

When analyzing the system stability through small-signal eigenvalue analysis, the eigenvalues can be calculated from (4.9) as

$$|sI - A| = s^2 + s\frac{R}{L} + \frac{d_1^2}{LC} - \frac{P_o}{CV_o^2}\left(s + \frac{R}{L}\right) = 0 \tag{4.13}$$

which can be represented by

$$|sI - A| = 1 + G(s)H(s) = P_{GH}(s) + KZ_{GH}(s) = 0 \tag{4.14}$$

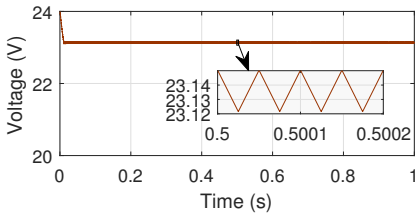


**Figure 4.3:** Output voltage of the DC-DC converter 1.

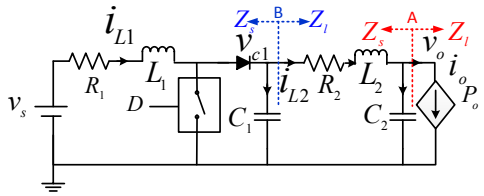


**Figure 4.4:** Converter 2: DC-DC step-up converter with CPL.

where $P_{GH}(s)$ and $Z_{GH}(s)$ are the transfer function of the pole and zero of the minor-loop gain, respectively; $K$ is a gain and in this case, $K = -P_o/(CV_o^2)$. Now we calculate the eigenvalues for the parameter of the converter given in Table 4.1. The system has complex conjugate eigenvalues with frequency $1881/(2\pi) = 300Hz$ as given in Table 4.2. The minor-loop transfer function has close-loop poles at the same frequency as the eigenvalues. The dc-dc converter is predicted to be stable by both the impedance-based and the eigenvalue-based analysis which has been further verified by simulation and the resulting time domain responses of the output voltage from simulation is shown in Fig. 4.3.

### Example 2

The relation between the characteristics equation and minor-loop gain has been derived in (4.14) for the DC-DC converter in Fig. 4.2 with only 2 state variables. To verify theoretically of this for more complex systems, we consider the DC-DC converter as shown in Fig. 4.4 with four states. Note that if the system has 5 or more states, it will be harder to show the characteristics equation of the eigenvalue analytically. The linearized model of the converter system can be represented by

$$\frac{dx}{dt} = \begin{bmatrix} -\frac{R_1}{L_1} & -\frac{d_1}{L_1} & 0 & 0 \\ \frac{d_1}{C_1} & 0 & -\frac{1}{C_1} & 0 \\ 0 & \frac{1}{L_2} & -\frac{R_2}{L_2} & -\frac{1}{L_2} \\ 0 & 0 & \frac{1}{C_2} & \frac{P_o}{C_2 V_o^2} \end{bmatrix} x + \begin{bmatrix} \frac{1}{L_1} \\ 0 \\ 0 \\ 0 \end{bmatrix} v_s \tag{4.15}$$

where $x = [i_{L1} \;\; v_{c1} \;\; i_{L2} \;\; v_o]^T$, the variables and constants are shown in Fig. 4.4. The characteristics equation of eigenvalue can be given by (4.16).

$$
\begin{aligned}
|sI - A| =& s^4 + s^3\left(\frac{R_1}{L_1} + \frac{R_2}{L_2}\right) + s^2\left(\frac{1}{L_2C_2} + \frac{1}{L_2C_1} + \frac{R_1R_2}{L_1L_2} + \frac{d_1^2}{L_1C_1}\right) \\
&+ s\left(\frac{R_1}{L_1L_2C_2} + \frac{R_1}{L_1L_2C_1} + \frac{d_1^2R_2}{L_1L_2C_1}\right) + \frac{d_1^2}{L_1L_2C_1C_2} \\
&- \frac{P_o}{C_2V_o^2}\left(s^3 + s^2\left(\frac{R_1}{L_1} + \frac{R_2}{L_2}\right) + s\left(\frac{d_1^2}{L_1C_1} + \frac{1}{L_2C_1} + \frac{R_1R_2}{L_1L_2}\right)\right) \\
&- \frac{P_o}{C_2V_o^2}\left(+\frac{R_1}{L_1L_2C_1} + \frac{d_1^2R_2}{L_1L_2C_1}\right)
\end{aligned} \tag{4.16}
$$

Now the impedance-based method is adopted at point A of Fig. 4.4. The minor-loop gain can be expressed by (4.17) which follows the relation derived in (4.14). Eigenvalues and close-loop poles from the impedance-based method are listed in the Table 4.2 for the parameters given in the Table 4.1. Both eigenvalues and close-loop poles have the same frequency of oscillation. Nyquist plot of minor-loop gain does not encircle the point (-1, j0) and there is no eigenvalue in the right-half plane; hence both the impedance-based and eigenvalue-based analysis predict the stability of the system accurately.

$$
GH = \frac{-\frac{P_o}{C_2V_o^2}\left(s^3 + s^2\left(\frac{R_1}{L_1} + \frac{R_2}{L_2}\right) + s\left(\frac{d_1^2}{L_1C_1} + \frac{1}{L_2C_1} + \frac{R_1R_2}{L_1L_2}\right) + \frac{R_1}{L_1L_2C_1} + \frac{d_1^2R_2}{L_1L_2C_1}\right)}{s^4 + s^3\left(\frac{R_1}{L_1} + \frac{R_2}{L_2}\right) + s^2\left(\frac{1}{L_2C_2} + \frac{1}{L_2C_1} + \frac{R_1R_2}{L_1L_2} + \frac{d_1^2}{L_1C_1}\right) + s\left(\frac{R_1}{L_1L_2C_2} + \frac{R_1+d_1^2R_2}{L_1L_2C_1}\right) + \frac{d_1^2}{L_1L_2C_1C_2}} \tag{4.17}
$$

The relation between the eigenvalues and poles-zeros of the minor-loop gain in (4.14) has been verified at point A of Fig. 4.4. Now the impedance-based stability analysis is adopted again at point B of Fig. 4.4 and the minor-loop gain at point B can be given by (4.18).

$$
GH = \frac{s^2\frac{1}{L_2C_1} + s\frac{R_1}{L_1L_2C_1} - \frac{P_o}{C_2V_o^2}\left(s\frac{1}{L_2C_1} + \frac{R_1}{L_1L_2C_1}\right)}{s^4 + s^3\left(\frac{R_1}{L_1} + \frac{R_2}{L_2}\right) + s^2\left(\frac{1}{L_2C_2} + \frac{R_1R_2}{L_1L_2} + \frac{d_1^2}{L_1C_1}\right) + s\frac{R_1}{L_1L_2C_2} + s\frac{d_1^2R_2}{L_1L_2C_1} + \frac{d_1^2}{L_1L_2C_1C_2} - \Psi_{CPL}} \tag{4.18}
$$

$$
\Psi_{CPL} = \frac{P_o}{C_2V_o^2}\left(s^3 + s^2\frac{R_1}{L_1} + s^2\frac{R_2}{L_2} + s\frac{R_1R_2}{L_1L_2} + s\frac{d_1^2}{L_1C_1} + \frac{d_1^2R_2}{L_1L_2C_1}\right)
$$

By comparing (4.16) and (4.18), it is noticed that they follow the relation between the eigenvalues and poles-zeros of the minor-loop gain derived in (4.14).

Now consider a system having $r$-number of states. The characteristics equation of eigenvalues for a system within this general form can be written as

$$
|sI - A| = (s + \alpha_1)(s + \alpha_2)\ldots(s + \alpha_n) + K(s + \beta_1)(s + \beta_2)\ldots(s + \beta_m) = 0 \tag{4.19}
$$

and the minor-loop gain from the impedance ratio can be written in general form as

$$
G(s)H(s) = \frac{KZ_{GH}(s)}{P_{GH}(s)} = \frac{K(s + \beta_1)(s + \beta_2)\ldots(s + \beta_m)}{(s + \alpha_1)(s + \alpha_2)\ldots(s + \alpha_n)} \tag{4.20}
$$

where $G(s)H(s)$ has $m$-number of zeros with a value $-\beta_1, -\beta_2 \ldots -\beta_m$ and $n$-number of poles with a value $-\alpha_1, -\alpha_2 \ldots -\alpha_n$; $m \neq n$ and $m, n \leq r$.

One important observation from (4.20) is that if a pole, $\alpha_i$ becomes equal to a zero $\beta_j$, the impact of that component (passive R-L-C or controller coefficient) is cancelled out in the representation of (4.20) and their impacts are not observable in the Nyquist plot of the minor-loop gain in the frequency domain analysis. This can happen in particular interfacing points of a source-load subsystem where the impact of that component will not be seen; however, if another interfacing point is considered to include the impact of the component that is previously neglected, it might neglect another component which indicates that impedance-based stability analysis is a local stability analysis method. On the other hand, the eigenvalue-based analysis includes the impact of all components and is a global stability analysis method.

## 4.3 Comparison Between the Eigenvalue and Impedance-based Stability for an HVDC system

This section presents the stability assessment comparison between the impedance-based and eigenvalue-based methods for a VSC-HVDC system. The theoretical analysis has been verified by time domain simulation and experiments.

### 4.3.1 The HVDC System Configuration

The two stability methods presented in the previous section have been compared for DC-DC converters. The DC-DC converter systems have fewer state variables and lower complexity compared to a VSC-based HVDC system. Thus, a two-terminal VSC-based HVDC system has been taken as an example of a more complex power electronics based power system. The HVDC system under study is depicted in Fig. 4.5 and the detailed controls have discussed in Chapter 3. The electrical parameters of the system are given in Table A.1. The inner-loop current controller and the outer-loop power controller of the P-VSC are tuned at $H_{cc}(s) = 4 + 800/s$ and $H_P(s) = 0.005 + 1/s$, respectively. The current compensator and the DC voltage controller of the Vdc-VSC are tuned at $H_{cc}(s) = 5 + 1000/s$ and $H_{vdc}(s) = 1 + 3/s$. The control tunings satisfy the standard bandwidth requirements and the system operates stably at the tuning as discussed in section 3.7.3 of Chapter 3.

### 4.3.2 State-Space Small-Signal Modeling of the Investigated HVDC system

The HVDC system shown in Fig. 4.5 can be presented in a state-space form by (4.21) through a nonlinear model where $x(t)$ is the state vector and $u(t)$ is the input vector. The detailed

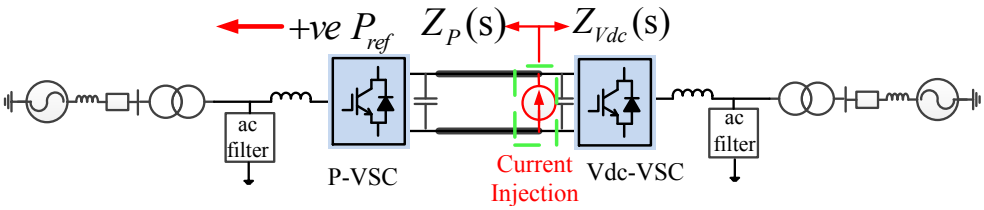


**Figure 4.5:** Investigated two-terminal VSC-HVDC system.

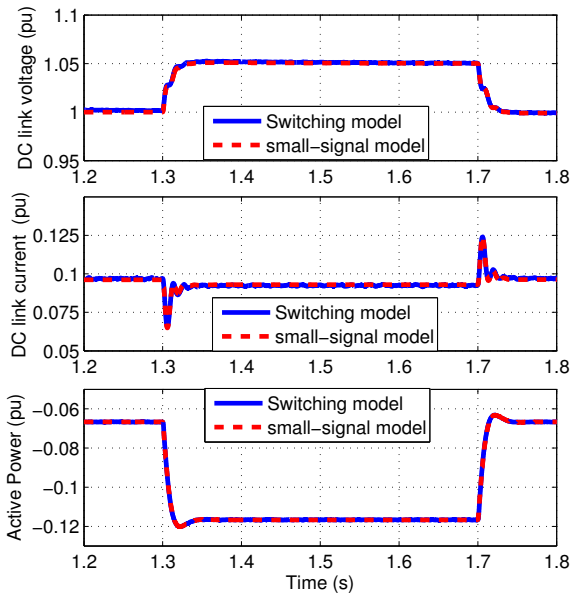


**Figure 4.6:** Time domain response comparison of switching model with the small-signal state-space analytical model of the HVDC system: (i) DC link voltage, (ii) DC link current and (iii) a step change of active power of P-VSC

analytical state-space modeling of an HVDC system has been described in Chapter 2.

$$\frac{dx}{dt} = f(x(t), u(t)) \tag{4.21a}$$

$$y = g(x(t), u(t)) \tag{4.21b}$$

The non-linearity of the model prevents direct application of classical linear analysis techniques. Therefore, a small-signal representation is derived for a steady-state operating point as given by

$$\frac{d\Delta x}{dt} \simeq A.\Delta x + B.\Delta u \tag{4.22a}$$

$$\Delta y \simeq C.\Delta x + D.\Delta u \tag{4.22b}$$

The state and input vectors are defined in chapter 2. The analytical state-space small-signal model developed has been validated by simulation with detailed switching model of the VSC. The results from simulations with the full nonlinear simulation model are therefore compared with results obtained from the linearized state-space small-signal model. The validated small-signal model is then used to further analyze the characteristics of the investigated system. Fig. 4.6 shows the comparison of time domain responses obtained from the switching model and the state-space small-signal model of the investigated system. As can be seen, both the small-signal model and the switching model have a very good agreement in time domain responses which validates the derivation of the state-space small-signal model.

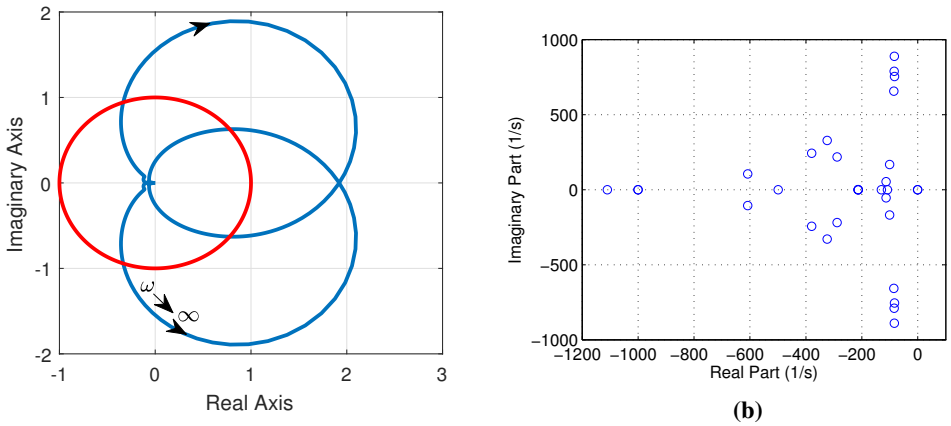


**Figure 4.7:** Stable System: (a) Nyquist plot of Impedance ratio (Red line is unit circle) and (b) Eigenvalue plot.

### 4.3.3 Impedance-based and Eigenvalue-based Stability Assessment Comparison for HVDC System

Assuming that the power reference of the P-VSC is negative, this means that the P-VSC injects power into the DC system and works as a rectifier, and the Vdc-VSC operates as an inverter. Therefore, the P-VSC operates as a current source while the Vdc-VSC as a current sink or load. The voltage, $V$ and the current, $I$ at interconnecting point can be given by (4.23) and (4.24), respectively.

$$V(s) = (V_{dc}(s) + I_P(s)Z_P(s)) \left(1 + \frac{Z_{Vdc}(s)}{Z_P(s)}\right)^{-1} \tag{4.23}$$

$$I(s) = \left(I_P(s) - \frac{V_{dc}(s)}{Z_P(s)}\right) \left(1 + \frac{Z_{Vdc}(s)}{Z_P(s)}\right)^{-1} \tag{4.24}$$

Hence, based on (4.23) and (4.24), the HVDC system will operate stably if the ratio of the DC voltage controlled-converter input impedance to the power controlled-converter output impedance, i.e., $Z_{Vdc}(s)/Z_P(s)$ satisfies the Nyquist stability criterion [59].

Fig. 4.7 (a) shows the Nyquist plot of the impedance ratio $Z_{Vdc}(s)/Z_P(s)$. As can be seen in Fig. 4.7 (a), the Nyquist plot does not encircle the point (-1, j0) and it intersects the unit circle with sufficient phase margin. Therefore, it has been predicted that the system will operate stably. The eigenvalue-based stability analysis has been carried out and resulting eigenvalue plot is shown in Fig. 4.7 (b). There is no eigenvalue in the RHP, therefore the system is predicted to be stable by both the impedance-based and eigenvalue-based stability methods.

To further validate the above theoretical analysis, time domain simulations and experiments have been carried out and resulting time domain responses from the simulation and the experiments are shown in Figs. 4.8 and 4.9, respectively. The system operates stably both in the

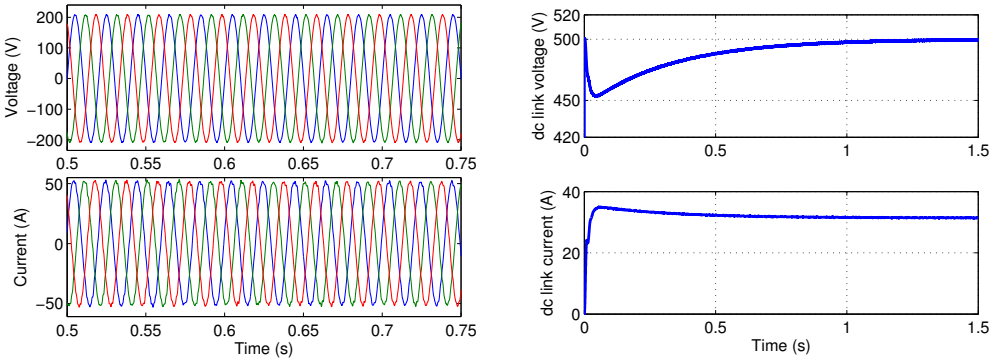


**Figure 4.8:** Simulation: (a) three phase voltages and currents of P-VSC and (b) DC link voltage and current.

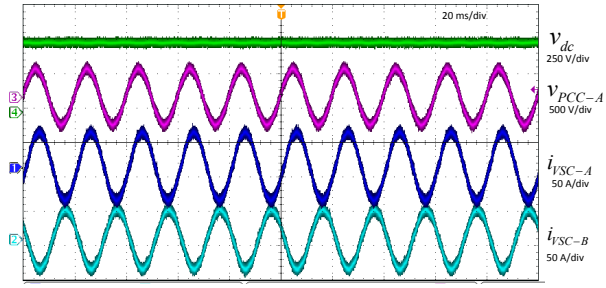


**Figure 4.9:** Experiment: (i) DC link voltage, (ii) phase-A voltage of P-VSC, (iii) phase-A current of P-VSC and (iv) phase-A current of Vdc-VSC.

simulation and the experiments which have been predicted from the impedance-based stability analysis and the eigenvalue based stability.

#### 4.3.3.1 Impact of the DC Voltage Controller Gain on the Stability

The impact of the controller dynamics on the stability has been investigated by both methods. The proportional gain of the DC voltage controller reduces to $0.03$ with a close-loop crossover frequency of $7.13$ Hz. The impedance frequency response and the Nyquist plot for this tuning is shown in Fig. 4.10. As can be seen in Fig. 4.10 (a), the DC voltage controlled-subsystem impedance becomes larger at low frequency for the lower value of proportional gain and it crosses the unit circle at frequency of $2.96$ Hz with low phase margin ($<20^0$) as shown in Fig. 4.10 (b). Since Nyquist plot does not encircle the point (-1, j0) and there is no pole in the RHP of the open-loop system, the system is predicted to be stable. However, the phase margin is low, the system could have a low-frequency oscillation at around $2.96$ Hz in the transient condition. A trajectory of the eigenvalues for decreasing value of the DC voltage controller proportional gain is shown in Fig. 4.11. As can be seen, two of the complex conjugate poles around 2.9 Hz

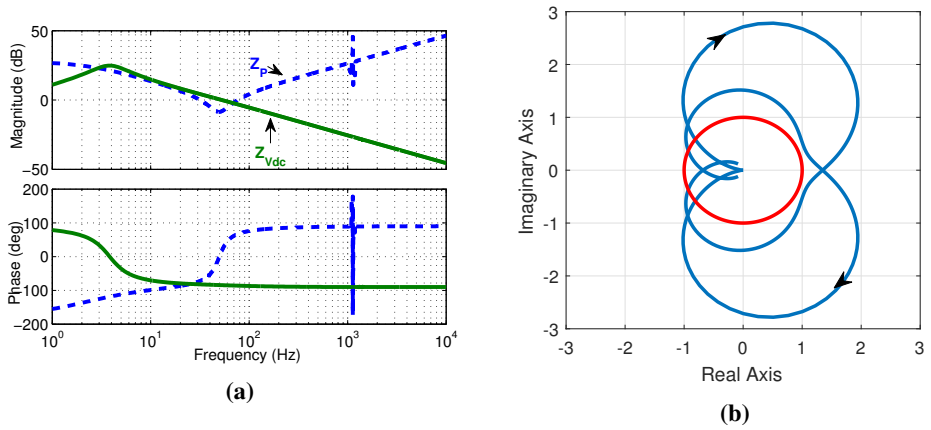


**Figure 4.10:** (a) Impedance of the subsystem for DC voltage control proportional gain of 0.03 and (b) the Nyquist plot of impedance ratio, $Z_{Vdc}(s)/Z_P(s)$.

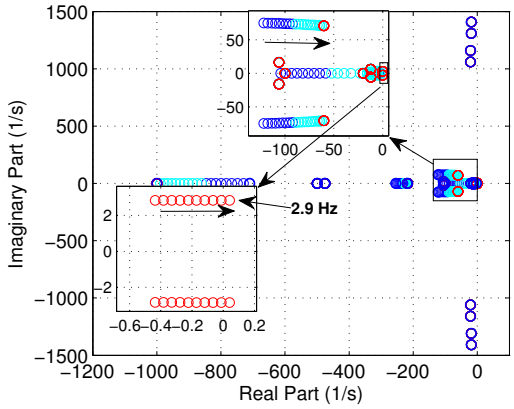


**Figure 4.11:** Trajectory of Eigenvalue for a change of the DC voltage controller proportional gain.

and 80 Hz have a significant impact on their damping term. They are moving towards the RHP. These two frequencies are the points that cross the voltage and power controlled-converter's impedances (which intersect the unit circle of the Nyquist plot). The eigenvalue at 80 Hz has sufficient damping; however, the eigenvalue at 2.9 Hz has low damping and it moves to the RHP for a proportional gain of the DC voltage controller lower than 0.03. A participation factor analysis has been carried to identify the contributing states to these two eigenvalues and it is found that the integral part of the DC voltage controller, DC link capacitance and the DC voltage measurement low-pass filter are the contributing states. A time domain simulation has been carried out and the time domain response of the DC voltage and the current and FFT of the DC current are shown in Fig. 4.12 (a). As can be seen, the system has a stable pole with oscillation frequency around 3 Hz as predicted in the frequency domain analysis by the Nyquist plot in Fig. 4.10 (b). This oscillation is also observed in the AC side as shown in Fig. 4.12 (b)

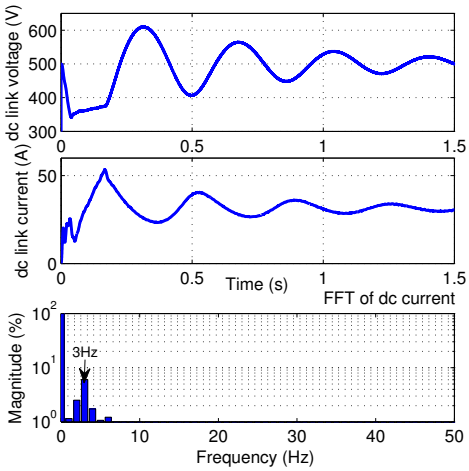


(a)

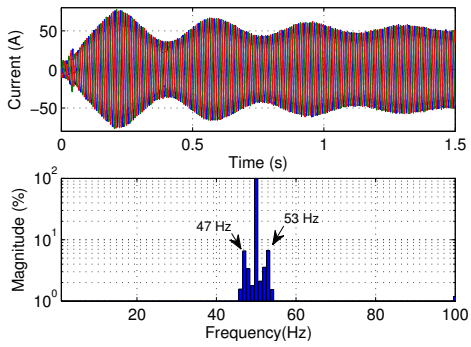


(b)

**Figure 4.12:** Simulation results: (a) The DC link voltage and current and FFT of DC current for DC voltage controller proportional gain of $0.03$, (b)The three-phase currents at PCC of Vdc-VSC for DC voltage controller proportional gain of $0.03$.

which is reflected by 50 Hz fundamental frequency, $f_1$ as $\pm(f - f_1)$ [47].

#### 4.3.3.2 Impact of the Power Controller Gain on the Stability

An example case is presented to show the impact of the power controlled-converter controller gain on the system stability by both methods. The power controller proportional gain of the P-VSC has been purposely increased to $0.0225$ while the initial value is $0.005$. The Nyquist plot of the minor-loop gain is shown in Fig. 4.13 (a) for these two power controller tuning and we see that there is no significant change in the entire Nyquist path. The Nyquist plot of the minor-loop gain does not encircle the point (-1, j0), therefore the system is predicted to be stable from the impedance-based stability analysis from DC side.

The eigenvalue plot for a power controller proportional gain of $0.0225$ is shown in Fig. 4.13 (b). As can be seen, the system has an unstable complex conjugate eigenvalue with 797 Hz frequency. This instability for $k_{pp}$=$0.0225$ has been predicted by the state-space small-signal analysis; however, it is not predicted by the impedance-based analysis from the DC side. The stability analysis results obtained from these two methods are contradictory. It has been discussed in section 4.2 that the eigenvalue-based analysis determines the stability of the whole system; however, in the case of the impedance-based method, some of the poles and zeros from the minor-loop gain might cancel each other resulting in some states being unobservable. A participation factor analysis has been carried out for the unstable eigenvalue and it is found that the states of the converter series inductor current and filter capacitor voltage are contributing to this unstable eigenvalue which indicates that the power controller of the P-VSC and the AC grid are interacting resulting in instability. To identify the interaction between the controller and the grid, the impedance-based analysis needs to be carried out at the AC interfacing point.

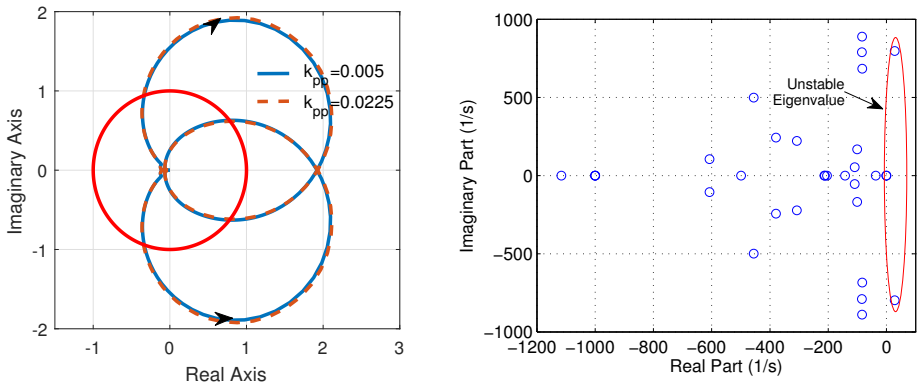


(a) (b)

**Figure 4.13:** (a) Nyquist plot of minor-loop gain for different value of power controller gain (Red-line is the unit circle) and (b) Eigenvalue plot for power controller proportional gain of 0.0225.

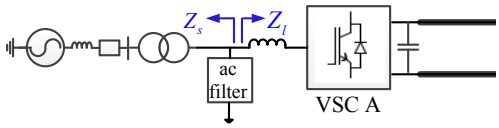


**Figure 4.14:** Power control VSC for impedance-based stability analysis from AC side.

Thus, a weakness of the DC impedance based method is that the instability caused by the active power control-loop can not be determined from the DC side by the impedance-based method. Moreover, it has been observed that the instability caused by the grid strength (grid impedance) [58], the AC side $LC$ filter, the inner-loop current controller gain and the PLL-loop gain can not be identified from the DC side by the impedance-based method, since there is no significant change in the Nyquist plot for a change of those components.

The impact of those passive components and the controller gain on the stability are observable from the AC side, therefore the AC impedance-based stability analysis is applied to identify the interactions. The AC impedance-based analysis can be adopted both in the sequence domain and dq-domain. Here in this case, a dq-domain impedance model is used. The impedance model of the P-VSC is derived in Chapter 3 and can be given by

$$\mathbf{Z^P_{dq}}(s) = \left(-\mathbf{Z_0}(s) + V_{dc}\mathbf{G_{PWM}(s)}\left(-H_P(s)\mathbf{G_{cc}}(s)\mathbf{G_{vp}} - \mathbf{G_{cc}}(s) - \mathbf{Z_{del}}\right)\right)\left(\mathbf{I} - V_{dc}\mathbf{G^P_C}(s)\right)^{-1}. \tag{4.25}$$

The impedance of the converter in Fig. 4.14 is the load impedance as

$$\mathbf{Z_l}(s) = \mathbf{Z^P_{dq}}(s) \tag{4.26}$$

and the source impedance, $Z_s$ in dq-domain is calculated as

$$\mathbf{Z_s}(s) = \left(\mathbf{Z_g^{-1}}(s) + \mathbf{Y_{cf}}(s)\right)^{-1}. \tag{4.27}$$

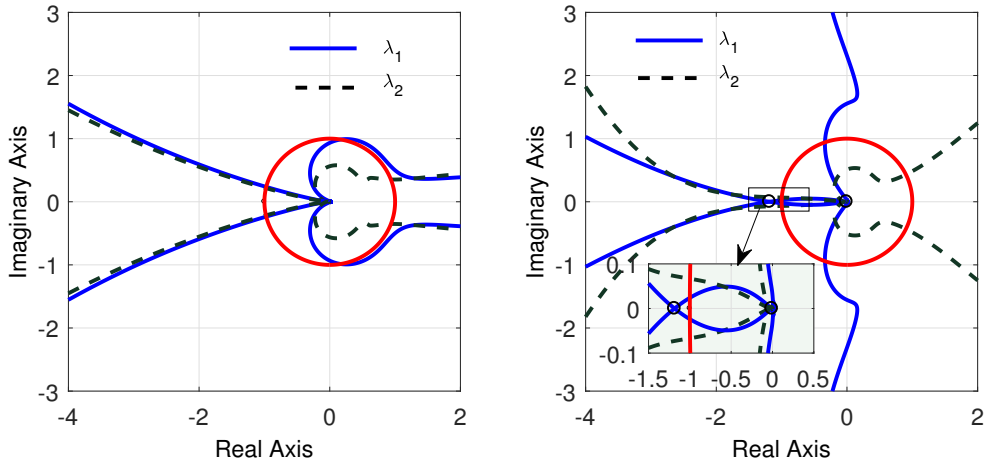


**Figure 4.15:** Characteristics Loci of minor-loop gain: (a) for $k_{pp} = 0.005$ and (b) for $k_{pp} = 0.0225$ (Red line is the unit circle).

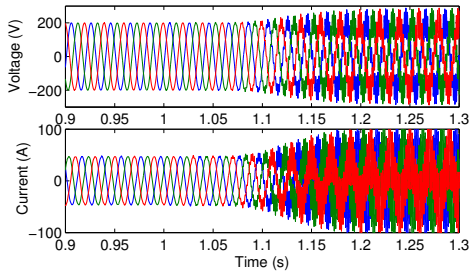


**Figure 4.16:** The three-phase voltages and currents of the P-VSC for a change of the power controller proportional gain from 0.005 to 0.0225 at 1 s.

Hence, the stability of the system can be determined by checking the Nyquist plot of the minor loop gain,

$$\mathbf{G}(s)\mathbf{H}(s) = (\mathbf{Z_s}(s))\,(\mathbf{Z_l}(s))^{-1}. \tag{4.28}$$

Fig. 4.15 shows the characteristics loci of the minor-loop gain for $k_{pp} = 0.005$ and $k_{pp} = 0.0225$. The $\lambda_1$ encircles the point (-1, j0) as shown in Fig. 4.15 (b) and becomes unstable when the power controller proportional gain increases to $k_{pp} = 0.0225$. The characteristics loci related to the d-axis dominated impedance becomes unstable since the power controller is implemented only in the d-axis. Hence, the AC impedance-based stability analysis (in dq-domain in this case) gives the same conclusion as the eigenvalue-based analysis for a change of power controller gain. The Nyquist plot of the $d$-channel minor loop gain encircles the point (-1, j0) at a frequency around 737 Hz for $k_{pp} = 0.0225$ and one of the complex conjugate

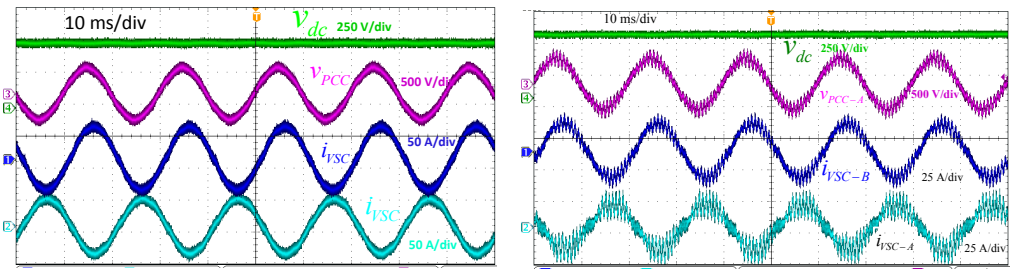


**(a)** **(b)**

**Figure 4.17:** Experiments: (i) dc link voltage, (ii) phase-A voltage of VSC-A, (iii) phase-A current of P-VSC and (iv) phase-A current of VSC-B. (a) $k_{pp} = 0.005$ and (b) $k_{pp} = 0.0225$.

poles moves to the right half-plane with the same frequency. To further verify the theoretical analysis, a time domain simulation and experiments have been carried out for a control tuning of the power controller at $k_{pp} = 0.0225$ and the resulting time domain responses from simulation and experiments are shown in Figs. 4.16 and 4.17 where they have high frequency oscillation and the system is unstable. In the experiments, the system is equipped with different protection and limits (current limit, voltage limit), therefore the voltages and currents do not increase exponentially as expected from the eigenvalue plot.

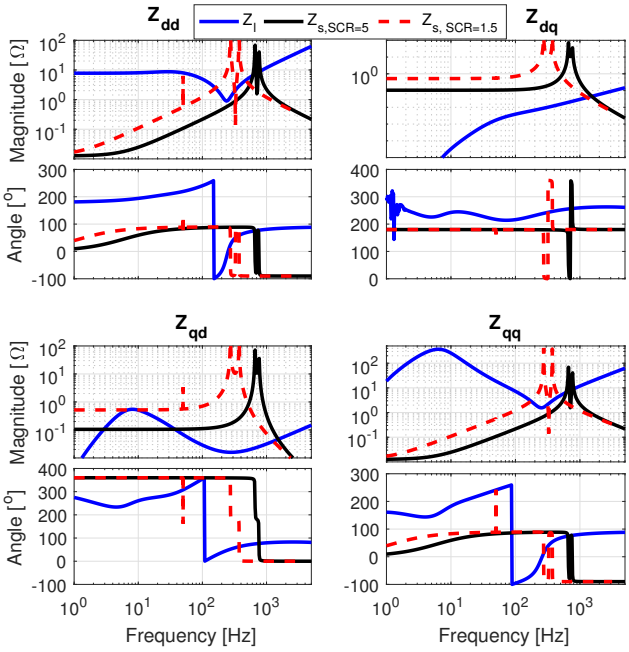


**Figure 4.18:** Impedance frequency responses of the converter ($Z_l$) and the Grid ($Z_s$) for different SCR.

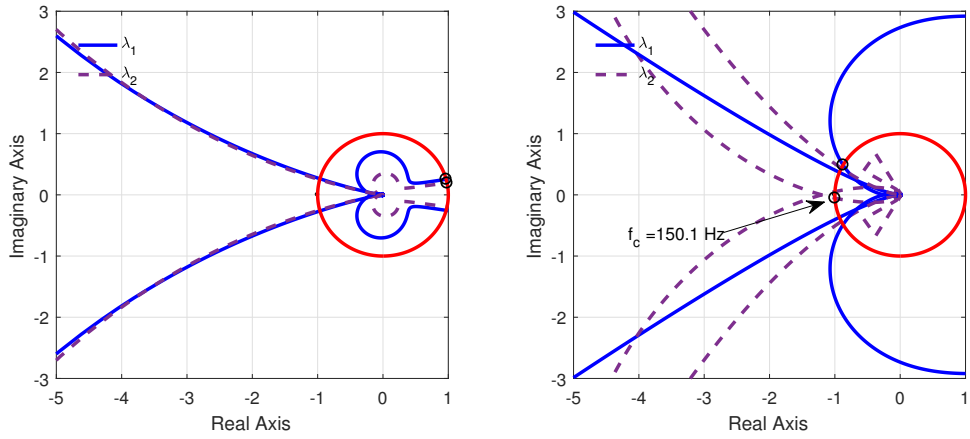


**Figure 4.19:** Characteristics loci of minor-loop gain: (a) SCR=5 and (b) SCR=1.5.

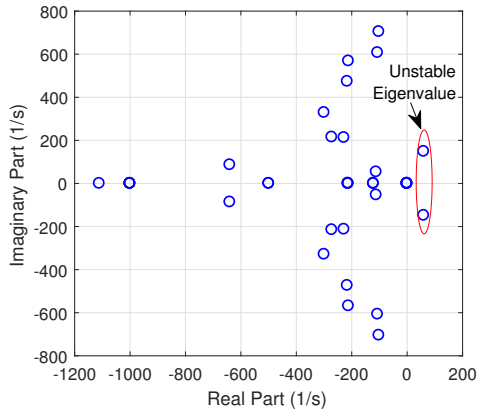


**Figure 4.20:** Eigenvalue plot for SCR=1.5.

#### 4.3.3.3 Impact of the Grid Impedance on the Stability

The impact of the grid impedance has been investigated by both methods. Initially, the grid short circuit ratio (SCR) is 5 for which the system operates stably. An inductance has been added in series with the grid of the dc voltage controlled VSC and the SCR becomes 1.5. Fig. 4.18 shows the impedance frequency responses of the Vdc-VSC and the grid for two values of the SCR. The diagonal elements of the grid and Vdc-VSC intersect each other at a point around 580 Hz when the SCR is 5 where both the grid impedance and the VSC impedance characteristics are inductive. For SCR=1.5, the diagonal elements of the impedances intersect around 150 Hz where the grid impedance characteristics are inductive and the Vdc-VSC impedance characteristics are capacitive. Fig. 4.19 characteristics loci of the minor-loop gain for this two cases of the SCR values. As can be seen, the system is stable for SCR=5 and the system predicted

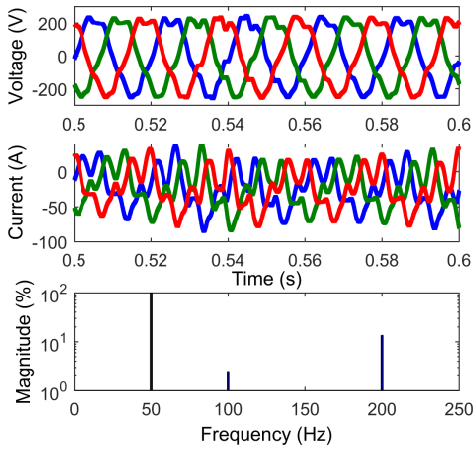


**Figure 4.21:** Time domain responses for SCR=1.5: (i) three-phase voltages and (ii) three-phase currents of VDC-VSC, and (iii) FFT of the voltages.

to be unstable for SCR=1.5 when the $\lambda_2$ encircles the point (-1, j0) at a frequency around 150 Hz. Eigenvalue-based small-signal stability analysis has been carried out and the resultant eigenvalue plot is shown in Fig. 4.20. The system has an unstable complex conjugate eigenvalue of $60.9 \pm j2\pi 148.4$ with around the same frequency as the impedance-based method. To further verified the theoretical analysis a time domain simulation has been carried out and the time domain responses are shown in Fig. 4.21. As predicted by both methods, the system is unstable. The time domain responses have oscillation frequencies at $(f \pm -f_1) = 150 \pm 50 = 100, 200$ Hz as predicted by frequency domain analysis. Hence, the instability caused by the grid strength can be predicted by the eigenvalue-based method and the impedance-based method from the AC side.

In an attempt to improve the instability caused by the grid strength, the impedance of the converter has been reshaped by re-tuning the current control-loop of the VSC. The current control-loop bandwidth has been reduced by decreasing the proportional gain of the current controller while the integral time constant keeps the same. Fig. 4.22 (a) shows the characteristics loci of the minor-loop gain for the case of re-tuning the current control-loop bandwidth. The characteristics loci of the minor-loop gain do not encircle the point (-1, j0), hence the system is predicted to be stable. For this control-loop tuning, eigenvalues have been calculated analytically and the resultant eigenvalues are shown in Fig. 4.22 (b). There is no eigenvalue in the RHP. Thus, both methods predict the stability of the system accurately which is further verified by time domain simulation.

### 4.3.4 Prediction of Sustained Harmonic Oscillation

Now the power controller has been tuned such that the system is predicted to be stable from the eigenvalue-based analysis; however the characteristics loci has a very low phase margin. The power controller is tuned at $k_{pp} = 0.0155$ and a trajectory of eigenvalue plot is shown in Fig. 4.23. The system is predicted to be stable with a critical pole at $-10 \pm j2\pi.780$. Time

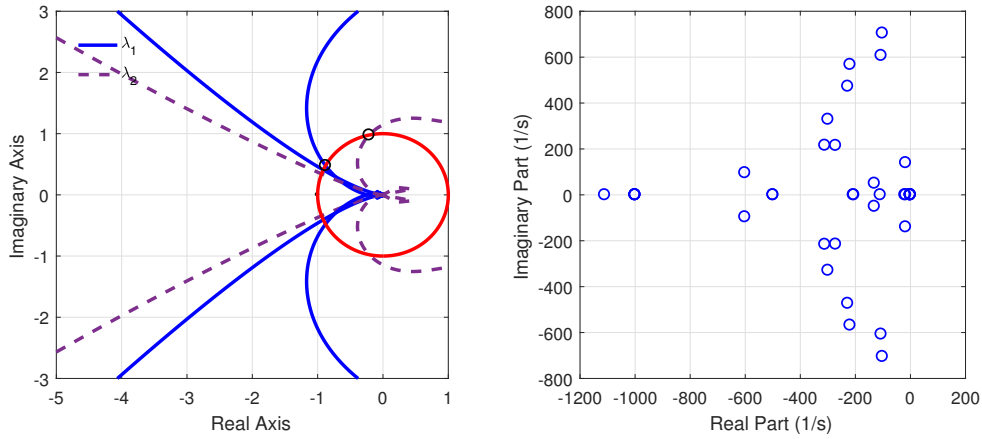


(a) (b)

**Figure 4.22:** (a) Characteristics loci of the minor-loop gain for retuning the current control-loop bandwidth and (b) eigenvalue plot.

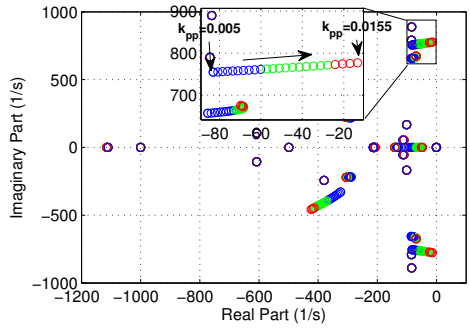


**Figure 4.23:** Eigenvalue trajectory for increasing value of $k_{pp}$ from $0.005$ to $0.0155$.

domain simulation has been carried out for this tuning resulting in time domain responses are shown in Fig. 4.24 (a). The simulation has been carried out for several hundreds of seconds and it has been observed that the voltages and currents have a sustained oscillation and they are neither dying out, nor increasing exponentially. An experiment has been carried for this tuning and resulting time domain responses from the experiment are shown in Fig. 4.24 (b) showing sustained oscillation as in the simulation. Even if there is no eigenvalue in the RHP, the system exhibits sustained harmonic oscillation.

As can be seen in Fig. 4.23, the two terminal system has one critical pole at $-10 \pm j2\pi.780$ with a frequency of oscillation 780 Hz. The frequency of the oscillation in the simulation and the experiments are the same as the one noticed in the critical eigenvalue. The system exhibits sustained harmonic oscillation even if there is no eigenvalue in the RHP. The critical eigenvalue at $-10 \pm j2\pi.780$ has sufficient negative real part. The two terminal HVDC system has one critical eigenvalue which introduces sustained harmonic oscillation. If we consider large-scale

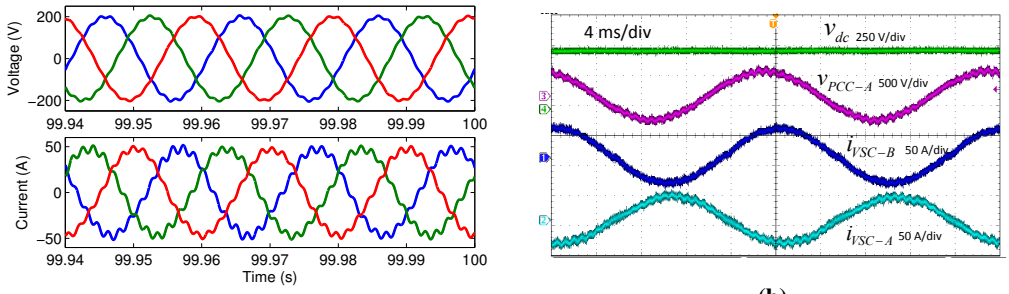


**(a)** **(b)**

**Figure 4.24:** (a) Simulation with detailed switching model of VSC: Voltages and currents of power controlled converter for low phase margin in the Nyquist plot and (b) Experiments for low phase margin in the Nyquist plot: (i) DC link voltage, (ii) phase-A voltage of P-VSC, (iii) phase-A current of Vdc-VSC and (iv) phase-A current of P-VSC.

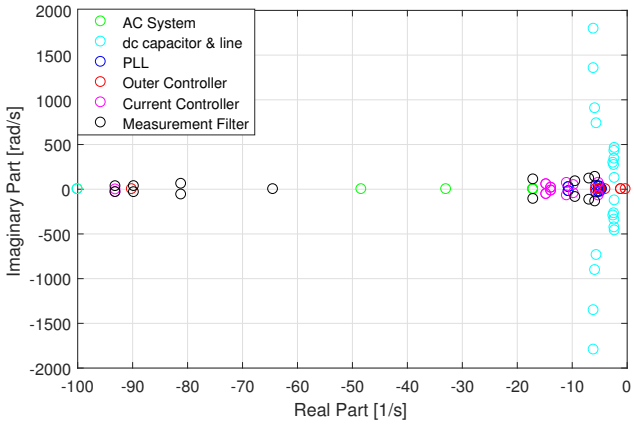


**Figure 4.25:** Eigenvalue plot of large scale MT-HVDC system for stable operation.

multi-terminal HVDC (MT-HVDC) system having multiple converters for stability analysis based on the eigenvalue analysis, the system could have several critical eigenvalues like the one observed in the two terminal systems. In order to show the stability analysis results from a large-scale MT-HVDC system, the eigenvalue based stability analysis has been carried out for a large-scale MT-HVDC system [33]. The detailed stability analysis has been described in [42]. Fig. 4.25 shows the eigenvalue plot for a large-scale MT-HVDC system. The eigenvalues are obtained by numerical simulation. Since there is no eigenvalue in the RHP, the system is predicted to be stable. As can be seen, the system has several eigenvalues in critical locations, and the system could exhibit sustained harmonic oscillation even when the system is predicted to be stable by the eigenvalue analysis. In this case, it not possible to identify precisely which critical eigenvalue will introduce sustained harmonic oscillations.

The impedance-based analysis has been carried for the tuning of the case of sustained harmonic

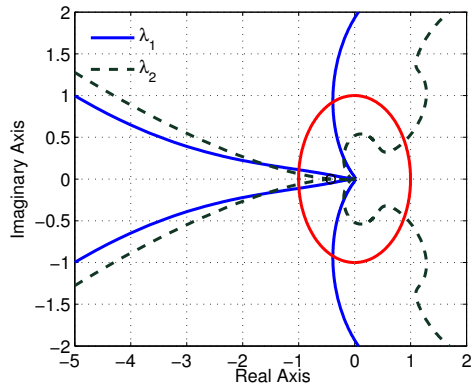


**Figure 4.26:** Characteristics Loci of minor-loop gain for $k_{pp} = 0.0155$ (Red-line is the unit circle).

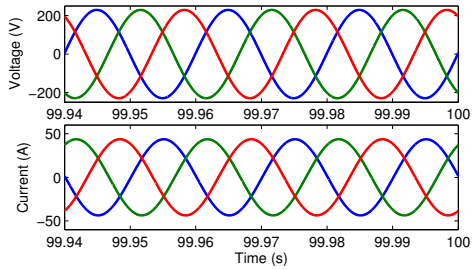


**Figure 4.27:** Simulation with average model of VSC: Voltages and currents of power-controlled converter for low phase margin in the Nyquist plot do not exhibit sustained oscillations.

oscillation. The characteristics loci of the minor-loop gain are shown in Fig. 4.26. Since characteristics loci of the minor-loop gain do not encircle the points (-1, j0), however they intersect the unit circle at a frequency around 780 Hz with a very low phase margin around $3.4^0$. The designed practice is that the phase-margin should be greater than $35^0$, however, there is no such rule for eigenvalue-based analysis. Thus, a low phase-margin in the characteristics loci plots indicate that the system can have sustained harmonic oscillation in power electronics-based power system while the eigenvalue method does not predict this oscillation caused by PWM switching since there is not eigenvalue in the RHP. To provide a confirmation of this, a simulation with an average model of the VSCs has been carried out resulting in the time domain responses are shown in Fig. 4.27. The system is free of sustained oscillations and is stable as predicted from the eigenvalue plot. The voltages and currents form the average model simulation are purely sinusoidal and do not contain any sustained oscillations.

Although both methods are based on the small-signal stability analysis, the modeling is not the same. The eigenvalue method does not include the model of the PWM while the impedance based analysis takes into account the real system since it is based on the measurement and the real system is a converter with implemented PWM for the modulation. It is also worth noticing that the impedance based analysis is a measurement based method and as such it will capture

all the small signal features of the real system. The analytical model of the impedance based analysis includes the PWM modeling and it verifies and validates the measurement-based impedance model. During the PWM switching in power electronics converter, the system states oscillate between two points on the loci. It is a kind of constantly switching between stable region to unstable region and vice-versa. Therefore, in order to ensure the overall system stability, this work recommends to study both the eigenvalue based analysis for global stability and the impedance-based analysis at local ac-dc interfacing point to avoid sustained harmonic oscillation in a power electronics based power system.

## 4.4 Conclusion

In this chapter, the small-signal stability assessment of power electronics based power systems has been investigated in the frequency domain by the impedance-based and eigenvalue analysis methods. Impacts of the converter controller's gains and the grid strength on the stability have been investigated analytically and the analytical results are further validated by simulation and experiments. Example cases have been presented how to restore the stability of VSC-based HVDC system by reshaping the impedance by re-tuning the converter controller. Based on the analysis, some observations are:

- The eigenvalue-based method can determine the stability of the entire system globally for an operating point. Two main drawbacks noticed when analyzing the stability and interaction phenomena based on eigenvalue analysis. The first drawback is that it requires detailed modeling of the entire system for state-space modeling. Secondly, the VSC systems are modeled based on the average modeling of the converters, which neglects the PWM, and processing delays resulting in that it cannot identify sustained harmonic oscillations in the VSC-based HVDC system. To address the limitation in the eigenvalue-based analysis, it is required to discretize the system, which will require much computational effort and is not feasible for VSC-based HVDC system.

- The impedance-based method is a measurement-based method and is an alternative to assess the stability of VSC-based HVDC system directly from field measurements. A weakness of the impedance method is the limited observability of certain states given its dependence on the definition of local source-load subsystems, which makes it necessary to investigate the stability at different subsystems interfaces. To address this limitation in the impedance-based method, this work discusses critical locations where the application of the method can reveal the impact of a passive component or a controller gain on the stability.

# Part II

# HVDC Connected Wind Farms

# Chapter 5

# Impedance-based Stability Analysis of Offshore Wind Farms and HVDC System

*This chapter presents a preliminary exploration of the possible origins of the sub-synchronous oscillation (SSO) and resonances observed in the interconnected system of wind farms and a VSC-based HVDC system. Moreover, this chapter proposes a method that enables to identify critical controllers' parameters (e.g. critical controller's bandwidth) in an interconnected system from a non-parametric impedance model obtained by measurements. The method suggested can reveal the internal controllers' dynamics of the wind farm from the non-parametric impedance frequency responses combined with a general analytical expression of the impedance and an identified identical transfer function when no information about the controllers is provided by the vendors due to the confidentiality and industry secrecy.*

This chapter is based on the following articles.

[1] **M. Amin**, M. Molinas and J. Lyu, "Oscillatory Phenomena between Wind Farms and HVDC Systems: The Impact of Control," in *2015 IEEE 16th Workshop on Control and Modeling for Power Electronics (COMPEL)*, Vancouver, BC, 2015, pp. 1-8.

[2] **M. Amin** and M. Molinas, "Understanding the Origin of Oscillatory Phenomena Observed Between Wind Farms and HVdc Systems," in *IEEE Journal of Emerging and Selected Topics in Power Electronics*, vol. 5, no. 1, pp. 378-392, March 2017.

[3] **M. Amin** and M. Molinas, "A Grey-box Method for Controller Parameter Estimation in HVDC-connected Wind Farms based on Non-parametric Impedance", *IEEE Transaction on Industrial Electronics*, 2017 (In Review)

## 5.1 Introduction

The stability of the offshore wind power network connected through a HVDC transmission line is a critical problem since there is no direct connection at AC collection (ACC) bus to a strong AC grid. Field experience has shown that SSO and harmonic resonance can occur between wind farms and HVDC systems [28], [32], [49]. The oscillations can appear in the presence

of background harmonics and is arguably resulting from the controller interaction of the wind energy conversion system (WECS) converter controller and HVDC converter controller [49], [55]. The root cause of these oscillations observed in the field are not entirely understood and they can be attributed to various sources within the components and controllers of the interconnected system. In this study, a full-scale type-four WECS is investigated which is connected to the main AC grid through a VSC-based HVDC system. The system is shown in Fig. 5.1. It has two wind farms which are connected to the ACC bus through an offshore sea cable. The power is transferred to the grid through an HVDC transmission system. There is no rotating machine connected to the ACC bus directly. The operation of the interconnected system is found to be poor without the closed-loop AC voltage controller at the ACC bus side HVDC converter. The system performance is improved when a close-loop AC voltage controller is used; however, an oscillatory phenomenon is observed when the closed loop AC voltage control is introduced due to the interaction of the controller and the impact of the impedance on the system dynamics. In order to understand this phenomenon, the impedance of both the wind farms and the HVDC system from the offshore AC collection point are analytically derived and the impedance-based stability criterion is adopted to analyze the stability of the interconnected system. The frequency domain impedance characteristics both for the wind farm and the HVDC rectifier from the offshore ACC point are presented to identify potential resonance points. The Nyquist plots of the impedance ratio of the HVDC converter to the wind farm indicate the potential resonances at low frequency. An active damping scheme is implemented in the current controller of the offshore HVDC rectifier in an attempt to improve the oscillatory phenomena. An analysis and time domain simulation results with its respective spectral analysis show that the implemented active damping is very effective in eliminating the oscillations observed in the interconnected system. The proposed active damping scheme can significantly reduce the magnitude of the source (HVDC system) impedance at low frequencies which improve the stability of the interconnected system.

A discussion of the role of the ratio between the bandwidths of the controllers of the interconnected areas is introduced, and an essential role as the root cause of the instability is proposed to be taken into account in re-shaping of the impedances to maintain the stability. Moreover, this work presents a novel technique to reveal and extract the internal control dynamics (critical controllers bandwidth) of the WECS inverter when the WECS system is assumed to be a 'grey box' by proposing a non-parametric impedance model based on measurements by using a system identification technique [76], [77], [101]–[103]. The method has potential immediate applicability in the wind industry based on the simplicity it offers to black/grey-box types of systems to guarantee the stability of the interconnection.

The rest of the chapter is organized as follows. Section 5.2 presents the modeling and the control of the HVDC system. Section 5.3 presents the modeling and the control of the WECS. Impedance-based stability analysis has been discussed in section 5.4. The SSO mitigation technique is explained in section 5.5. Impedance-based Stability Analysis based on the 'Grey Box' approach is presented in section 5.6. Extraction of WECS inverter controllers' parameters is shown in section 5.7. Impedance-based interaction analysis is discussed in section 5.8. The interconnected system is stabilized by re-tuning the PLL and AC voltage controller bandwidth in section 5.9. Finally, the chapter is concluded in section 5.10.

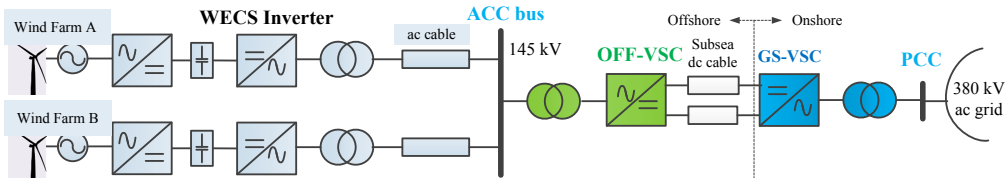


**Figure 5.1:** Overview of investigated system structure: VSC-based HVDC system for integration of offshore wind farm.

## 5.2 HVDC System Modeling and Control

This section presents the modeling and the control of the VSC-based HVDC system with the purpose of integrating offshore wind farms.

### 5.2.1 Investigated HVDC System Configuration

The HVDC system depicted in Fig. 5.1 consists of converter transformers, offshore HVDC rectifier (OFF-VSC), subsea DC cable and grid side onshore HVDC inverter (GS-VSC). The VSC-HVDC system has a capacity of 200 MVA equivalent. The OFF-VSC is connected to the ACC bus through a 145/200 kV, 50 Hz transformer with the same rating as the converter. The GS-VSC is connected to the main AC grid of 380 kV through a 200/380 kV, 50 Hz, 200 MVA transformer. The HVDC-link DC voltage is 400 kV and the length of the DC line is 200 km. The parameters of the HVDC system is given Table 5.1.

### 5.2.2 Control of the VSC-HVDC

The HVDC system converters have different control objectives depending on their location and the system modeling. The point-to-point connection HVDC system used with the purpose of integrating wind farms must have the DC and AC voltage control objectives. The OFF-VSC behaves as a voltage source to the AC terminal and regulates the offshore AC voltage and the frequency. It supplies a sinusoidal voltage to the ACC bus. The GS-VSC regulates the HVDC-link DC voltage and the reactive power. In this work, the focus is to study the interaction between the WECS inverter (WECS-I) and the OFF-VSC HVDC converter, therefore the details of modeling, control and impedance model will be presented only for the OFF-VSC HVDC assuming that the DC voltage controller of the GS-VSC is providing a constant DC voltage input to the OFF-VSC.

The overview of the control structure of OFF-VSC is shown in Fig. 5.2. An outer-loop PI-controller is used to obtain the d- and the q-axis current reference of the OFF-VSC. A current-controller in an SRF is assumed to limit the current during abnormal operation. The reference currents to current controller, $i_{Ld,ref}$ and $i_{Lq,ref}$ can be defined by

$$\begin{bmatrix} i_{Ld,ref} \\ i_{Lq,ref} \end{bmatrix} = \overbrace{\begin{bmatrix} H_{vac}(s) & 0 \\ 0 & H_{vac}(s) \end{bmatrix}}^{\mathbf{G_v(s)}} \left( \begin{bmatrix} v_{od,ref} \\ v_{oq,ref} \end{bmatrix} - \begin{bmatrix} v_{od} \\ v_{oq} \end{bmatrix} \right) \tag{5.1}$$

and the PI AC voltage controller transfer function is

$$H_{vac}(s) = k_{pvac} + k_{ivac}/s \tag{5.2}$$

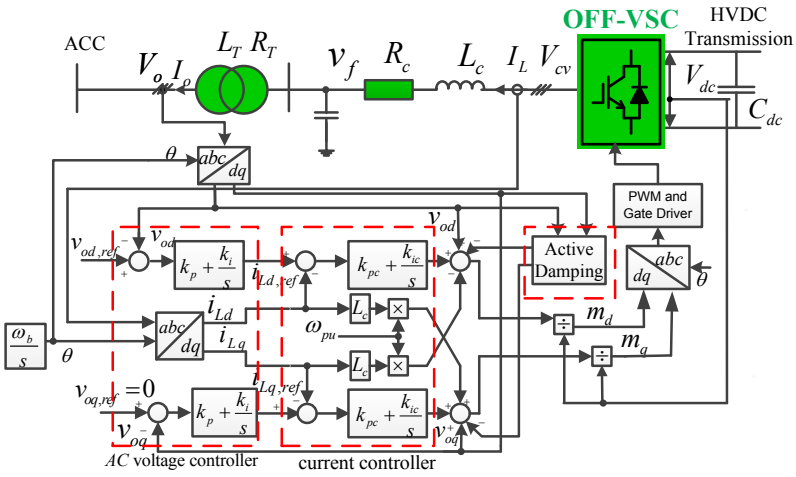


**Figure 5.2:** Overview of control structure of offshore HVDC converter, OFF-VSC.

**Table 5.1:** The VSC-HVDC system parameters

| Parameter | Value | Parameter | Value |
|---|---|---|---|
| Rated Power, $S_b$ | 200 MVA | $L_c$ | 0.08 pu |
| Rated AC voltage | 200 kV | $R_c$ | 0.003 pu |
| Rated frequecy | 50 Hz | $C_f$ | 0.074 pu |
| Trans. inductance | 0.15 pu | $V_{dc}$ | 400 kV |
| Trans. resistance | 0.005 pu | $L_{dc}$ | 2.615 mH/km |
| Grid inductance | 0.0271 pu | $R_{dc}$ | 0.0011 Ω/km |
| Grid resistance | 0.0191 pu | $C_{dc}$ | 4.4 pu |

where, $v_{od,ref}$ and $v_{oq,ref}$ are the reference d-axis and q-axis voltage, respectively; $k_{pvac}$ and $k_{ivac}$ are the proportional and integral gain of the PI AC voltage controller. The inner-loop current-controller depicted in Fig. 5.2 is assumed to be the widely used SRF PI-controller of the VSC with decoupling term. The modulation index references obtained from the current controllers, including the feed-forward terms can be given by

$$\begin{bmatrix} m_{d.ref} \\ m_{q,ref} \end{bmatrix} = \mathbf{G_{cc}}(s) \begin{bmatrix} i_{Ld,ref} \\ i_{Lq,ref} \end{bmatrix} - (\mathbf{G_{cc}}(s) + \mathbf{Z_{del}}) \begin{bmatrix} i_{Ld} \\ i_{Lq} \end{bmatrix} + \begin{bmatrix} v_{od} \\ v_{oq} \end{bmatrix}. \tag{5.3}$$

The current-controller is tuned based on the symmetrical optimum criteria [94] and is found to be $H_{cc}(s) = 0.6366 + 7.5/s$ in pu and the control-loop bandwidth is 400 Hz with 90 degrees phase margin. The AC voltage controller proportional gain is kept 0.5 in pu with a time constant of 12.5 ms for the integral term and the control loop crossover frequency is 185 Hz with 60-degree phase margin.

## 5.3 Wind Energy Conversion System Modeling and Control

This section presents the modeling and the control of the wind energy conversion system.

### 5.3.1 Wind Farm System Configuration

The investigated system shown in Fig. 5.1 has two wind farms which are connected to the AC collection point through a 25/145 kV transformer and a 10 km long undersea cable. The wind turbine generators (WTGs) are assumed to be a full-scale type-four WECS as depicted in Fig. 5.3. Each wind farm is assumed to have 28 turbines with 2 MW rating each. To simplify the system model, 28 turbines are lumped into one unit of 56 MW generation capacity.

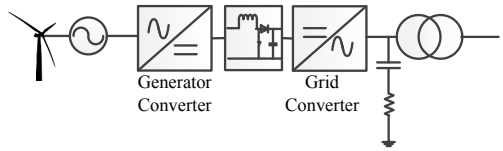


**Figure 5.3:** Investigated wind turbine generator including full-scale converter and filter

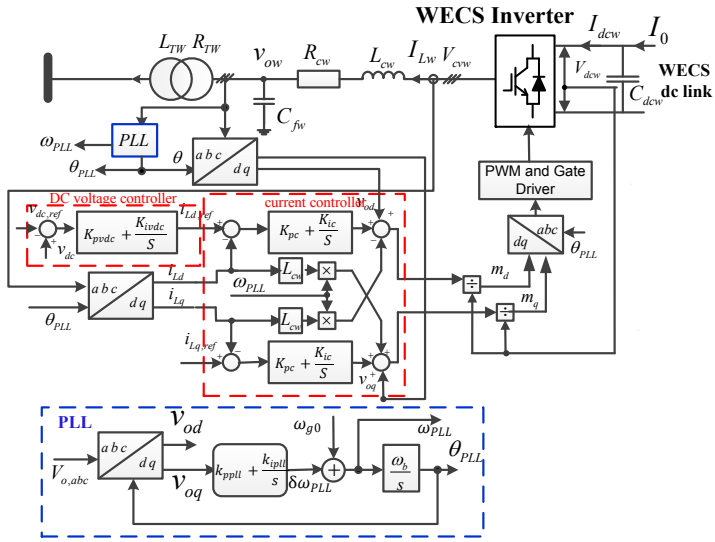


**Figure 5.4:** Overview of the control structure of WECS Inverter.

### 5.3.2 Control of the WECS

A full-scale converter system is utilized to transfer the energy produced by the WECS. In generator side, a full bridge diode rectifier is used which simplifies the converter control interaction. It transfers the energy produced by the wind generator to the DC side. A two level VSC converter is used in grid side. In between these two AC-DC converters, a DC-DC converter is used. The overall control structure of the WECS-I is shown in Fig. 5.4. The controls implemented in the WECS are in the following.

- The WECS-I regulates the WECS DC-link voltage and the reactive power.

- The WECS generator side converter is a simple full bridge diode rectifier [104]. The speed of the generator is controlled by means of controlling the DC link current of the WECS. A DC-DC converter is used to regulate the DC link current of the WECS which inner control loop is the DC-link current controller and the outer control-loop is a generator speed controller of the WTG.

The inner-loop current controller is assumed to be the widely used SRF PI controller of the VSC with decoupling term. An outer-loop PI-controller is used to regulate the DC-link voltage of the WECS. The parameters of the WECS-I is given in Table 5.2.

A PLL is used to track the frequency [86]. A second order PLL is assumed as shown in Fig. 5.4. The integral part of the PLL is used to remove the quasi-steady-state phase error and it appears when synchronous frequency deviates from its nominal value. In steady-state, the q-axis component of the ACC voltage is zero, hence the proportional term of the PI PLL is sufficient to keep $\delta\omega_{PLL}$ to zero. The bandwidth of the PLL-loop must be sufficiently small to reject the harmonic resonance [90]. By a rule, it should be 10 times less than the inner current control-loop bandwidth, $\alpha_{cc} = k_{pc}/L_c$ [105].

**Table 5.2:** Parameter of ACC side WECS VSC

| Parameter | Value | Parameter | Value |
|---|---|---|---|
| Rated Power, $S_b$ | 56 MW | $L_{cw}$ | 0.15 pu |
| Rated AC voltage | 575 V | $R_{cw}$ | 0.15/50 pu |
| Rated DC voltage | 1100 V | $C_{fw}$ | 0.0344 pu |
| Trans. inductance | 0.04 pu | f | 50 Hz |
| Trans. resistance | 0.005 pu | $C_{dcw}$ | 6.16 pu |
| $L_{cable}$ | 0.2526 mH/km | $R_{cable}$ | 0.0843 Ω/km |
| $C_{cable}$ | 0.1837 $\mu$F/km | Cable length | 10 km |

## 5.4 Impedance-based Stability Analysis and Time Domain Simulation

This section presents the impedance-basted stability analysis of wind farms connected via HVDC system. The frequency domain analysis has been further verified by time domain simulations.

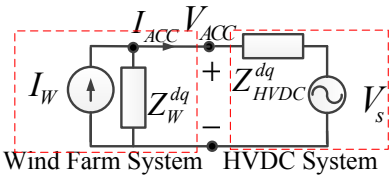


**Figure 5.5:** Impedance based equivalent model of offshore AC grid system

### 5.4.1 Impedance Model of the Interconnected System of Wind Farm and HVDC

For stability analysis, the equivalent small-signal impedance model of the interconnected system is shown in Fig. 5.5 where the HVDC subsystem from the ACC point is modeled by its Thevenin equivalent consisting of a voltage source, $\mathbf{V_s}$ with a series equivalent impedance, $\mathbf{Z^{dq}_{HVDC,ACC}}$ and the wind farm subsystem is modeled by its Norton equivalent circuit consisting of an ideal current source, $\mathbf{I_w}$ in parallel with an equivalent impedance, $\mathbf{Z^{dq}_{W,ACC}}$. The impedances are in the dq-frame and a 2x2 matrix.

### 5.4.2 Impedance of the HVDC System from AC Collection Bus

The HVDC system impedance, $\mathbf{Z^{dq}_{HVDC,ACC}}$ in (5.4) is found together with the parallel connection of the HVDC inverter output filter impedance and series connection of transformer impedance as

$$\mathbf{Z^{dq}_{HVDC,ACC}}(s) = \mathbf{Z_{T,dq}}(s) + \left(\mathbf{Z^{-1}_{dq,OFF-VSC}}(s) + \mathbf{Z^{-1}_{Cf,dq}}(s)\right)^{-1}. \tag{5.4}$$

where $\mathbf{Z_{T,dq}}(s)$ is the impedance of the HVDC VSC transformer, $\mathbf{Z_{Cf,dq}}(s)$ is the impedance of the capacitive filter and $\mathbf{Z_{dq,OFF-VSC}}(s)$ is the impedance of the OFF-VSC. In order to calculate the total impedance from the ACC point, all impedances are converted to dq-domain using the same system transformation angle.

The analytical impedance model of the OFF-VSC is derived as follows. The dynamic equations of the OFF-VSC in per unit (pu) can be given by [82], [83]

$$\begin{bmatrix} v_{od} \\ v_{oq} \end{bmatrix} = \begin{bmatrix} m_d \\ m_q \end{bmatrix} V_{dc} - \overbrace{\begin{bmatrix} R_c + sL_c/\omega_b & -\omega_1 L_c \\ \omega_1 L_c & R_c + sL_c/\omega_b \end{bmatrix}}^{\mathbf{Z_0}(s)} \begin{bmatrix} i_{Ld} \\ i_{Lq} \end{bmatrix}. \tag{5.5}$$

In order to obtain the impedance model of the OFF-VSC in the frequency domain, the modulating signal, $\mathbf{m_{dq}}$ is expressed as a function of $\mathbf{i_{Ldq}}$ and $\mathbf{v_{odq}}$ in the frequency domain. Applying linearization on (5.1) and (5.3) and after rearranging, the modulation index of OFF-VSC is written as

$$\begin{bmatrix} \tilde{m}_{d.ref} \\ \tilde{m}_{q,ref} \end{bmatrix} = \left(\mathbf{I} - \mathbf{G_{cc}}(s)\mathbf{G_v}(s)\right) \begin{bmatrix} \tilde{v}_{od} \\ \tilde{v}_{oq} \end{bmatrix} - \left(\mathbf{G_{cc}}(s) + \mathbf{Z_{del}}\right) \begin{bmatrix} \tilde{i}_{Ld} \\ \tilde{i}_{Lq} \end{bmatrix}. \tag{5.6}$$

Assuming the DC voltage controller performance of GS-VSC is quite satisfactory and providing a constant DC voltage, therefore for simplification of analysis, it is reasonable to assume a constant DC voltage input to the OFF-VSC. By doing this, we are ruling out any influence of background harmonics coming from the on-shore grid. Now after linearizing (5.5) and inserting (5.6), gives the impedance model of the HVDC rectifier, OFF-VSC in $dq$-frame and can be given by

$$\begin{aligned} \mathbf{Z_{dq,OFF-VSC}}(\mathbf{s}) = &- \left(\mathbf{I} - V_{dc}\mathbf{G_{PWM}}(s)\mathbf{I} + V_{dc}\mathbf{G_{PWM}}(s)\mathbf{G_{cc}}(s)\mathbf{G_v}(s)\right)^{-1} \\ &\left(\mathbf{Z_0}(s) + V_{dc}\mathbf{G_{PWM}}(s)\left(\mathbf{G_{cc}}(s) + \mathbf{Z_{del}}\right)\right). \end{aligned} \tag{5.7}$$

### 5.4.3 The Impedance of the Wind Farms from AC Collection Bus

The impedance of the wind farm from ACC point can be given by

$$\mathbf{Z^{dq}_{W,ACC}}(s) = \frac{1}{n}\left(\mathbf{Z_{cable,dq}}(s) + \mathbf{Z_{T,dq}}(s) + \left(\mathbf{Z^{-1}_{dqw}}(s) + \mathbf{Z^{-1}_{Cf,dq}}(s)\right)^{-1}\right) \tag{5.8}$$

where $\mathbf{Z_{cable,dq}}(s)$ is the impedance of the offshore AC cable, $\mathbf{Z_{T,dq}}(s)$ is the impedance of the WECS-I transformer, $\mathbf{Z_{Cf,dq}}(s)$ is the impedance of the capacitive filter, $n$ is the number of wind farms connected in parallel. The wind farms are identical in structure and control, and two wind farms are connected to the ACC bus, hence $n = 2$. The impedances are in dq-frame and a 2x2 matrix. All the impedances are transformed to dq-frame with the system frequency transformation angle. The WECS-I regulates the DC-link voltage. The impedance model of the DC voltage control VSC is derived in chapter 3 and can be given in frequency domain as

$$\begin{aligned}\mathbf{Z_{dqw}}(s) =& \left(\mathbf{I} - V_{dc}\mathbf{G_A^{-1}}(s)\mathbf{G_C^{Vdc}}(s) + \mathbf{G_D}\mathbf{G_{vd}}\mathbf{G_A^{-1}}(s)\mathbf{G_C^{vdc}}(s)\right)^{-1} \\ & \left(-\mathbf{Z_0}(s) + V_{dc}\mathbf{G_A^{-1}}(s)\mathbf{G_B}(s) - \mathbf{G_D}\mathbf{G_{vi}} - \mathbf{G_D}\mathbf{G_{vd}}\mathbf{G_A^{-1}}(s)\mathbf{G_B}(s)\right). \end{aligned} \tag{5.9}$$

If the output power of the wind farms differs from each other, it is necessary to calculate the impedance of the wind farm separately for individual operating point and the total impedance of the wind farms can be calculated based on the impedance calculation rule.

### 5.4.4 Impedance-Based Stability Analysis

Based on this representation in Fig. 5.5, the response of the ACC bus voltage can be written as

$$\mathbf{V_{ACC,dq}} = \left(\mathbf{V_{s,dq}} + \mathbf{Z^{dq}_{HVDC,ACC}}(s)\mathbf{I_{W,dq}}\right)\left(\mathbf{I} + \left(\mathbf{Z^{dq}_{HVDC,ACC}}(s)\right)\left(\mathbf{Z^{dq}_{W,ACC}}(s)\right)^{-1}\right)^{-1}. \tag{5.10}$$

For system stability studies, it is assumed that

1. The AC voltage of OFF-VSC is always stable when unloaded; and
2. The WECS current is stable when it is connected to a stable source.

Therefore, the stability of the interconnected system depends on the second term of right-hand side of (5.10) and the ACC bus voltage will be stable if and only if the impedance ratio, $(\mathbf{Z^{dq}_{HVDC,ACC}}(s))/(\mathbf{Z^{dq}_{W,ACC}}(s))$ which can be defined as the minor loop gain of feedback control system as

$$\mathbf{G}(s)\mathbf{H}(s) = \left(\mathbf{Z^{dq}_{HVDC,ACC}}(s)\right)\left(\mathbf{Z^{dq}_{W,ACC}}(s)\right)^{-1} \tag{5.11}$$

meets the Generalized Nyquist Stability Criterion (GNC) [45], [46].

The impedance ratio in dq-domain is a 2x2 matrix, hence multi-variable Nyquist stability criteria need to be applied to determine the stability of the interconnected system. The off-diagonal elements have an important role on the stability [56], [57]; however, their impact can be neglected in some cases, for example, in the case when the converter operates in unity power factor mode [52], [54], or when the matrix of the minor loop gain is diagonally dominant [106]. The diagonal elements of the HVDC rectifier impedance are 10 times higher than the off-diagonal elements, and are diagonal dominant. The reactive power reference of the wind power inverter is zero, which means, the wind power inverter is operating in unity power factor mode. Moreover, diagonal elements of the wind farm impedance seen from the AC collection bus are 10 dB higher than the off-diagonal elements and are diagonally dominant. Since the matrix is diagonally dominant over the entire Nyquist path, the stability of the interconnected system can be determined by the d-axis and q-axis impedance ratios and the off-diagonal elements can be ignored.

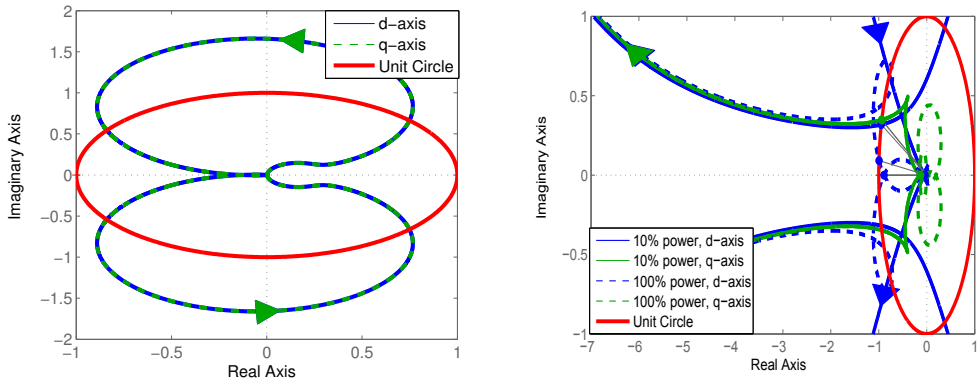


**Figure 5.6:** Nyquist plot of minor-loop gain: (a) the HVDC system connected with a CPL and (b) the wind farms connected with an ideal grid.

### 5.4.5 Stability of the HVDC System with No-Load and CPL

The first assumption is trivial and minimum requirements for an HVDC transmission system installed in the purpose of integrating wind farms [49] and it has been verified for two cases, case 1: with no load condition and case 2: by connecting a CPL. The power of the CPL is equivalent to the power of the wind farms. Note that the wind farms have been disconnected. The stability analysis has been performed by checking the Nyquist plot of the impedance ratio where the CPL load is simulated as $\mathbf{Z}^{\mathbf{dq}}_{\mathbf{W,ACC}}(s)$ and the Nyquist plot is shown in Fig. 5.6 (a). Since the Nyquist plots do not encircle the point (-1, j0) and there is no pole in the RHP, the HVDC system operates stably which is further confirmed in a time domain simulation. There is no oscillation in both the AC side and the DC side of the HVDC rectifier. The input DC voltage of the HVDC rectifier is constant; therefore, for simplification of analytical analysis, it is reasonable to replace the onshore DC voltage controlled HVDC VSC by a DC voltage source and the onshore GS-VSC controllers do not affect the analysis. However, if the HVDC system is unstable (for example oscillatory behaviour in the DC link voltage) before connecting to the wind farms, then it will be a stability problem of the HVDC system itself and it will not be an interaction phenomenon of the controllers of the WECS-I and the OFF-VSC.

### 5.4.6 Stability of the Wind Farm with an Ideal Grid

The wind turbine model has a drive train based on a 2-masse model, a pitch control and a speed regulator which can introduce oscillation if they are not properly designed. Hence, the second assumption must be verified. In this paper, this assumption is verified by frequency domain analysis and also by the numerical simulation. To identify if there is any oscillation coming from the wind power inverters, the wind farms have been connected to an ideal grid instead of the HVDC system. Fig. 5.6 (b) shows the Nyquist plot of the minor-loop gain for 10% and 100% wind power output where the HVDC system impedance is simulated by an ideal grid. The phase margin of the Nyquist plot of the d-axis impedance ratio is becoming smaller

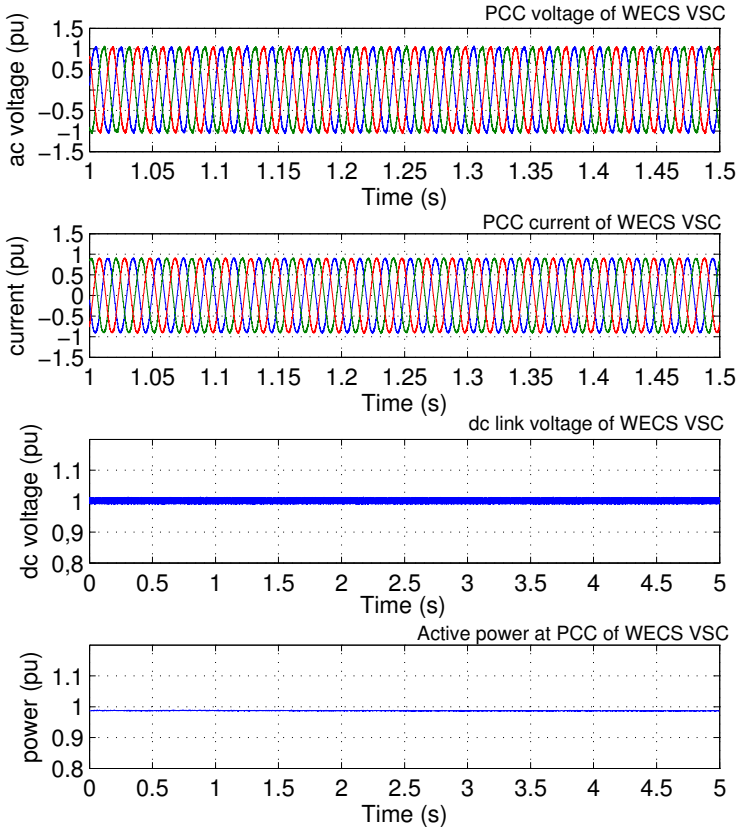


**Figure 5.7:** The PCC voltages and currents of the WECS, the DC link voltage of WECS and the PCC active power of WECS when it is connected to an ideal AC grid

for the high wind power output meaning that the stability margin is reduced, while the q-axis impedance remains the same, since the q-axis impedance does not depend on the active power [50]. Moreover, if the grid strength is reduced by increasing the grid impedance, the phase margin of the Nyquist plot becomes smaller which decreases the stability margin of the system. The high output power causes high output current which increases the losses and reactive power consumption in the system and can provoke the instability.

Fig. 5.7 shows the PCC voltages and currents of the WECS VSC, the WECS DC-link voltage and the active power at PCC of the WECS inverter. The wind farm system operates stably and there is no oscillation either in the AC side or in the DC-link of the WECS which has confirmed that there is no intrinsic oscillation coming from the wind farms. As can be seen in Fig. 5.7, the wind power output is constant; therefore, the turbine mechanical control system including the generator and the diode rectifier and the DC-DC converter can be replaced by a constant power

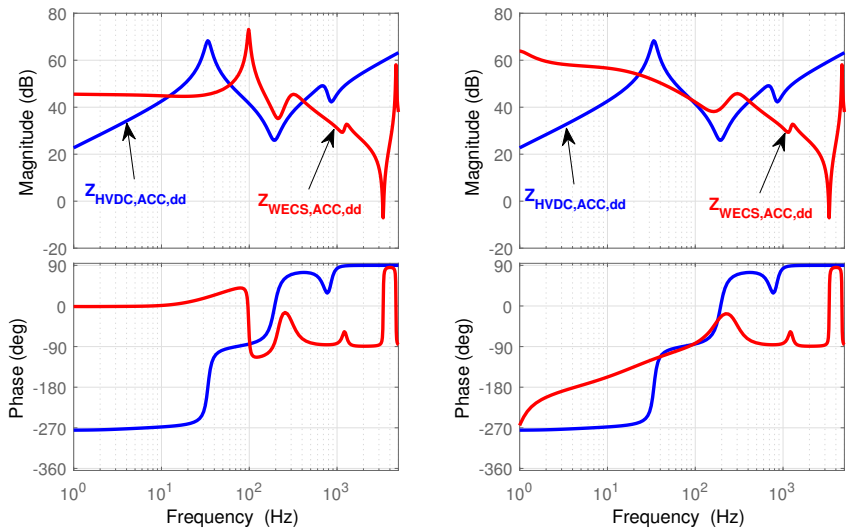


**Figure 5.8:** The d-axis and q-axis impedance of the HVDC system and the wind farms seen from ACC bus. (Left-side figure is the d-axis impedance and the right-side Fig. is the q-axis impedance.)

source in the analytical formulations; hence these assumptions on the generator side converter and the DC-DC converter do not affect the results of the analysis. However, if the wind farms become unstable in an ideal grid connected mode, then the cause of the oscillation will not be an interaction problem of the wind farm inverter and the HVDC rectifier. It will be a stability problem of the wind farm itself.

### 5.4.7 Stability of the HVDC System with Wind Farm

Since both the HVDC system and the wind farms are operating stably separately, the wind farms have now been connected to the HVDC system. Fig. 5.8 shows the diagonal elements of the impedance of the HVDC system and the wind farms seen from the ACC bus. As can be seen, both diagonal elements of the HVDC system impedance, $Z_{HVDC,ACC,dd}$ and $Z_{HVDC,ACC,qq}$ are equal in magnitude and phase, since the OFF-VSC does not have any PLL. The first resonance point in the HVDC rectifier impedance is resulting from the integral term of the PI inner-loop current control and the outer loop AC voltage controller and the second resonance is because of the $LCL$-filter. Similarly, $Z_{W,ACC,dd}$ impedance of the wind farms has a low frequency resonance point resulting from the cascaded DC voltage and current control; however in the $Z_{W,ACC,qq}$ impedance, there is no outer-loop control, thus there is no resonant point similar to the d-axis impedance at low frequency. The next resonance is from the $LCL$-filter. The wind power impedances have also some other resonances at high frequencies which are caused by the offshore AC cable.

Fig. 5.9 shows the Nyquist plot of the minor-loop gain when the wind farms produce 10% and 100% of rated power and there is no pole in the RHP. As can be seen, the $Z_{qq}$ impedance ratio satisfies the GNC, it doesn't encircle the point (-1, j0), which means that the interconnected

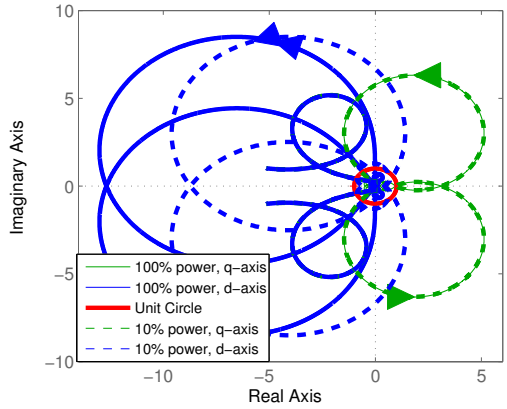


**Figure 5.9:** Nyquist plot of minor-loop gain for 10% and 100% wind power output (Blue-line is for the $d$-axis impedance ratio; green-line is for the $q$-axis impedance ratio and red-line is the unit circle.)

system is stable for the $q$-axis impedance ratio; however, the $Z_{dd}$ impedance ratio encircles the point (-1, j0) regardless of the power level. Therefore, the interconnected system is unstable for the d-axis impedance ratio. As can be seen from the d-axis Nyquist plot as shown in Fig. 5.9, the impedance ratio intersects the unit circle several times. The first intersecting point is at around 14.5 Hz as shown in the d-axis impedance in Fig. 5.8; therefore the system has one of the unstable eigenvalues with 14.5 Hz frequency and will have oscillatory behaviour at around 14.5 Hz which is caused by the resonance point introduced by the cascaded control loop of the HVDC rectifier and the wind power inverter. The q-axis HVDC impedance intersects the wind power inverter impedance several times as shown in Fig. 5.8; however the system is predicted to be stable by the GNC plot for the q-axis impedance as shown in Fig. 5.9. As can be seen in Fig. 5.9, the system is unstable regardless of the power levels and it indicates that the instability phenomena is caused by the controller interaction and not because of the power (energy) flow. There is no change in the Nyquist plot of the q-axis impedance, since q-axis impedance does not depend on the active power flow [50].

At 50 Hz base, the bandwidth of the current control loop of the wind power inverter is assumed to be less than (0.2x2kHz/50=) 8 pu. Applying modulus optimum criteria [94], the current controller is tuned at $H_{cc}(s) = 0.573 + 3.6/s$ in pu and the control loop bandwidth is 200 Hz with 90 degree phase margin. Since the current control loop is modeled as a low pass-filter and the high frequency is removed by the high pass-filter, the frequency around 14.5 Hz predicted in impedance characteristics has a significant impact on system stability. The PLL PI controller transfer function is $H_{PLL}(s) = 0.0844 + 4.6908/s$ in pu and the control loop bandwidth is 9 Hz. The system is unstable predicted by GNC even the bandwidth of the PLL of the wind power inverter is sufficiently low to reject the low frequency.

To validate the small-signal analysis above, a detailed time domain simulation model of the interconnected system as depicted in Fig. 5.1 has been built with detailed switching model of the VSC in the MATLAB/Simulink environment associated with the SimPowerSystem Blockset. Fig. 5.10 (a) shows the resulting 3-phase AC voltages and currents at the ACC bus from the time

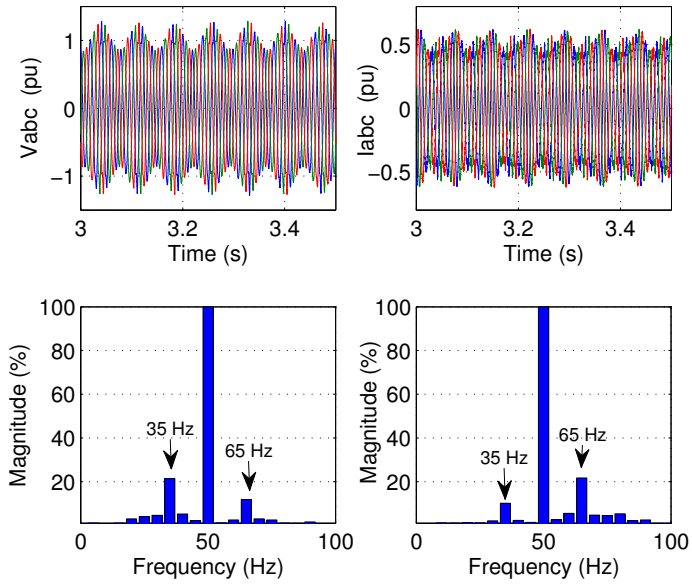


**(a)**

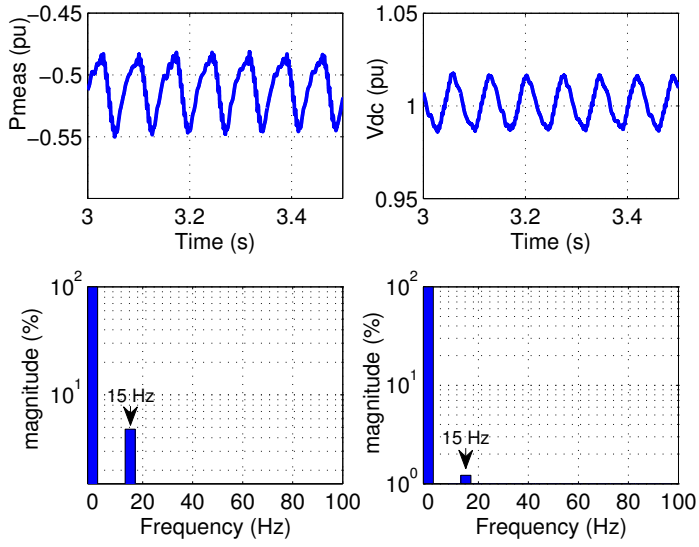


**(b)**

**Figure 5.10:** Offshore side: (a) The 3-phase instantaneous voltage and current at offshore ACC and FFT of them and (b) Active power at offshore ACC of OFF-VSC, DC voltage of HVDC system and FFT of them.

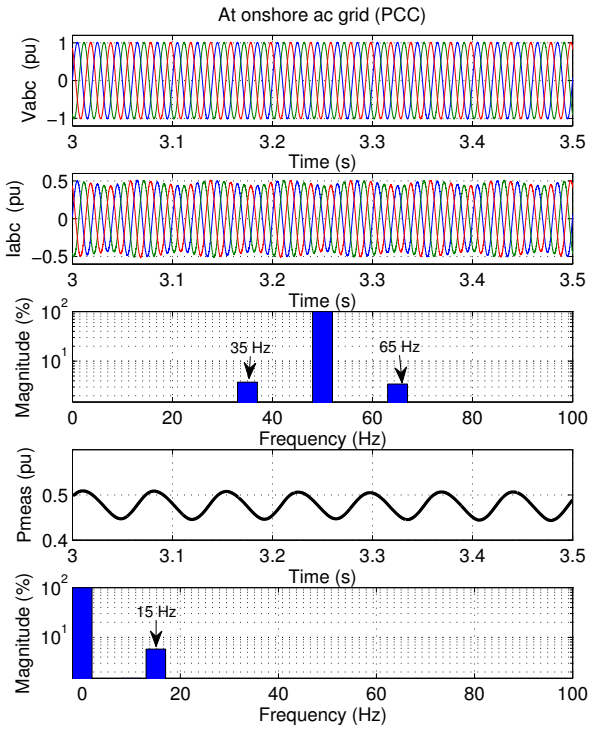


**Figure 5.11:** Onshore side: The 3-phase instantaneous voltage and current at PCC, FFT of current, measured active power and FFT of active power at onshore PCC of VSC-B.

domain simulation. The spectrum from FFT of them is also shown in Fig. 5.10 (a). It can be seen from the FFT, both the voltages and currents at the ACC bus have low frequency oscillation at around 35 Hz and 65 Hz. As predicted from the d-axis Nyquist plot of the impedance ratio, there is a low frequency oscillation at 15 Hz which is transformed into $abc$-frame as $\pm(f - f_1)$ [48]. The active power measured at the offshore ACC bus, the HVDC link DC voltage and FFT of them are shown in Fig. 5.10 (b). Both the active power at the ACC bus and the DC-link voltage of the HVDC system are the DC quantity and have an oscillation at around 15 Hz as predicted from the impedance-based analysis. This oscillation is noticed both for $H_{PLL}(s) = 0.0844 + 4.6908/s$ and $H_{PLL}(s) = 0.0844 + 0.0/s$ and results from the interaction between the HVDC rectifier controller and the wind power inverter controller.

This oscillation is moving towards the main AC grid through the HVDC link. The 3-phase instantaneous voltages and currents, FFT of current, the active power and the FFT of the active power at the onshore PCC of the GS-VSC are shown in Fig. 5.11. No AC voltage oscillation is noticed at the onshore PCC of the GS-VSC since it is connected to a strong AC grid; however, the same frequency of oscillation in the current and the power are identified. This oscillation is propagating from the wind farms and the HVDC system.

**Table 5.3:** The source and the load bandwidth, the bandwidth ratio and the stability from the GNC.

| Case number | Source Bandwidth (HVDC Rectifier) $BW_s$ | Load Bandwidth (WFs inverter) $BW_L$ | Bandwidth Ratio $BW_s/BW_L$ | Generalized Nyquist Stability Criterion |
|---|---|---|---|---|
| 1 | 185 Hz | 200 Hz | 0.925 (<1) | Encircles (-1, j 0) [Fig. 14] |
| 2 | 315 Hz | 200 Hz | 1.575 (>1) | Does not encircle (-1, j 0) [Fig. 17] |
| 3 | 336 Hz | 200 Hz | 1.680 (>1) | Does not encircle (-1, j 0) |
| 4 | 185 Hz | 100 Hz | 1.850 ( >1) | Does not encircle (-1, j 0) |

## 5.5 SSO Mitigation Technique from HVDC Connected Wind Farm

This section presents the mitigation technique of electrical oscillations observed between wind farms and the HVDC system.

### 5.5.1 Reshaping the impedance by Modifying the Control Bandwidth of Converters

The impedance of both the HVDC system and the wind farms can be reshaped by modifying the bandwidth of the controllers. Thus, the impact of the control bandwidth of the HVDC rectifier and the WECS inverter on the stability is discussed below.

#### 5.5.1.1 Impact of the Current Control Loop Bandwidth of the HVDC Rectifier

Fig. 5.12 shows the Nyquist plot of the impedance ratio for a modified bandwidth of the HVDC rectifier controller as an example case where the current controller is tuned at $H_{cc} = 1.2366 + 7.5/s$ in pu and the control loop bandwidth is 773 Hz with 90-degree phase margin while the original bandwidth was 400 Hz. For this current control tuning, the bandwidth of the AC voltage control loop (which is the source) becomes 315 Hz with 65-degree phase margin and

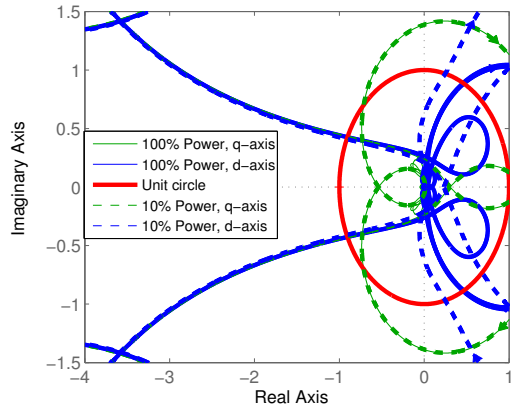


**Figure 5.12:** Nyquist plot of impedance ratio for 315 Hz bandwidth of AC voltage control loop of HVDC rectifier for 10% and 100% wind power output.

the bandwidth ratio of the source to the load (WECS inverter) becomes greater than 1 (case 2 in Table 5.3) while the original bandwidth ratio was less than 1 case 1 in Table 5.3). As can be seen in Fig. 5.12, the Nyquist plots do not encircle the point (-1, j0); hence the system is stable which is further confirmed by numerical simulation.

#### 5.5.1.2 Impact of the AC Voltage Control Loop Bandwidth of the HVDC Rectifier

An example case has been shown for an increased bandwidth of the source (the AC voltage control loop of the HVDC rectifier) while the current control-loop bandwidth remains the same. The source bandwidth is increased by increasing the proportional gain of the AC voltage controller to $H_{vac} = 0.75 + 40/s$. The crossover frequency becomes 336 Hz with 50-degree phase margin and the bandwidth ratio of the source to the load becomes greater than 1 (case 3 in Table 5.3). The interconnected system operates stably which is confirmed by checking the GNC plot and by numerical simulation.

#### 5.5.1.3 Impact of the Current Control Loop Bandwidth of the WECS Inverter

Another example case is shown for a decreased bandwidth of the wind power inverter to 100 Hz with 90-degree phase margin while the source bandwidth remains the same. This is done such a way that it has sufficient phase margin in the Nyquist plot of the minor-loop gain. For this tuning, the bandwidth ratio becomes larger than 1 (case 4 in Table 5.3) and the interconnection becomes stable which is confirmed by the GNC and in the numerical simulation. The WECS inverters are a very low power level compared to the HVDC rectifier, therefore, it is not possible to make the current control-loop bandwidth of the WECS inverter lower than the AC-voltage control-loop of the HVDC rectifier in real world application.

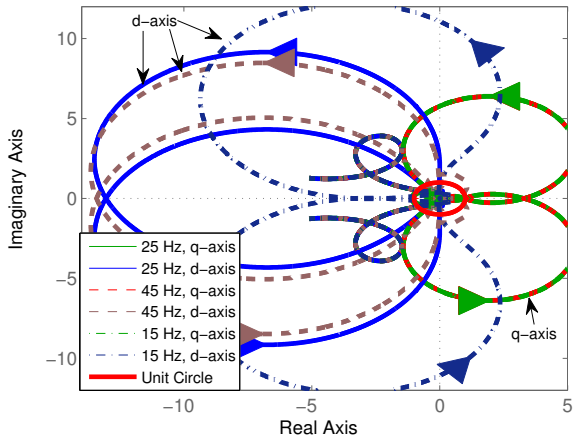


**Figure 5.13:** Nyquist plot of impedance ratio for different bandwidths of the wind power inverter's DC voltage control loop.

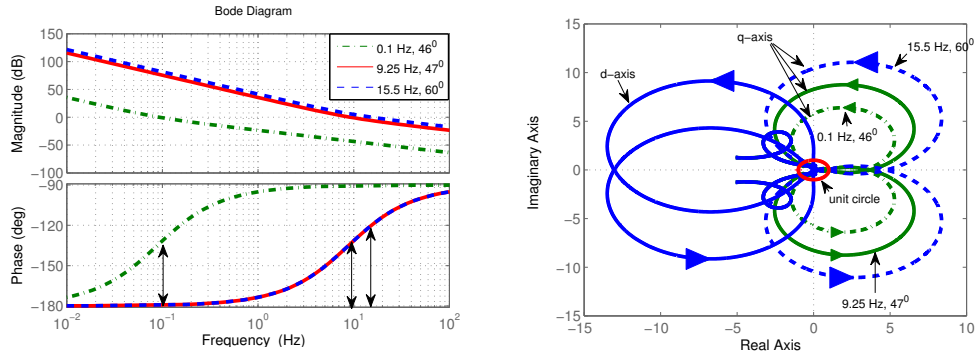


**Figure 5.14:** (a) Wind power inverter's PLL loop gain for different PLL bandwidths and (b) Nyquist plot of impedance ratio for different bandwidth of the PLL for the controller bandwidth of case 1 of the Table 5.3

#### 5.5.1.4 Impact of the DC Voltage Control Loop Bandwidth of the WFs Inverter

Since the oscillation frequency is around 15 Hz, which is similar to the control loop bandwidth of the PLL and DC link voltage control, their participation in the oscillation has been investigated. First, the impact of the DC voltage control loop bandwidth on the stability has been investigated. Initially, the DC voltage controller is tuned with a loop bandwidth of 25 Hz and 160-degree phase margin. Fig. 5.13 shows the Nyquist plots for different bandwidths of the WECS inverter's DC voltage control loop. It has been observed that the higher bandwidth of the DC voltage control loop the more unstable the system becomes, while lower bandwidth makes the system stable but degrades the system performance significantly which is not desirable. The bandwidth of the DC voltage control loop has no impact on the q-axis impedance as shown in Fig. 5.13. The interconnected system remains unstable for different bandwidths of the DC voltage control loop of the WECS inverter; thus the observed oscillation is not directly related to the bandwidth of the DC voltage controller.

#### 5.5.1.5 Impact of the PLL Loop Bandwidth of the WECS Inverter

The interconnected system has now been investigated for different bandwidths of the PLL. The initial bandwidth of the PLL is 9 Hz with 46-degree phase margin for which 15 Hz oscillation has been observed. Fig. 5.14 (a) shows the PLL loop gain and Fig. 5.14 (b) shows the Nyquist plot of the impedance ratio for 0.1 Hz, 9.25 Hz and 15.5 Hz PLL bandwidth for the tuning of case 1 in Table 5.3. As can be seen in Fig. 5.14 (a), the PLL loop gains are stable with sufficient phase margin; however the interconnected system is unstable for the d-axis minor loop gain from Fig. 5.14 (b). The PLL bandwidth has an impact only on the q-axis impedance [50]; therefore the phase margin of the q-axis Nyquist plot is reducing for higher bandwidths of the PLL. On the other hand, the d-axis impedance remains the same for a change of the PLL bandwidth. Thus, the PLL is not participating in the observed oscillation, since the system is predicted to be unstable only for the d-axis Nyquist plot.

Table 5.3 shows the source and the load bandwidth, the bandwidth ratio and the stability from

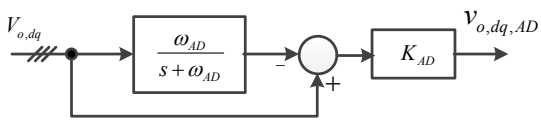


**Figure 5.15:** Implemented active damping scheme

the bandwidth ratio of the interconnected system. From the above test, it is found that the interconnected system operates stably as long as the loop bandwidth ratio of the source to the load becomes larger than 1. The ratio between the bandwidths of the interconnected areas has an essential role in the root cause of instability and is a strong factor to be taken into account in the shaping of the impedances to maintain the stability. The control-loop bandwidth is limited by the switching frequency of the VSC; therefore it is not reasonable to increase the bandwidth of the control-loop, and on the other hand the slower bandwidth decreases the system performance. Alternately, an active damping scheme in the current compensator of the HVDC rectifier can be used to remove the SSO. The detailed modeling and analysis of the proposed active damping scheme are described below.

### 5.5.2 Reshaping the impedance of the HVDC system by Implementing an Active Damping Scheme on the HVDC Rectifier

The phase voltage at ACC bus including the oscillatory components at different frequency in time domain can be written as

$$v_{abc}(t) = V\cos(2\pi f_1 t + \theta) + \sum V_f \cos(2\pi f_f t + \phi_f) \tag{5.12}$$

where $V$ corresponds to the magnitude of the fundamental voltage at frequency $f_1$; $\theta$ is phase angle of 3 phase voltage (0, $2\pi/3$, $4\pi/3$) and $V_f$ corresponds to the magnitude of voltages at different frequency, $f_f$ with phase $\phi_f$. In frequency domain, it can be written by (5.13) where $V_1 = (V/2)e^{\pm j\theta}$ and others follow the similar notation and in the $dq$-domain, it can be represented by (5.14) [48].

$$V_a[f] = \begin{cases} V_1 & f = \pm f_1 \\ \sum V_f & f = \pm f_f \end{cases} \tag{5.13}$$

$$V_{od}[f] = \begin{cases} V\cos(\theta) & DC\ \ Component \\ \sum V_f[f] & f = \pm(f_f - f_1) \end{cases} \tag{5.14a}$$

$$V_{oq}[f] = \sum \mp jV_f[f] \quad f = \pm(f_f - f_1) \tag{5.14b}$$

The active damping is designed to suppress the oscillating term from (5.14). The active damping is, based on injecting a voltage component of counter-phase with detected oscillation in order to produce a cancellation effect, done with the OFF-VSC adding the modulating signal to the reference voltage in (5.3). The oscillation is first isolated by high pass filtering and is then multiplied by a gain $k_{ad}$. The high pass filter function is implemented by subtracting from the measured voltage signals a low pass filtered version of the same voltages as shown in Fig. 5.15. The damping voltage reference is given by (5.15) where $\omega_{AD}$ is the cut-off frequency of

the applied low-pass filter.

$$v_{o,dq,AD} = k_{ad}(-\frac{\omega_{AD}}{s+\omega_{AD}} v_{o,dq} + v_{o,dq}) = \overbrace{\frac{k_{ad}s}{s+\omega_{AD}}}^{\rho_{AD}(s)} v_{o,dq} \tag{5.15}$$

Including the active damping term, the modulation index references of (5.3) from the current controller can be written as

$$\begin{aligned}\begin{bmatrix} m_{d.ref} \\ m_{q,ref} \end{bmatrix} =& \mathbf{G_{PWM}}(s)\mathbf{G_{cc}}(s) \begin{bmatrix} i_{Ld,ref} \\ i_{Lq,ref} \end{bmatrix} - \mathbf{G_{PWM}}(s)(\mathbf{G_{cc}}(s) + \mathbf{Z_{del}}) \begin{bmatrix} i_{Ld} \\ i_{Lq} \end{bmatrix} \\ &+ \mathbf{G_{PWM}}(s)\mathbf{G_{AD}}(s) \begin{bmatrix} v_{od} \\ v_{oq} \end{bmatrix}\end{aligned} \tag{5.16}$$

where

$$\mathbf{G_{AD}}(s) = \begin{bmatrix} 1-\rho_{AD}(s) & 0 \\ 0 & 1-\rho_{AD}(s) \end{bmatrix}.$$

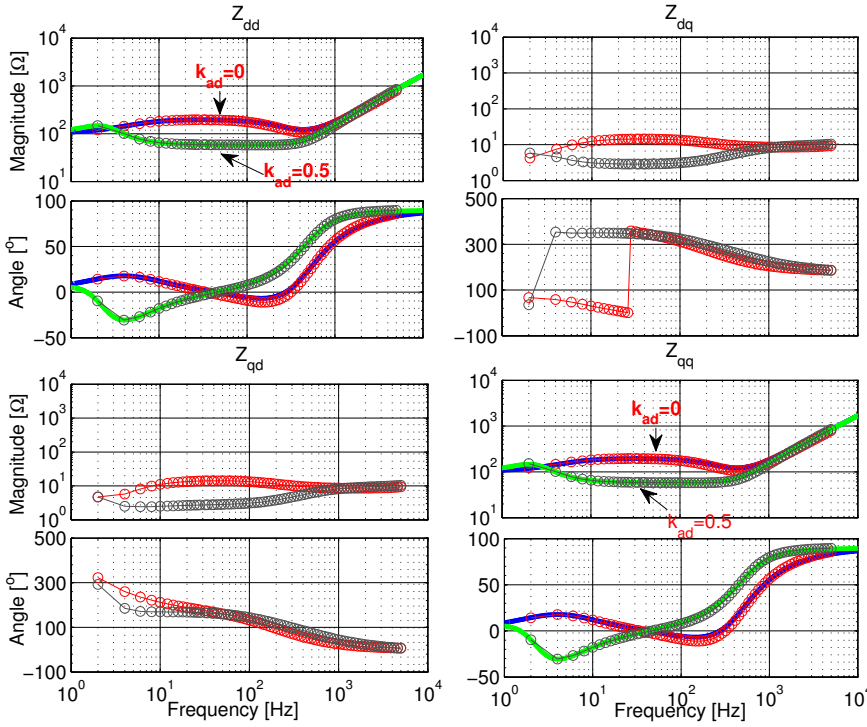


**Figure 5.16:** Comparison of output impedance of HVDC rectifier, OFF-VSC with ($k_{ad} = 0.5$) and without ($k_{ad} = 0.0$) active damping. (Solid line is analytical model and the circles are from numerical simulation)

The impedance-based stability analysis is adopted again to analyze the stability of the system with the proposed damping scheme. The impedance model derived in (5.7) for the HVDC converter OFF-VSC is modified to include the damping term and is given by

$$\begin{aligned}\mathbf{Z}^{\mathbf{dq}}_{\mathbf{OFF-VSC}}(s) = &- \left(\mathbf{I} - V_{dc}\mathbf{G_{PWM}}(s)\mathbf{G_{AD}}(s) + V_{dc}\mathbf{G_{PWM}}(s)\mathbf{G_{cc}}(s)\mathbf{G_v}(s)\right)^{-1} \\ &\left(\mathbf{Z_0}(s) + V_{dc}\mathbf{G_{PWM}}(s)\left(\mathbf{G_{cc}}(s) + \mathbf{Z_{del}}\right)\right). \end{aligned} \tag{5.17}$$

The impedance model derived analytically is verified by numerical simulation and the result is compared with impedance model derived in (5.7) for the case without the damping term. Fig. 5.16 shows the impedance model verification of the HVDC rectifier where $k_{ad} = 0$ means that the active damping term is disabled and $k_{ad} = 0.5$ means that the active damping term is enabled with a damping gain of 0.5. The cut-off frequency of the low-pass filter is set to 3.18 Hz. As can be seen, the proposed active damping can significantly reduce the magnitude of the input impedance of the HVDC rectifier at low frequencies which means that it reduces the source impedance in (5.10) and extends the stability margin by increasing both phase-margin and gain-margin in the GNC of the interconnected system.

Fig. 5.17 shows the diagonal elements of the HVDC system and the wind farm's impedance seen from ACC bus including the active damping term. By comparing the case without damping term as shown in Fig. 5.8, the resonance point at low frequency in the HVDC system can be effectively removed by reshaping the impedance and the HVDC system impedances do not intersect the impedance of the wind famr at any frequency lower than 100 Hz. The remaining resonance point in the HVDC system is resulting from the $LCL$-filter.

Fig. 5.18 shows the Nyquist plot of the minor-loop gain of the interconnected system. As can be seen, neither the $d$-axis nor the $q$-axis input impedance ratio of the HVDC system and the wind

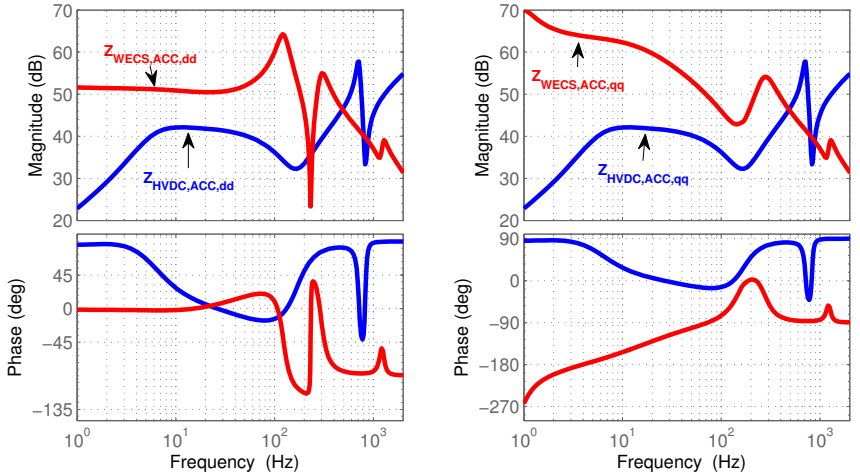


**Figure 5.17:** The d-axis and q-axis impedance of HVDC converter, $Z_{HVDC,ACC,dq}$ and wind power inverter, $Z_{W,ACC,dq}$ seen from ACC bus including active damping term

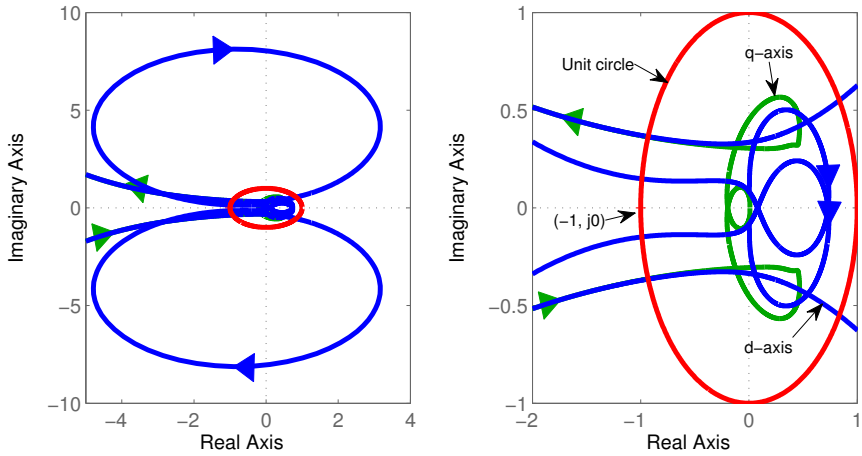


**Figure 5.18:** Nyquist plot of impedance ratio with active damping gain of 0.5 (Left Fig. is full view and right figure is zoom view)

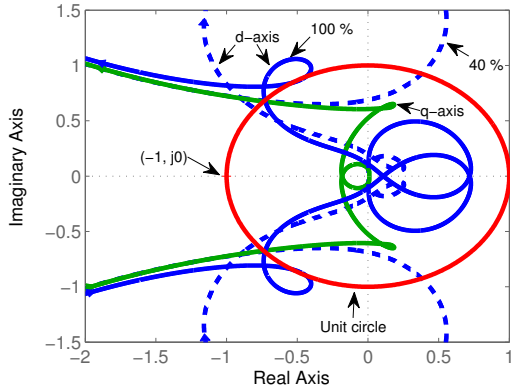


**Figure 5.19:** Nyquist plot of impedance ratio with active damping gain of 0.5 for different wind power loading

farm encircle the point (-1, j0) and there is no pole in the RHP which predicts that the interconnected system will be stable. The stability analysis discussed is performed for an equilibrium point with 100% wind power output. However, it might not be valid for other operating points; therefore, it is necessary to perform the stability analysis for all possible operating points. In this analysis, the stability analysis is performed for various operating points from 10%-100% wind power output power. Fig. 5.19 shows the Nyquist plot of the minor-loop gain for two operating points at 40% and 100% wind power output with the active damping term for a case of comparison and the interconnected system is predicted to be stable for both power levels.

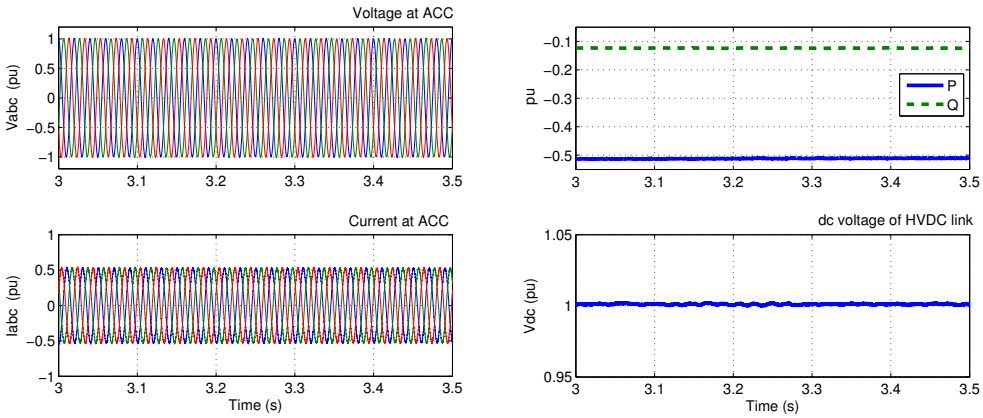


**(a)** **(b)**

**Figure 5.20:** Simulation results with active damping: (a) The 3-phase AC voltage and current at ACC bus and (b) the active and reactive power at ACC of HVDC rectifier, VSC A and DC link voltage of HVDC system.

To verify the theoretical analysis, a detailed simulation model of the interconnected system including the damping scheme in controller of the HVDC rectifier has been built. The control structure including the damping scheme is shown in Fig. 5.2. The cut-off frequency of the low-pass filter of the active damping is kept such that the output of the filter is only the DC component of the offshore ACC voltage. The active damping gain can be kept from 0 to 1. The system is investigated with the active damping for a damping gain of 0.5 and the cut-off frequency of 3.18 Hz. The time domain simulations have been carried out for different operating points and the system is found to be stable for all operating points. The 3-phase instantaneous AC voltages and currents at ACC bus from the time domain simulation are shown in Fig. 5.20 (a) and the active and reactive power at the ACC bus and the DC link voltage of the HVDC system are shown in Fig. 5.20 (b). From the time domain simulation it is clear that the system is stable as predicted by the theoretical analysis.

## 5.6 Impedance-based Stability Analysis based on the 'Black/Grey Box' approach

This section presents the stability analysis of the wind farms connected via HVDC system when the WECS is assumed to be a 'black-box'.

### 5.6.1 System Parameters and Numerical Simulation

The interconnected system under study is depicted in Fig. 5.1. The parameters of the HVDC system and the wind farms are chosen to be different then the system studied in the previous section. The electrical circuit parameters of the HVDC system are given in Table 5.4. The current-controller of the HVDC rectifier is tuned at $H_{cc}(s) = 0.6366 + 14.25/s$ in pu with 90-degrees phase margin at 400 Hz crossover frequency. The AC voltage control-loop is tuned

**Table 5.4:** The VSC-HVDC system parameters

| Parameter | Value | Parameter | Value |
|---|---|---|---|
| Rated Power, $S_b$ | 500 MVA | $L_c$ | 0.08 pu |
| Rated AC voltage | 220 kV | $R_c$ | 0.00285 pu |
| Trans. inductance | 0.1 pu | $C_f$ | 0.074 pu |
| Trans. resistance | 0.01 pu | $V_{dc}$ | 360 kV |

**Table 5.5:** Parameters of the each WECS VSC

| Parameter | Value | Parameter | Value |
|---|---|---|---|
| Rated Power, $S_b$ | 150 MW | $L_{wf}$ | 0.12 pu |
| Rated AC voltage | 575 V | $R_{wf}$ | 0.00285 pu |
| Rated DC voltage | 1100 V | $C_{wf}$ | 0.074 pu |
| Trans. inductance | 0.04 pu | f | 50 Hz |
| Trans. resistance | 0.005 pu | $C_{dc}$ | 4 pu |

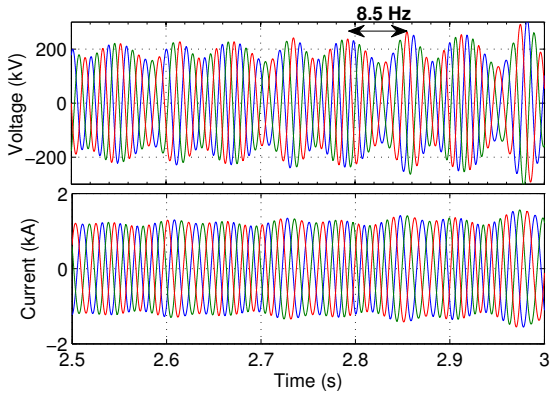


**Figure 5.21:** Unstable: Three phase voltages and currents at ACC bus.

at $H_{vac}(s) = 0.09 + 40/s$ with 40-degree phase margin at 80 Hz crossover frequency. The switching frequency of HVDC VSC is 2 kHz. The AC voltage control-loop bandwidth is around 5 times less than the inner-loop current controller and that satisfies the standard bandwidth ratio [91]. Therefore, the HVDC system is expected to operate stably.

The electrical circuit parameters of WECS are given in Table 5.5. The WECS is assumed a 'black/grey box' and no information about the internal control parameter is available. It is assumed that the control-loops of the WECS have been tuned with sufficient phase margin to ensure the stable operation. A time domain simulation has been carried out and the resulting time domain responses are shown in Fig. 5.21. The system is unstable in the time domain simulation even all the parameters and controller satisfies the standard modeling and tuning. As can be seen in Fig. 5.21, the voltages and currents have an oscillation with a frequency around 8.5 Hz and are increasing exponentially. One can assume that the instability is resulting due to

- the imperfect control tuning and modeling of the HVDC system and wind farms or
- the interaction between the controls of wind farms and HVDC system.

The first assumption can be checked by disconnecting the wind farms from the HVDC system and simulation can be carried out separately by connecting a simple $R-L$ load or a CPL with the HVDC system and an AC grid with the wind farms as discussed in subsections 5.4.5 and 5.4.6. Thus, a CPL with the same rated power of the wind farm has been connected to the HVDC system and a time domain simulation has been carried out. The system is found to be stable from the time domain simulation; therefore, the HVDC system is stable itself for this tuning. Now the wind farm has been connected to a strong AC grid and the time domain simulation confirms that the wind farms operate stably without the HVDC system. Thus, the instability is resulting from the control interaction of the HVDC rectifier and the WECS inverter.

### 5.6.2 Identification of Impedance Model of the WECS Inverter

The following steps are taken to obtain the transfer function of the aggregated non-parametric impedance model of the wind farms. A single WTG has been connected to the main AC grid without the HVDC transmission line and the impedance frequency responses have been measured from 1 Hz to 5 kHz with 75 measurement points in the dq-frame [92], [93], [107]. The measurement set-up is shown in Fig. 5.22. The measurement point has been selected randomly in logarithmic scale. More measurement point will give a better approximation of the impedance model. A system identification technique (SIT) [76], [77], [101]–[103] has been used to estimate the transfer function for each element of the non-parametric dq-domain impedance matrix as

$$Z^{dq}_{WECS-I-SIT}(s) = \frac{b_m s^m + b_{m-1}s^{m-1} + ... + b_o}{a_n s^n + a_{n-1}s^{n-1} + ... + a_o} \tag{5.18}$$

where $b_m$, $b_{m-1}$,...$b_o$, $a_n$, $a_{n-1}$,...$a_o$ are constant coefficients and $m$ and $n$ are the order of the zero and pole of the impedance model. The order of the transfer function will be the same for different control strategies. If we increase the order of the transfer function it will increase the computational complexity and on the other hand, if we reduce the order, the accuracy of the estimated transfer function will be compromised. It is is a trade-off between computational complexity and accuracy of the transfer function estimation. The order of the transfer function does not depend on the control strategy of the WECS inverter. The order of the transfer function is selected (5 in this case) such that the error between the measurement impedance responses

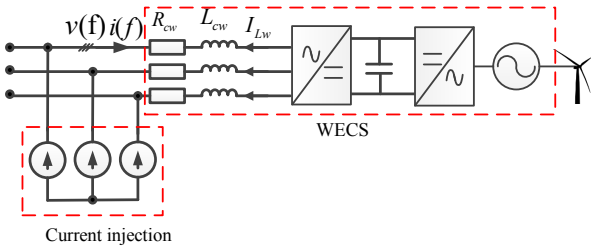


**Figure 5.22:** Impedance measurement set up from the wind turbine generator.

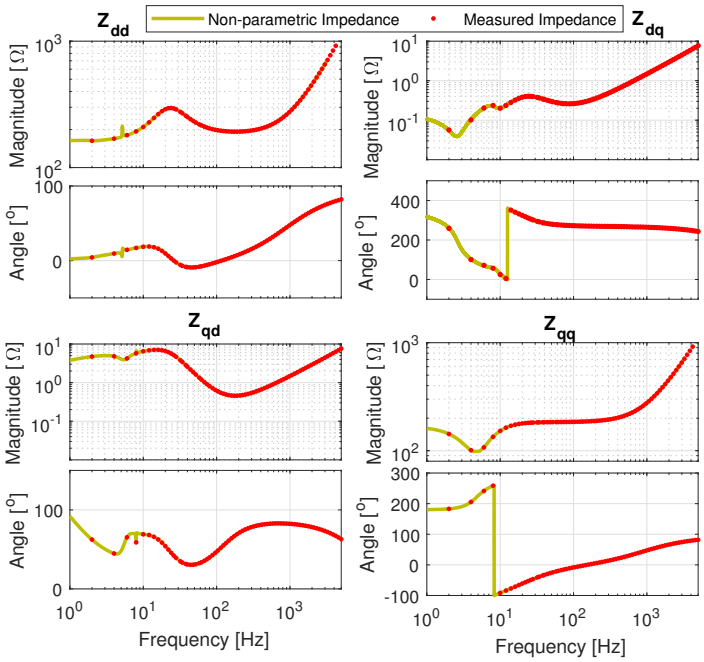


**Figure 5.23:** Impedance frequency responses of the WECS (Solid line is model identification and the dots are from measurement).

and the responses from the non-parametric model becomes less than $0.10\%$ up to the measured frequency range. Fig. 5.23 shows the non-parametric impedance frequency responses from the model identification with the measured impedance by point-by-point simulation. As can be seen, the obtained transfer function of the non-parametric impedance model has a very good agreement with the measured impedance frequency responses both magnitude and phase.

### 5.6.3 Stability Analysis

As discussed, the stability of the interconnected system can be predicted by checking the GNC of (5.11). The $RLC$ parameter of the capacitive filter of the WECS, the WECS transformer and sub-sea cable of the interconnected system are assumed to be known. Hence, the stability of the entire system can be effectively determined based on the impedance-based approach before connecting to the main AC grid since all the parameters are now available for stability analysis. Fig. 5.24 shows the frequency domain stability analysis results for the simulation result presented in the previous section. As can be seen, the $Z_{qq}$ impedance dominated characteristics loci plot encircles the point (-1, j0) at frequency 8.5 Hz, the system becomes unstable.

The proposed stability analysis method based on the aggregated non-parametric impedance model predicts the stability of the interconnected system of the wind farms and the HVDC system even though no information of the WECS control system is known. The impedance-based stability is a small-signal stability analysis and is valid only for a small-range of operating point; however, the wind turbines operate at various wind speeds and provide variable output power,

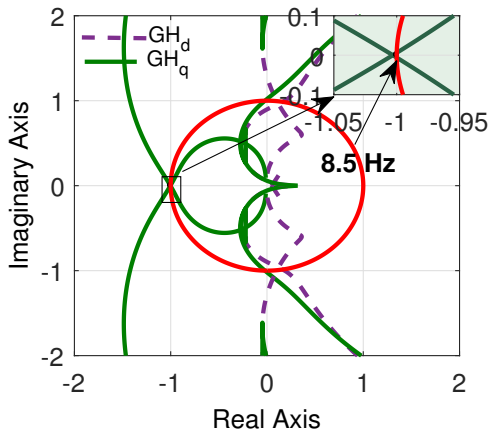


**Figure 5.24:** Characteristics loci of the minor-loop gain (Red-line is the unit circle).

therefore, the stability analysis needs to be carried out at all the operating condition by obtaining a non-parametric impedance model for various operating points and checking the GNC. Though the interconnected system is unstable, it is not clear yet which controller is participating in the observed oscillation.

## 5.7 Extraction of WECS Inverter Controllers' Parameters

This Section presents a method to reveal the internal dynamics of WECS inverter from the non-parametric impedance model while the WTGs are considered to be a grey/black box.

The measured diagonal elements of the WECS inverter impedance can be represented by a transfer function from the SIT as

$$Z^{dd}_{WECS-I-SIT}(s) = \frac{b_{d5}s^5 + b_{d4}s^4 + ... + b_{do}}{a_{d4}s^4 + a_{d3}s^3 + ... + a_{do}} \tag{5.19a}$$

$$Z^{dd}_{WECS-I-SIT}(s) = \frac{b_{q5}s^5 + b_{q4}s^4 + ... + b_{qo}}{a_{q4}s^4 + a_{q3}s^3 + ... + a_{qo}}. \tag{5.19b}$$

The analytical impedance model of the WECS inverter in (5.9) is in dq-frame and a 2x2 matrix. The diagonal elements of (5.9) can be expressed as a function of control-loop transfer function as

$$Z^{dd}_{WECS-I}(s) = \frac{Z_c(s) + \frac{D_d}{sC_{dc}}D_d + \left(V_{DC} - \frac{D_d}{sC_{dc}}I_d\right)\frac{Z_c\psi_n(s)}{\psi_d(s)}}{1 - \left(V_{DC} - \frac{D_d}{sC_{dc}}I_d\right)\frac{H_{PWM}(s)}{\psi_d(s)}} \tag{5.20a}$$

$$Z^{qq}_{WECS-I}(s) = \frac{Z_c(s) + \frac{D_q^2}{sC_{dc}} + G_{cc-ol}(s)Z_c(s)}{1 - V_{DC}H_{PWM}(s) - G_{PLL}(s)\psi_{PLL}(s)} \tag{5.20b}$$

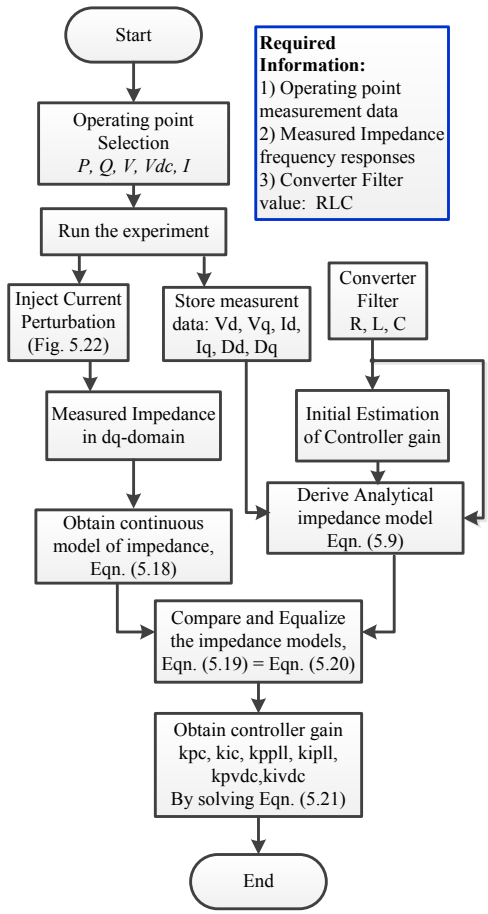


**Figure 5.25:** Illustration of controller gain extraction method from measured impedance.

where

$$
\begin{aligned}
\psi_n(s) &= (D_d G_{vdc-ol}(s)(1 + G_{cc-ol}(s)) + G_{cc-ol}(s)) \\
\psi_d(s) &= 1 + I_d Z_c(s) G_{vdc-ol}(s)(1 + G_{cc-ol}(s)) \\
\psi_{PLL}(s) &= G_{cc-ol}(s) Z_c(s) I_d - V_{DC} H_{PWM}(s) V_d + V_{DC} D_d. \\
G_{cc-ol} &= H_{pwm} \left(k_{pc} + k_{ic}/s\right)/Z_0 \\
G_{cc-cl} &= G_{cc-ol}/(1 + G_{cc-ol}) \\
G_{vdc-ol} &= \left(k_{pvdc} + k_{ivdc}/s\right) G_{cc-cl}/(sC_{dc})
\end{aligned}
$$

and $G_{cc-ol}(s)$ and $G_{vdc-ol}(s)$ are the open-loop transfer function of the current and the DC voltage control-loop, respectively, and $Z_c(s) = R_{cw} + sL_{cw}$.

The analytical impedance model of (5.20) is replaced by the measured impedance model of

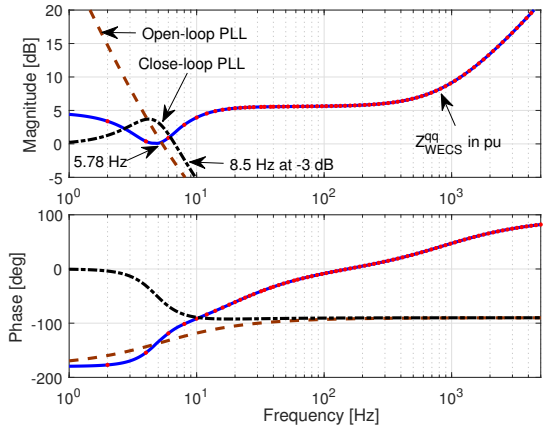


**Figure 5.26:** Control-loop gain of the PLL and the q-axis impedance of the WECS inverter (Solid line is model identification and the dots are from simulation).

(5.19) as

$$Z^{dd}_{WECS-I-SIT}(s) = \frac{Z_c(s) + \frac{D_d}{sC_{dc}}D_d + \left(V_{DC} - \frac{D_d}{sC_{dc}}I_d\right)\frac{Z_c\psi_n(s)}{\psi_d(s)}}{1 - \left(V_{DC} - \frac{D_d}{sC_{dc}}I_d\right)\frac{H_{PWM}(s)}{\psi_d(s)}} \tag{5.21a}$$

$$Z^{qq}_{WECS-I-SIT}(s) = \frac{Z_c(s) + \frac{D_q^2}{sC_{dc}} + G_{cc-ol}(s)Z_c(s)}{1 - V_{DC}H_{PWM}(s) - G_{PLL}(s)\psi_{PLL}(s)}. \tag{5.21b}$$

In (5.21), all the elements are known from the measurement data except the proportional and integral gain of the current controller, DC voltage controller and the PLL. Two equations are obtained with six unknown variables. In order to solve these equations, (5.21) is represented in $j\omega$-domain and the required number of equations can be obtained at different frequencies from the measurement data and by separating them in real and imaginary part. Now solving those equations by iteration, the controller gains are obtained. The controller bandwidth extraction method is presented through a flow chart as shown in Fig. 5.25.

The bandwidth information of the PLL is extracted from the $Z_{qq}$ impedance, since the PLL has the most dominant impact on the $Z_{qq}$ impedance. Fig. 5.26 shows the frequency response of the control-loop gain of the PLL where the PLL open-loop gain has a phase margin 47-degree at 5.78 Hz and the close-loop has a bandwidth around 8.5 Hz. Moreover, Fig. 5.26 shows the $Z_{qq}$ impedance of the wind farm inverter from the SIT and the numerical simulation. As can be seen, the impedance has a resonance at a low frequency around 5 Hz which indicates crossover frequency of the PLL open-loop gain. The bandwidth is calculated at -3dB magnitude, therefore if we move forward 3 dB more, the frequency is found 8.5 Hz which is the close-loop bandwidth of the PLL. This extraction method gives the system designer a view of the control bandwidth range which is useful for the design of the entire system to avoid the control interaction phenomena.

The method is presented for the decoupled d-q control of a WECS VSC as an example of controller bandwidth estimation, however, this procedure can be applied to other type of controllers of the VSC to extract the controller dynamics. In a real world application, we will not know which control method is implemented in the VSC, however, the impedance frequency response would be different based on the implemented control. An example of the impedance frequency responses of the WECS system for two different control strategies has been shown in [81]. One is based on the dq-frame control and the other is the synchronverter control [81], [108]. As can be seen in [81], the impedance frequency responses are different for the different control strategies which enable the method estimating the controller dynamics even when the control strategy is unknown. In order to identify controller dynamics for other type of converter control and to generalize the extraction method, first it is necessary to derive the analytical expression of the impedance model of the VSC for different control methods and then the analytical impedance model and the measured impedance are equalized and the equations are solved to estimate the control dynamics as illustrated in Fig. 5.25.

## 5.8 Impedance-based Interaction Analysis

In order identify which controller is participating in this oscillation, the diagonal elements of the HVDC rectifier and WECS inverter impedance model has been studied since the diagonal elements are dominating along the entire Nyquist path. The diagonal elements of the HVDC rectifier impedance from (5.7) can be written by

$$Z^{dd}_{OFF-VSC}(s) = Z^{qq}_{OFF-VSC}(s) = \frac{V_{dc}H_{PWM}(s)H_{cc}(s) + R_c + sL_c}{1 - H_{PWM}(s) + V_{dc}H_{PWM}(s)H_{cc}(s)H_{vac}(s)}. \tag{5.22}$$

which can be written as a function of current control-loop as

$$Z^{dd}_{OFF-VSC}(s) = Z^{qq}_{OFF-VSC}(s) = \frac{1}{G_{cc-cl,OFF-VSC}(s)H_{vac}(s)} \tag{5.23}$$

where $G_{cc-cl,OFF-VSC}(s)$ is the close-loop transfer function of the current control-loop and can be written as

$$G_{cc-cl,OFF-VSC}(s) = \frac{V_{dc}H_{PWM}(s)H_{cc}(s)/\left(R_c + sL_c\right)}{1 + V_{dc}H_{PWM}H_{cc}/\left(R_c + sL_c\right)}. \tag{5.24}$$

Including the filter capacitor, the diagonal elements of the HVDC system can be given by

$$Z^{dd}_{HVDC,ACC}(s) = Z^{qq}_{HVDC,ACC}(s) = \frac{Z_{dig,OFF-VSC}(s)}{1 + sC_f Z_{dig,OFF-VSC}(s)} \tag{5.25}$$

which can be expressed as a function of AC voltage control-loop as

$$Z^{dd}_{HVDC,ACC}(s) = Z^{qq}_{HVDC,ACC}(s) = \frac{1}{sC_f(G_{vac-ol}(s) + 1)} \tag{5.26}$$

where $G_{vac-ol}(s)$ is the open-loop transfer function of the AC voltage control-loop and can be given by

$$G_{vac-ol}(s) = H_{vac}(s)G_{cc-cl}(s)\frac{1}{sC_f}. \tag{5.27}$$

From (5.26), it is concluded that the HVDC rectifier impedance depends on the open-loop transfer function of the AC voltage controller. The higher control bandwidth of the AC voltage control-loop is meaning the lower impedance magnitude of the HVDC system. Moreover, the $Z_{dd}$ and $Z_{qq}$ impedances are equal in magnitude and do not depend on the operating point.

The diagonal elements of the WECS inverter impedance in (5.20) indicate that the $Z_{dd}$ impedance of the WECS inverter depends on the outer-loop DC voltage controller, inner-loop current controller and operating point, and the $Z_{qq}$ impedance depends on the close-loop PLL bandwidth, inner-loop current controller and the operating point.

The passive components such as inductor, capacitor and resistor have an equal impact on both the $Z_{dd}$ and $Z_{qq}$ impedance; however, the controllers in the wind farm inverters are different since the d-axis has outer-loop DC voltage control while the q-axis has PLL synchronization loop. As can be seen in Fig. 5.24, the d-axis impedance dominated Nyquist plot has sufficient phase margin and is far from the stability marginal point while the characteristic loci of the q-axis dominated impedance encircles the point (-1, j0). Thus the controllers in the q-axis are interacting resulting in instability in the interconnected areas. The source HVDC rectifier's most outer control in the q-axis is the AC voltage control and the wind farms inverter's most outer controller in the q-axis is the PLL. The controllers in the HVDC rectifier and WECS inverter with the slowest bandwidth are dominating part in the impedance magnitude at low frequencies, therefore the AC voltage controller of the HVDC rectifier and the PLL of the WECS inverter are interacting resulting in the instability.

To confirm the instability resulting in the interaction of the AC voltage controller of the HVDC rectifier and the WECS inverter, a state-space model has been derived for the system and the participation factor analysis has been carried out for the unstable eigenvalues to identify the contribution of the states. Fig. 5.27 shows the trajectory of the eigenvalues for a change of proportional gain of the AC voltage controller. The system has an unstable complex conjugate eigenvalue at $1.9 \pm j2\pi8.5$ with a oscillation frequency of 8.5 Hz for $k_{pvac} = 0.09$. This is

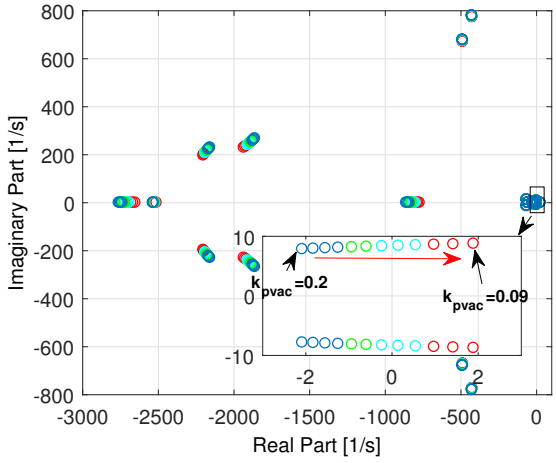


**Figure 5.27:** Trajectory of eigenvalue for a change of proportional gain of AC voltage controller.

the unstable case that is observed in the time domain simulation shown in Fig. 5.21 and the frequency domain analysis are shown in Fig. 5.24. From the participation factor analysis, it is found that the PLL and the AC voltage controller are the most contributing states to this unstable eigenvalue. The participation factor analysis proves that the instability is resulting in the interaction of the AC voltage controller and the PLL which gives the same conclusion as the presented impedance-based method from the impedance-based method.

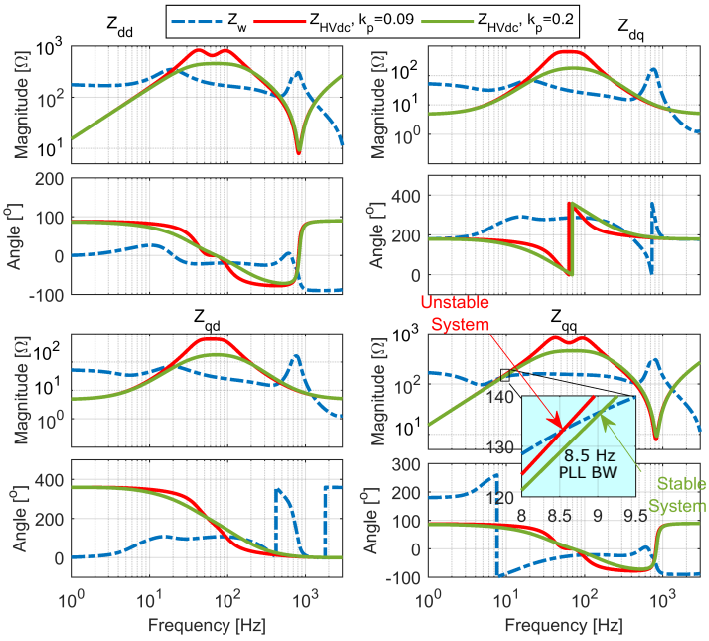


**Figure 5.28:** Impedance frequency responses of the wind farms and the HVDC system from AC collection point for two cases of AC voltage controller tuning (Dash-dot line is for the wind farms, solid lines are for the HVDC system for two control tuning of the AC voltage control).

## 5.9 Stabilization Method by Re-tuning the PLL and AC Voltage Controller

Fig. 5.28 shows the impedance frequency responses of the wind farm and the HVDC system from the AC collection point. The HVDC rectifier impedances are shown for two cases with proportional gain 0.09 and 0.2 of the AC voltage controller. Since the system becomes unstable only for the $Z_{qq}$ impedance, the $Z_{qq}$ impedance is of the most interest. The $Z_{qq}$ impedance of the HVDC rectifier behaves as an inductive up to a frequency around 40 Hz and it becomes a bandpass filter at a frequency of the AC voltage control-loop bandwidth. However, the $Z_{qq}$ impedance of the wind farm behaves capacitive up to the crossover frequency of the PLL-loop and shows the characteristics of a band reject filter. As can be seen in Fig. 5.28, the $Z_{qq}$ impedance of the wind farm intersects the HVDC impedance at 8.5 Hz for the AC voltage-controller proportional gain 0.09. From the close-loop transfer function of the PLL, the bandwidth is found 8.5 Hz. The system becomes unstable if the $Z_{qq}$ impedance magnitude of the HVDC system

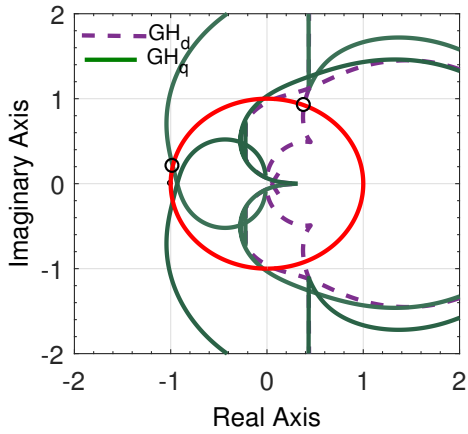


**Figure 5.29:** Characteristics loci of the minor-loop gain for retuning ac voltage controller (Red-line is the unit circle).

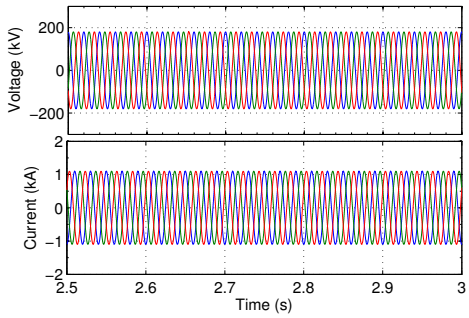


**Figure 5.30:** Stable: Three phase voltages and currents at ACC bus.

becomes larger than $Z_{qq}$ impedance magnitude of the wind farms at a frequency below the bandwidth of the PLL. In order to avoid interaction phenomena between the AC voltage controller of the HVDC rectifier and the PLL of the WECS inverter, the controls of the both VSCs need to be re-tuned in such a way that the $Z_{qq}$ impedance magnitude of the HVDC system is kept lower than the $Z_{qq}$ impedance magnitude of the wind farm at the frequency of the PLL bandwidth.

Based on (5.26), the higher bandwidth of the AC voltage controller of the HVDC OFF-VSC reduces impedance magnitude of the HVDC system. Initially, the AC voltage controller bandwidth of OFF-VSC was five times lower than the inner-loop current controller bandwidth. A standard practice for the converter designer is that the outer-loop bandwidth should be three to ten times smaller than the inner control loop [105]. Therefore, in a first attempt, the bandwidth of the AC voltage control loop has been increased. The ac voltage controller proportional gain is increased to 0.2 and the control-loop phase margin is 58 degrees with 132 Hz crossover frequency while previously the crossover frequency was 80 Hz. Hence, the bandwidth of the AC voltage controller becomes three times smaller than the inner current control-loop. The

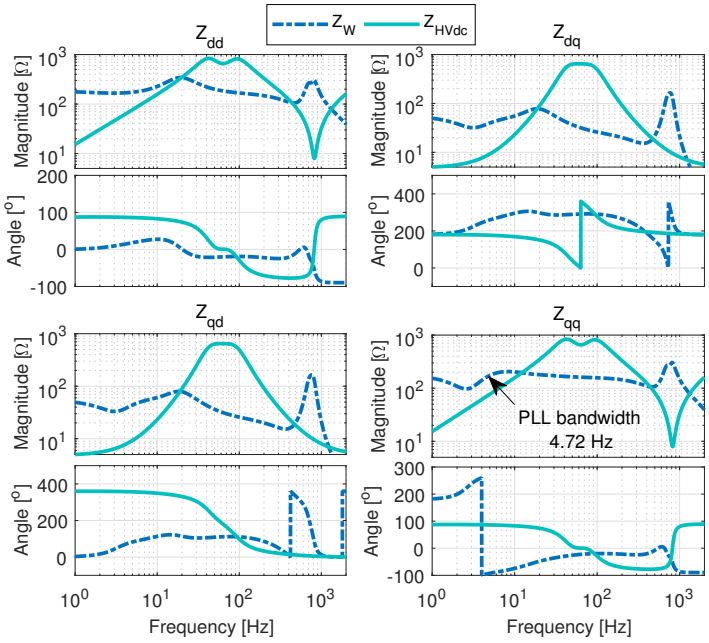


**Figure 5.31:** Impedance frequency responses of the wind farms and the HVDC system from AC collection point for re-tuning the PLL (Solid line is the HVDC and dash line is for the wind farms).

impedance frequency responses is shown in Fig. Fig. 5.28 for this AC voltage tuning. As can be seen in Fig. 5.28, the $Z_{qq}$ impedance of the wind farm intersects the HVDC impedance at around 9 Hz for the new tuning of the AC voltage-controller. The $Z_{qq}$ impedance magnitude of the HVDC system becomes smaller than the impedance magnitude of the wind farm at the frequency below the bandwidth of the WECS-I PLL. Frequency domain stability analysis has been carried out for this new tuning of the AC voltage control of the HVDC OFF-VSC. Fig. 5.29 shows the frequency domain stability analysis results for this tuning. As can be seen, the loci plots do not encircle the point (-1, j0), hence the system will operate stably. To further verify the theoretical analysis, a time domain simulation has been carried out for the new control tuning of the AC voltage control loop while other control-loops bandwidth remain the same. Fig. 5.30 shows the time domain responses from the simulation. The system operates stably for this tuning.

A general rule is observed that if the PLL open-loop phase margin is more than 40-degree and the close-loop bandwidth is 10 times smaller than the open-loop crossover frequency of the AC voltage controller, the system operates stably. Another example is shown to prove this observation by re-tuning the PLL loop-gain at 3.17 Hz crossover frequency with 42-degree phase margin and the PLL close-loop control bandwidth is 4.72 Hz for the unstable case of Fig. 5.24. Fig. 5.31 shows the impedance frequency responses of wind farms from the AC collection point together with the HVDC impedance for new tuning of the PLL. As can be seen, the $Z_{qq}$ impedance magnitude of the wind farms does not intersect the HVDC impedance at frequency below the cutoff frequency of the PLL-loop. Fig. 5.32 shows the characteristics loci plots of

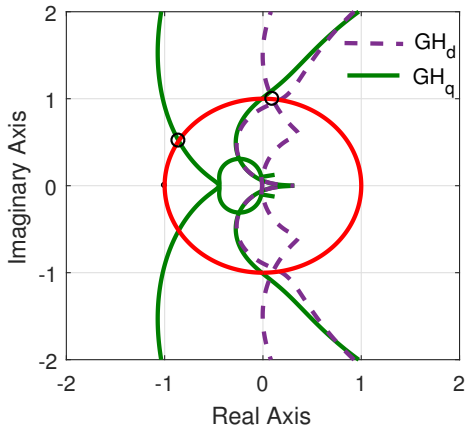


**Figure 5.32:** Stable case: Nyquist plots of minor-loop gain for retuning of the PLL.

the minor-loop gain. As can be seen, the loci plots do not encircle the point (-1, j0), the system operates stably which has been confirmed by time domain simulation. The mitigation method presented for re-tuning the PLL is applicable for any grid tied inverter for example, the wind and solar power application. The q-axis impedance of the grid must not intersect the grid tied inverter impedance below the bandwidth of the PLL.

## 5.10 Conclusion

This chapter presents a preliminary exploration of the possible origins of the SSO and resonances observed in the interconnected system of wind farms and a VSC based HVDC system. The SSO and sub-harmonic resonance phenomena at low frequency are observed depending on the control implementation and components of the wind farm and the HVDC system. Analytical derivations of the impedance frequency responses for both the wind farm and the HVDC are derived and the potential resonance points are identified from the Nyquist plot of the impedance ratio. These resonance points are also observed in the form of oscillations in the time domain simulations of the wind farm and the HVDC system. A closer and step by step analysis of each component and controller of the wind farms and the HVDC system indicate the possible sources for these oscillations. The SSO originated in the AC collection bus is arguably originated by the interaction between the WECS inverter controller and the HVDC rectifier. For testing the impact of the controllers in mitigating the observed oscillations, an active damping scheme in the current compensator of the HVDC rectifier is proposed to improve such oscillation phenomena. The detailed analytical modeling of the damping scheme has been presented and the performance of the active damping scheme has been verified by time domain simulation. The oscillations are effectively eliminated with the active damping scheme. A discussion of the role of the ratio between the bandwidths of the controllers of the interconnected areas is introduced, and an essential role as the root cause of the instability is proposed to be taken into account in the re-shaping of the impedances to maintain the stability.

Moreover, this work presents a novel technique to reveal and extract the internal control dynamics (critical controllers bandwidth) of the WECS inverter when the WECS system is assumed to

be a 'black/grey box' by proposing a non-parametric impedance model based on measurements by using a system identification technique. The method has potential immediate applicability in the wind industry based on the simplicity it offers to black/grey-box types of systems to guarantee the stability of the interconnection. An application of this method is: an electric power company (EPC) will install an HVDC connected wind farms. The EPC will get the WTG model from the WECS company and HVDC system from the HVDC company. Before installation, the EPC will have access the simulation model (both WECS and HVDC converter) and can study the system. Simulation models are still a grey-box model and the control structures are unknown. If the EPC finds the interconnected system unstable, using the method presented in this chapter, they can identify which part of the control provokes the instability and based on this knowledge, the EPC can ask the WECS company or the HVDC company to re-design the control system that guarantees the system operates stably.

# Chapter 6

# Impact of Self-synchronisation WECS on the MMC-HVDC Connected Wind farm: Impedance-based Analysis

*This chapter presents a controller for the WECS inverter based on the synchronverter concept. The design of the synchronverter is embedded in the VSC to mimic the way synchronous generator synchronize. The detailed analysis and the results presented show the benefits of this controller and its potential for stability. The results highlight the synchronverter's ability in keeping better performance in point of stability and control in integrating offshore wind farm through MMC-based HVDC system.*

This chapter is based on the following articles.

[1] **M. Amin** and M. Molinas, "Self-synchronisation of wind farm in MMC-based HVDC system," in *2016 IEEE Electrical Power and Energy Conference (EPEC)*, Ottawa, Canada, 2016

[2] **M. Amin**, A. Rygg and M. Molinas, "Self-synchronisation of wind farm in MMC-based HVDC system: Stability Investigation," *IEEE Transaction on Energy Conversion*, vol. 32, no. 2, pp. 458-470, June 2017.

## 6.1 Introduction

The WECS is connected to the grid through power electronics converters which require a dedicated synchronization unit such as a PLL to synchronize with the AC grid. A slow synchronization unit could directly affect the control performance and degrade the system stability but a complex synchronization unit, on the other hand, adds significant computational burden to the controller [88], [105]. Moreover, the offshore wind farms are far from the shore and connected to the grid through the HVDC transmission system. As a result, the wind power inverters see a very weak grid due to the long transmission line and introduce a instability problem. The wind power inverter-controller and the wind farm side HVDC converter-controller interact each other which result in a electrical oscillation [49], [55].

This work proposes a control scheme for the WECS inverter based on the synchronverter concept [109]. The interconnected system under this study includes a WECS employing full scale converter connected to the main AC grid through a MMC-based HVDC system. A type-IV full-scale WECS is considered for this investigation. A self-synchronization control technique is implemented to the ACC bus side WECS inverter which does not require a PLL. This converter mimics the synchronous generator (SG) and can automatically synchronize itself before connecting to the grid and can track the ACC bus frequency after connection [109].

Synchronverter based inverters can relatively easy integrate distributed generation; however, determining the stability of synchronverter is not easy due to the non-linearities of the controller. Examples of non-linearities are calculation of the real and reactive power, the coupling between the frequency and the field excitation current loops, initial self-synchronization frequency loops. Continuous efforts have been made to investigate the stability of such system by different approaches. The impedance-based stability analysis approach is the simple method for analyzing the stability of such interconnected system of the wind farms and MMC-HVDC system. Therefore, the impedance-based stability method is adopted to determine the stability of the interconnected system. Once the source and load impedances are obtained, the Nyquist Stability Criterion is applied to predict the stability of the interconnected system.

The rest of the chapter is organized as follows. Section 6.2 describes the synchronverter-based modeling and control of the WECS. Section 6.3 presents the modeling and control of the MMC-based HVDC system for the purpose of integrating offshore wind farms. Section 6.4 presents the analytical impedance modeling of the synchronverter-based WECS and the MMC-based HVDC system. An impedance-based stability analysis has also been performed in this section. Detailed time domain simulation has been explained in section 6.5. Finally, Section 6.6 concludes this chapter.

## 6.2 Synchronverter-based WECS control

The wind farm consists of WTGs based on the two-level full power back-to-back converter. The grid side VSC of the WECS is decoupled with generator side VSC by the DC-link capacitor, thus the generator side VSC does not interact with the AC grid. Any simple control structure can be implemented in the generator side VSC. In this study Field Oriented Control scheme has been implemented on the generator side VSC and will not be discussed in detailed. The control scheme of the grid side VSC is based on the synchronverter concept. The detailed has been described below.

### 6.2.1 Overview of the Synchronverter Technology

Control system that enables self-synchronization of grid-connected converters is a research topic of high interest. Several researches have been conducted to develop the control for power electronics converters having no dedicated synchronization unit and at the same time emulate the inertia and damping as a synchronous machine [108], [110], [111]. One of the first implementations called Virtual Synchronous Machine (VSM) was presented in [112]. In [111] it was shown that the VSM-concept is equivalent to droop controllers in converter-based micro grids. Another implementation called Synchronverter was proposed in[108]. Other similar concepts can be found in [113]–[115]. The main difference between implementations lies in the control system details, for example the presence of current controller and fault-ride-through capability.

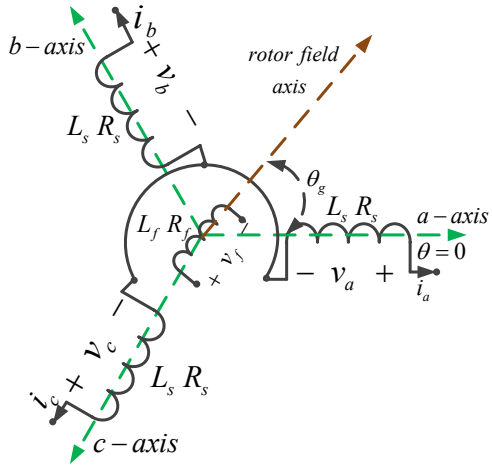


**Figure 6.1:** Structure of three-phase round-rotor SG

Another important function is the initial synchronization method, i.e. the ability to connect to an existing grid without any harmful transient or over current. One approach of controlling VSC is known as synchronverter [108]. The synchronverter is an inverter without PLL that mimics the synchronisation mechanism inherent to the SG. At the initial development of synchronverter, it requires a PLL for initial synchronization and later a self-synchronized synchronverter has been developed where the inverter can synchronize with the grid without a dedicated synchronization unit [109], [116]. Synchronverter based control becomes a promising technique in various applications, such as integrating distributed generation [117], HVDC transmission [118], [119], MMC [120]. Since most of the power plants are connected to the AC grid through SG, synchronverter provides better flexibility and control in integrating offshore wind farm through HVDC transmission system due to its implementation which is based on the SG theory.

For the purpose of implementing the synchronverter control strategy, we recall the structure of an idealized three-phase round rotor SG as shown in Fig. 6.1 [121]. The stator winding is assumed to be a concentrated coil having self-inductance $L$ and mutual-inductance $M$ with a typical value of $1/2L_s$. The field winding is assumed to be a concentrated coil having self-inductance $L_f$. The phase terminal voltage, $\mathbf{v_{abc}} = [v_a \;\; v_b \;\; v_c]^T$ can be written as

$$\mathbf{v_{abc}} = -R_s \mathbf{i_{abc}} - L_s \frac{d\mathbf{i_{abc}}}{dt} + \mathbf{e_{abc}} \tag{6.1}$$

where, $\mathbf{i_{abc}} = [i_a \;\; i_b \;\; i_c]^T$ is the stator phase currents vector; $R_s$ and $L_s = L + M$ are the stator winding resistance and inductance, respectively and $\mathbf{e_{abc}} = [e_a \;\; e_b \;\; e_c]^T$ is the back electromotive force (EMF) due to the rotor movement and can be given by

$$\mathbf{e_{abc}} = M_g \dot{\theta}_g \widetilde{\sin}\theta_\mathbf{g} \tag{6.2}$$

where $M_g$ is the flux field; $\theta_g$ is the rotor angle and

$$\widetilde{\sin}\theta_\mathbf{g} = [sin\theta_g \;\; sin(\theta_g - \frac{2\pi}{3}) \;\; sin(\theta_g + \frac{2\pi}{3})].$$

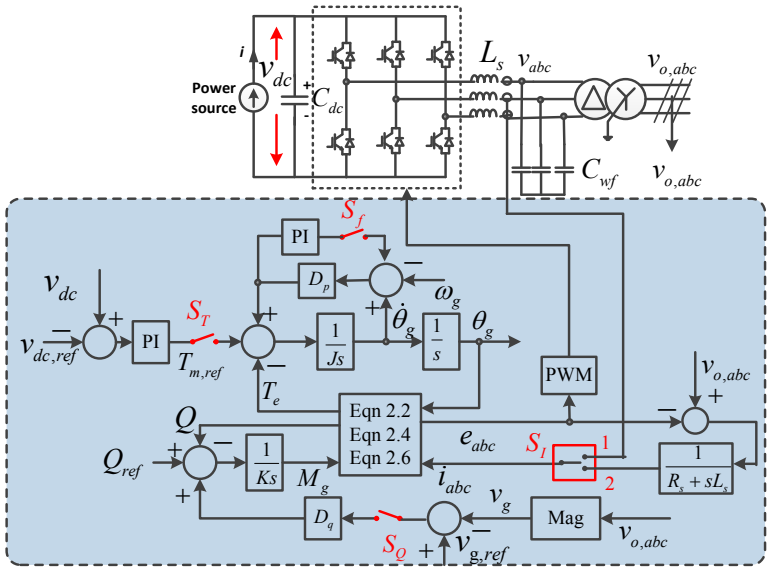


**Figure 6.2:** Synchronverter (Grid-side WECS VSC) including both the electrical circuit part and electronic part.

The mechanical part of the machine can be written by

$$J\ddot{\theta}_g = T_m - T_e - D_p\dot{\theta}_g \tag{6.3}$$

where $J$ is the moment of inertia of all the parts rotating with the rotor; $T_m$ is the mechanical torque; $T_e$ is the electromagnetic torque and $D_p$ is a damping factor. The electromagnetic torque, $T_e$ can be found from the energy stored in the magnetic field of the machine and can be given by

$$T_e = M_g \left\langle \mathbf{i_{abc}}, \widetilde{\sin}\theta_{\mathbf{g}} \right\rangle \tag{6.4}$$

where $< ., . >$ denotes the conventional inner product in $\mathbb{R}^3$. The real power, $P$ and reactive power, $Q$ generated by SG can be given by, respectively

$$P = M_g\dot{\theta}_g \left\langle \mathbf{i_{abc}}, \widetilde{\sin}\theta_{\mathbf{g}} \right\rangle \tag{6.5}$$

$$Q = M_g\dot{\theta}_g \left\langle \mathbf{i_{abc}}, \widetilde{\mathbf{cos}}\theta_{\mathbf{g}} \right\rangle . \tag{6.6}$$

### 6.2.2 Synchronverter-based Control of the WECS Inverter

In this work, a control strategy based on synchronverter is adopted for the WECS where the grid-side VSCs of the WECS run as a synchronous machine. The synchronverter concept is developed based on the SG model (6.1)-(6.6). The electrical circuit of the synchronverter including the controller part is given in Fig. 6.2. The electrical circuit part consists of power switches, $LC$ filter and step-up transformer. The lower part of the Fig. 6.2 can be called electronic part of the synchronverter which controls the switches of the power part. Such a control

structure is assumed to be equivalent to an SG with a capacitor bank connected in parallel with the stator terminal [108].

The voltage in (6.2) corresponds to the back EMF of a virtual rotor. The inverter switches are operated such that over a switching period, the converter outputs are to be equal to $\mathbf{e_{abc}}$ as given in (6.2) and it is achieved by a PWM technique.

The swing equation for the synchronverter can be given by

$$\ddot{\theta}_g = \frac{1}{J}(T_m - T_e - D_p\dot{\theta}_g) \tag{6.7}$$

where the mechanical torque, $T_m$ is a control input and electrical torque, $T_e$ depends on $\mathbf{i_{abc}}$ and $\theta_g$ according to (6.4).
To have similar behaviour as SG, the following frequency droop control loop is proposed

$$T_m = T_{m,ref} + D_p(\omega_g - \dot{\theta_g}) \tag{6.8}$$

where $T_{m,ref}$ is the mechanical torque applied to the rotor. The synchronverter regulates the WECS DC-link voltage and reactive power. The WECS DC-link voltage is controlled by controlling the mechanical torque and it is generated by a PI-controller as shown in Fig. 6.2 and can be given by

$$T_{m,ref} = (k_{pvdc} + \frac{k_{ivdc}}{s})(v_{dc} - v_{dc,ref}) \tag{6.9}$$

where $k_{pvdc}$ and $k_{ivdc}$ are the proportional and integral gain of the WECS DC-link voltage-controller, respectively.

In order to regulate the field excitation, $M_g$, the reactive power is controlled by a voltage-droop control-loop using voltage droop coefficient, $D_q$. The control of reactive power is shown in the lower part of Fig. 6.2 where the inner-loop is the voltage (amplitude) loop and the outer-loop is the reactive power loop. The time constant, $\tau_v$ of voltage loop can be estimated by $\tau_v \approx \frac{K}{\dot{\theta} D_q}$ as variation $\dot{\theta}$ is very small where $K$ follows if $\tau_v$ and $D_q$ have been chosen. Magnetic field excitation, $M_g$ and reactive power reference, $Q_{m,ref}$ can be given by

$$M_g = \frac{1}{Ks}(Q_{g,ref} - Q) \tag{6.10}$$

$$Q_{m,ref} = Q_{ref} + D_q(v_{g,ref} - v_g) \tag{6.11}$$

where $v_g$ is the output voltage magnitude. The output voltage magnitude is calculated using Clarke transformation as

$$v_\alpha + jv_\beta = v_{oa} + v_{ob} + v_{oc}$$

$$v_g = \sqrt{v_\alpha^2 + v_\beta^2}.$$

The structure of classical generators for which controls are well-known can be adopted with the synchronverter. Initially, the frequency droop coefficient, $D_p$ is chosen such that a frequency drop of 0.5% causes the torque to increase by 100% from its nominal value and the voltage droop coefficient, $D_q$ is chosen such that a drop of 5% voltage causes the reactive power to increase by 100%. However, these parameters can not be directly used in a synchronverter based

WECS. A specific tuning method based on the eigenvalues and participation factor analysis of individual states is presented in [118]. The optimized parameters used in this work are $D_p = 102$ and $D_q = 52696$. The time response for the frequency droop and voltage droop are kept 1 ms and 80 ms, respectively. The voltage controller proportional gain is set to 5 and the response time is 100 ms.

## 6.3 MMC-HVDC System Modeling and Control

This section presents the modeling and control of the MMC-based HVDC system with purpose of integrating offshore wind farms.

### 6.3.1 MMC-HVDC System configuration

The MMC-based HVDC system comprises converter transformer, wind farm side MMC (WF-MMC), sub-sea DC cable and the grid side MMC (GS-MMC). The GS-MMC converter regulates the HVDC-link DC voltage. An energy based DC voltage control has been implemented on the GS-MMC. The energy based control implementation for MMC has been discussed in [73]. Assuming the DC voltage controller performance is satisfactory and provides a constant DC voltage at the WF-MMC converter DC side, the GS-MMC-HVDC converter can be replaced by a constant DC voltage source in the analytical impedance model derivation of the WF-MMC [49]. The WF-MMC behaves a voltage source at AC terminal for the wind farms and provides a sinusoidal voltage to the offshore ACC bus.

### 6.3.2 Modeling and the Control of the WF-MMC HVDC

Many researches have been focused on modeling [122]–[125] and controlling the MMC for example, model predictive control [15], [126], energy based control [73], proportional and resonance (PR) regulator in a stationary frame [65], PI controller in a synchronous rotating frame [127], [128]. The PR regulator in the stationary abc-frame and the PI controller in the synchronous rotating ($dq$-) frame are simple methods and easy to implement compared to other methods. In theory, the PR regulator in stationary frame is equivalent to the PI regulator in the synchronous rotating frame [129]; hence the PR parameters are the same as the PI parameters. The advantage of the PR regulator over PI-regulator is that the need for the synchronous dq transformation in three-phase system can be avoided. Moreover, the PR regulator can be implemented for selective harmonic compensation without requiring excessive computation resources [130]. For example, it can be used to eliminate second harmonic circulating current.

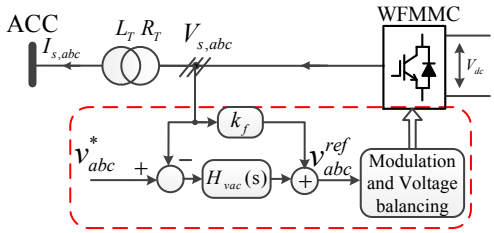


**Figure 6.3:** Control of the WF-MMC HVDC: PR-based AC voltage control.

An AC voltage controller as shown in Fig. 6.3 is adopted in the WF-MMC to provide an AC

**Table 6.1:** Parameters of the MMC-HVDC system

| Parameter | Value |
|---|---|
| Rated Power | 50 MVA |
| Rated AC voltage | 110 kV |
| Rated DC voltage | 220 kV |
| Arm inductance, $L_a$ | 0.0616 H (0.08 pu) |
| Arm resistance, $R_a$ | 1.21 Ω (0.005 pu) |
| Submodule capacitance, $C_{SM}$ | 1 mF |
| System fequency, f | 50 Hz |
| AC voltage controller gain, $k_p, k_r$ | 0.1, 20 |
| CCSC gain, $k_p, k_r$ | 20, 0 |

voltage source for the wind farm. The controller is implemented in the $abc$-reference frame and a PR-controller is used to achieve the zero steady state error for sinusoidal quantities [65]. The modulation voltage reference in the stationary $abc$-frame can be given by

$$v_{abc}^{ref} = H_{vac}(s) \times (v_{abc}^{*} - v_{abc}) + k_f v_{abc} \tag{6.12}$$

where $v_{abc}^{*}$ is the reference AC voltage in $abc$-domain; $k_f$ is the feed forward gain of the AC voltage and $H_{vac}$ is the PR-controller transfer function as

$$H_{vac} = k_{p,vac} + \frac{k_{r,vac}s}{s^2 + \omega_{1f}^2} \tag{6.13}$$

where $k_{p,vac}$ and $k_{r,vac}$ are the proportional and resonance coefficient of the AC voltage controller, respectively.

A CCSC is also implemented to limit the circulating current through the switches. The circulating current flowing in each phase consists of a DC component and low-order harmonic components, mainly the negative sequence component with the frequency twice the fundamental [131]–[133]. Therefore, in order to restrain the second order harmonic current, a CCSC is adopted in the *abc*-reference. The reference voltage generated by the CCSC can be expressed as

$$v_c^{ref} = H_{cc}(s)(i_c^{ref} - i_c) + R_a i_c^{ref} \tag{6.14}$$

where $H_{cc}(s)$ is a PR-controller with resonance frequency 2x$\omega_{1f}$; $i_c^{ref}$ is the circulating current reference and $R_a i_c^{ref}$ is introduced to compensate the voltage drop on the parasitic resistance in the steady-state.

Many researches have been conducted on the design and the parameters selection for MMC [122], [123], [125]. In this work, the arm resistance has been calculated based on the standard parameters used in [73] where the arm resistance and inductance are 0.005 pu and 0.08 pu, respectively. A detailed method has been presented in [122] on how to determine the sub-module capacitance which has been adopted in this work to select the value of the sub-module capacitance. The parameters of the MMC-HVDC are given in Table 6.1.

## 6.4 Impedance-based Stability Analysis of Interconnected System of MMC-HVDC and Wind Farm

The impedance-based stability analysis method is adopted to determine the stability of the interconnected system of Wind farms and MMC HVDC system. In order to apply the impedance-based stability analysis, deriving the impedance model is a prerequisite, therefore, first impedance models of the synchronverter and the MMC-HVDC system have been derived in sequence domain.

### 6.4.1 Impedance Model of the Synchronverter

The AC impedance model of the synchronverter can be obtained from (6.1) by dividing the phase voltage by current, therefore $\mathbf{e_{abc}}$ needs to be presented in term of phase voltage and current.

It is assumed that both the reactive power generation and reference are zero. Applying linearization on (6.7)-(6.11), a small-signal model of $\tilde{\dot{\theta}}_g$ can be written as

$$\tilde{\dot{\theta}}_g = \frac{H_{vdc}(s)}{(Js + D_p)}\tilde{v}_{dc} + \frac{D_q I_0 sin\theta_{g0}}{Ks\,(Js + D_p)}\tilde{v}_g - \frac{M_{g0} sin\theta_{g0}}{(Js + D_p)}\tilde{i}_a \tag{6.15}$$

where $H_{vdc}(s) = k_{pvdc} + k_{ivdc}/s$ and $I_0 = (I_{a0}/2)e^{-j\theta_g}$.

For a steady-state operating point of the wind farm, the output wind power characteristics is similar to the behaviour of a CPL and it can be represented by a negative impedance, $R$ in steady-state. For the single-phase system, the power balance between the AC and DC side can be written as

$$P_{ph} = \frac{v_{dc}^2}{3R} = v_a i_a \tag{6.16}$$

which can be written small-signal form by

$$\tilde{v}_{dc} = \frac{3R}{2V_{dc0}}(V_0\tilde{i}_a + I_{a0}\tilde{v}_a). \tag{6.17}$$

The reactive power of the synchronverter is assumed to be zero which gives $cos\theta_{g0} = 0$ and $sin\theta_{g0} = 1$. Hence, linearizing (6.2) at $sin\theta_{g0} = 1$ and inserting (6.15) and (6.17), $e_a$ can be obtained

$$e_a = \overbrace{\left(-\frac{D_q\dot{\theta}_{g0}}{Ks} + \frac{3RH_{vdc}M_{g0}I_0}{2V_{dc0}\,(Js + D_p)} + \frac{M_{g0}D_qI_0}{Ks\,(Js + D_p)}\right)}^{G_v}\tilde{v}_a + \overbrace{\left(\frac{3RH_{vdc}M_{g0}V_0}{2V_{dc0}\,(Js + D_p)} - \frac{(M_{g0})^2}{(Js + D_p)}\right)}^{G_i}\tilde{i}_a \tag{6.18}$$

This converter does not have any PLL and it is assumed that there is no coupling term. Therefore, the positive and negative sequence impedance is assumed to be equal. Linearizing (6.1) and inserting (6.18), the impedance model of the synchronverter can be obtained as

$$Z_{SYNC} = -\frac{\tilde{v}_a}{\tilde{i}_a} = \frac{R_s + sL_s - G_i}{1 - G_v}. \tag{6.19}$$

Including the filter capacitor $C_{fw}$ and transformer impedance, $Z_{T,WECS}$, the total impedance of Synchronverter is given by

$$Z_{TOTAL} = \frac{Z_{SYNC}}{1 + sC_{fw}Z_{SYNC}} + Z_{T,WECS}. \tag{6.20}$$

The impedance model derived analytically is verified by numerical simulation in MATLAB Simulink. A perturbation current (5% of steady-state current) in abc-domain at different frequencies from 1 Hz to 5 kHz is injected in shunt and the voltage is measured. FFT tool is used to analyze the different harmonic voltages and currents. The impedance is calculated by dividing the voltage by current at each frequency. The impedance frequency response of the synchronverter is shown in Fig. 6.4. The analytical model has a good agreement both the magnitude and phase with the impedance frequency responses obtained by numerical simulation which validates the correctness of derived impedance model.

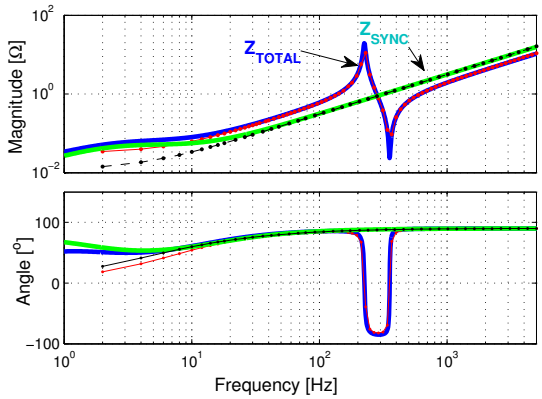


**Figure 6.4:** Impedance model verification of Syncronverter (Solid line is model prediction and point-line is from numerical simulation).

As can be seen from the impedance in Fig. 6.4, the impedance characteristics of synchronverter alone is similar to the behaviour of simple $RL$ circuit. It is due to having similar control structure as an SG. In comparison with decoupled $dq$-domain control structure, it has less cascaded control structure which reduces the interaction between controllers and as a consequence, the impedance behaviour becomes similar to a simple $RL$ circuit instead of being a higher order system. Including the filter capacitance and transformer inductance, it becomes a $LCL$ circuit and resonance peak depends on the circuit passive components.

The $dq$ frame control is also implemented on the WECS inverter to have a view of a comparison of the performance with the proposed technique. The electrical circuit parameters and rated power remain the same for both the synchronverter control and the $dq$-based control. The inner-loop current control is assumed and in the outer-loop, a DC voltage control is implemented in the $dq$ frame control. The current controller is tuned based on the modulus optimum criteria and the outer-loop DC voltage controller is tuned based on the symmetrical optimum tuning criteria [94]. The detailed control structure of the $dq$ frame control is given in chapter 5.

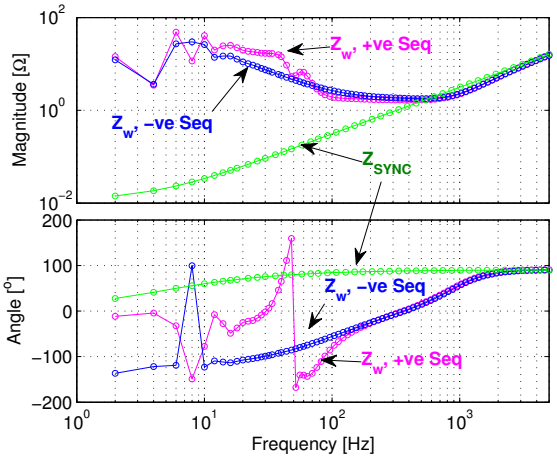


**Figure 6.5:** Comparison of Impedance frequency response between Synchronverter control mode and dq-domain control mode with PLL obtained from numerical simulation.

Fig. 6.5 shows a comparison of the impedance frequency responses between synchronverter control mode and the PLL based synchronization in the $dq$-domain control mode. Both positive and negative sequence impedances are presented for the $dq$-domain control. As can be seen from the impedance of $dq$-domain control, at frequency higher than 2 kHz, it is inductive; however, below 2 kHz the impedance curves are composite and consist of different resonance points. In addition, the magnitudes of the impedances are significantly higher than synchronverter impedance. With different resonance points in the impedance characteristics of dq-domain control, the system is more prone to oscillatory behaviour and the high impedance magnitude could result in voltage instability problems.

### 6.4.2 Analytical Impedance model of the WF-MMC HVDC

In this subsection, an impedance model of the MMC-HVDC has been derived in sequence domain including the dynamics of the close-loop AC voltage control and the CCSC. Internal dynamics of MMC can be described as a third order system and are given by [134]

$$\frac{C}{N}\frac{dv_c^{\Sigma}}{dt} = -\frac{v_s^{ref} i_s}{v_d} + \left(1 - \frac{2v_c^{ref}}{v_d}\right) i_c \tag{6.21}$$

$$\frac{C}{N}\frac{dv_c^{\Delta}}{dt} = \left(1 - \frac{2v_c^{ref}}{v_d}\right)\frac{i_s}{2} - \frac{2v_s^{ref} i_c}{v_d} \tag{6.22}$$

$$L_a\frac{di_c}{dt} = \frac{v_d}{2} - \frac{v_c^{\Sigma}}{4} + \frac{v_c^{ref} v_c^{\Sigma}}{2v_d} + \frac{v_s^{ref} v_c^{\Delta}}{2v_d} - R_a i_c. \tag{6.23}$$

Combining (6.12), (6.14), (6.21) and (6.22) and applying linearization and laplace transformation, and rearranging, it can be obtained [65]

$$G_g\tilde{v}_g + G_{is}\tilde{i}_s + \tilde{i}_c G_{ic} = 0 \tag{6.24}$$

where,

$$
\begin{aligned}
G_g =& 2 - \frac{2Ni_{c0}(k_f - H_v)}{sCv_d}\left(\frac{1}{2} - \frac{R_0 i_c^{ref}}{v_d}\right) - 2(k_f - H_v) + \frac{k_f Nm(k_f - H_v)i_{s0}}{2sCv_d} \\
G_{is} =& sL_a + R_a + \frac{N}{sC}\left(\frac{1}{2} - \frac{R_a i_c^{ref}}{v_d}\right)^2 + \frac{k_f Nm^2}{4sC} \\
G_{ic} =& \frac{N}{sC}\left(\frac{1}{2} - \frac{R_a i_c^{ref}}{v_d}\right)\left(\frac{H_{cc} i_{s0}}{v_d} - k_f m\right) - \frac{k_f Nm}{2sC}\left(1 + \frac{2(H_{cc} - R_a)i_{c0}}{v_d}\right).
\end{aligned}
$$

The circulating current suppression depends on the proper selection of the CCSC gain, therefore the controller-coefficients have a significant impact on the impedance of the MMC. Even the CCSC suppresses the 2nd-harmonic component of circulating current, in steady-state, the circulating current can have some ripples that need to be considered. Hence, it is necessary to find an expression of the circulating current in terms of the phase voltage and current. Combining (6.12), (6.14) and (6.23) and applying linearization in the frequency domain, and rearranging, it can be obtained

$$
\tilde{i}_c = \frac{G_B}{G_A}\tilde{v}_g + \frac{G_C}{G_A}\tilde{i}_s \tag{6.25}
$$

where

$$
\begin{aligned}
G_A =& sL_a + R_a - \frac{N}{sC}\left(\frac{R_a i_c^{ref}}{2v_d} - \frac{1}{4}\right)\left(1 - \frac{2i_{c0}(R_a - H_{cc})}{v_d}\right) - \frac{k_f NmR_a i_{s0}}{4sCv_d} + \frac{k_f Nm^2}{4sC} + H_{cc} \\
G_B =& \frac{Ni_{s0}(H_v - k_f)}{sCv_d}\left(\frac{R_a i_c^{ref}}{2v_d} - \frac{1}{4}\right) + \frac{k_f Nmi_{c0}(H_v - k_f)}{2sCv_d} \\
G_C =& -\frac{k_f Nm}{2sC}\left(\frac{R_a i_c^{ref}}{2v_d} - \frac{1}{4}\right) + \frac{k_f Nm}{8sC} - \frac{k_f NmR_a i_c^{ref}}{4sCv_d}.
\end{aligned}
$$

Now combining (6.24), (6.25), it can be obtained the impedance model of the WF-MMC as

$$
Z_{MMC} = -\frac{\tilde{v}_g}{\tilde{i}_s} = \left(G_{is} + \frac{G_{ic}G_C}{G_A}\right)\left(G_v + \frac{G_{ic}G_B}{G_A}\right)^{-1}. \tag{6.26}
$$

Including the transformer impedance, the impedance of the MMC-HVDC system from the ACC point can be obtained

$$
Z_{WFMMC} = Z_{MMC} + Z_{TransF}. \tag{6.27}
$$

The MMC does not have any PLL, therefore both positive and negative sequence impedances are equal in magnitude and the phase. The impedance model derived analytically is verified by comparing the frequency response of the analytical model with the impedance obtained by numerical simulation. Fig. 6.6 shows the comparison between the impedance frequency responses of the analytical model and measured from the numerical simulation, which indicates that the analytical model has a good agreement with the measured impedance both magnitude and phase.

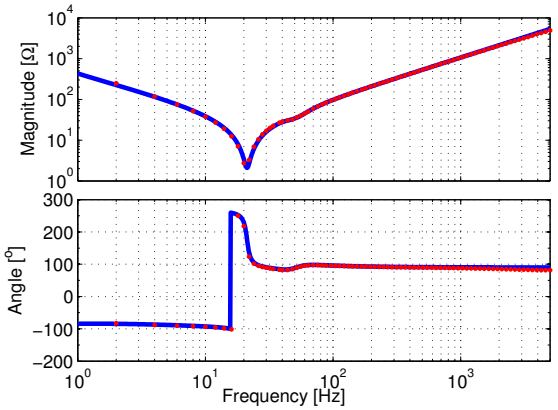


**Figure 6.6:** Frequency response of the WF-MMC HVDC impedance model. (Solid-line is the analytical model and the points are from numerical simulation).

The impedance characteristics of the WF-MMC can be divided into two parts. The first part is the low-frequency part which has capacitive characteristics and the impedance behaviour is inductive for high frequencies. The resonance peak depends on both the internal dynamics of the MMC and the control parameter, for example, the arm inductance, SM capacitance, number of SM, AC voltage controller coefficient, and the CCSC gain.

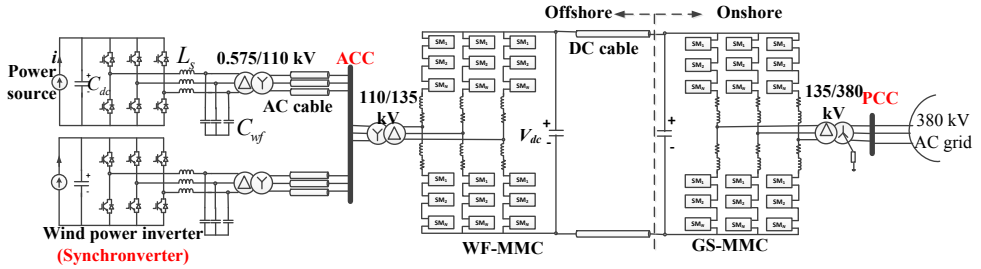


**Figure 6.7:** Simplified configuration of interconnected system of wind farms and MMC-based HVDC transmission system.

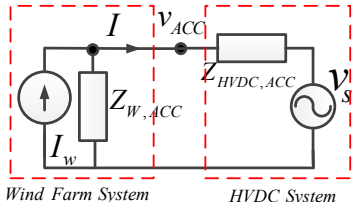


**Figure 6.8:** Equivalent small signal impedance model of interconnected system of wind farms and MMC-based HVDC transmission system.

### 6.4.3 Impedance-based Stability Analysis of the Interconnected System

Fig. 6.7 shows the investigated interconnected system of the wind farms and HVDC system and Fig. 6.8 shows the small-signal equivalent impedance model of the interconnected system. The MMC-HVDC system is modeled by its Thevenin equivalent circuit in the form of an ideal voltage source, $(V_s)$ in series with the MMC-HVDC impedance, $Z_{HVDC,ACC}$ while the aggregated wind farms is modeled by its Norton equivalent circuit consisting of an ideal current source $(I_W)$ in parallel with the wind farm impedance, $Z_{W,ACC}$. $Z_{HVDC,ACC}$ is the impedance of the MMC-HVDC system defined in (6.27) including transformer leakage inductance and

The impedance of the wind farm can be obtained by

$$Z_{W,n} = Z_{TOTAL} + Z_{ac,cable} \tag{6.28}$$

where n=1,2,3,... is the number of wind farms and $Z_{ac,cable}$ is the AC cable impedance and $Z_{TOTAL}$ is defined in (6.20). The investigated system under this study has two wind farms,

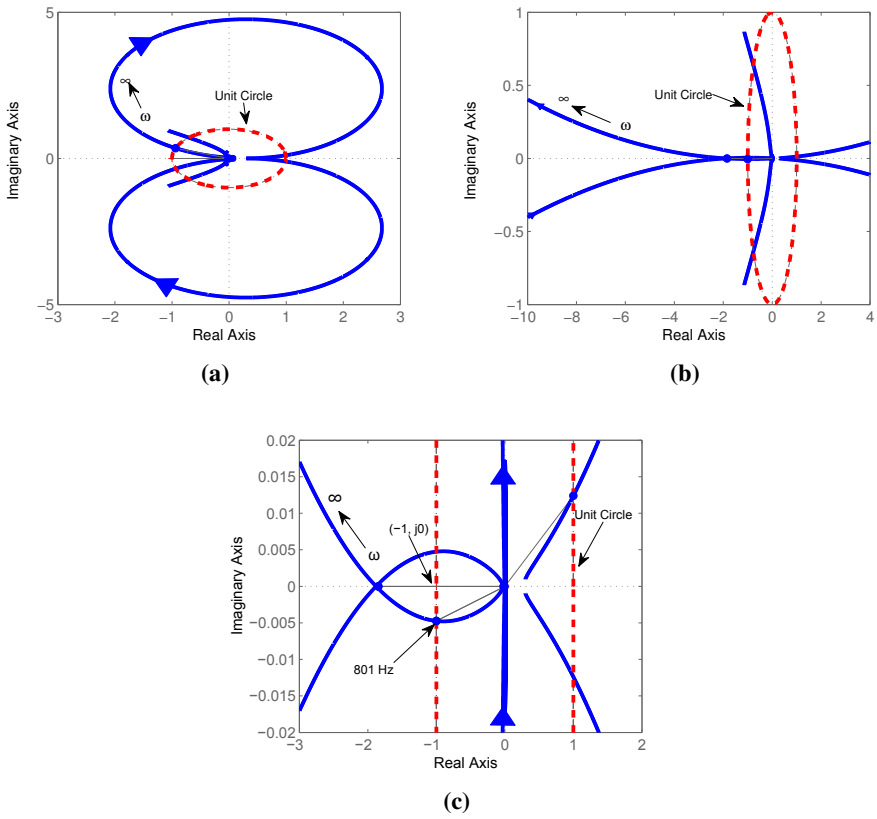


**Figure 6.9:** (a) Nyquist plot of minor loop gain (impedance ratio); (b) Nyquist plot of minor loop gain for high value of wind power inverter inductor and (c) zoom view of (b) (blue line is minor loop gian and red line is unit circle).

hence the total impedance of the wind farm can be given by

$$Z_{W,ACC} = 1/\left(\frac{1}{Z_{WP1}} + \frac{1}{Z_{WP2}}\right). \tag{6.29}$$

Based on the representation of Fig. 6.8, the minor-loop gain can be defined by

$$G(s)H(s) = \left(Z_{HVDC,ACC}(s)\right)/\left(Z_{W,ACC}(s)\right) \tag{6.30}$$

and the stability of the interconnected system can be determined by checking the Nyquist Stability Criterion on (6.30). The impedance of the MMC-based HVDC system and the wind farms are calculated for full power loading and Fig. 6.9 (a) shows the Nyquist plot of the minor-loop gain. As can be seen from the Nyquist plot, the minor loop gain does not encircle the point (-1, j0) and there is no pole in the RHP, therefore the system is predicted to operate stably.

An example case is presented to show that it can predict the instability of the interconnected system. The filter inductor of the WECS inverter is purposely increased to 0.5 mH while it is 0.05 mH initially. By increasing this inductor we are reducing the power rating of the wind power inverter. However, the impedance is calculated for the base power condition with 5 MW wind power output and resulting Nyquist plot of the minor-loop gain is shown 6.9 (b). As can be seen from the zoom view of the Nyquist plot ( Fig. 6.9 (b)) in 6.9 (c), the minor-loop gain encircles the point (-1, j0), the interconnected system is predicted to be unstable. The minor loop gain crosses the unit circle at three different frequencies, however, the crossing point at a frequency around 801 Hz is the closest point to (-1, j0).

## 6.5 Time domain Simulation of Interconnected System of MMC-HVDC and Wind Farm

The interconnected system is shown in Fig. 6.7. The wind farms are connected to the ACC bus through a 0.575/110 kV transformer. Each wind farm is assumed to have 5 turbines with 1 MW rating each. To simplify the system model, 5 turbines are lumped into one unit of 5 MW generation capacity. The generator side VSC is supplying the full power to the ACC bus through grid side WECS VSC and it is necessary to regulate the DC-link voltage of the WECS. The control topology of the synchronverter is implemented in grid side WECS VSC. It, mimics the SG, regulates the DC-link voltage of the WECS and the reactive power. In addition, it has a frequency droop and AC voltage droop as like as a conventional SG. The parameters of the WECS are given in Table 6.2. These wind farms are integrated to the main AC grid through an

**Table 6.2:** Parameter of the synchronverter (ACC bus side VSC of WECS)

| Parameter | Value | Parameter | Value |
|---|---|---|---|
| Rated Power, $S_b$ | 5 MW | $L_wf$ | 0.05 mH |
| Rated AC voltage | 575 V | $R_wf$ | 0.01 Ω |
| Rated DC voltage | 1100 V | $C_{wf}$ | 1 mF |
| frequency droop, $D_p$ | 102.3344 | $k_{vdc}$ | 5 |
| Voltage droop, $D_q$ | 5.2696e4 pu | $k_{ivdc}$ | 5/100e-3 |

MMC-based HVDC transmission system. The MMC-HVDC system has a capacity of 50 MVA equivalent. The MMC converter transformer is 110/135 kV, 50 Hz and same rating as the MMC converters. The HVDC link DC voltage is 220 kV.

In order to validate the above theoretical analysis, the interconnected system as shown in Fig. 6.7 has been built in MATLAB/Simulink environment association with the SimPowerSystem Block-set with the detailed switching model of the WECS VSC and the MMC with 24 SMs per leg. The SMs are based on the half-bridge module. A balancing algorithm is used to balance the SMs capacitor voltage. A MATLAB code has been implemented to generate the PWM signal for the switches. The simulation parameters are the same as the analysis done in the frequency domain using Nyquist stability criteria and the parameters of MMC-HVDC system and the synchronverter-based WECS are given in Table 6.1 and Table 6.2.

To validate the proposed synchronverter control, case studies to show the initial self-synchronisation property of the system have been included. The detailed self-synchronization of the synchronverter in power control mode including the droop control has been discussed [109]. The synchronverter based WECS inverter regulates the DC-link voltage instead of the active power which requires one additional switch, $S_T$ for initial self-synchronization as shown in Fig. 6.2. The controls has four switches which are $S_T$, $S_f$, $S_Q$ and $S_I$. The switch $S_T$ is turned on with circuit breaker. The function of switches $S_f$, $S_Q$ and $S_I$ has been described in [109], therefore it has not been discussed in detailed. Fig. 6.10 (a) shows the phase-A grid voltage and the voltage at the PCC of the WECS inverter at initial self-synchronization when the circuit breaker has been turned on at 2 s to connect synchronverter-based WECS. As can be seen, the synchronverter-based WECS can successfully synchronize with the AC collection bus. Fig. 6.10 (b) shows the DC link voltage, active and reactive power and the frequency of the WECS inverter during the initial synchronization and the steady-state operation. Simulation is started at t=0 s. The DC-link capacitor of the WECS has been charged through a diode bridge rectifier. The synchronverter control estimates the grid frequency from the virtual current. The circuit breaker is turned on at t=2 s and at the same time, the switch $S_T$ is turned on which is providing the torque reference to regulate the DC-link voltage. At t=5 s, the WECS is exporting active power to the grid with a ramp rate 20%/s. The interconnected system operates stably in the time domain simulation as predicted by the frequency domain stability analysis in the previous subsection (Fig. 6.9 (a)). More simulations have been carried out to investigate the controller performance and to prove the feasibility of this control method. The simulation results have been discussed in the following.

The first simulation has been carried out to investigate the performance of PR-controller based WF-MMC HVDC system. Fig. 6.11 shows the MMC arm voltages, currents, circulating currents and cell voltages for the WF-MMC in a steady-state condition. Two small-signal disturbances are applied. At 0.5 s the wind output power has been reduced due to a low wind speed which reduces the arm currents, circulating currents and cell voltages. The arm voltages remain the same. The time domain responses show that a small-signal variation of the wind power does not have any impact on the stability. As discussed in [65], without the CCSC, the system can have low frequency oscillation. Therefore, in order to study the performance of the CCSC, the CCSC has been turned off for 0.5 s from 1 s to 1.5 s. As can be seen, when the CCSC has been turned off, the circulating currents has been increased which has increased the SMs capacitor voltages, however, there is no instability or electrical oscillation in the system similar to the

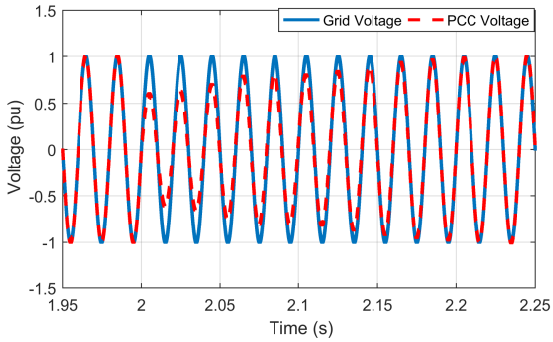


**(a)**

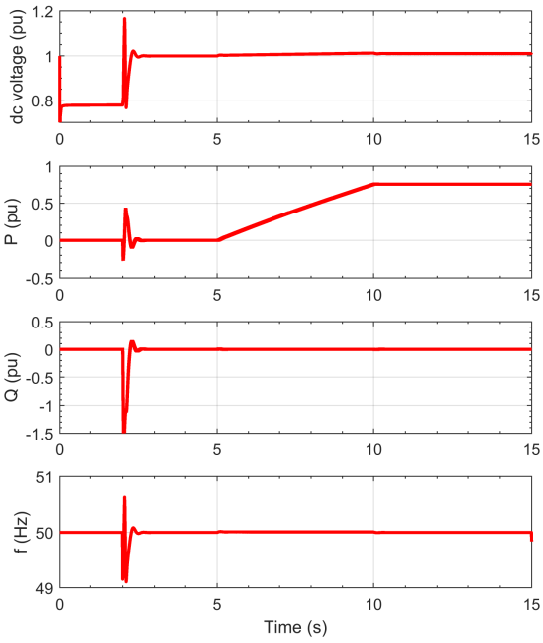


**(b)**

**Figure 6.10:** Initial self-synchronization: (a) phase-A grid voltage and voltage at point of common coupling and (b) DC link voltage, active power, reactive power and frequency.

phenomena noticed in [65] without CCSC and the interconnected system of wind farms and HVDC operates stably.

The second time domain simulation has been carried out to show the performance of the WECS DC-link voltage controller and the resulting time domain responses are presented in Figures 6.12 and 6.13. As can be seen from the time domain response, the system operates stably as predicted by the Nyquist plot in the previous subsection.

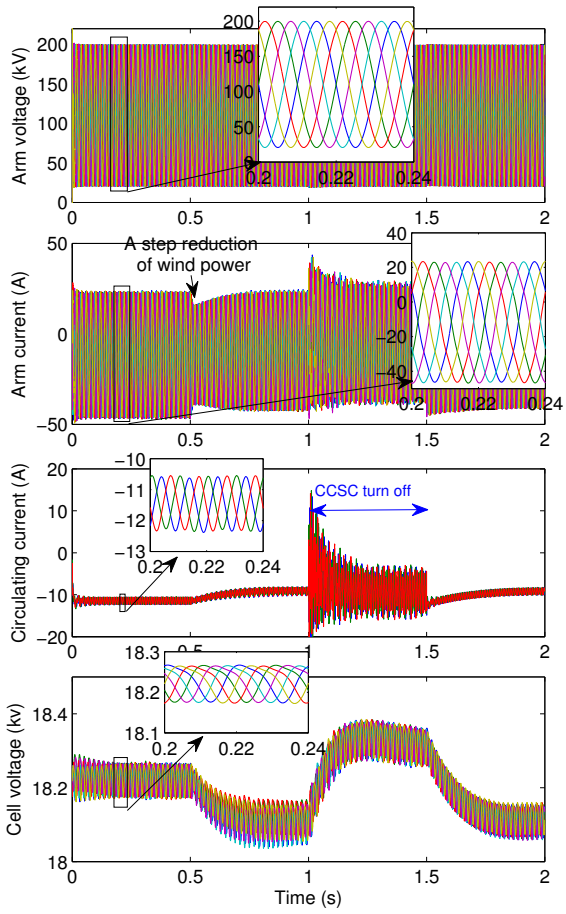


**Figure 6.11:** Wind farm side MMC arm voltages, arm currents, circulating currents and cell voltages for WFMMC.

Moreover, two transient events are introduced to show the performance of the control designed for the synchronverter-based WECS. At 1 s, a step increase of 0.04 pu DC voltage reference to the synchronverter is applied and at 2.5 s, a step reduction of 0.07 pu active power has been applied. The DC-link voltage of the WECS is shown in Fig. 6.12. The performance of the DC voltage controller is satisfactory, it follows the reference voltage. When the DC voltage reference is step-up 0.04 pu at 1 s, the voltage-controller tracks the reference, the delay to follow the reference depends on the DC voltage PI-controller time response. The output power step reduction is applied at 2.5 s which reduces the WECS DC-link current and follows the DC voltage reduction; however the synchronverter DC-link voltage control function recovers the DC voltage and follows the reference value in the steady-state. The active and reactive power of the wind farm is shown in Fig. 6.13. The wind farm active power has no oscillatory component. The reactive power has good response during the transient events, since the voltage

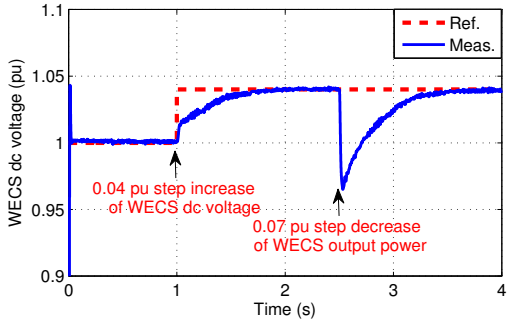


**Figure 6.12:** The DC-link voltage of WECS.

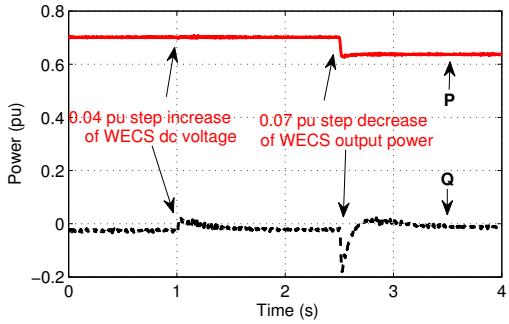


**Figure 6.13:** The active and reactive power output of Synchronverter based WECS.

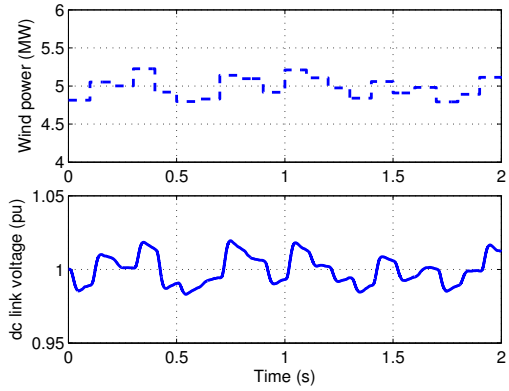


**Figure 6.14:** Response of the WECS DC-link voltage with variable wind power, (i) variable wind power and (ii) WECS DC-link voltage.

of AC collection bus is supported by the synchronverter by means of controlling the reactive power. As can be seen, the behaviour of the wind power inverter is a kind of first order system and is similar to an SG. It does not have any oscillatory behaviour.

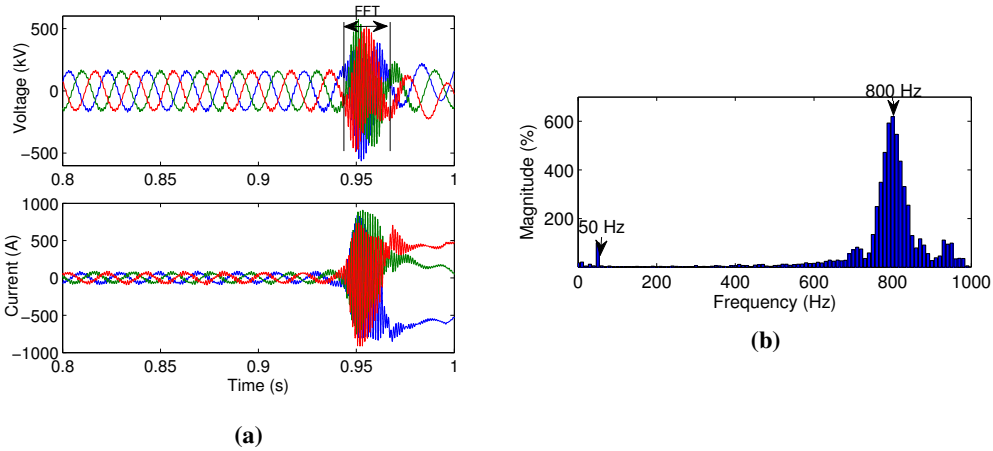


**Figure 6.15:** (a) Three-phase AC voltages and currents at ACC bus for high value of filter inductor of WECS and (b) FFT of AC voltage.

The wind power is varying continuously due to the variation of the wind speed, therefore a variable wind profile has been used to study the performance of the synchronverter-based WECS. Fig. 6.14 shows the applied variable wind power and the responses of the DC-link voltage of the WECS for the variable wind power. Since the wind power is varying, the DC-link voltage is also varying accordingly and remains in the operating range (0.95-1.05 pu). The variation of wind power does not have any impact on the stability of the system. Since the stability analysis has been performed for the small-signal, the system remains stable for the small-signal range. To ensure the stability of the system, the stability analysis has been performed for the entire operating range.

A time domain simulation has been carried out for the higher value of the WECS inverter filter inductor. This inductor is purposely increased to 0.5 mH as described in the previous section while the wind farm output remains the same at the rated value. Fig.6.15 shows the three-phase AC voltages and currents at the ACC bus and FFT of the voltage. As can be seen, the system is unstable for this condition. The system operates few ms to s depending on the interconnected system parameters in the simulation, however, in the real world, the system is equipped with many switchgear and protection system which prevent the system operation. An FFT is performed to check the frequency of the oscillation and the most dominant frequency is found around 800 Hz in an unstable condition which is predicted in the frequency domain analysis in the previous subsection.

## 6.6 Conclusion

This work proposes a controller for WECS inverter based on the synchronverter concept. A synchronverter is introduced on the grid side of WECS VSC where the wind farms are connected to the AC network through a MMC-based HVDC transmission system. The design of the synchronverter is embedded in the VSC to mimic the way SG synchronise. The control strategy supports the ACC bus voltage that helps to achieve a stable system. The observed results show

that this controller minimizes the control interactions compared to the decoupled *dq*-frame, since the synchronverter control does not require a dedicated synchronization unit and it results in less cascaded control blocks. In order to determine the stability of the interconnected system, an impedance based stability method is adopted. The impedances of both the wind power inverter and MMC-HVDC converter are analytically derived and the analytical model is verified by comparing the frequency responses obtained from the numerical simulation. The detailed analysis and the results presented show the benefits of this controller and its potential for stability. The results highlight the synchronverter's ability in keeping better performance in point of stability and control in integrating offshore wind farm through MMC-based HVDC system.

# Chapter 7

# Conclusion

*This chapter presents the concluding remarks of the thesis and discusses some recommendations for the future investigation.*

## 7.1 Concluding Remarks

### 7.1.1 Stability and Interaction Analysis of VSC-HVDC Systems

VSC-based HVDC systems have received considerable attention in transmitting power to long distances and also integrating offshore wind farms due to having superior advantages compared to the traditional AC transmission system. It is expected that two AC power systems will be connected via HVDC link which will gradually be expanded to MT-HVDC systems. Due to the complexity of the VSC based interconnections and many components with nonlinear nature, different stability and interaction phenomena will be observed. Therefore, it is necessary to preassess their impact that each additional terminal will have on the stability before connecting to the main AC grids. Continuous efforts have been made to investigate the stability and interaction analysis of such systems by different approaches in time and frequency domains. Different instability and interaction phenomena such as interaction of the converters controllers and the grid have not been thoroughly studied so as to identify every potential system malfunction.

This Thesis has focused on the small-signal stability and interaction analysis of such systems. In order to characterize interaction phenomena, the small-signal stability methods in frequency domain were employed. Green colors as shown in Fig. 1.5 indicate the methods treated in this thesis.

One of the established methods used for the stability and interaction analysis in frequency domain is based on the state-space small-signal modeling and the eigenvalue analysis. The method can be used to study the large-scale MT-HVDC system. In order to use this method, the system needs to be represented by a small-signal state-space form. Deriving the state-space model for a large system require much computational effort and it is difficult to model large-system analytically in a state-space form. Traditional power system analyzing tools like DigSilent PF use RMS/phasor based modeling to study such large scale systems where the dynamics of the network components are neglected. Therefore, it is an important to understand what simplification is reasonable when studying the VSC-based HVDC system. This Thesis first studied the im-

pact of the state-space modeling fidelity on the small-signal stability assessments of VSC-based HVDC systems. From this study, the following points are noted as a basis towards general guidelines on assessing the results obtained from the traditional power system stability tools used RMS/phasor modeling, containing VSC-based transmission scheme. The RMS/phasor model ignores states corresponding to network dynamics. This simplification is justifiable in limited cases when the poles related to the network dynamics do not have a significant impact on the system stability. Moreover, the results obtained from RMS/Phasor model does not reflect the actual system stability. Underestimation or overestimation of the system stability can be observed. To estimate the actual system stability, all the states need to be considered in system modeling when assessing the stability of the VSC-based HVDC system.

The small-signal stability and interaction analysis based on the system eigenvalue analysis have been used to illustrate the particular challenges that can occur during a step-wise construction of a large-scale MT-HVDC transmission system, assuming that the network dynamics are designed in such a way that they do not have a significant impact on the stability. During step wise construction of large-scale MT-HVDC systems, it is observed that the critical poles move towards the imaginary axis, which provokes the system to lose the stability and introduce the interaction phenomena. Some of the negative real poles in a point-to-point connection HVDC system become oscillatory in MT-HVDC systems which indicate that adding more converters, the system becomes more prone to voltage instability. The stability has been improved by retuning the controller properly and by ensuring the optimized value of the network dynamics for MT-HVDC systems.

Two main drawbacks are noticed when analyzing the stability and interaction phenomena based on eigenvalue analysis. The first drawback is that it requires detailed modeling of the entire MT-HVDC system for state-space modeling. Secondly, the VSC systems are modeled based on the average modeling of the converters which neglects the modulation (PWM) and processing delays resulting in that it cannot identify sustained harmonic oscillations in the VSC-based HVDC system. Therefore, an alternative approach has been used in this Thesis to overcome these drawbacks when studying the VSC-based large-scale MT-HVDC system.

This alternative approach, the impedance-based analysis method does not require the detailed modeling of the entire system, except for validation of components impedances. In order to apply the impedance-based approach, obtaining the impedance model is the prerequisite. Therefore, the impedance models for the HVDC VSCs and MMC with different control objectives such as the current control, power control, DC voltage control, the AC voltage control, and synchronverter-based control are analytically derived. In some cases, the detailed information of the model of the VSCs is not available due to confidentiality and industry secrecy. A method based on the impedance measurement combined with a model identification technique has been developed to obtain the non-parametric impedance model which is used to analyze the stability and interaction phenomena. Once the source and load impedances are identified, the impedance-based stability analysis is applied to determine the stability of the VSC-HVDC system. The systems remain stable as long as the minor-loop gain of the negative feedback control system, that is the impedance ratio of the source (grid) - HVDC VSCs (load) subsystem, satisfies the Nyquist stability criterion. The critical locations where the application of the impedance-based method can reveal the impact of a passive component and the controller gains of the VSC-based HVDC system on the stability has been presented.

A weakness of the impedance method is the limited observability of certain states given its dependence on the definition of local source-load subsystems which makes it necessary to investigate the stability at different subsystems. The state-space modeling and the eigenvalue analysis can determine the stability of the entire system regardless of the location of the origin of instability; however, it cannot determine the sustained harmonic oscillation since the VSC is assumed to be an average model and PWM delays are neglected. This can be overcome using the discrete time modeling; however, too complex computation efforts will be required in a discrete time modeling implementation, which makes it unfeasible for application to large scale HVDC systems. On the hand, the impedance-based analysis can overcome this limitation; however, it requires studying the stability at every possible interfacing point. Therefore, in order to ensure the overall system stability in a large scale MT-HVDC system, the results of this research recommend using both approaches; the eigenvalue based analysis for global stability and the impedance-based analysis at local AC-DC interfacing point to avoid sustained harmonic oscillation.

### 7.1.2 Interaction Analysis between HVDC and Wind Farms

The offshore wind farms are far from the shore and the HVDC transmission line is one feasible way to integrate the offshore wind farms to the AC grid. The stability of the offshore wind power network connected through HVDC transmission line is a critical problem since the offshore AC collection bus is not connected to a strong AC grid. Moreover, no rotating machine is connected directly to the AC collection bus since the wind turbine generators are connected to the AC collection point through AC-DC-AC converters due to their variable speed operation. This work investigated the potential causes of electrical oscillations observed between the wind farms and the HVDC system by investigating the impact of the controllers and the components in the wind farm inverter and in the VSC-HVDC transmission system. A discussion of the role of the ratio between the bandwidths of the controllers of the interconnected areas is introduced, and their significant role as the root cause of the instability is presented. This is then taken into account in the re-shaping of the impedances by re-tuning the controller gains to maintain stability. This Thesis presents a novel technique to reveal and extract the internal control dynamics (critical controllers bandwidth) of the WECS inverter when the WECS system is assumed to be a 'Black/Grey Box' by identifying a non-parametric impedance model based on measurements by using a system identification technique. The method has potential immediate applicability in the wind industry based on the simplicity it offers to black/grey-box types of systems to guarantee the stability of the interconnection.

The stability properties of a WECS inverter controller based on the emulation of some properties of the synchronous machine, the synchronverter, are investigated. The impedance model of the synchronverter has been derived to understand the properties of the synchronverter control scheme. The detailed analysis and the results presented show the benefits of this controller and its potential for stability. The synchronverter has better stability properties compared to the PLL based dq-domain control in point of stability and control in integrating offshore wind farm through MMC-based HVDC system, since the impedance of the synchronverter reflects a simple resistive-inductive (R-L) characteristic.

## 7.2 Future Work

Interconnected power systems like the ones treated in this thesis, exhibit - aside from the complex network topology and rich dynamic behaviour of the individual network components - a highly nonlinear network coupling among different components. These interconnected power systems are pervasive in control dynamics, which as shown in this Thesis, are at the core of some of the observed interaction phenomena. Despite their omnipresence, these complex network interactions with coupled control dynamics are still poorly understood. In this research, we revealed some partial insights by means of small signal stability analysis, which resolved some of the control and dynamic problems. These insights however only partially explain the observed phenomena and, by the methods used in this research, are obviously limited to small signal phenomena. In future work, it will be essential to fully understand the complex and nonlinear coupling strongly influenced by the control dynamics, to provide precise conditions and control design guidelines for guaranteeing stability and controllability of these complex and non-linearly-coupled network dynamics.

# Appendices

# Appendix A

B-Matrix for PQ control converter

$$\begin{pmatrix}
0 & 0 & 0 & 0 & 0 \\
0 & 0 & 0 & 0 & -V_{od0}\omega_b \\
\frac{K_{pc}K_{pp}\omega_b}{Lc} & 0 & 0 & 0 & 0 \\
0 & \frac{-K_{pc}K_{pp}\omega_b}{Lc} & 0 & 0 & 0 \\
K_{pp} & 0 & 0 & 0 & 0 \\
0 & -K_{pp} & 0 & 0 & 0 \\
0 & 0 & 0 & -\frac{cos\delta\theta_{PLL0}\omega_b}{Lg} & i_{oq0}\omega_b \\
0 & 0 & 0 & \frac{sin\delta\theta_{PLL0}\omega_b}{Lg} & -i_{od0}\omega_b \\
0 & 0 & 0 & 0 & 0 \\
0 & 0 & 0 & 0 & 0 \\
0 & 0 & 0 & 0 & 0 \\
0 & 0 & 0 & 0 & 0 \\
0 & 0 & 0 & 0 & 0 \\
0 & 0 & 0 & 0 & 0 \\
0 & 0 & 0 & 0 & 0 \\
0 & 0 & 0 & 0 & 0 \\
k_{17,1} & k_{17,2} & 0 & 0 & 0 \\
0 & 0 & \frac{\omega_b}{L_{dc}} & 0 & 0 \\
0 & 0 & 0 & 0 & 0 \\
1 & 0 & 0 & 0 & 0 \\
0 & -1 & 0 & 0 & 0
\end{pmatrix} \tag{A.1}$$

Elements of B-Matrix of PQ control converter

$$k_{17,1} = \frac{-i_{Ld0}K_{pc}K_{pp}\omega_b}{C_{dc}V_{dc0}}$$
$$k_{17,2} = \frac{i_{Lq0}K_{pc}K_{pp}\omega_b}{C_{dc}V_{dc0}}$$

A-Matrix for PQ control converter

$$
\begin{pmatrix}
0 & w_b w_{g0} & \frac{w_b}{C_f} & 0 & 0 & 0 & -\frac{w_b}{C_f} & 0 & 0 & 0 & 0 \\
-w_b w_{g0} & 0 & 0 & \frac{w_b}{C_f} & 0 & 0 & 0 & -\frac{w_b}{C_f} & 0 & 0 & 0 \\
-\frac{K_{AD} w_b}{L_c} & 0 & -\frac{K_{pc} w_b}{L_c} - \frac{R_c w_b}{L_c} & -w_b \varepsilon_{PLL0} K_{i,PLL} & \frac{K_{ic} w_b}{L_c} & 0 & 0 & 0 & \frac{K_{AD} w_b}{L_c} & 0 & -\frac{K_{pc} K_{pp} w_b}{L_c} \\
0 & -\frac{K_{AD} w_b}{L_c} & w_b \varepsilon_{PLL0} K_{i,PLL} & -\frac{K_{pc} w_b}{L_c} - \frac{R_c w_b}{L_c} & 0 & \frac{K_{ic} w_b}{L_c} & 0 & 0 & 0 & \frac{K_{AD} w_b}{L_c} & 0 \\
0 & 0 & -1 & 0 & 0 & 0 & 0 & 0 & 0 & 0 & -K_{pp} \\
0 & 0 & 0 & -1 & 0 & 0 & 0 & 0 & 0 & 0 & 0 \\
\frac{w_b}{L_g} & 0 & 0 & 0 & 0 & 0 & -\frac{R_g w_b}{L_g} & w_b w_{g0} & 0 & 0 & 0 \\
0 & \frac{w_b}{L_g} & 0 & 0 & 0 & 0 & -w_b w_{g0} & -\frac{R_g w_b}{L_g} & 0 & 0 & 0 \\
\omega_{AD} & 0 & 0 & 0 & 0 & 0 & 0 & 0 & -\omega_{AD} & 0 & 0 \\
0 & \omega_{AD} & 0 & 0 & 0 & 0 & 0 & 0 & 0 & -\omega_{AD} & 0 \\
i_{od0}\omega_{PQ} & i_{oq0}\omega_{PQ} & 0 & 0 & 0 & 0 & V_{od0}\omega_{PQ} & 0 & 0 & 0 & -\omega_{PQ} \\
-i_{oq0}\omega_{PQ} & i_{od0}\omega_{PQ} & 0 & 0 & 0 & 0 & 0 & -V_{od0}\omega_{PQ} & 0 & 0 & 0 \\
\omega_{LP,PLL} & 0 & 0 & 0 & 0 & 0 & 0 & 0 & 0 & 0 & 0 \\
0 & \omega_{LP,PLL} & 0 & 0 & 0 & 0 & 0 & 0 & 0 & 0 & 0 \\
0 & 0 & 0 & 0 & 0 & 0 & 0 & 0 & 0 & 0 & 0 \\
0 & 0 & 0 & 0 & 0 & 0 & 0 & 0 & 0 & 0 & 0 \\
\frac{i_{Ld0}(K_{AD}-1)w_b}{C_{dc}V_{dc0}} & \frac{i_{Lq0}(K_{AD}-1)w_b}{C_{dc}V_{dc0}} & C_{17,3} & C_{17,4} & -\frac{i_{Ld0}K_{ic}w_b}{C_{dc}V_{dc0}} & -\frac{i_{Lq0}K_{ic}w_b}{C_{dc}V_{dc0}} & 0 & 0 & -\frac{i_{Ld0}K_{AD}w_b}{C_{dc}V_{dc0}} & -\frac{i_{Lq0}K_{AD}w_b}{C_{dc}V_{dc0}} & \frac{i_{Ld0}K_{pc}K_{pp}w_b}{C_{dc}V_{dc0}} \\
0 & 0 & 0 & 0 & 0 & 0 & 0 & 0 & 0 & 0 & 0 \\
0 & 0 & 0 & 0 & 0 & 0 & 0 & 0 & 0 & 0 & 0 \\
0 & 0 & 0 & 0 & 0 & 0 & 0 & 0 & 0 & 0 & -1 \\
0 & 0 & 0 & 0 & 0 & 0 & 0 & 0 & 0 & 0 & 0
\end{pmatrix}
$$

$$
\begin{pmatrix}
0 & 0 & 0 & 0 & 0 & 0 & 0 & 0 & 0 & 0 & 0 \\
0 & 0 & 0 & 0 & 0 & 0 & 0 & 0 & 0 & 0 & 0 \\
-\frac{K_{pc}K_{pp}w_b}{L_c} & 0 & 0 & -\frac{i_{Lq0}w_b K_{p,PLL}}{V_{od0}} & -i_{Lq0}w_b K_{i,PLL} & 0 & \frac{K_{pc}w_b K_{AD,dc}}{L_c} & 0 & -\frac{K_{pc}w_b K_{AD,dc}}{L_c} & \frac{K_{ip}K_{pc}w_b}{L_c} & 0 \\
0 & \frac{K_{pc}K_{pp}w_b}{L_c} & 0 & \frac{i_{Ld0}w_b K_{p,PLL}}{V_{od0}} & i_{Ld0}w_b K_{i,PLL} & 0 & 0 & 0 & 0 & 0 & \frac{K_{ip}K_{pc}w_b}{L_c} \\
-K_{pp} & 0 & 0 & 0 & 0 & 0 & K_{AD,dc} & 0 & -K_{AD,dc} & K_{ip} & 0 \\
0 & K_{pp} & 0 & 0 & 0 & 0 & 0 & 0 & 0 & 0 & K_{ip} \\
0 & 0 & 0 & 0 & 0 & \frac{\sin(\Delta\theta_{PLL0})V_{g0}w_b}{L_g} & 0 & 0 & 0 & 0 & 0 \\
0 & 0 & 0 & 0 & 0 & \frac{\cos(\Delta\theta_{PLL0})V_{g0}w_b}{L_g} & 0 & 0 & 0 & 0 & 0 \\
0 & 0 & 0 & 0 & 0 & 0 & 0 & 0 & 0 & 0 & 0 \\
0 & 0 & 0 & 0 & 0 & 0 & 0 & 0 & 0 & 0 & 0 \\
-\omega_{PQ} & 0 & 0 & 0 & 0 & 0 & 0 & 0 & 0 & 0 & 0 \\
0 & -\omega_{PQ} & 0 & 0 & 0 & 0 & 0 & 0 & 0 & 0 & 0 \\
0 & 0 & -\omega_{LP,PLL} & 0 & 0 & 0 & 0 & 0 & 0 & 0 & 0 \\
0 & 0 & 0 & -\omega_{LP,PLL} & 0 & 0 & 0 & 0 & 0 & 0 & 0 \\
0 & 0 & 0 & \frac{1}{V_{od0}} & 0 & 0 & 0 & 0 & 0 & 0 & 0 \\
0 & 0 & 0 & \frac{w_b K_{p,PLL}}{V_{od0}} & w_b K_{i,PLL} & 0 & 0 & 0 & 0 & 0 & 0 \\
\frac{i_{Ld0}K_{pc}K_{pp}w_b}{C_{dc}V_{dc0}} & -\frac{i_{Lq0}K_{pc}K_{pp}w_b}{C_{dc}V_{dc0}} & 0 & 0 & 0 & 0 & C_{17,17} & \frac{wb}{C_{dc}} & \frac{i_{Ld0}K_{pc}w_b K_{AD,dc}}{C_{dc}V_{dc0}} & -\frac{i_{Ld0}K_{ip}K_{pc}w_b}{C_{dc}V_{dc0}} & -\frac{i_{Lq0}K_{ip}K_{pc}w_b}{C_{dc}V_{dc0}} \\
0 & 0 & 0 & 0 & 0 & 0 & -\frac{w_b}{L_{dc}} & -\frac{R_{dc}w_b}{L_{dc}} & 0 & 0 & 0 \\
0 & 0 & 0 & 0 & 0 & 0 & \omega_{AD,dc} & 0 & -\omega_{AD,dc} & 0 & 0 \\
-1 & 0 & 0 & 0 & 0 & 0 & 0 & 0 & 0 & 0 & 0 \\
0 & 1 & 0 & 0 & 0 & 0 & 0 & 0 & 0 & 0 & 0
\end{pmatrix}
$$

Elements of A-Matrix of PQ control converter

$$C_{17,3} = -\frac{-2i_{Ld0}k_{pc}\omega_b + V_{od0}\omega_b + k_{\text{ic}}i_{Ld0}\omega_b + k_{ip}k_{pc}\gamma_{\text{P0}}\omega_b}{C_{\text{dc}}V_{\text{dc0}}}$$

$$C_{17,4} = -\frac{-2i_{Lq0}k_{pc}\omega_b + k_{ic}i_{Lq0}\omega_b + k_{ip}k_{pc}\gamma_{\text{Q0}}\omega_b}{C_{\text{dc}}V_{\text{dc0}}}$$

$$C_{17,17} = -\frac{\omega_b k_{pc}i_{Ld0}^2 - \left(V_{od0} + k_{ic}i_{Ld0} + k_{pc}\left(k_{ip}\gamma_{P0} - V_{dc0}k_{AD,dc}\right)\right)i_{Ld0}}{C_{dc}V_{dc0}^2} + \frac{\omega_b i_{Lq0}\left(i_{Lq0}k_{pc} - k_{ip}\gamma_{Q0}k_{pc} - k_{ic}i_{Lq0}\right)}{C_{dc}V_{dc0}^2}$$

**Table A.1:** The investigated two-terminal DC system parameters

| Parameter | Value |
|---|---|
| Rated Power, $S_b$ | 150 kVA |
| Rated AC voltage | 280 V |
| Rated frequecy | 50 Hz |
| Rated DC voltage | 500 V |
| Trans. inductance | 0.04 pu |
| Trans. resistance | 0.005 pu |
| Grid inductance | 0.16 pu |
| X/R ratio | 7 |
| Series inductance and resistance of VSC-A | 1.55 mH, 0.01 Ω |
| Filter Capacitance of P-VSC | 50 $\mu$F ($\Delta - Connection$) |
| DC link capacitance of P-VSC | 3 mF |
| Series inductance and resistance of VSC-B | 2.1 mH, 0.01 Ω |
| Filter Capacitance of Vdc-VSC | 75 $\mu$F ($\Delta - Connection$) |
| DC link capacitance of Vdc-VSC | 3 mF |
| DC line inductance and resistance | 1.66 mH and 0.2Ω |

# Bibliography


[1] N. Flourentzou, V. G. Agelidis and G. D. Demetriades, "Vsc-based hvdc power transmission systems: An overview", *IEEE Transactions on Power Electronics*, vol. 24, no. 3, pp. 592–602, 2009.

[2] D. Povh, "Use of hvdc and facts", *Proceedings of the IEEE*, vol. 88, no. 2, pp. 235–245, 2000.

[3] B. Andersen and C. Barker, "A new era in hvdc?", *IEE Review*, vol. 46, no. 2, pp. 33–39, 2000.

[4] Y. Zhou, D. Zhuojiang and Y. Fenwang, "The development of hvdc transmission system", in *2012 Third International Conference on Digital Manufacturing Automation*, 2012, pp. 907–910.

[5] *List of hvdc projects*, Accessed 01 Feb 2017. [Online]. Available: https://en.wikipedia.org/wiki/List_of_HVDC_projects.

[6] H. Rao, "Architecture of nan'ao multi-terminal vsc-hvdc system and its multi-functional control", *CSEE Journal of Power and Energy Systems*, vol. 1, no. 1, pp. 9–18, 2015.

[7] G. D. Kamalapur, V. R. Sheelavant, S. Hyderabad, A. Pujar, S. Baksi and A. Patil, "Hvdc transmission in india", *IEEE Potentials*, vol. 33, no. 1, pp. 22–27, 2014.

[8] X. Chen, H. Sun, J. Wen, W. J. Lee, X. Yuan, N. Li and L. Yao, "Integrating wind farm to the grid using hybrid multiterminal hvdc technology", *IEEE Transactions on Industry Applications*, vol. 47, no. 2, pp. 965–972, 2011.

[9] C. Wolff and T. Elberling, "Kontek hvdc cable link", *IEEE Power Engineering Review*, vol. 20, no. 10, pp. 16–17, 2000.

[10] S. Taggart, G. James, Z. Dong and C. Russell, "The future of renewables linked by a transnational asian grid", *Proceedings of the IEEE*, vol. 100, no. 2, pp. 348–359, 2012.

[11] J. Lin, "Integrating the first hvdc-based offshore wind power into pjm system -a real project case study", *IEEE Transactions on Industry Applications*, vol. 52, no. 3, pp. 1970–1978, 2016.

[12] G. Asplund, "Ultra high voltage transmission", *ABB Rev*, vol. 2, pp. 22–27, 2007.

[13] W. Wang, A. Beddard, M. Barnes and O. Marjanovic, "Analysis of active power control for vsc-hvdc", *IEEE Transactions on Power Delivery*, vol. 29, no. 4, pp. 1978–1988, 2014.

[14] M. Saeedifard and R. Iravani, "Dynamic performance of a modular multilevel back-to-back hvdc system", *IEEE Transactions on Power Delivery*, vol. 25, no. 4, pp. 2903–2912, 2010.

[15] J. Qin and M. Saeedifard, "Predictive control of a modular multilevel converter for a back-to-back hvdc system", *IEEE Transactions on Power Delivery*, vol. 27, no. 3, pp. 1538–1547, 2012.

[16] A. Nami, J. Liang, F. Dijkhuizen and G. D. Demetriades, "Modular multilevel converters for hvdc applications: Review on converter cells and functionalities", *IEEE Transactions on Power Electronics*, vol. 30, no. 1, pp. 18–36, 2015.

[17] G. T. Son, H. J. Lee, T. S. Nam, Y. H. Chung, U. H. Lee, S. T. Baek, K. Hur and J. W. Park, "Design and control of a modular multilevel hvdc converter with redundant power modules for noninterruptible energy transfer", *IEEE Transactions on Power Delivery*, vol. 27, no. 3, pp. 1611–1619, 2012.

[18] K. Friedrich, "Modern hvdc plus application of vsc in modular multilevel converter topology", in *2010 IEEE International Symposium on Industrial Electronics*, 2010, pp. 3807–3810.

[19] B. Gemmell, J. Dorn, D. Retzmann and D. Soerangr, "Prospects of multilevel vsc technologies for power transmission", in *2008 IEEE/PES Transmission and Distribution Conference and Exposition*, 2008, pp. 1–16.

[20] S. Debnath, J. Qin, B. Bahrani, M. Saeedifard and P. Barbosa, "Operation, control, and applications of the modular multilevel converter: A review", *IEEE Transactions on Power Electronics*, vol. 30, no. 1, pp. 37–53, 2015.

[21] C. Oates, "Modular multilevel converter design for vsc hvdc applications", *IEEE Journal of Emerging and Selected Topics in Power Electronics*, vol. 3, no. 2, pp. 505–515, 2015.

[22] G. P. Adam and B. W. Williams, "Half- and full-bridge modular multilevel converter models for simulations of full-scale hvdc links and multiterminal dc grids", *IEEE Journal of Emerging and Selected Topics in Power Electronics*, vol. 2, no. 4, pp. 1089–1108, 2014.

[23] S. Cole, K Karoui, T. K. Vrana, O. Fosso, J Curis, A Denis and C. C. Liu, "A european supergrid: Present state and future challenges", in *Proc. 17th Power Systems Computation Conference*, 2011.

[24] A. Orths, D. Green, L. Fisher, E. Pelgrum and F. Georges, "The european north- sea countries offshore grid initiative - results", in *2013 IEEE Power Energy Society General Meeting*, 2013.

[25] *Hvdc links in europe*, Accessed 01 Feb 2017. [Online]. Available: http://www.eee.manchester.ac.uk/our-research/research-groups/pc/researchareas/powerelectronics/vsc/.

[26] W. Qiao and Y. Mao, "Overview of shanghai hvdc flexible transmission demonstration project", *East China Electr Power*, vol. 37, no. 7, pp. 1137–1140, 2011.

[27] *State grid corporation of china, zhejiang zhoushan islands multi-terminal hvdc flexible projects have been approved*, http://www.sgcc.com.cn/ywlm/mediacenter/corporatenews/07/308893.shtml, Accessed 01 Feb 2017.

[28] *Abb news: Borwin1*, http://new.abb.com/systems/hvdc/references/borwin1, Accessed 01 Feb 2017.

[29] *Statnett: Skagerrak-4*, http://www.statnett.no/en/Projects/Skagerrak-4/, Accessed 01 Feb 2017.

[30] *Hvdc projects and benefits being proposed in the u.s.* http://blog.masfieldservices.com/hvdc-projects-and-benefits-being-proposed-in-the-u-s/, Accessed 01 Feb 2017.

[31] *Renewa: Dirty electricity' probe at borwin1*, http://renews.biz/68145/dirty-electricity-probe-at-borwin1/, Accessed 11 June 2014.

[32] J. Lv, P. Dong, G. Shi, X. Cai, H. Rao and J. Chen, "Subsynchronous oscillation of large dfig-based wind farms integration through mmc-based hvdc", in *2014 International Conference on Power System Technology*, 2014, pp. 2401–2408.

[33] T. K. Vrana, Y. Yang, D. Jovcic, S. Dennetière, J. Jardini and H. Saad, "The cigre b4 dc grid test system", *Electra*, vol. 270, no. 1, pp. 10–19, 2013.

[34] P. Kundur, J. Paserba, V. Ajjarapu, G. Andersson, A. Bose, C. Canizares, N. Hatziargyriou, D. Hill, A. Stankovic, C. Taylor, T. V. Cutsem and V. Vittal, "Definition and classification of power system stability ieee/cigre joint task force on stability terms and definitions", *IEEE Transactions on Power Systems*, vol. 19, no. 3, pp. 1387–1401, 2004.

[35] P. Kundur, *Power System Stability And Control*. New York: McGraw-Hill, 1994.

[36] G. Pinares and M. Bongiorno, "Modeling and analysis of vsc-based hvdc systems for dc network stability studies", *IEEE Transactions on Power Delivery*, vol. 31, no. 2, pp. 848–856, 2016.

[37] Y. Song and C. Breitholtz, "Nyquist stability analysis of an ac-grid connected vsc-hvdc system using a distributed parameter dc cable model", *IEEE Transactions on Power Delivery*, vol. 31, no. 2, pp. 898–907, 2016.

[38] J. Beerten, S. Cole and R. Belmans, "Modeling of multi-terminal vsc hvdc systems with distributed dc voltage control", *IEEE Transactions on Power Systems*, vol. 29, no. 1, pp. 34–42, 2014.

[39] J. Beerten and R. Belmans, "Analysis of power sharing and voltage deviations in droop-controlled dc grids", *IEEE Transactions on Power Systems*, vol. 28, no. 4, pp. 4588–4597, 2013.

[40] M. K. Zadeh, M. Amin, J. A. Suul, M. Molinas and O. B. Fosso, "Small-signal stability study of the cigre dc grid test system with analysis of participation factors and parameter sensitivity of oscillatory modes", in *2014 Power Systems Computation Conference*, 2014, pp. 1–8.

[41] G. O. Kalcon, G. P. Adam, O. Anaya-Lara, S. Lo and K. Uhlen, "Small-signal stability analysis of multi-terminal vsc-based dc transmission systems", *IEEE Transactions on Power Systems*, vol. 27, no. 4, pp. 1818–1830, 2012.

[42] M. Amin, M. Zadeh, J. A. Suul, E. Tedeschi, M. Molinas and O. B. Fosso, "Stability analysis of interconnected ac power systems with multi-terminal dc grids based on the cigre dc grid test system", in *3rd Renewable Power Generation Conference (RPG 2014)*, 2014.

[43] J. Beerten, S. D'Arco and J. A. Suul, "Identification and small-signal analysis of interaction modes in vsc mtdc systems", *IEEE Transactions on Power Delivery*, vol. 31, no. 2, pp. 888–897, 2016.

[44] M. Amin, Rygg and M. Molinas, "Impedance-based and eigenvalue based stability assessment compared in vsc-hvdc system", in *8th Annual IEEE Energy Conversion Congress & Exposition (ECCE 2016)*, Sep. 2016, pp. 1–8.

[45] R. D. Middlebrook, "Input filter considerations in design and application of switching regulators", in *1976 IEEE Ind. Appl. Soc. Annu. Meeting*, 1976, pp. 366–382.

[46] J. Sun, "Impedance-based stability criterion for grid-connected inverters", *IEEE Transactions on Power Electronics*, vol. 26, no. 11, 2011.

[47] M. Cespedes and J. Sun, "Impedance modeling and analysis of grid-connected voltage-source converters", *IEEE Transactions on Power Electronics*, vol. 29, no. 3, pp. 1254–1261, 2014.

[48] M. Cespedes and J. Sun, "Modeling and mitigation of harmonic resonance between wind turbines and the grid", in *2011 IEEE Energy Conversion Congress and Exposition*, Sep. 2011, pp. 2109–2116.

[49] H. Liu and J. Sun, "Voltage stability and control of offshore wind farms with ac collection and hvdc transmission", *IEEE Journal of Emerging and Selected Topics in Power Electronics*, vol. 2, no. 4, pp. 1181–1189, 2014.

[50] B. Wen, D. Dong, D. Boroyevich, R. Burgos, P. Mattavelli and Z. Shen, "Impedance-based analysis of grid-synchronization stability for three-phase paralleled converters", *IEEE Transactions on Power Electronics*, vol. 31, no. 1, pp. 26–38, 2016.

[51] B. Wen, D. Boroyevich, R. Burgos, P. Mattavelli and Z. Shen, "Analysis of d-q small-signal impedance of grid-tied inverters", *IEEE Transactions on Power Electronics*, vol. 31, no. 1, pp. 675–687, 2016.

[52] R. Burgos, D. Boroyevich, F. Wang, K. Karimi and G. Francis, "On the ac stability of high power factor three-phase rectifiers", in *2010 IEEE Energy Conversion Congress and Exposition*, 2010, pp. 2047–2054.

[53] B. Wen, D. Boroyevich, R. Burgos, P. Mattavelli and Z. Shen, "Small-signal stability analysis of three-phase ac systems in the presence of constant power loads based on measured d-q frame impedances", *IEEE Transactions on Power Electronics*, vol. 30, no. 10, 2015.

[54] B. Wen, D. Boroyevich, R. Burgos, P. Mattavelli and Z. Shen, "D-q impedance specification for balanced three-phase ac distributed power system", in *2015 IEEE Applied Power Electronics Conference and Exposition (APEC)*, 2015, pp. 2757–2771.

[55] M. Amin and M. Molinas, "Understanding the origin of oscillatory phenomena observed between wind farms and hvdc systems", *IEEE Journal of Emerging and Selected Topics in Power Electronics*, vol. 5, no. 1, pp. 378–392, 2017.

[56] A. Rygg, M. Molinas, C. Zhang and X. Cai, "A modified sequence-domain impedance definition and its equivalence to the dq-domain impedance definition for the stability analysis of ac power electronic systems", *IEEE Journal of Emerging and Selected Topics in Power Electronics*, vol. 4, no. 4, pp. 1383–1396, 2016.

[57] S. Shah and L. Parsa, "Sequence domain transfer matrix model of three-phase voltage source converters", in *2016 IEEE Power and Energy Society General Meeting (PESGM)*, 2016, pp. 1–5.

[58] L. Xu, L. Fan and Z. Miao, "Dc impedance-model-based resonance analysis of a vsc-hvdc system", *IEEE Transactions on Power Delivery*, vol. 30, no. 3, pp. 1221–1230, 2015.

[59] M. Amin, M. Molinas, J. Lyu and X. Cai, "Impact of power flow direction on the stability of vsc-hvdc seen from the impedances nyquist plot", *IEEE Transactions on Power Electronics*, vol. 32, no. 10, pp. 8204–8217, 2017.

[60] L. Xu and L. Fan, "Impedance-based resonance analysis in a vsc-hvdc system", *IEEE Transactions on Power Delivery*, vol. 28, no. 4, pp. 2209–2216, 2013.

[61] S. Lissandron, L. D. Santa, P. Mattavelli and B. Wen, "Experimental validation for impedance-based small-signal stability analysis of single-phase interconnected power systems with grid-feeding inverters", *IEEE Journal of Emerging and Selected Topics in Power Electronics*, vol. 4, no. 1, pp. 103–115, 2016.

[62] H. Liu, S. Shah and J. Sun, "An impedance-based approach to hvdc system stability analysis and control development", in *2014 International Power Electronics Conference (IPEC-Hiroshima 2014 - ECCE ASIA)*, 2014, pp. 967–974.

[63] J. Sun, "Autonomous local control and stability analysis of multiterminal dc systems", *IEEE Journal of Emerging and Selected Topics in Power Electronics*, vol. 3, no. 4, pp. 1078–1089, 2015.

[64] B. Wen, D. Boroyevich, R. Burgos, P. Mattavelli and Z. Shen, "Inverse nyquist stability criterion for grid-tied inverters", *IEEE Transactions on Power Electronics*, vol. 32, no. 2, pp. 1548–1556, 2017.

[65] J. Lyu, X. Cai and M. Molinas, "Frequency domain stability analysis of mmc-based hvdc for wind farm integration", *IEEE Journal of Emerging and Selected Topics in Power Electronics*, vol. 4, no. 1, pp. 141–151, 2016.

[66] M. Bradt, B. Badrzadeh, E. Camm, D. Mueller, J. Schoene, T. Siebert, T. Smith, M. Starke and R. Walling, "Harmonics and resonance issues in wind power plants", in *2011 IEEE Power and Energy Society General Meeting*, 2011, pp. 1–8.

[67] L. Fan and Z. Miao, "Mitigating ssr using dfig-based wind generation", *IEEE Transactions on Sustainable Energy*, vol. 3, no. 3, pp. 349–358, 2012.

[68] K. N. B. M. Hasan, K. Rauma, A. Luna, J. I. Candela and P. Rodriguez, "Harmonic compensation analysis in offshore wind power plants using hybrid filters", *IEEE Transactions on Industry Applications*, vol. 50, no. 3, pp. 2050–2060, 2014.

[69] L. Wang, X. Xie, Q. Jiang, H. Liu, Y. Li and H. Liu, "Investigation of ssr in practical dfig-based wind farms connected to a series-compensated power system", *IEEE Transactions on Power Systems*, vol. 30, no. 5, pp. 2772–2779, 2015.

[70] N. Prabhu and K. R. Padiyar, "Investigation of subsynchronous resonance with vsc-based hvdc transmission systems", *IEEE Transactions on Power Delivery*, vol. 24, no. 1, pp. 433–440, 2009.

[71] R. K. Varma, S. Auddy and Y. Semsedini, "Mitigation of subsynchronous resonance in a series-compensated wind farm using facts controllers", *IEEE Transactions on Power Delivery*, vol. 23, no. 3, pp. 1645–1654, 2008.

[72] Y. Mishra, S. Mishra, F. Li, Z. Y. Dong and R. C. Bansal, "Small-signal stability analysis of a dfig-based wind power system under different modes of operation", *IEEE Transactions on Energy Conversion*, vol. 24, no. 4, pp. 972–982, 2009.

[73] G. B. Diaz, J. A. Suul and S. D'Arco, "Small-signal state-space modeling of modular multilevel converters for system stability analysis", in *2015 IEEE Energy Conversion Congress and Exposition (ECCE)*, 2015.

[74] Y. Wang, X. Wang, F. Blaabjerg and Z. Chen, "Harmonic instability assessment using state-space modeling and participation analysis in inverter-fed power systems", *IEEE Transactions on Industrial Electronics*, vol. 64, no. 1, pp. 806–816, 2017.

[75] M. Amin and M. Molinas, "Impedance based stability analysis of vsc-based hvdc system", in *2015 IEEE Eindhoven PowerTech*, 2015, pp. 1–6.

[76] L. Ljung, *System Identification: Theory for the User*. Prentice Hall PTR, 1999.

[77] B. Wahlberg, "System identification using kautz models", *IEEE Transactions on Automatic Control*, vol. 39, no. 6, pp. 1276–1282, 1994.

[78] M. Amin, J. A. Suul, S. D'Arco, E. Tedeschi and M. Molinas, "Impact of state-space modelling fidelity on the small-signal dynamics of vsc-hvdc systems", in *11th IET International Conference on AC and DC Power Transmission*, 2015.

[79] M. Amin and M. Molinas, "Small-signal stability assessment of power electronics based power systems: A discussion of impedance- and eigenvalue-based methods", *IEEE Transactions on Industry Application*, vol. 53, no. 5, 2017.

[80] M. Amin and M. Molinas, "A grey-box method for controller parameter estimation in hvdc-connected wind farms based on non-parametric impedance", *IEEE Transaction on Industrial Electronics*, 2017, In review.

[81] M. Amin, A. Ardal and M. Molinas, "Self-synchronisation of wind farm in mmc-based hvdc system: A stability investigation", *IEEE Transactions on Energy Conversion*, vol. 32, no. 2, pp. 458–470, 2017.

[82] V. Blasko and V. Kaura, "A new mathematical model and control of a three-phase ac-dc voltage source converter", *IEEE Transactions on Power Electronics*, vol. 12, no. 1, pp. 116–123, 1997.

[83] N. Kroutikova, C. A. Hernandez-Aramburo and T. C. Green, "State-space model of grid-connected inverters under current control mode", *IET Electric Power Applications*, vol. 1, no. 3, pp. 329–338, 2007.

[84] S. D'Arco, J. A. Suul and M. Molinas, "Implementation and analysis of a control scheme for damping of oscillations in vsc-based hvdc grids", in *2014 16th International Power Electronics and Motion Control Conference and Exposition*, 2014.

[85] O. Mo, M. Hernes and K. Ljøkelsøy, "Active damping of oscillations in lc-filter for line connected, current controlled, pwm voltage source converters", in *Proc. 10th European Conf. Power Electron. Applicat*, 2003.

[86] V. Kaura and V. Blasko, "Operation of a phase locked loop system under distorted utility conditions", *IEEE Transactions on Industry Applications*, vol. 33, no. 1, 1997.

[87] *Digsilent powerfactory simulation software*, http://www.digsilent.de/index.php/products-powerfactory.html, Accessed: 2014-09-30.

[88] T. Midtsund, J. A. Suul and T. Undeland, "Evaluation of current controller performance and stability for voltage source converters connected to a weak grid", in *The 2nd International Symposium on Power Electronics for Distributed Generation Systems*, 2010, pp. 382–388.

[89] J. Z. Zhou and A. M. Gole, "Vsc transmission limitations imposed by ac system strength and ac impedance characteristics", in *10th IET International Conference on AC and DC Power Transmission (ACDC 2012)*, 2012.

[90] R. Ottersten, "On control of back-to-back converters and sensor-less induction machine drives", PhD thesis, Dept. Elect. Power Eng., Chalmers Univ. Technol., Gothenburg, Sweden, 2003.

[91] L. Harnefors, "Analysis of subsynchronous torsional interaction with power electronic converters", *IEEE Transactions on Power Systems*, vol. 22, no. 1, pp. 305–313, 2007.

[92] G. Francis, R. Burgos, D. Boroyevich, F. Wang and K. Karimi, "An algorithm and implementation system for measuring impedance in the d-q domain", in *2011 IEEE Energy Conversion Congress and Exposition*, 2011, pp. 3221–3228.

[93] A. Rygg, M. Molinas, C. Zhang and X. Cai, "Frequency-dependent source and load impedances in power systems based on power electronic converters", in *2016 Power Systems Computation Conference (PSCC)*, 2016.

[94] C. Bajracharya, M. Molinas, J. A. Suul and T. Undeland, "Understanding of tuning techniques of converter controllers for vsc-hvdc", in *Nordic Workshop on Power and Industrial Electronics (NORPIE)*, 2008.

[95] W. W. Weaver, R. D. Robinett, D. G. Wilson and R. C. Matthews, "Metastability of pulse power loads using the hamiltonian surface shaping method", *IEEE Transactions on Energy Conversion*, vol. 32, no. 2, pp. 820–828, 2017.

[96] O. Dranga, B. Buti, I. Nagy and H. Funato, "Stability analysis of nonlinear power electronic systems utilizing periodicity and introducing auxiliary state vector", *IEEE Transactions on Circuits and Systems I: Regular Papers*, vol. 52, no. 1, pp. 168–178, 2005.

[97] T. Hu, "A nonlinear-system approach to analysis and design of power-electronic converters with saturation and bilinear terms", *IEEE Transactions on Power Electronics*, vol. 26, no. 2, pp. 399–410, 2011.

[98] M. K. Zadeh, R. Gavagsaz-Ghoachani, J. P. Martin, B. Nahid-Mobarakeh, S. Pierfederici and M. Molinas, "Discrete-time modeling, stability analysis, and active stabilization of dc distribution systems with multiple constant power loads", *IEEE Transactions on Industry Applications*, vol. 52, no. 6, pp. 4888–4898, 2016.

[99] A. Rygg, M. Amin, M. Molinas and B. Gustavsen, "Apparent impedance analysis: A new method for power system stability analysis", in *2016 IEEE 17th Workshop on Control and Modeling for Power Electronics (COMPEL)*, 2016.

[100] N. S. Nise, *Control Systems Engineerin*. John Wiley & Sons, Inc. New York, NY, USA, 2000.

[101] P. Eykhoff, *System Identification*. Wiley, London, 1974.

[102] D. Chinarro, *System Engineering Applied to Fuenmayor Karst Aquifer (San JuliÃąn de Banzo, Huesca) and Collins Glacier (King George Island, Antarctica)*. Springer International Publishing, Switzerland, 2014.

[103] P. E. Wellstead, "Non-parametric methods of system identification", *Automatica*, vol. 17, no. 1, pp. 55 –69, 1981.

[104] Q. Wang and L. Chang, "An intelligent maximum power extraction algorithm for inverter-based variable speed wind turbine systems", *IEEE Transactions on Power Electronics*, vol. 19, no. 5, pp. 1242–1249, 2004.

[105] L. Harnefors, M. Bongiorno and S. Lundberg, "Input-admittance calculation and shaping for controlled voltage-source converters", *IEEE Transactions on Industrial Electronics*, vol. 54, no. 6, pp. 3323–3334, 2007.

[106] H. H. Rosenbrock, *Computer-Aided Control System Design*. NY: Academic Press, 1974, pp. 142–149.

[107] J. Huang, K. A. Corzine and M. Belkhayat, "Small-signal impedance measurement of power-electronics-based ac power systems using line-to-line current injection", *IEEE Transactions on Power Electronics*, vol. 24, no. 2, pp. 445–455, 2009.

[108] Q. C. Zhong and G. Weiss, "Synchronverters: Inverters that mimic synchronous generators", *IEEE Transactions on Industrial Electronics*, vol. 58, no. 4, pp. 1259–1267, 2011.

[109] Q. C. Zhong, P. L. Nguyen, Z. Ma and W. Sheng, "Self-synchronized synchronverters: Inverters without a dedicated synchronization unit", *IEEE Transactions on Power Electronics*, vol. 29, no. 2, pp. 617–630, 2014.

[110] J. A. Suul, S. D'Arco and G. Guidi, "Virtual synchronous machine-based control of a single-phase bi-directional battery charger for providing vehicle-to-grid services", *IEEE Transactions on Industry Applications*, vol. 52, no. 4, pp. 3234–3244, 2016.

[111] S. D'Arco and J. A. Suul, "Equivalence of virtual synchronous machines and frequency-droops for converter-based microgrids", *IEEE Transactions on Smart Grid*, vol. 5, no. 1, pp. 394–395, 2014.

[112] H. P. Beck and R. Hesse, "Virtual synchronous machine", in *2007 9th International Conference on Electrical Power Quality and Utilisation*, 2007.

[113] M. Ashabani and Y. A. R. I. Mohamed, "Novel comprehensive control framework for incorporating vscs to smart power grids using bidirectional synchronous-vsc", *IEEE Transactions on Power Systems*, vol. 29, no. 2, pp. 943–957, 2014.

[114] M. Ashabani, F. D. Freijedo, S. Golestan and J. M. Guerrero, "Inducverters: Pll-less converters with auto-synchronization and emulated inertia capability", *IEEE Transactions on Smart Grid*, vol. 7, no. 3, pp. 1660–1674, 2016.

[115] J. Alipoor, Y. Miura and T. Ise, "Power system stabilization using virtual synchronous generator with alternating moment of inertia", *IEEE Journal of Emerging and Selected Topics in Power Electronics*, vol. 3, no. 2, pp. 451–458, 2015.

[116] Q. C. Zhong, G. C. Konstantopoulos, B. Ren and M. Krstic, "Improved synchronverters with bounded frequency and voltage for smart grid integration", *IEEE Transactions on Smart Grid*, vol. PP, no. 99, 2017.

[117] Q. C. Zhong, Z. Ma, W. L. Ming and G. C. Konstantopoulos, "Grid-friendly wind power systems based on the synchronverter technology", *Energy Conversion and Management*, vol. 89, pp. 719–726, 2015.

[118] R. Aouini, B. Marinescu, K. B. Kilani and M. Elleuch, "Synchronverter-based emulation and control of hvdc transmission", *IEEE Transactions on Power Systems*, vol. 31, no. 1, pp. 278–286, 2016.

[119] S. Dong, Y. Chi and Y. Li, "Active voltage feedback control for hybrid multiterminal hvdc system adopting improved synchronverters", *IEEE Transactions on Power Delivery*, vol. 31, no. 2, pp. 445–455, 2016.

[120] C. Li, J. Xu and C. Zhao, "A coherency-based equivalence method for mmc inverters using virtual synchronous generator control", *IEEE Transactions on Power Delivery*, vol. 31, no. 3, pp. 1369–1378, 2016.

[121] J. J. Grainger and W. D. Stevenson, *Power System Analysis*. New York: McGraw-Hill, 1994.

[122] Z. Xu, H. Xiao and Z. Zhang, "Selection methods of main circuit parameters for modular multilevel converters", *IET Renewable Power Generation*, vol. 10, no. 6, pp. 788–797, 2016.

[123] Y. Li, "Arm inductance and sub-module capacitance selection in modular multilevel converter", Master's thesis, University of Tennessee, USA, 2013.

[124] M. Zygmanowski, B. Grzesik and R. Nalepa, "Capacitance and inductance selection of the modular multilevel converter", in *2013 15th European Conference on Power Electronics and Applications (EPE)*, 2013.

[125] L. M. Cunico, G. Lambert, R. P. Dacol, S. V. G. Oliveira and Y. R. de Novaes, "Parameters design for modular multilevel converter (mmc)", in *2013 Brazilian Power Electronics Conference*, 2013.

[126] M. Vatani, B. Bahrani, M. Saeedifard and M. Hovd, "Indirect finite control set model predictive control of modular multilevel converters", *IEEE Transactions on Smart Grid*, vol. 6, no. 3, pp. 1520–1529, 2015.

[127] A. Jamshidifar and D. Jovcic, "Small-signal dynamic dq model of modular multilevel converter for system studies", *IEEE Transactions on Power Delivery*, vol. 31, no. 1, pp. 191–199, 2016.

[128] J. Beerten, G. B. Diaz, S. D'Arco and J. A. Suul, "Comparison of small-signal dynamics in mmc and two-level vsc hvdc transmission schemes", in *2016 IEEE International Energy Conference (ENERGYCON)*, 2016.

[129] D. N. Zmood, D. G. Holmes and G. H. Bode, "Frequency-domain analysis of three-phase linear current regulators", *IEEE Transactions on Industry Applications*, vol. 37, no. 2, pp. 601–610, 2001.

[130] R. Teodorescu, F. Blaabjerg, M. Liserre and P. C. Loh, "Proportional-resonant controllers and filters for grid-connected voltage-source converters", *IEE Proceedings - Electric Power Applications*, vol. 153, no. 5, pp. 750–762, 2006.

[131] S. Rohner, S. Bernet, M. Hiller and R. Sommer, "Modelling, simulation and analysis of a modular multilevel converter for medium voltage applications", in *2010 IEEE International Conference on Industrial Technology*, 2010.

[132] Q. Tu, Z. Xu, H. Huang and J. Zhang, "Parameter design principle of the arm inductor in modular multilevel converter based hvdc", in *2010 International Conference on Power System Technology*, 2010.

[133] Q. Tu, Z. Xu and L. Xu, "Reduced switching-frequency modulation and circulating current suppression for modular multilevel converters", *IEEE Transactions on Power Delivery*, vol. 26, no. 3, pp. 2009–2017, 2011.

[134] L. Harnefors, A. Antonopoulos, S. Norrga, L. Angquist and H. P. Nee, "Dynamic analysis of modular multilevel converters", *IEEE Transactions on Industrial Electronics*, vol. 60, no. 7, pp. 2526–2537, 2013.